

**The Use of Visible Light Absorbing  
Bismuth-Containing Semiconductors  
as Heterogeneous Photocatalysts for  
Selective Chemical Transformations**

Christopher Adam Unsworth

Doctor of Philosophy

University of York

Chemistry

August 2017

## Abstract

Bismuth-containing semiconducting materials were used as visible light absorbing heterogeneous photocatalysts for selective chemical transformations. The work demonstrates the importance of kinetic control in achieving selectivity; either through photocatalyst inhibition or through the presence of reagents capable of fast reactions with known intermediates.

Bismuth oxide ( $\beta$ - $\text{Bi}_2\text{O}_3$ ), bismuth ferrite ( $\text{BiFeO}_3$ ), bismuth tungstate microflowers ( $\text{Bi}_2\text{WO}_6$ ) and bismuth vanadate nanoparticles ( $\text{nan-BiVO}_4$ ) were synthesised and characterised by PXRD, SEM, DRUVS and BET. The bismuth-containing oxides were compared as photocatalysts for the aerobic oxidation of benzyl alcohol. The highest benzyl alcohol conversion (88%) and benzaldehyde selectivity (95%) was achieved with the use of  $\text{nan-BiVO}_4$ . Further modifications to  $\text{nan-BiVO}_4$  resulted in materials that were less active for selective benzyl alcohol oxidation than unmodified  $\text{nan-BiVO}_4$ .

Further study of  $\text{nan-BiVO}_4$  as a heterogeneous photocatalysts for the selective oxidation of *para*-substituted benzyl alcohols was carried out. It was found that alcohol conversions and aldehyde selectivities were affected by by-product inhibition. The addition of 1 mol% 4-methoxybenzoic acid significantly reduced 4-methoxybenzyl alcohol conversion (to 49%). Isotopically labelled benzyl alcohols were used to show that  $\alpha$  C-H bond cleavage was not rate limiting. However, changes in charge carrier lifetimes observed using TRPLS suggested that the charge carriers associated to the lifetimes observed were relevant to benzyl alcohol oxidation.

Bismuth-containing semiconductors were also investigated as trifluoromethylation heterogeneous photocatalysts.  $\text{nan-BiVO}_4$  was capable of oxytrifluoromethylation of styrene via the reduction of Umemoto's reagents. The highly selective reaction produced the corresponding trifluoromethylated ketone in an 88% yield.

Platinised bismuth tungstate ( $0.15\text{-Pt-Bi}_2\text{WO}_6$ ) was found to give high conversions and product selectivities for the formation of Photo-Giese products (phenylacetic acid conversion = 99%, Photo-Giese product selectivity = 94%). Several coupling products were synthesised from different carboxylic acids and electron deficient alkenes. Competitive adsorption from by-products inhibition had an impact on acid conversions and Photo-Giese product selectivities.

# Table of Contents

Abstract .....	2
Table of Contents .....	3
Table of Figures, Schemes and Tables .....	8
Accompanying materials.....	20
Acknowledgements .....	21
Declaration .....	22
1 Introduction .....	23
1.1 Photocatalysis .....	23
1.2 Light absorbing semiconducting materials.....	28
1.3 Application of heterogeneous semiconducting photocatalysts .....	35
1.4 Understanding heterogeneous photocatalytic selectivity .....	37
1.4.1 Substrate attraction.....	38
1.4.2 Substrate adsorption .....	39
1.4.2.1 Size exclusion .....	39
1.4.2.2 Surface adsorbed transition states that aid selectivity .....	39
1.4.3 Intermediate and product desorption.....	46
1.4.4 Reactions in solution .....	47
1.5 Summary of selectivity and opportunities for investigation .....	50
1.6 Project aims .....	50
2 The Direct Comparison of Bismuth-Containing Semiconductors for the Heterogeneous Photocatalytic Oxidation of Benzyl Alcohol Selectivity into Benzaldehyde .....	52
2.1 Introduction .....	52
2.1.1 Bismuth containing semiconductors .....	52
2.1.2 Photocatalytic application of bismuth containing semiconductors .....	54
2.1.3 Comparing photocatalysts .....	56
2.1.4 Objectives.....	57

2.2	Materials synthesis and characterisation .....	57
2.2.1	Bismuth tungstate ( $\text{Bi}_2\text{WO}_6$ ) .....	58
2.2.2	Bismuth ferrite .....	62
2.2.3	Bismuth oxide .....	65
2.2.4	Bismuth vanadate .....	68
2.2.5	Photocatalyst comparison.....	71
2.3	Modifying bismuth vanadate.....	78
2.3.1	Heterojunction synthesis by milling .....	79
2.3.2	Doping.....	81
2.3.3	Modified bismuth vanadate catalyst comparison.....	83
2.4	Conclusions .....	84
3	Selective Benzyl Alcohol Oxidation and Product Inhibition using Bismuth Vanadate Nanoparticles .....	86
3.1	Introduction .....	86
3.1.1	Heterogeneous photocatalytic benzyl alcohol oxidation.....	86
3.1.2	Objectives.....	87
3.2	Selective benzyl alcohol oxidation.....	87
3.2.1	Kinetics and comparison to bulk $\text{BiVO}_4$ and Degussa P25 $\text{TiO}_2$ .....	87
3.2.2	Steric and electronic effects .....	92
3.2.3	Inhibition .....	95
3.2.4	Ketone and carboxylic acid inhibition .....	97
3.2.5	Catalyst recycling and stability .....	102
3.2.6	Mechanism .....	103
3.2.6.1	Use of isotopically labelled benzyl alcohols.....	103
3.2.6.2	Time resolved photoluminescence.....	107
3.2.6.3	Proposed mechanism .....	111
3.3	Conclusions .....	112

4	Heterogeneous Photocatalytic Trifluoromethylation .....	114
4.1	Introduction .....	114
4.1.1	Trifluoromethylation reagents.....	114
4.1.2	Thermal trifluoromethylation with copper.....	115
4.1.3	Photolytic trifluoromethylation.....	116
4.1.4	Objectives.....	119
4.2	Trifluoromethylation .....	119
4.2.1	Reduction of Umemoto 1 for the trifluoromethylation of styrene .....	119
4.2.2	Reduction of Umemoto 1 for the trifluoromethylation of aromatics .....	123
4.2.3	Attempted reduction of pyridyl trifluoroacetyl ester for the trifluoromethylation of aromatics .....	124
4.2.4	Catalyst degradation.....	126
4.3	Conclusions .....	129
5	Photo-Kolbe and Photo-Giese Chemistry with Platinised Bismuth-containing Semiconductors .....	130
5.1	Introduction .....	130
5.1.1	Photocatalyst adaptation.....	130
5.1.2	Photo-Kolbe chemistry.....	132
5.1.3	Visible light absorption and Photo-Giese chemistry.....	133
5.1.4	Objectives.....	135
5.2	Results and Discussion .....	135
5.2.1	Platinization and Characterisation.....	135
5.2.2	Attempted Photo-Kolbe dimerization .....	142
5.2.3	Photo-Giese C-C cross coupling .....	145
5.2.4	Optimisation.....	148
5.2.5	Substrate scope and inhibition .....	151
5.2.6	Catalyst recycling.....	160
5.3	Conclusion.....	163

6	Conclusions and Future Work.....	164
6.1	Conclusions .....	164
6.2	Future Work .....	165
7	Experimental .....	168
7.1	Characterisation.....	168
7.1.1	Semiconductor characterisation .....	168
7.1.2	Organic molecule characterisation.....	169
7.1.3	Blue LED calibration .....	170
7.1.4	Control experiments.....	171
7.2	Chapter 2 Experimental.....	172
7.2.1	Materials and Reagents .....	172
7.2.2	Bismuth ferrite ( $\text{BiFeO}_3$ ) synthesis <sup>177</sup> .....	172
7.2.3	Bismuth oxide nanoparticle ( $\beta\text{-Bi}_2\text{O}_3$ ) synthesis <sup>134</sup> .....	172
7.2.4	Bismuth tungstate nanoflower ( $\text{Bi}_2\text{WO}_6$ ) synthesis <sup>186</sup> .....	173
7.2.5	Ethylenediaminetetraacetic acid (EDTA) mediated bismuth vanadate nanoparticle (nan- $\text{BiVO}_4$ ) synthesis <sup>137</sup> .....	173
7.2.6	Bulk bismuth vanadate synthesis .....	173
7.2.7	Benzyl alcohol aerobic oxidation utilising blue light irradiated semiconducting photocatalysts .....	174
7.3	Chapter 3 Experimental.....	174
7.3.1	Materials and Reagents .....	174
7.3.2	Synthesis of $\alpha\text{-D}_2\text{-(4-methoxy)benzyl alcohol}$ .....	175
7.3.3	Synthesis of $^{18}\text{O}$ -labelled (4-methoxy)benzyl alcohol.....	175
7.3.4	Benzyl alcohol aerobic oxidation utilising blue light irradiated semiconducting nan- $\text{BiVO}_4$ .....	176
7.3.5	Time resolved photoluminescence spectroscopy.....	178
7.4	Chapter 4 Experimental.....	178
7.4.1	Materials and Reagents .....	178

7.4.2	Photocatalytic synthesis of 3,3,3-trifluoro-1-phenyl-propan-1-one (4.1) using blue light irradiated bismuth vanadate nanoparticles and Umemoto's reagent (5-(trifluoromethyl)dibenzothiophenium tetrafluoroborate).....	179
7.4.3	Photocatalytic synthesis of trifluoromethylated dibenzothiophene (4.5-4.8) using blue light irradiated bismuth vanadate nanoparticles (nan-BiVO <sub>4</sub> ) and Umemoto's reagent (5-(trifluoromethyl)dibenzothiophenium tetrafluoroborate) .	180
7.4.4	Trifluoromethylation of aromatics utilising blue light irradiated bismuth vanadate nanoparticles (nan-BiVO <sub>4</sub> ) and pyridyl trifluoroacetyl ester.....	182
7.5	Chapter 5 Experimental.....	185
7.5.1	Materials and Reagents .....	185
7.5.2	Photocatalytic formation of platinum nanoparticles on semiconductor surfaces (0.15-Pt-Bi <sub>2</sub> WO <sub>6</sub> and 0.15-Pt-BiVO <sub>4</sub> ) .....	185
7.5.3	Photocatalytic dimerization of phenylacetic acid using blue light irradiated 0.15-Pt-Bi <sub>2</sub> WO <sub>6</sub> .....	185
7.5.4	Photocatalytic Giese reaction between phenylacetic acid analogues and electron deficient alkenes initiated by blue light irradiated platinised bismuth tungstate (0.15-Pt-Bi <sub>2</sub> WO <sub>6</sub> ) .....	186
7.5.5	Photocatalytic Giese reaction between phenoxyacetic acid and electron deficient alkenes initiated by blue light irradiated platinised bismuth tungstate (0.15-Pt-Bi <sub>2</sub> WO <sub>6</sub> ).....	189
	Abbreviations and terms .....	192
	References .....	192

## Table of Figures, Schemes and Tables

Figure 1.1 – Organic molecules used as homogeneous photocatalysts .....	25
Figure 1.2 – Ruthenium and iridium centred homogeneous photocatalysts .....	27
Figure 1.3 – Simplified band theory showing the band structures of metals, semiconductor and insulators. $E_f$ shows the ..... Fermi energy of these generic solids. ....	28
Figure 1.4 - The wavefunctions for a chain of 1D periodically arranged atoms generated from Bloch functions where (a) $k = 0$ and (b) $k = \pi/a$ .....	29
Figure 1.5 - Energy against wavenumber for a 1D chain of atoms with overlapping s orbitals and overlapping p- $\sigma$ orbitals. The energy is derived from the linear combination of atomic orbitals on this chain. The values of $k$ are limited to $-\pi/a \leq k < \pi/a$ . ....	30
Figure 1.6 - The movement of a free electron along a 1D chain of periodically spaced atoms. (a) shows an electron with $\lambda = \pi/a$ ; (b) shows an electron with a wavelength much longer than the atomic spacing, $a$ . ....	31
Figure 1.7 - The energy of a free electron moving through a 1D chain of periodically spaced atoms, derived from free electron theory, against quantum wavenumber. The values of $k$ are limited to $-\pi/a \leq k < \pi/a$ . Deviations from free electron theory arise from the variation in potential from the periodically arranged atoms which has a maximal effect when $k = \pm \pi/a$ . ....	33
Figure 1.8 - Polarons in a solid lattice of blue cations and orange anions. (a) shows a small polaron localised on one cation; (b) shows a large polaron that will move freely throughout the lattice, $R$ indicates the radius of lattice distortion caused by the polarons. ....	35
Figure 1.9 – Adsorption of nitrobenzene to silver metal supported by a titania photocatalyst. A model system of $Ti_4O_{10}H_4/Ag_4+C_6H_5NO_2$ was used to generate this optimised structure via DFT. Reprinted with permission from H. Tada, <i>ChemPhysChem</i> , 2005, <b>6</b> , 1537 – 1543. Copyright 2005 John Wiley & Sons. <sup>104</sup> .....	45
Figure 1.10 – (a) The ineffective desorption of benzaldehyde from $TiO_2$ which results in poor benzaldehyde selectivity (b) Effective desorption of benzaldehyde from $WO_3$ coated $TiO_2$ to ensure selective benzyl alcohol oxidation; (c) the suggested migration of charge showing the movement of photo-generated holes to titania and photoelectrons to	



WO <sub>3</sub> . Reprinted with permission from Y. Shiraishi, <i>Chem. Eur. J.</i> , 2011, <b>17</b> , 9816-9824. Copyright 2011 John Wiley & Sons. <sup>20</sup> .....	47
Figure 2.1 – The crystal structures of a) orthorhombic bismuth tungstate and b) monoclinic bismuth vanadate showing the channels of bismuth centres which can help charge carrier mobility through these materials. In a) green centres correspond to bismuth ions and in b) purple centres correspond to bismuth ions. Oxygen anions are in red and the grey colours show transition metal centred octahedra and tetrahedra in a) and b) respectively. a) Adapted with permission from M. Maczka, <i>J. Raman Spectrosc.</i> , 2010, <b>41</b> , 1059–1066. Published by John Wiley & Sons, Ltd. <sup>167</sup> b) Adapted with permission from M. Oshikiri, <i>J. Phys. Chem. B</i> , 2006, <b>110</b> , 9188-9194. Copyright 2006 American Chemical Society. <sup>168</sup> .....	53
Figure 2.2 – The density of states (black trace from XPS and XAS, grey trace from XES) and orbital characteristics around the bandgap of monoclinic bismuth vanadate. Adapted with permission from I. D Sharp, <i>Chem. Mater.</i> , 2014, <b>26</b> , 5365–5373. <sup>160</sup> Copyright 2014 American Chemical Society. ....	53
Figure 2.3 – SEM of Bi <sub>2</sub> WO <sub>6</sub> .....	59
Figure 2.4 - PXRD of Bi <sub>2</sub> WO <sub>6</sub> consistent with crystalline orthorhombic Bi <sub>2</sub> WO <sub>6</sub> (JCPDS No. 39-0256). ....	60
Figure 2.5 – N <sub>2</sub> isotherm for Bi <sub>2</sub> WO <sub>6</sub> .....	61
Figure 2.6 – The Tauc plot used to estimate the band-gap for the indirect semiconductor, Bi <sub>2</sub> WO <sub>6</sub> .....	61
Figure 2.7 – SEM of synthesised BiFeO <sub>3</sub> .....	63
Figure 2.8 – PXRD of BiFeO <sub>3</sub> consistent with rhombohedrally distorted perovskite bismuth ferrite (JCPDS No. 20-0169).....	64
Figure 2.9 – N <sub>2</sub> isotherm of BiFeO <sub>3</sub> .....	64
Figure 2.10 – The Tauc plot used to estimate the band-gap of the direct semiconductor, BiFeO <sub>3</sub> .....	65
Figure 2.11 – An illustration for the synthesis of β-Bi <sub>2</sub> O <sub>3</sub> with literature characterisation data. A) PXRD of the final β-Bi <sub>2</sub> O <sub>3</sub> and the intermediate Bi metal product. B), C) and D) SEM images of the final β-Bi <sub>2</sub> O <sub>3</sub> nanosphere. Adjusted with permission from J. Nan., <i>Appl. Catal. B</i> , 2013, <b>140–141</b> , 433–443. <sup>134</sup> Printed by Elsevier. ....	66
Figure 2.12 – SEM of β-Bi <sub>2</sub> O <sub>3</sub> flakes .....	67

Figure 2.13 – PXRD of $\beta$ -Bi <sub>2</sub> O <sub>3</sub> consistent with crystalline tetragonal bismuth oxide (JCPDS No. 78-1793). .....	67
Figure 2.14 – N <sub>2</sub> isotherm of $\beta$ -Bi <sub>2</sub> O <sub>3</sub> .....	68
Figure 2.15 – The Tauc plot used to estimate the band-gap of the direct semiconductor, $\beta$ -Bi <sub>2</sub> O <sub>3</sub> .....	68
Figure 2.16 - SEM of nan-BiVO <sub>4</sub> .....	69
Figure 2.17 – PXRD for nan-BiVO <sub>4</sub> consistent with crystalline monoclinic BiVO <sub>4</sub> (JCPDS no. 14-0688) .....	70
Figure 2.18 – N <sub>2</sub> isotherm for nan-BiVO <sub>4</sub> .....	70
Figure 2.19 - The Tauc plot used to estimate the band-gap of the indirect semiconductor, nan-BiVO <sub>4</sub> .....	71
Figure 2.20 – The adapted commercially available blue LED flood light (both off and on) and its emission spectrum showing emission wavelengths consistent with blue light only (400 to 560 nm).....	72
Figure 2.21 – The transmission of light through a >400 nm band pass filter, showing that light with wavelengths shorter than 400 nm pass through the filter. A 1 kW Hg[Xe] arc lamp was used as an emission source with a broad range of emission wavelengths in this region.....	73
Figure 2.22 – Gas chromatograph for the reaction mixture from the oxidation of benzyl alcohol selectively to benzaldehyde with blue light irradiated nan-BiVO <sub>4</sub> .....	73
Figure 2.23 – Benzyl alcohol calibration curve of concentration against GC peak area at a retention time of 3.0 min. The standard error for this linear regression was used to calculate error from the average differences between the data points and the linear regression. The error in peak area on each data point was calculated as +/- 0.4. ....	74
Figure 2.24 - Benzaldehyde calibration curve of concentration against GC peak area at a retention time of 2.7 min. The standard error for this linear regression was used to calculate error from the average differences between the data points and the linear regression. The error in peak area on each data point was calculated as +/- 0.3. ....	75
Figure 2.25 – Band positions for nan-BiVO <sub>4</sub> , Bi <sub>2</sub> WO <sub>6</sub> and $\beta$ -Bi <sub>2</sub> O <sub>3</sub> vs NHE. ....	77
Figure 2.26 – An SEM image and EDX mapping of BiVO <sub>4</sub> /Bi <sub>2</sub> WO <sub>6</sub> . The EDX mapping shows that V and W can be found throughout the sample.....	79

Figure 2.27 – PXRD for BiVO <sub>4</sub> /Bi <sub>2</sub> WO <sub>6</sub> . The peaks labelled V are consistent with crystalline monoclinic BiVO <sub>4</sub> (JCPDS no. 14-0688). The peaks labelled W are consistent with crystalline orthorhombic Bi <sub>2</sub> WO <sub>6</sub> (JCPDS No. 39-0256).....	80
Figure 2.28 – The Tauc plot used to estimate the band gap of BiVO <sub>4</sub> /Bi <sub>2</sub> WO <sub>6</sub> made up of indirect semiconductors .....	81
Figure 2.29 – SEM of a) Mo-doped BiVO <sub>4</sub> and b) W-doped BiVO <sub>4</sub> .....	82
Figure 2.30 – PXRD of a) Mo-doped BiVO <sub>4</sub> consistent with crystalline monoclinic BiVO <sub>4</sub> (JCPDS no. 14-0688) and b) W-doped BiVO <sub>4</sub> consistent with crystalline monoclinic BiVO <sub>4</sub> (JCPDS no. 14-0688) but also showing evidence of crystalline tetragonal schellite BiVO <sub>4</sub> (JCPDS no. 14-0133). .....	82
Figure 2.31 – The Tauc plots for used to estimate the band-gaps of a) Mo-doped BiVO <sub>4</sub> and b) W-doped BiVO <sub>4</sub> .....	83
Figure 3.1 – The conversion of 4-methoxybenzyl alcohol into 4-methoxybenzaldehyde as a function of time. Number of moles of starting material and product were obtained using <sup>1</sup> H NMR peak intensities against a known amount of maleic acid as an internal calibrant. The line for theoretical conversion was derived from the zero-order rate constant, $k_0 = 5.4 \text{ mmol dm}^{-3} \text{ h}^{-1}$ .....	88
Figure 3.2 – SEM of bulk BiVO <sub>4</sub> .....	89
Figure 3.3 – PXRD for bulk BiVO <sub>4</sub> . This data is consistent with crystalline monoclinic BiVO <sub>4</sub> (JCPDS no. 14-0688) .....	89
Figure 3.4 – Tauc plot showing the Kubelka-Munk function against photon energy for both bulk and nan-BiVO <sub>4</sub> .....	90
Figure 3.5 – An example <sup>1</sup> H NMR ( <i>d</i> <sub>6</sub> -DMSO, 400 MHz) from the oxidation of 4-methoxybenzyl alcohol and method for calculating conversion and selectivity. Reaction conditions: 0.1 mmol nan-BiVO <sub>4</sub> , 0.1 mmol 4-methoxybenzyl alcohol, 10 mL acetonitrile, 1 atm O <sub>2</sub> , 30 min blue LED irradiation. 100 μmol maleic acid was added and used an internal standard. ....	91
Figure 3.6 – The effect of the addition of para substituted benzaldehydes to the photooxidation of 4-methoxybenzyl alcohol by nan-BiVO <sub>4</sub> . Reaction conditions: 0.1 mmol nan-BiVO <sub>4</sub> , 0.1 mmol 4-methoxybenzyl alcohol, 10 mL acetonitrile and 1 atm dioxygen. Percentage conversions were calculated from <sup>1</sup> H NMR. ....	95

Figure 3.7 - A selection of the $^1\text{H}$ NMR spectra (400 MHz, $d_6$ -DMSO) for the 4-methoxybenzyl alcohol inhibition reactions using: a) 3 equiv. 4-methoxybenzaldehyde and b) 4 equiv. 4-methoxybenzaldehyde containing a signal consistent with the meta-protons of 4-methoxybenzoic acid, at 6.97 ppm. The signals have been integrated against a known amount of maleic acid. Other expected signals at 3.78 ( $\text{CH}_3\text{O}$ ) and 7.86 ppm ( $o\text{-H}_{\text{Ar}}$ ) consistent with 4-methoxybenzoic acid cannot be used for quantification due to overlap with signals attributable to 4-methoxybenzaldehyde. ....	97
Figure 3.8 – Inhibition of 4-methoxybenzyl alcohol conversion with various amounts of 4-methoxybenzoic acid. Mol% is relative to the amount of 4-methoxybenzyl alcohol. Reaction conditions: 0.1 mmol nan- $\text{BiVO}_4$ , 0.1 mmol 4-methoxybenzyl alcohol, 10 mL acetonitrile and 1 atm dioxygen. Percentage conversions were calculated from $^1\text{H}$ NMR. ....	99
Figure 3.9 – Gas Chromatograms for the oxidation of: a) 0.1 mmol 4-(trifluoromethyl)benzyl alcohol and b) 4-nitrobenzyl alcohol by 0.1 mmol blue light irradiated nan- $\text{BiVO}_4$ with 1 atm $\text{O}_2$ , 10 mL acetonitrile. Reaction time = 3 h. Gas Chromatography was performed on an Agilent/HP 6890, with an injection volume of 1 $\mu\text{L}$ , using compressed air as a carrier gas at 1 $\text{mL min}^{-1}$ , a flame ionised detector at 250 $^\circ\text{C}$ , and Chrompack DB-5ms column between 90 and 300 $^\circ\text{C}$ with ramp rate 20 $^\circ\text{C min}^{-1}$ . ....	100
Figure 3.10 – Recycle of nan- $\text{BiVO}_4$ (0.1 mmol) for the selective photooxidation of 4-methoxybenzyl alcohol (0.1 mmol per repeat) into 4-methoxybenzaldehyde, blue LED irradiation for 3 h for each reaction, 1 atm $\text{O}_2$ , 10 mL acetonitrile. ....	102
Figure 3.11 - PXRD for used nan- $\text{BiVO}_4$ . This data is consistent with crystalline monoclinic $\text{BiVO}_4$ (JCPDS no. 14-0688). ....	103
Figure 3.12 – SEM of used nan- $\text{BiVO}_4$ . The image shows agglomerated nanoparticles ca. 50 – 100 nm in size. ....	103
Figure 3.13 – The breaking of the 5 membered metallocycle proposed in literature that mediated O atom exchange in alcohol oxidation. O atoms coloured red were from a dioxygen molecule and O atoms coloured blue were from an alcohol molecule. <sup>258, 259</sup> ....	107
Figure 3.14 – a) Emission spectrum for a 1 $\text{mg mL}^{-1}$ dispersion of $\text{BiVO}_4$ dispersed in dry, nitrogen degassed acetonitrile, excitation wavelength = 380 nm. b) Decay curve for nan- $\text{BiVO}_4$ , excitation wavelength = 380 nm, emission wavelength = 440 nm. ....	108

Figure 3.15 – Formation energies for defect sites calculated using a model for n-type BiVO <sub>4</sub> and the transitions that lead to the emissions observed in Figure 3.14 energies quoted vs NHE. V <sub>vac</sub> – V vacancy; V <sub>Bi</sub> – V at a Bi site; V <sub>int</sub> – V in an interstitial site; O <sub>int</sub> – O in an interstitial site; Bi <sub>V</sub> – Bi at a V site; O <sub>vac</sub> – Bi vacancy; Bi <sub>vac</sub> – Bi vacancy. <sup>269</sup> .....	110
Figure 4.1 – The structures of trifluoromethylating reagents Umemoto 1 and Umemoto 2.....	115
Figure 4.2 – The major product of the oxytrifluoromethylation of styrene using blue light irradiated nan-BiVO <sub>4</sub> or Bi <sub>2</sub> WO <sub>6</sub> and Umemoto 1.....	120
Figure 4.3 – Structures of compounds <b>4.2</b> , <b>4.3</b> and <b>4.4</b> that are byproducts in the formation of compound <b>4.1</b> .....	120
Figure 4.4 – H-F HMBC (500 MHz, CDCl <sub>3</sub> ) for a mixture of compounds <b>4.5</b> , <b>4.6</b> , <b>4.7</b> and <b>4.8</b> formed from the reduction and rearrangement of Umemoto <b>1</b> by blue LED light irradiated nan-BiVO <sub>4</sub> .....	123
Figure 5.1 – Representation of the CoPi:BiVO <sub>4</sub> electrodes synthesised by Wang, Li et al. Reprinted with permission from C. Li, <i>J. Phys. Chem. C.</i> , 2012, <b>116</b> , 5082-5089. Copyright 2012 American Chemical Society. <sup>4</sup> .....	131
Figure 5.2 – An illustration the Schottky barrier that forms at the interface of a semiconductor and a metal nanoparticle. ....	131
Figure 5.3 - PXRD of 0.15-Pt-Bi <sub>2</sub> WO <sub>6</sub> consistent with crystalline orthorhombic Bi <sub>2</sub> WO <sub>6</sub> (JCPDS No. 39-0256). ....	138
Figure 5.4 - The Tauc plot used to estimate the band-gap for the indirect semiconductor, 0.15-Pt-Bi <sub>2</sub> WO <sub>6</sub> .....	138
Figure 5.5 – TEM images showing spherical nanoparticles on the surface of 0.15-Pt-Bi <sub>2</sub> WO <sub>6</sub> .....	139
Figure 5.6 – SAED of 0.15-Pt-Bi <sub>2</sub> WO <sub>6</sub> showing diffraction patterns of orthorhombic Bi <sub>2</sub> WO <sub>6</sub> and Pt metal.....	140
Figure 5.7 - PXRD of 0.15-Pt-BiVO <sub>4</sub> consistent with crystalline monoclinic BiVO <sub>4</sub> (JCPDS No. 14-0688). ....	140
Figure 5.8 - The Tauc plot used to estimate the band-gap for the indirect semiconductor, 0.15-Pt-BiVO <sub>4</sub> .....	141

Figure 5.9 – TEM images of 0.15-Pt-BiVO <sub>4</sub> .....	141
Figure 5.10 – Example gas chromatogram of the reaction mixture from the attempted dimerization of phenylacetic acid with blue LED light irradiated 0.15-Pt-BiVO <sub>4</sub> .....	142
Figure 5.11 – An example calibration curve for bibenzyl concentration against GC peak area for the peak with R <sub>t</sub> = 6.1 min that is characteristic of the presence of bibenzyl. The standard error for this linear regression was used to calculate error from the average differences between the data points and the linear regression. The error in peak area on each data point was calculated as +/- 0.8. ....	143
Figure 5.12 – Examples of the <sup>1</sup> H NMR peaks, recorded at 400 MHz in CDCl <sub>3</sub> , that give evidence of the successful coupling of a benzyl radical to methacrolein to form product <b>5.1</b> . a – the peak consistent with the methylene group adjacent to the phenyl group and another methylene group that is diastereotopically split. b – the peaks consistent with the diastereotopically split methylene group adjacent to functionalities b and c. c – the peak consistent with a methine group coupled to protons in methylene group, methyl group and the aldehyde proton. The peak given between 2.00 and 2.10 ppm also contains a singlet at 2.01 ppm consistent with an acetonitrile solvent impurity.....	146
Figure 5.13 – Full <sup>1</sup> H NMR spectrum (CDCl <sub>3</sub> , 400 MHz) of the crude reaction mixture of the 24 h Photo-Giese reaction of phenylacetic acid and methacrolein resulting in <b>5.1</b> formation. Other observable peaks present in this spectrum can be associated to trace starting materials (methacrolein - 6.3 ppm and phenylacetic acid – 3.6 ppm), products (bibenzyl - 2.8 ppm) and solvent impurity (acetonitrile – 2.0 ppm and water – 1.5 ppm). .....	147
Figure 5.14 – GC calibration curve for Photo-Giese product <b>5.1</b> showing concentration of product against peak area at R <sub>t</sub> = 4.8 min. The standard error for this linear regression was used to calculate error from the average differences between the data points and the linear regression. The error in peak area on each data point was calculated as +/- 0.3.	147
Figure 5.15 – An example gas chromatogram from a Photo-Giese reaction mixture coupling phenylacetic acid with methacrolein to form compound <b>5.1</b> with blue light irradiated 0.15-Pt-Bi <sub>2</sub> WO <sub>6</sub> .....	148
Figure 5.16 – A section of the <sup>1</sup> H NMR (400 MHz, d <sub>3</sub> -MeCN) of the crude reaction mixture from the Photo-Giese coupling reaction between phenylacetic acid and acrolein, showing peaks consistent with aliphatic proton environments found in <b>5.2</b> and a broad peak consistent with polymer formation. ....	153

Figure 5.17 – The $^1\text{H}$ NMR spectrum of compound <b>5.3</b> ( $\text{CDCl}_3$ , 400 MHz). .....	155
Figure 5.18 – Aliphatic region of the $^1\text{H}$ NMR spectrum of compound <b>5.4</b> ( $\text{CDCl}_3$ , 400 MHz) showing the complex multiplets that are characteristic of coupling of phenylacetic acid and $\alpha$ -methylene- $\gamma$ -butyrolactone and subsequent reduction and protonation. ....	155
Figure 5.19 - Aliphatic region of the $^1\text{H}$ NMR spectrum of compound <b>5.5</b> ( $\text{CDCl}_3$ , 400 MHz) showing the complex multiplets that are characteristic of coupling of phenoxyacetic acid and cyclohexenone and subsequent reduction and protonation. Solvent impurity (water in $\text{CDCl}_3$ – 1.6 ppm) is also observed in this spectrum. ....	159
Figure 5.20 – A graph showing the results of the catalyst recycling experiment for the Photo-Giese reaction between phenylacetic acid (0.1 mmol) and methacrolein (0.25 mmol) photocatalysed by blue LED irradiated 0.15-Pt- $\text{Bi}_2\text{WO}_6$ . Irradiation time was 15 h for each reaction, other conditions for each reaction include 3 mL dry acetonitrile and a $\text{N}_2$ atmosphere.....	161
Figure 5.21 – a) PXRD of 0.15-Pt- $\text{Bi}_2\text{WO}_6$ consistent with crystalline orthorhombic $\text{Bi}_2\text{WO}_6$ (JCPDS No. 39-0256); b) The Tauc plot used to estimate the band-gap for the indirect semiconductor, 0.15-Pt- $\text{Bi}_2\text{WO}_6$ . ....	161
Figure 5.22 – Section of ATRIR for the 0.15-Pt- $\text{Bi}_2\text{WO}_6$ photocatalyst before and after use in 5 Photo-Giese reactions coupling phenylacetic acid and methacrolein and inhibit the binding of phenylacetic acid and subsequently slow the rate of the intended Photo-Giese reaction.....	162
Scheme 1.1 – Heterogeneous photocatalysis using an irradiated semiconductor.....	34
Scheme 1.2 – Size exclusion for selective heterogeneous photocatalysis with $\text{Al}_2\text{O}_3$ coated $\text{TiO}_2$ . Reprinted with permission from D. Friedmann, <i>Green Chem.</i> , 2016, <b>18</b> , 5391-5411. Published by Royal Society of Chemistry. <sup>4</sup> .....	39
Scheme 1.3 – Selective aerobic oxidation reactions with visible light irradiated titania. ....	40
Scheme 1.4 – Oxygen atom exchange via a 5 centred metallocycle on the surface of $\text{TiO}_2$ during alcohol oxidation which ensures aldehyde selectivity. <sup>112</sup> .....	41

Scheme 1.5 – Radical formation processes associated to UV irradiation of titanium dioxide in water. Reprinted with permission from M. A. Lazar, <i>RSC Adv.</i> , 2013, 3, 4130–4140. Published by the Royal Society of Chemistry. <sup>1</sup> .....	42
Scheme 1.6 – Visible light photocatalysis with titanium dioxide via substrate surface adsorption through a heteroatom (X = N, O, S). Reprinted with permission from X. Chen, <i>Chem. Soc. Rev.</i> , 2014, <b>43</b> , 473-486. Published by Royal Society of Chemistry. <sup>3</sup> .....	43
Scheme 1.7 – Selective aminobenzene formation via heterogeneous photocatalysis.....	44
Scheme 1.8 – Thiol-ene and decarboxylative C-C bond coupling reactions using irradiated titania. <sup>30, 33</sup> .....	48
Scheme 1.9 – The use of visible light irradiated titanium dioxide for dehydrogenative coupling reactions of tetrahydroisoquinoline derivatives with CH <sub>3</sub> NO <sub>2</sub> and KCN. <sup>70</sup> ....	49
Scheme 1.10 – Sulphoxidation of alkanes and epoxidation of alkenes using irradiated titania.....	50
Scheme 2.1 – The oxidation of aerobic benzyl alcohol oxidation by visible light irradiated orthorhombic bismuth tungstate selectively into benzaldehyde. ....	54
Scheme 2.2 – The aerobic oxidation of <i>N</i> -tertbutyl benzyl amine with visible light irradiated monoclinic bismuth vanadate .....	55
Scheme 2.3 – The mechanism for the irradiated Bi <sub>2</sub> O <sub>3</sub> initiated thiol-ene reaction. Reprinted with permission from O. O Fadeyi et al., <i>Org. Lett.</i> , 2015, <b>17</b> , 5756–5759. <sup>35</sup> Copyright 2015 American Chemical Society. ....	55
Scheme 2.4 – The formation mechanism for orthorhombic Bi <sub>2</sub> WO <sub>6</sub> nanoplates. Reprinted with permission from C. Zhang and Y. Zhu., <i>Chem. Mater.</i> , 2005, <b>17</b> , 3537-3545. <sup>187</sup> Copyright 2005 American Chemical Society. ....	58
Scheme 2.5 – Literature method for the growth of BiFeO <sub>3</sub> with a flower-like morphology. Adapted with permission from Sakar et al., <i>Mater. Res Bull.</i> , 2013, <b>48</b> , 2878–2885. <sup>177</sup> Published by Elsevier.....	62
Scheme 3.1 – The synthesis of $\alpha$ -D <sub>2</sub> -4-methoxybenzyl alcohol via reduction with LiAlD <sub>4</sub> .....	104
Scheme 3.2 – The use of $\alpha$ -D <sub>2</sub> -4-methoxybenzyl alcohol to observe the lack of H atom exchange and a secondary kinetic isotope effect. ....	105



Scheme 3.3 – Synthesis of $^{18}\text{O}$ labelled 4-methoxybenzyl alcohol unselectively from the hydrolysis of 4-methoxybenzyl chloride with sodium hydride and $\text{H}_2^{18}\text{O}$ .....	105
Scheme 3.4 – Oxidation of $^{18}\text{O}$ labelled 4-methoxybenzyl alcohol to observe oxygen atom exchange. Ratio of $^{16}\text{O}$ : $^{18}\text{O}$ observed was 2:1 by ESI-MS. ....	106
Scheme 3.5 – The charge carrier dynamics of bismuth vanadate as shown by transient absorption. Reprinted with permission from J. T. M. Kennis, <i>J. Phys. Chem. C</i> , 2014, <b>118</b> , 27793–27800. <sup>268</sup> Copyright 2014 American Chemical Society. ....	109
Scheme 3.6 – Proposed mechanism for the oxidation of benzyl alcohol with nan- $\text{BiVO}_4$ .....	112
Scheme 4.1 – The reduction of a trifluoromethylated compound to enable the functionalisation of reductants to provide products of interest.....	114
Scheme 4.2 – Literature examples of thermal trifluoromethylation reactions of alkenes and aromatics using Umemoto reagents. <sup>284, 286, 287</sup> .....	116
Scheme 4.3 – Ruthenium centred photocatalysts used in trifluoromethylation reactions of alkenes with visible light and Umemoto reagents. <sup>62, 288</sup> .....	117
Scheme 4.4 – Trifluoromethylation of benzene with a ruthenium photocatalyst, irradiated with blue LED light, and a pyridinyl trifluoroacetyl ester. <sup>32</sup> .....	117
Scheme 4.5 – The use of graphitic carbon nitride in the trifluoromethylation of benzene with $\text{CF}_3\text{SO}_2\text{Cl}$ and visible light. ....	118
Scheme 4.6 – Proposed mechanism for the formation of products observed in the trifluoromethylation of styrene via the reduction of Umemoto 1 with blue LED light irradiated nan- $\text{BiVO}_4$ .....	121
Scheme 4.7 – Proposed mechanism for the trifluoromethylation of dibenzothiophene from the reduction of Umemoto’s reagent by blue light irradiated nan- $\text{BiVO}_4$ . The formation of compound <b>4.6</b> is given here as an example.....	124
Scheme 4.8 – The use of irradiated nan- $\text{BiVO}_4$ in trifluoromethylation and trifluoroacylation of aromatics .....	126
Scheme 4.9 – The proposed mechanism for bismuth catalysed Friedel-Crafts acylation of 2,4,6-trimethoxybenzene to form compound <b>4.10</b> .....	127
Scheme 4.10 – An illustration showing a scheme for the photolytic degradation of nan- $\text{BiVO}_4$ into the Bi centred Friedel-Craft catalyst .....	128

Scheme 5.1 – Photo-Kolbe dimerization of phenylacetic acid to bibenzyl, carbon dioxide and hydrogen by UV light irradiated platinised titanium dioxide.....	133
Scheme 5.2 – Literature examples of photochemical Giese reactions initiated through decarboxylation of carboxylic acids. <sup>30, 326, 332</sup> .....	134
Scheme 5.3 - The formation of Pt NPs thermally through the reduction a platinum precursor at elevated temperature under a flow of dihydrogen gas. ....	136
Scheme 5.4 – The photochemical platinization of blue LED light irradiated bismuth tungstate in an ethanol:water solvent mixture.....	137
Scheme 5.5 – An illustration of the proposed mechanism for bibenzyl, benzyl alcohol and benzaldehyde formation from the oxidation of phenylacetic acid with a blue LED light irradiated platinised semiconductor. ....	144
Scheme 5.6 – The Photo-Giese reaction between phenylacetic acid and methacrolein for the formation of <b>5.1</b> and carbon dioxide facilitated by 0.15-Pt-Bi <sub>2</sub> WO <sub>6</sub> irradiated by blue LEDs. ....	145
Scheme 5.7 – Proposed mechanism for the Photo-Giese reaction initiated by the decarboxylative photooxidation of phenylacetic acid by irradiated 0.15-Pt-Bi <sub>2</sub> WO <sub>6</sub> ..	148
Scheme 5.8 – Photo-Giese reactions between phenylacetic acid and methyl methacrylate for the formation of compound <b>5.3</b> and between phenylacetic acid and $\alpha$ -methylene- $\gamma$ -butyrolactone for the formation of compound <b>5.4</b> . ....	154
Scheme 5.9 – An illustration showing the capacity for a benzyl radical to propagate into a polymer through repeated reaction with molecules of acrolein. ....	156
Scheme 5.10 – The decarboxylative photooxidation of phenoxyacetic acid and subsequent Photo-Giese reactions with electron deficient alkenes, to form <b>5.5</b> and <b>5.6</b> , initiated by blue light irradiation of 0.15-Pt-Bi <sub>2</sub> WO <sub>6</sub> . ....	157
Scheme 5.11 – Comparison of electronic effects between a benzyl radical and a phenoxy methyl radical formed from the decarboxylation of phenylacetic acid and phenoxyacetic acid respectively.....	160
Table 2.1 – The results of the use of various blue light irradiated bismuth containing semiconductors in the aerobic oxidation of benzyl alcohol into benzaldehyde.....	75

Table 2.2 – The results of the use of blue light irradiated photocatalysts for the aerobic oxidation of benzyl alcohol selectively to benzaldehyde.....	83
Table 3.1 – The comparison of nan-BiVO <sub>4</sub> , bulk BiVO <sub>4</sub> and P25 TiO <sub>2</sub> as photocatalysts for 4-methoxybenzyl alcohol oxidation .....	90
Table 3.2 – Repeats of 4-methoxybenzyl alcohol for error determination. ....	92
Table 3.3 – The photocatalytic oxidation of substituted benzyl alcohols using blue LED light irradiated nan-BiVO <sub>4</sub> . ....	93
Table 3.4 - The extended photocatalytic oxidation of substituted benzyl alcohols using blue LED light irradiated nan-BiVO <sub>4</sub> .....	94
Table 3.5 – The effect of the addition of para substituted benzoic acids to the photooxidation of 4-methoxybenzyl alcohol by nan-BiVO <sub>4</sub> . ....	98
Table 3.6 - The effect of the addition of para substituted acetophenone to the photooxidation of 4-methoxybenzyl alcohol by nan-BiVO <sub>4</sub> .....	98
Table 3.7 – Excited state lifetimes for BiVO <sub>4</sub> in acetonitrile .....	110
Table 5.1 – Results of the attempted Photo-Kolbe dimerizations with 0.15-Pt-Bi <sub>2</sub> WO <sub>6</sub> and 0.15-Pt-BiVO <sub>4</sub> .....	142
Table 5.2 - Photocatalyst optimisation. Results of Photo-Giese reactions with varying amounts of platinum on bismuth tungstate .....	149
Table 5.3 – Photo-Giese reaction optimisation. Results of Photo-Giese reactions varying the quantity of methacrolein used .....	151
Table 5.4 – Photo-Giese reaction scope – Results of Photo-Giese reactions between phenylacetic acids and electron deficient alkenes initiated by blue light irradiated 0.15-Pt-Bi <sub>2</sub> WO <sub>6</sub> .....	152
Table 7.1 – The irradiance obtained from 2 cm away from the 30W blue LED array .	171

## **Accompanying materials**

A compact disk with an electronic copy of this thesis, copies of all data files, an excel spreadsheet entitled “Thesis Data Index” and a folder entitled “Reprint copyright permissions” are attached at the back of this thesis. The excel spreadsheet “Thesis Data Index” cross-references thesis chapter and folder name with the experiments conducted. Each experiment is accompanied with a list detailing the type of study and/or the data source used for the corresponding experiment. Inside the folder entitled “Reprint copyright permissions” are the pdf files detailing the permissions obtained for reprinting figures that are included in this thesis.

## **Acknowledgements**

I'd like to thank the Engineering and Physical Sciences Research Council and the University of York for providing the financial support needed for me to complete my PhD. I'd also like to thank my parents Gail and Paul Unsworth for providing the financial support so that I can continue working into my 4<sup>th</sup> year. Although, this financial support was significant and essential, it pales in comparison to the continual support that they have given me throughout my upbringing. As a result, giving thanks to my parents feels terribly insufficient.

The people that I have lived with during my PhD were those confronted most by my struggling attempt through my studies. As a result, I'd like to thank George Morgan, Katy Unsworth and Hannah How for coping as best they could with the side-effects of said struggle. Katy Unsworth, my sister, gets a specific thank you for dealing with me for the longest of the 3, this probably deserves some kind of medal. Hannah How along with other University of York Swimming and Water Polo club members (Jacob Shaw in particular) probably deserve a similar medal. However, George Morgan gets possibly the most special thank you for providing a stable and happy relationship for me to confide in and to be distracted by. It is only due to this that my sanity has remained as close as is possible to something resembling normal levels.

I need to give thanks to Richard Douthwaite and Victor Chechik for their ongoing support and advice as supervisors throughout my PhD. I also need to thank those in the Department of Chemistry at the University of York that have provided friendship whilst I carried out my work. Of these, Ellis Wilde has provided much of the fuel needed (cake and coffee) for me to complete my work and so deserves individual thanks. Other individuals who have provided much support, and so deserve thanks, include Andrew Grantham, Ben Coulson, Brendan Garrett, Daniel Raines, Danielle Jowett, Julia Sarju, Lucy Milner, Luisa Ciano, Natalie Pridmore, Robert Mitchell, Sindhu Suravaram and Thomas Sanderson.

## Declaration

The research described in this thesis was carried out between October 2013 and August 2017. This declare that this work is original and my own, with the following exceptions:

- Transmission electron diffraction and specific area electron diffraction were carried out in conjunction with Dr Robert Mitchell (York JEOL Nanocentre)
- Heteronuclear multiple bond coupling nuclear magnetic resonance experiments were carried out in conjunction with Miss Heather Fish
- Time resolved photoluminescence spectroscopy and X-ray fluorescence were carried out in conjunction with Mr Ben Coulson (PhD Student)
- Electrospray ionisation mass spectrometry was carried out by Mr Karl Heaton
- Inductively coupled plasma mass spectrometry was carried out by Dr Emma Dux.

The following work has been published in the Journal of Catalysis, with the reference: C. A. Unsworth, B. Coulson, V. Chechik and R. E. Douthwaite, *J. Catal.*, 2017, **354**, 152-159.

- The synthesis and characterisation of nan-BiVO<sub>4</sub> and bulk BiVO<sub>4</sub> in chapters 2 and 3 respectively
- The study of nan-BiVO<sub>4</sub> as a heterogeneous photocatalyst for the selective oxidation of various para-substituted benzyl alcohols in chapter 3
- The inhibition of the oxidation of 4-methoxybenzyl alcohol with ketones, aldehydes and carboxylic acids in chapter 3
- The oxidation of  $\alpha$ -D<sub>2</sub>-4-methoxybenzyl alcohol for kinetic isotope effect work in chapter 3
- Time resolved photoluminescence studies with nan-BiVO<sub>4</sub> and bulk BiVO<sub>4</sub> in chapter 3

This thesis has not been submitted for any other degree at this or any other academic institution.

# 1 Introduction

Within the chemical industry, the transformation of organic compounds is very important in the production of a wide range of consumer facing products on the market. The production of many highly valuable pharmaceutical, cosmetic, agricultural, food and fragrance products is dependent on a number of different processes used in the chemical industry; however, these large-scale processes once established are difficult to change. As a result, many reactions on an industrial scale still use unsustainable, energy inefficient and wasteful reaction processes that use and generate toxic and harmful compounds. Many companies are seeking to change these processes to alternatives which are more aligned with new environmental policy and are less costly. The utilisation of selective photocatalysis is one method that is being explored as a sustainable and green alternative to current processes.<sup>1-7</sup>

The amount of solar energy that strikes the surface of the earth every hour is enough to provide for the global energy need for an entire year.<sup>8,9</sup> This is an awesome, natural and renewable resource and the drastic and urgent need for the utilisation of alternative energy sources has provided inspiration for a range of work in many different research areas. In the field of chemistry, the absorption of photons across the electromagnetic spectrum has been studied extensively, particularly in relation to chemical analysis.<sup>10-13</sup> However, the study of the utilisation of solar wavelengths of light to enact chemical change via the making or breaking of bonds is a much smaller field and is one that faces many challenges.<sup>6</sup> These challenges include the ability to use a broad range of wavelengths found in the solar light that hits the earth's surface and the ability to selectively make or break bonds. This work outlined in this thesis explores these challenges in order to provide further understanding of how to utilise light to activate reactions that selectively yield valuable chemical products.

## 1.1 Photocatalysis

Photocatalysis is the use of light to accelerate a chemical reaction via a substance which is capable of absorbing photons but remains unchanged by said chemical reaction. The photons used in photocatalysis often have wavelengths that are consistent with UV or visible light where absorption leads to electronic transitions. The absorption of a photon of sufficient energy is needed to overcome the energy gap between discrete energy levels in a photoactive species in order to create an excited state. Excited photoactive species have different redox properties to the ground state of said species. As a result, excited

## Chapter 1

photoactive compounds are able to initiate redox reactions that are not possible in the ground state. Photocatalysis is valuable because the process induces the catalytic turnover of a chemical transformation under specific, controllable irradiation conditions. Chemical transformation occurs as a result of electron transfer between an excited state and a desired target. Multiple electron transfer often forms stable oxidation or reduction products,<sup>14-29</sup> but single electron transfer can also be used to initiate radical chemistry.<sup>30-37</sup> Electron transfer also mediates the return to the ground state of a photoactive material and so enables the aforementioned catalytic turnover.

Photocatalysis is distinct from catalysis. A photocatalyst requires the absorption of light to create a catalytic cycle that results in a chemical transformation without the photocatalyst undergoing any permanent change. A catalyst requires thermal activation to induce a chemical transformation without the catalyst undergoing any permanent change, but unlike photocatalysis, catalysis can take place in the absence of light. The use of UV or visible light photons for catalyst activation has specific advantages over thermal activation for the same reactions.<sup>7</sup> These photons can pass through reagents without changing their own properties or those of the reagents. The result of this is that photons can pass into complex reaction mixtures and will only interact with an intended target in order to a desired excited state. This attribute has the additional benefit that photolytic activation, particularly with the use of visible light, is generally safer than thermal activation. The wavelength and direction of UV and visible light photons can be easily controlled with the use of filters, lenses and mirrors. Moreover, narrow band UV and visible light emission is possible with the use of lasers and LEDs. Thermal activation is generally not as selective and will create thermally excited states in all species of a reaction mixture. Thermal activation is also less controllable as it is often passed through materials by conduction or convection. As a result, generally, thermal activation of catalytic processes is more likely to also initiate undesired side reaction pathways.<sup>7</sup>

Homogeneous photocatalysts can be either organic compounds or inorganic metal complexes; as long as the lifetime of the excited state of a molecule is long enough so that electron transfer is competitive with relaxation, a molecule can function as a photocatalyst.<sup>7, 38, 39</sup> Intersystem crossing after excitation to triplet excited states is needed to achieve long lifetimes as emission from a singlet excited state to the ground singlet state is spin allowed whereas emission from a triplet excited state to the ground singlet state is spin disallowed.



## Chapter 1

UV absorbing molecules such as *p*-dicyanobenzene and its derivatives have been used as photocatalysts for decarboxylative radical synthesis,<sup>40</sup> methyl methacrylate polymerisation,<sup>41</sup> and the aerobic oxygenation of toluene.<sup>42</sup> Dyes capable of the absorption of broad parts of the visible light spectrum, such as fluorescein, eosin Y and Rose Bengal have been used for similar reactions, Figure 1.1. In a comparative study, methylene blue, fluorescein and eosin Y were all used under visible light irradiation in the controllable polymerisation of methacrylates.<sup>43</sup> Selective photocatalysis under visible light irradiation with the use of eosin Y has enabled aerobic cross dehydrogenative coupling reactions.<sup>44</sup> Rose Bengal has also been used as a photosensitizer in the  $\alpha$ -alkylation of aldehydes in conjunction with a imidazolidinone organocatalyst.<sup>38</sup> 9-Mesityl-10-methylacridinium perchlorate is a molecule that has been synthesised to function as a organo-photocatalyst, an example of its use is in the alkylation of allylic/benzylic species via photo-oxidation and subsequent deprotonation of radical cations.<sup>45</sup>

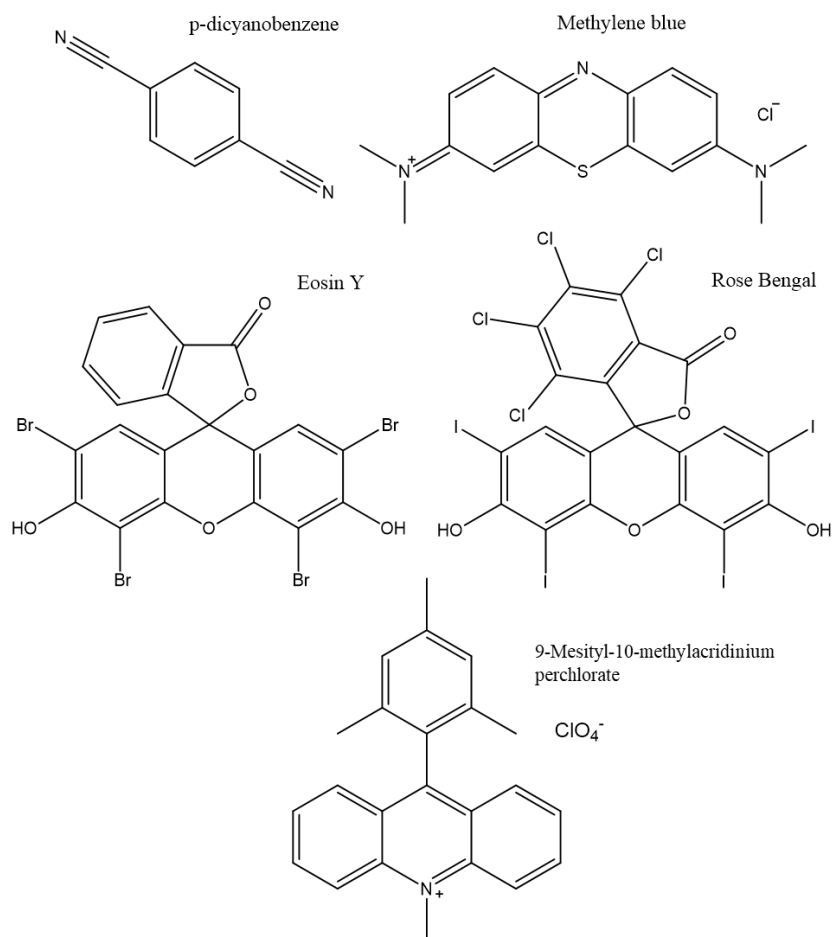


Figure 1.1 – Organic molecules used as homogeneous photocatalysts

A wide range of different metals have been used to make photocatalytic complexes. Cobalt and nickel centres have been used extensively as hydrogen reducing

## Chapter 1

photocatalysis for fuel production.<sup>46, 47</sup> Solar irradiation of copper and iron complexes has been reported to aid in photochemical remediation of organic waste in aqueous systems.<sup>48-50</sup> Iron has also been used for carbon dioxide reduction in complexes with porphyrins.<sup>51</sup> Zinc porphyrin sensitizers have also been coupled with other photocatalysts for hydrogen evolution.<sup>52</sup>

However, the most successful and widely used homogeneous photocatalysts are polypyridyl ruthenium and iridium complexes, Figure 1.2.<sup>2, 5, 7, 39</sup>  $\text{Ru}(\text{bpy})_3^{2+}$  has been the most popular ruthenium centred photocatalytic complex; it is known to absorb at 450 nm and generates stable and long lived triplet excited states with lifetimes of 1.1  $\mu\text{s}$ .<sup>53</sup>  $\text{Ru}(\text{bpy})_3^{2+}$  also has an excited state that enables the complex to act as a good reductant ( $\text{Ru}^{2+*} \rightarrow \text{Ru}^{3+} + \text{e}^-$ , +0.53 V vs. NHE) and a good oxidant ( $\text{Ru}^{2+*} + \text{e}^- \rightarrow \text{Ru}^+$ , -1.05 V vs. NHE).<sup>54</sup> Once these  $\text{Ru}^{3+}$  or  $\text{Ru}^+$  species are formed, via oxidation and reduction respectively, these ruthenium centres can undergo the complementary reduction or oxidation respectively to return to the starting complex,  $\text{Ru}(\text{bpy})_3^{2+}$ . This process can be repeated upon the absorption of another visible light photon.  $\text{Ir}(\text{ppy})_3$  and  $\text{Ir}(\text{ppy})_2(\text{dtbbpy})^+$  are examples of iridium based photocatalytic complexes that display high absorption efficiencies and generate long lived excited states.  $\text{Ir}(\text{ppy})_3$  absorbs at 375 nm to generate excited states with lifetimes of 2.0  $\mu\text{s}$ ,<sup>55</sup> whereas  $\text{Ir}(\text{ppy})_2(\text{dtbbpy})^+$  absorbs at 460 nm to generate excited states with lifetimes of 550 ns.<sup>56</sup> Both complexes are capable of acting in a similar manner to that described above for  $\text{Ru}(\text{bpy})_3^{2+}$ ; excitation of these complexes leads to excited states which can act as good oxidants and reductants to form species which undergo oxidation and reduction respectively to return to the original metal oxidation state. The long lived triplet excited states of these complexes facilitate high quantum yields;<sup>53-56</sup> quantum yield for a radiation induced process describes the likelihood of photon absorption leading to a desired chemical transformation. Another commonly used related term in photocatalytic studies is quantum efficiency which is the ratio of the number of photoelectrons generated by a photoactive material to the number of incident photons.

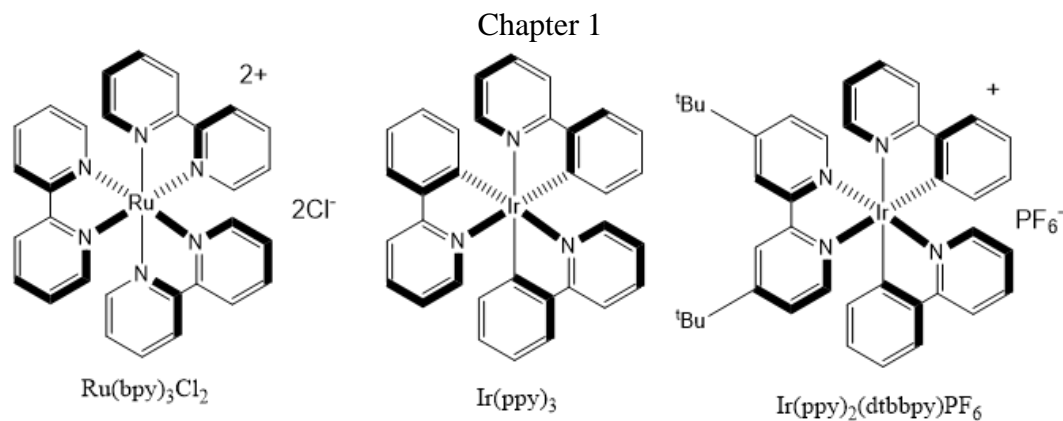


Figure 1.2 – Ruthenium and iridium centred homogeneous photocatalysts

$\text{Ru}(\text{bpy})_3^{2+}$  has been used in analogous reaction systems to the cross dehydrogenative coupling reactions<sup>57</sup> and the  $\alpha$ -alkylation of aldehydes<sup>58</sup> discussed above that were achieved with an organic photocatalyst.  $\text{Ru}(\text{bpy})_3^{2+}$  has also found use as a photocatalyst for alkene reduction,<sup>59</sup> reductive dehalogenation,<sup>60</sup> radical cyclisation,<sup>61</sup> trifluoromethylation,<sup>32, 62, 63</sup> as well as alcohol<sup>64</sup> and halide<sup>65</sup> oxidation.  $\text{Ir}(\text{ppy})_2(\text{dtbbpy})^+$  has also been used as a radical cyclisation<sup>61</sup> and cross dehydrogenative coupling photocatalyst.<sup>66</sup> However, these reactions required the use of complex sacrificial reagents in order to complete the photocatalytic cycle. The use of dual catalysis is known to remove the need for these sacrificial reagents. Coupling iridium based photocatalytic cycles with hydrogen atom transfer organocatalytic cycles has been used to alkylate heteroaromatic compounds using alcohols as alkylating reagents.<sup>67</sup> In addition, the coupling of ruthenium and iridium based photocatalytic cycles with palladium and nickel catalytic cycles respectively has enabled photocatalytic cross coupling reactions between diazonium salts and arylpyridines<sup>68</sup> and between carboxylic acids and aryl halides.<sup>69</sup>

It is clear that homogeneous photocatalysts can be applied to a diverse range of different chemical transformations. However, it is evident that these homogeneous inorganic photocatalysts contain elements that are expensive and not highly abundant; far fewer examples have been reported using transition metal photocatalysts made of abundant elements such as iron, cobalt and nickel.<sup>46-51</sup> In addition, the use of any homogeneous photocatalyst requires relatively complicated separation techniques in order to purify reaction mixtures and it is often found that photocatalysts cannot be retrieved after use, due to degradation.<sup>3</sup> As a result, homogeneous photocatalysts can rarely be reused. Homogeneous catalysts are catalysts that activate the chemical transformation of reactants that exist in the same phase as the catalyst, whereas heterogeneous catalysts are catalysts that activate the chemical transformation of reactants that exist in a different phase to that of the catalyst. Heterogeneous semiconducting photocatalysts remain

unchanged after use,<sup>28, 70-73</sup> are often made of abundant elements<sup>23, 24, 72, 74-77</sup> and can be separated from reaction mixtures easily and so are much more suitable candidates for repeated use. As the reuse of a catalyst is essential for the economic viability of a process, heterogeneous photocatalysis is much more suitable for application in industry.

## 1.2 Light absorbing semiconducting materials

In solid materials, the overlap of a high number of atomic orbitals leads to molecular orbital energy levels that are effectively continuous and separated by a very small energy gap. Groupings of energy levels are generally described as bands. The electronic nature of solids can be described by the density of states at the energy of the highest occupied molecular orbital, the Fermi level. Semiconductors are non-metallic materials that have a small band gap between the highest occupied energy level at the top of a valence band and the lowest unoccupied energy level at the bottom of a conductance band. The band gap in semiconductors is small enough so that light can be used to excite electrons from the valence band to the conductance band of these materials. A material would be described as insulating if this band gap was large. If, the Fermi level was found within a continuous band then, the material would be described as metallic. This simplified description of band theory is demonstrated in Figure 1.3.

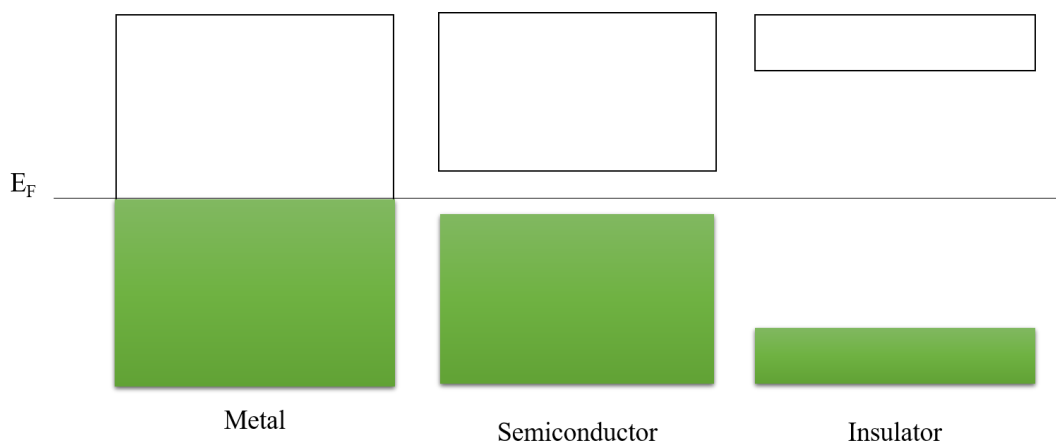


Figure 1.3 – Simplified band theory showing the band structures of metals, semiconductor and insulators.  $E_f$  shows the Fermi energy of these generic solids.

The simple description of band theory is useful for showing how semiconductors are able to absorb visible or UV photons. However, a slightly more complex model is necessary to be able to discuss other important phenomena associated with semiconducting materials. One simple model for a solid is a one-dimensional chain of atoms.<sup>78</sup> For a one-

## Chapter 1

dimensional chain of atoms, the Bloch function can be used to describe the wavefunction of an electron moving along this chain, Equation 1.1.

Equation 1.1 - 
$$\psi(x) = e^{ikx}u(x)$$

$\psi(x)$  represents the wavefunction;  $x$  represents the position of the electron;  $u(x)$  represents a periodic function where  $u(x) = u(x+a)$ ,  $a$  represents the atomic spacing and  $k$  represents a continuous quantum number which follows the following conditions  $-\pi/a \leq k < \pi/a$ , called the wave number.

If, atomic orbitals are applied to the linear chain of atoms, then the wavefunction for these atomic orbitals becomes the periodic function and the exponential function gives the amplitude of the Bloch function. From Figure 1.4, we can see that the Bloch function has a wave-like form where the wavelength equates to  $2\pi/k$ .

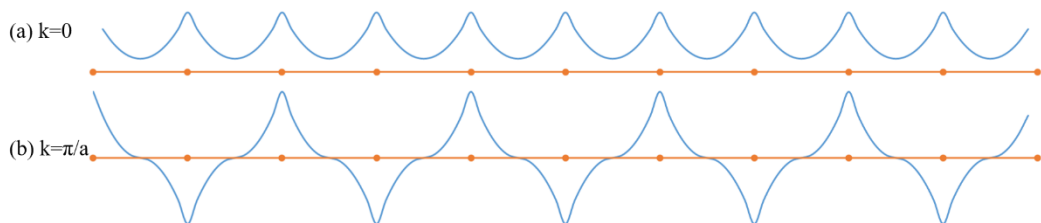


Figure 1.4 - The wavefunctions for a chain of 1D periodically arranged atoms generated from Bloch functions where (a)  $k = 0$  and (b)  $k = \pi/a$

For  $s$  orbitals on this atomic chain, the wavefunction for the linear combination of atomic orbitals can be represented by using the Bloch function, Equation 1.2. These are known as Bloch sums.

Equation 1.2 - 
$$\psi(x) = \sum e^{ikna} \chi(x)$$

$\psi(x)$  represents wave function for the atom at position  $n$ .  $na$  is the distance down the chain to atom  $n$  and  $\chi(x)$  represents the wavefunction of one atomic orbital.

It can be shown that when  $k = 0$ , all the  $s$  orbitals are in phase and have the lowest energy due to the bonding overlapping orbital interactions. When  $k = \pi/a$ , the wavefunction corresponds to entirely anti-phase interactions between neighbouring orbitals and so the energy for this wavefunction is the highest possible energy due to the antibonding nature of these interactions. The energy of the generated wavefunction can be plotted against values of  $k$  as a band structure diagram, Figure 1.5. Equation 1.3 gives the energy of the linear combination of atomic orbitals in this chain.

Equation 1.3 -

$$E(k) = \alpha + 2\beta\cos(ka)$$

$\alpha$  represents the energy of an electron in one isolated orbital;  $\beta$  represents the interaction between neighbouring atomic orbitals.  $E(k)$  represents the energy for a particular quantum wavenumber.

The inclusion of  $p\sigma$  orbitals show that for the same value of  $k$ , the linear combination of atomic orbitals results in different energy trends.  $k = 0$  for  $p\sigma$  orbitals, the atomic orbitals align in the same direction meaning that the interaction between neighbouring orbitals is entirely antibonding.  $k = 0$  gives the highest energy linear orbital combination due to its antibonding nature.  $k = \pi/a$  results in the lowest energy combination as neighbouring orbitals have opposing orientation and an entirely bonding nature.

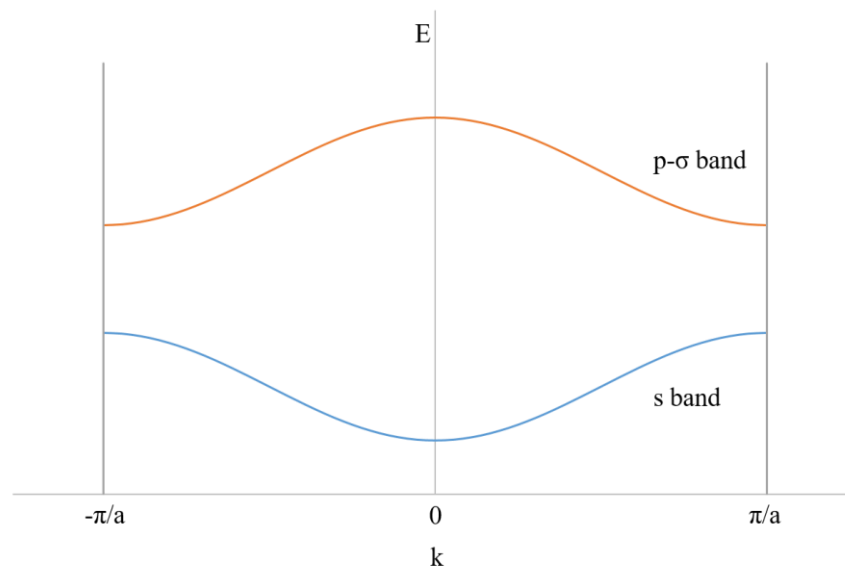


Figure 1.5 - Energy against wavenumber for a 1D chain of atoms with overlapping  $s$  orbitals and overlapping  $p\sigma$  orbitals. The energy is derived from the linear combination of atomic orbitals on this chain. The values of  $k$  are limited to  $-\pi/a \leq k < \pi/a$ .

In relation to real systems, the  $\beta$  coefficient in Equation 1.3 can be used to describe the width of a band and is closely linked to the type of bonding present. Weakly overlapping orbitals from highly ionic materials will have small  $\beta$  values whereas highly overlapping orbitals and covalent bonding give rise to high  $\beta$  values and wide bands. Wider bands can be associated to narrower band gaps and so  $\beta$  values and types of bonding can become important when comparing semiconducting and insulating non-metallic materials.

It is possible to also model solids from the perspective of free-electron theory. Electrons moving along a 1D line in a constant potential can be given wavefunctions of the form  $\psi$

## Chapter 1

$= \cos(kx)$  or  $\psi = \sin(kx)$  where, as before,  $k$  is related to the wavelength of an electron,  $\lambda = 2\pi/k$ . The energy of these electrons is the combination of the potential energy ( $V_0$ ) and kinetic energy of that electron, Equation 1.4.

Equation 1.4 - 
$$E(k) = \frac{\hbar^2 k^2}{2m} + V_0$$

$\hbar$  represents the reduced Planck's constant and  $m$  is the mass of an electron.

Electrons moving along a chain of atoms will not experience a constant potential. The potential energy of the electron will depend on the distance to nearest atom. As a result, the periodic nature of the chain of atoms affects the energy of the electron as it moves. For low  $k$  values this effect is small, however when  $k$  approaches  $\pi/a$  described above the effect of potential is significant so that the sine and cosine curves for the electron's wavefunction match the atom spacing in the 1D chain, Figure 1.6.

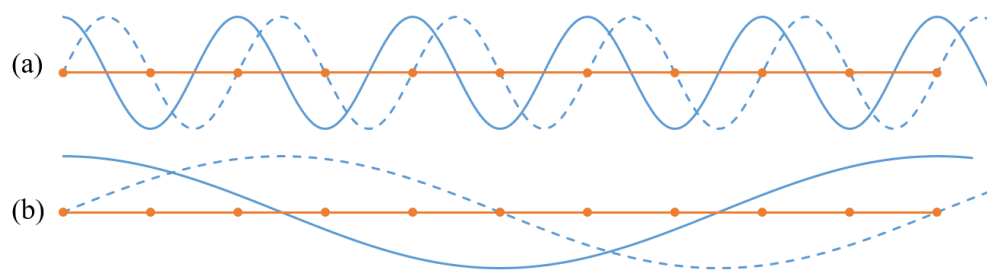


Figure 1.6 - The movement of a free electron along a 1D chain of periodically spaced atoms. (a) shows an electron with  $\lambda = \pi/a$ ; (b) shows an electron with a wavelength much longer than the atomic spacing,  $a$ .

Figure 1.7 shows electron energies for values of  $k$  between  $-\pi/a$  and  $\pi/a$ , using the free electron theory. It can be observed that a band gap appears at the limits of the values of  $k$  used. This is as a result of the sine and cosine wavefunctions when  $k = \pi/a$  or  $-\pi/a$  giving different energies.

It is interesting to note how band gaps form in these 2 different models for a solid system. Band gaps in the linear combination of atomic orbitals arise from the difference between bonding and antibonding combinations of different atomic orbitals. In free electron theory, band gaps arise from the interaction between electrons and a periodic potential from regularly arranged atoms. However, qualitatively, the band structure diagrams generated from the linear combination of atomic orbitals and free electron theory look similar.

## Chapter 1

If a more quantitative assessment is made from these 2 models then some interesting phenomena that are present in semiconducting materials can be discussed. If  $k$  is small then a power series can be used to expand the cosine function in Equation 1.3 to give Equation 1.5.

Equation 1.5 - 
$$E(k) = \alpha + 2\beta - (ka)^2\beta$$

For low  $k$  values, the s band is made up of bonding interactions. Therefore, it is acceptable to say that  $V_o = \alpha + 2\beta$ . Equation 1.4 and Equation 1.5 can be equated to give Equation 1.6.

Equation 1.6 - 
$$m = \frac{-\hbar^2}{2\beta a^2}$$

Equation 1.6 suggests that the mass of an electron is inversely proportional to the overlap between neighbouring atoms and the spacing between adjacent atoms. This suggests that the mass of an electron can be treated as a variable as the amount of adjacent orbital overlap is not always inversely proportional to the square of the spacing between adjacent atoms. The effective mass of an electron,  $m^*$ , can be used to discuss the mobility of an electron through a material. Electrons in wide bands have a small effective mass and will move faster through a material relative to electrons in narrow bands which behave as heavy and will have a low mobility through a material. Charge carrier mobility is an important consideration when discussing semiconductors as charge carriers must be able to move through the material, once generated, in order to carry out the required redox chemistry.



## Chapter 1

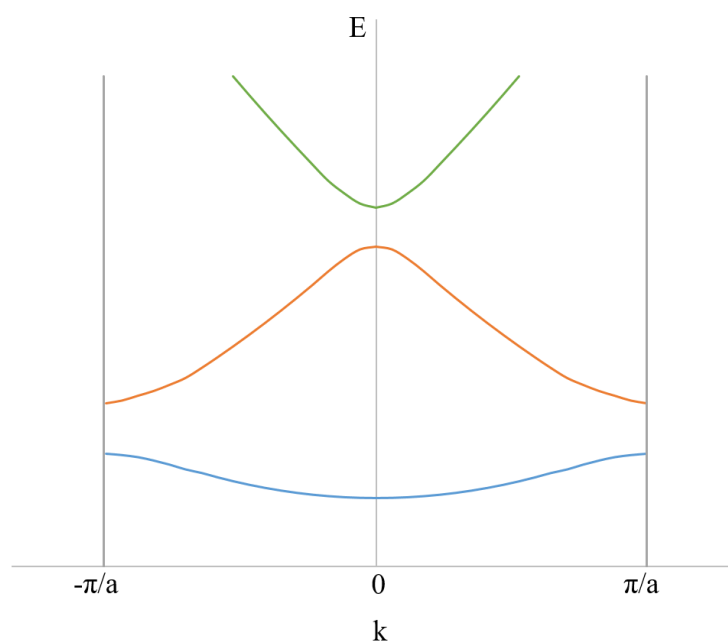


Figure 1.7 - The energy of a free electron moving through a 1D chain of periodically space atoms, derived from free electron theory, against quantum wavenumber. The values of  $k$  are limited to  $-\pi/a \leq k < \pi/a$ . Deviations from free electron theory arise from the variation in potential from the periodically arranged atoms which has a maximal effect when  $k = \pm \pi/a$ .

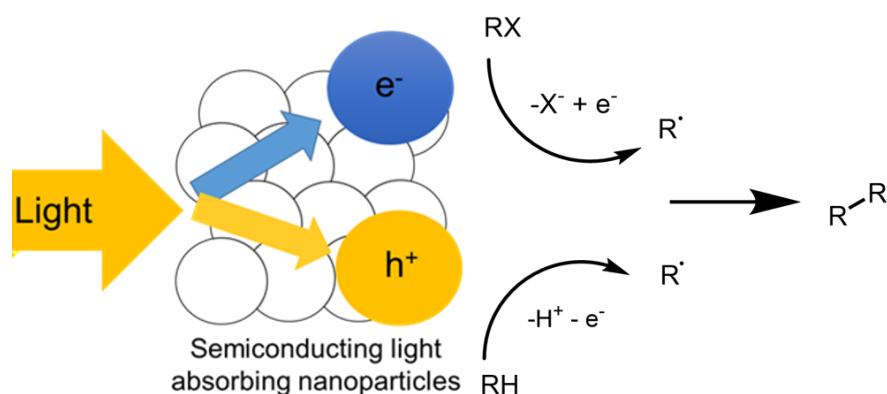
Placing the effective mass of the electron in Equation 1.4 and differentiating this equation twice gives Equation 1.7 which indicates that the effective mass is inversely proportional to the change in the  $E(k)$  curve.

Equation 1.7 -

$$\frac{d^2E}{dk^2} = \frac{\hbar^2}{m^*}$$

$m^*$  represents the effective mass of an electron.

At the top of full valence bands, positively charged holes are generated which will travel in the opposite direction to electrons when under an applied field. The relationship between effective mass and the change in  $E(k)$  is consistent with the formation of holes. The absorption of photons by semiconductors promotes an electron to an empty conduction band and leaves behind holes in the valence band of this material. These holes can oxidise surface bound species and the electrons generated can reduce surface bound species, Scheme 1.1. These charge carriers are the basis of how semiconductors can behave as heterogeneous photocatalysts.



Scheme 1.1 – Heterogeneous photocatalysis using an irradiated semiconductor.

For photons to be absorbed by a semiconducting material a selection rule can be applied. Transitions occur between Bloch functions with the same wavenumber, i.e.  $\Delta k = 0$ . Semiconductors where their lowest energy transitions are allowed have a direct band gap, whereas semiconductors with a lowest energy transition between different  $k$  values have an indirect band gap. Indirect band gap transitions can occur due to lattice vibrations as the  $k$  selection rule is based upon periodic atomic spacings and so any break in periodicity allows for indirect transitions. Indirect transitions in semiconductors have a reduced electron-hole recombination rate as recombination is also a forbidden transition. As electron-hole recombination has been reported to be rate limiting when using semiconductors in photocatalysis, indirect, band gap semiconductors often are utilised. It should also be noted that absorption of light is less in indirect semiconductors in comparison to direct semiconductors due to the aforementioned selection rule.

The charge carriers, generated by the absorption of photons in semiconductors, have the effect of distorting the lattice of ions around the charge carriers as they travel through the material. A moving charge carrier accompanied by the lattice polarisation that travels with this charge carrier is called a polaron.<sup>78</sup>

An electron or hole placed in an unfilled orbital on an atom in a solid will create a band as a result of the orbital of this charge carrier overlapping with orbitals on adjacent atoms. This charge carrier can be delocalised and therefore stabilised. However, if this charge species is kept on this atom, the polarisation of the lattice around this atom will also stabilise the electron. Large polarons are more highly stabilised by the delocalisation of this charge carrier in the band created through orbital overlap. These polarons will travel through a material. Small polarons experience a larger stabilising force from the polarisation of the lattice around this charge carrier. As a result, small polarons are

trapped at the site on an atom. Small and large polarons are represented in a schematic in Figure 1.8. Small polarons can be thermally activated in order to move to another atomic centre in the lattice. The chemical implication of small polarons is that a small polaron will change the oxidation state of the atom at which the polaron is trapped.

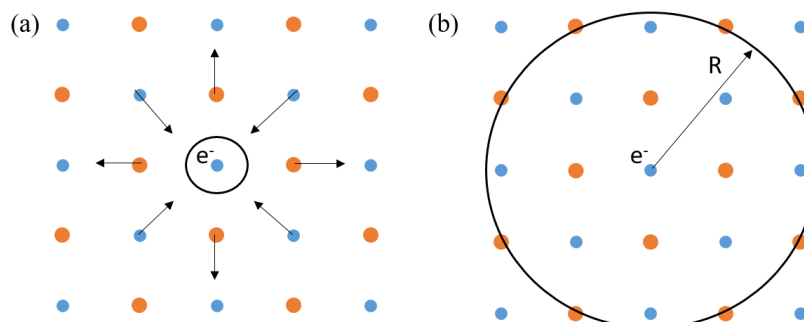


Figure 1.8 - Polarons in a solid lattice of blue cations and orange anions. (a) shows a small polaron localised on one cation; (b) shows a large polaron that will move freely throughout the lattice,  $R$  indicates the radius of lattice distortion caused by the polarons.

Polarons are important in heterogeneous photocatalysis as small polarons are often found at defect sites from which redox reactions occur. These defects create inter-band energy levels which allow for lower energy light absorption relative to the photon energy required to bridge the band gap. In addition, the trapping of small polarons can extend the lifetime of the photo-generated charge carriers meaning that there is an increased likelihood that they are used in a redox reaction. However, these charge carriers should be preferably trapped at the surface of a material in order to interact with a surface bound substrate and induce a chemical reaction<sup>79, 80</sup>. Otherwise, small polarons trapped in the bulk will act as recombination centres for electrons and holes.

Section 1.2 earlier mainly describes the bulk electronic structure of semiconductors. The features described have a significant impact on a material's capacity to absorb light and the efficiency of charge transfer. However, chemical transformation via heterogeneous photocatalysis occurs at the surface of a photocatalyst. Therefore, it is important to investigate what happens when charge carriers reach the surface of a photocatalyst and are able to interact with substrates found there.

### 1.3 Application of heterogeneous semiconducting photocatalysts

Heterogeneous photocatalysts have found use in a wide range of applications.<sup>4, 81-88</sup> The first use of a novel heterogeneous photocatalyst is often in the degradation of a dye or

## Chapter 1

complex organic compound in aqueous solution designed to mimic the degradation of organic pollutants in wastewater streams.<sup>87</sup> A large number of different semiconducting heterogeneous photocatalysts have been utilised in such systems including, but not limited to: TiO<sub>2</sub>,<sup>88</sup> carbon nitride,<sup>89</sup> ZnO,<sup>90</sup> Fe<sub>2</sub>O<sub>3</sub>,<sup>91</sup> BiOX (X = Cl, Br, I),<sup>92</sup> BiVO<sub>4</sub>,<sup>93</sup> WO<sub>3</sub>,<sup>94</sup> BiFeO<sub>3</sub>,<sup>95</sup> CdS,<sup>96</sup> SrTiO<sub>3</sub>,<sup>97</sup> AgBr,<sup>98</sup> Ag<sub>3</sub>PO<sub>4</sub>,<sup>99</sup> Bi<sub>2</sub>WO<sub>6</sub><sup>100</sup> and Bi<sub>2</sub>O<sub>3</sub>.<sup>101</sup>

Heterogeneous photocatalysts have also been found to be effective in the removal of harmful metal cationic species, such as Cr<sup>6+</sup>,<sup>102</sup> Cu<sup>2+</sup>,<sup>103</sup> U<sup>6+</sup><sup>104</sup> and As<sup>3+</sup>,<sup>105</sup> from model waste-stream systems via photocatalytic reduction, using water as sacrificial reductant. Similar systems are known to be active in the photocatalytic degradation of harmful bacteria for the purpose of decontamination and self-cleaning surfaces.<sup>83</sup> Moreover, semiconducting materials have been applied as photocatalysts for the degradation of gaseous compounds and VOCs with the aim of reducing air pollution.<sup>81</sup>

Heterogeneous photocatalytic degradation studies examine the oxidation and conversion of harmful material in great detail and show that the semiconducting material can be repeatedly used in the desired degradation reaction. It is often suggested that the degradation of organic compounds results in the formation of compounds such as carbon dioxide, water and other inorganics as the final products of repeated oxidation; this process is also known as mineralization.<sup>106</sup> However, product formation is not always monitored or considered and so an assumption is made that the degradation of the undesired starting material does not result in the formation of harmful and undesired products.

In cases where photocatalytic degradation is unselective, a complicated mixture of many different, low value compounds can form in quantities that are below the limits of detection. In the photocatalytic degradation of bacteria, detection limits can cause significant problems as regrowth of a culture has previously been observed after studies which appear to initially show complete degradation.<sup>107</sup> In studies focussing upon the photocatalytic removal of metallic cations from waste-streams, the product formed can have a significant impact on further photocatalysis. The reduction of cationic metal species results in the formation of metal nanoparticles which adsorb to the surface of the heterogeneous photocatalyst.<sup>103, 108-110</sup> If a high number of nanoparticles cover a high proportion of the photocatalytic surface then the metal provides a blocking layer between photocatalyst and substrate and so the rate of photocatalysis slows significantly.<sup>111</sup> From these examples, it can be suggested that aiming to degrade or remove compounds considered as waste from a contaminated system, without any forethought as to the

potential products, is irresponsible and potentially dangerous. As a result, in the field of heterogeneous photocatalysis, aiming to carry out selective chemical transformations, especially for the synthesis of targeted value-added products, should be a priority. In order to do so effectively, it is important to try and understand the interactions which are necessary in achieving selective heterogeneous photocatalysis.

### **1.4 Understanding heterogeneous photocatalytic selectivity**

The Langmuir-Hinshelwood mechanism shows how rate of adsorption is important in heterogeneous catalytic transformations. In the Langmuir-Hinshelwood mechanism, 2 molecules adsorb to neighbouring sites to form surface bound intermediates which then react to form a desired product. Each of the 2 reactants is in equilibrium with its respective surface bound transition state. As both transition states are required to form the final product, the rate constants associated to these equilibria have a strong impact on the overall reaction rate. The Eley-Rideal mechanism only involves the formation of an adsorption equilibrium between one reactant and one surface bound transition state. However, the equilibrium constants associated to adsorption and desorption are still important in obtaining a desired product selectivity. This is because the second reactant molecule, which does not adsorb to the catalytic surface, will only react with the surface adsorbed transition state that is in equilibrium with the other reactant molecule. These mechanisms show the importance of adsorption to heterogeneous catalytic selectivity; however this is not the only important interaction in a selective heterogeneous photocatalytic reaction system.

In an ideal photocatalytic system for selective transformation, a substrate would be attracted to and adsorb to a photocatalyst surface, be oxidised or reduced to quickly form a stable product and then undergo desorption so that this product cannot be oxidised or reduced further. In addition, no other reactive species would be generated in order to react with the desired product further, in solution after desorption.

Substrate attraction, adsorption and product desorption are all fundamental to heterogeneous photocatalysis.<sup>1</sup> However, heterogeneous photocatalytic selective chemical transformations are often much more complicated than the ideal described above. In some cases, transition state formation at the catalyst surface is necessary to mediate multiple electron transfer reactions.<sup>21, 25, 26, 112</sup> Where single electron transfer occurs, this often results in the desorption of radicals that require the presence of another species in solution that will react quickly with these radicals in order to selectively produce a stable product.<sup>30, 33</sup> Furthermore, complementary redox reactions are necessary

in order to avoid high levels of electron-hole recombination. This means that other reagents are needed in the reaction mixture that undergo these complementary redox reactions. The products of these complementary reactions can be reactive and can therefore have an impact on the desired chemical transformation. Complementary reaction products can inhibit a reaction through competitive surface binding or by taking part in a competitive by-product pathway.<sup>1</sup> Alternatively, the products of complimentary redox reactions can promote the selectivity of the desired reaction by forming part of a necessary surface bound transition state.<sup>112</sup>

Achieving selectivity with heterogeneous photocatalysis can be as a result of many different interactions. As a result, it was decided that the following section should be used to examine the interactions associated to substrate attraction, adsorption and desorption as well as the reactions that occur after desorption that result in the selective formation of a particular product.

### 1.4.1 Substrate attraction

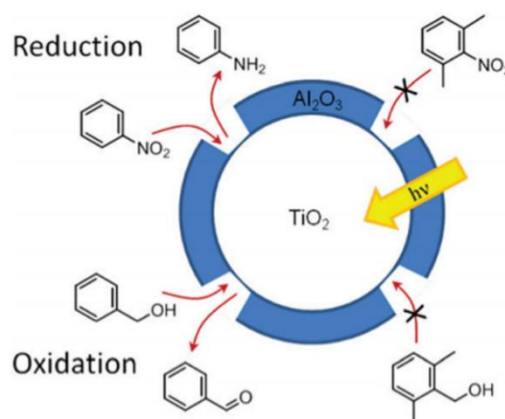
Various attractive forces can be used to bring a substrate to a photocatalytic surface and such forces have been used most often in selective degradation of a specific target molecule in a mixture.<sup>1</sup> Metal oxide semiconductors are inherently hydrophilic which enables the attraction of water to a photocatalyst surface; for materials such as titania this eventually leads to the formation of •OH radicals under UV irradiation. However, it has been shown that, through the surface functionalisation of n-octyl chains, the surface of titania can become hydrophobic. This modified photocatalyst was used to selectively degrade 4-nonylphenol over unsubstituted phenol under UV irradiation.<sup>113</sup> Electrostatic attraction has also been used to good effect in the selective degradation of ionic dyes such as methylene blue (cationic) and methylene orange (anionic) with UV irradiated titania;<sup>114</sup> changes in pH can be used to change the surface charge of a semiconducting material.<sup>115</sup>

In both of these examples, the adsorption of the targeted substrates to the surface of the respective photocatalysts is unlikely to be chemoselective, as would be the case if hydrogen-bonding or covalent bonding were the key adsorption interactions. 4-Nonylphenol would likely adsorb through van der Waals interactions and electrostatic interactions would be the source of adsorption for ionic dyes. It could be suggested that the lack of chemoselectivity in adsorption leads to the unselective degradation observed. With this, it could be suggested that the method of substrate adsorption is more important than the method of substrate attraction with regards to achieving selectivity.

## 1.4.2 Substrate adsorption

### 1.4.2.1 Size exclusion

Adsorption to a photoactive surface is important in achieving good charge transfer from photocatalyst to substrate. The effect of a lack of adsorption has been observed in porous materials that have been able to selectively degrade molecules based upon molecular size. A core-shell P25-mesoporous silica composite has shown selective degradation of 2-nitrophenol in a mixture of 2-nitrophenol, 4-phenylphenol and 4-nitro-2,6-diphenylphenol in water and irradiated with UV light. 2-Nitrophenol was the only molecule small enough to pass into the pores (2.7 nm in diameter) and adsorb to the titania in any significant quantity and therefore be photolytically degraded.<sup>116</sup> Size exclusion due to limited adsorption has also been observed in Al<sub>2</sub>O<sub>3</sub> coated TiO<sub>2</sub>, where nanocavities were created so that unsubstituted nitrobenzene and benzyl alcohol could be reduced and oxidised respectively, under UV irradiation. 2,6-Dimethyl substituted analogues were too sterically hindered for adsorption and so the photoredox processes for 2,6-dimethyl-1-nitrobenzene and 2,6-dimethylbenzyl alcohol could not take place, Scheme 1.2.<sup>117</sup>



Scheme 1.2 – Size exclusion for selective heterogeneous photocatalysis with Al<sub>2</sub>O<sub>3</sub> coated TiO<sub>2</sub>. Reprinted with permission from D. Friedmann, *Green Chem.*, 2016, **18**, 5391-5411. Published by Royal Society of Chemistry.<sup>4</sup>

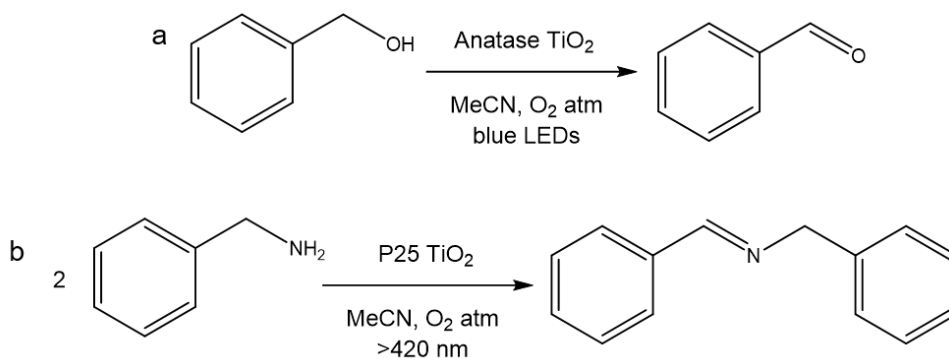
### 1.4.2.2 Surface adsorbed transition states that aid selectivity

Titanium dioxide is the most widely used across all fields associated to heterogeneous photocatalyst and has been shown to be a selective photocatalyst for a wide range of different and useful chemical transformations.<sup>1, 3</sup> Titanium dioxide under UV irradiation unselectively oxidises alcohols into a mixture of corresponding aldehydes, acids and further oxidation products.<sup>118, 119</sup> However, the selective aerobic oxidation of benzyl alcohols to their corresponding aldehydes has been achieved with anatase TiO<sub>2</sub> dispersed

## Chapter 1

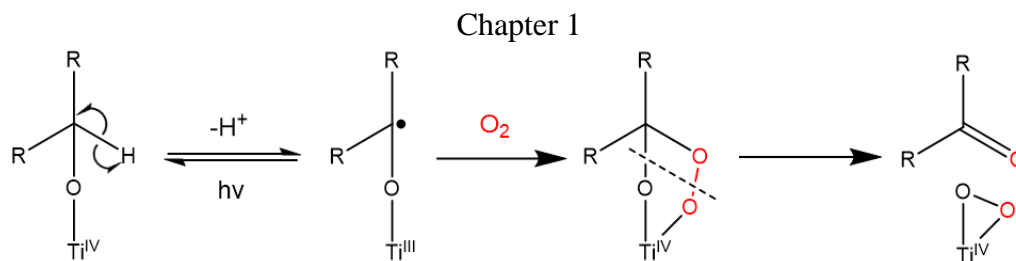
in acetonitrile irradiated by blue LEDs in the presence of a dioxygen atmosphere showing benzaldehyde selectivities of >99%, Scheme 1.3a.<sup>15</sup> Rutile titania nanorods under similar conditions have also been shown to convert benzyl alcohols to benzaldehydes with 99% selectivity; a Xe lamp with a >420 nm filter was used to irradiate the rutile titania nanorods in this system.<sup>120</sup> The dioxygen present was essential for these reactions to take place and it has been claimed that benzyl alcohol oxidation and dioxygen reduction leads to the formation of a metallocyclic intermediate which allows for oxygen atom exchange, Scheme 1.4. The use of <sup>18</sup>O labelled benzyl alcohol showed complete oxygen atom exchange with <sup>16</sup>O<sub>2</sub> to result in only the formation of <sup>16</sup>O labelled benzaldehyde. It was claimed that a concurrent bond cleavage across this ring mediated this oxygen exchange and enabled selective benzaldehyde formation as a result.<sup>112</sup> An important assumption was made in arriving at this conclusion. The work assumed that the only method of <sup>16</sup>O incorporation into the benzaldehyde product was via titania surface mediated photocatalytic exchange involving dioxygen. Water found in the atmosphere or at the surface of the photocatalyst and the photocatalyst itself could have also acted as sources of <sup>16</sup>O.

The aerobic and highly selective oxidation of benzyl amine to *N*-benzyl-1-phenylmethanimine (98% selectivity) using Degussa P25 titanium dioxide dispersed in acetonitrile and irradiated by a 300 W Xe lamp with a >420 nm filter, Scheme 1.3b, supported the suggestion that oxygen exchange via a metallocyclic intermediate occurred. This is because benzaldehyde was also detected and it was suggested that the final imine formed from the nucleophilic attack of unoxidized benzyl amine on the carbonyl group of benzaldehyde.<sup>21</sup>



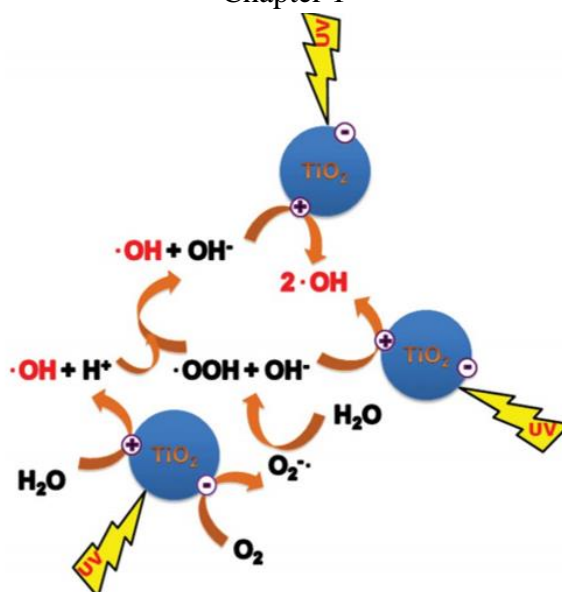
Scheme 1.3 – Selective aerobic oxidation reactions with visible light irradiated titania.





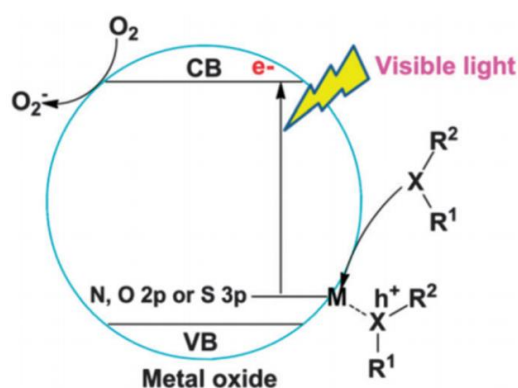
Scheme 1.4 – Oxygen atom exchange via a 5 centred metallocycle on the surface of  $\text{TiO}_2$  during alcohol oxidation which ensures aldehyde selectivity.<sup>112</sup>

A competing but not necessarily mutually exclusive theory associated to explaining the observed selectivity with the use of titania in heterogeneous photocatalysis is linked to the effect that adsorption has on the ability of titanium dioxide to absorb visible light. Nearly all of the highly selective chemical transformations using titanium dioxide (product selectivities >90%) utilised visible light ( $\lambda >400$  nm). However, rutile and anatase titanium dioxide are the most widely used polymorphs of the photocatalyst and have band gaps of 3.05 eV (400 nm) and 3.20 eV (390 nm) respectively.<sup>84, 121, 122</sup> The band gaps of rutile and anatase titania mean that only photons with wavelengths consistent with UV light can be used to separate electrons and holes. Titanium dioxide irradiated with UV light often results in unselective oxidation in the presence of dioxygen and/or water. The conduction band potential of anatase  $\text{TiO}_2$  is reducing enough (-0.15 V vs NHE) so that photoexcited electrons can be used in the reduction of dioxygen to a superoxide ( $\bullet\text{O}^{2-}$ ) radical anion.<sup>20</sup> In addition, the valence band potential of  $\text{TiO}_2$  is oxidising enough (+2.95 V vs NHE) so that holes can oxidise water and ultimately lead to  $\bullet\text{OH}$  radical formation.<sup>20</sup> The formation of both of these radical species together is associated with non-selective autoxidation of organic compounds to carbon dioxide, water and other inorganic compounds, Scheme 1.5.<sup>1, 106, 123</sup> However, the use of organic solvents, inert atmospheres and visible light increases selectivity significantly as a result of avoiding the formation of such radical species.<sup>1</sup>



Scheme 1.5 – Radical formation processes associated to UV irradiation of titanium dioxide in water. Reprinted with permission from M. A. Lazar, RSC Adv., 2013, 3, 4130–4140. Published by the Royal Society of Chemistry.<sup>1</sup>

It has been suggested that visible light absorption of titania avoids the formation of these radicals associated to auto-oxidation and has been made possible by the adsorption of organic molecules through their electron rich heteroatoms binding to surface metal centres, Scheme 1.6. In each of the examples where visible light irradiated titania was used as a selective photocatalyst, a fundamental oxidation occurred via the adsorption of a heteroatom to the surface of titania. A surface defect state with an energy higher than the top of the valence band was created. The difference in energy between the top of the valence band and the defect energy level meant that visible light absorption was possible and the electron-rich nature of the heteroatoms meant that electron donation to the photocatalyst was easily achieved.<sup>17, 21, 25, 26, 33</sup> Subsequent transfer of these electrons to the conduction band meant that photoreduction could occur.<sup>3</sup> Studies that suggested that selectivity was achieved through this visible light absorption often used UV-vis to show the increased absorption of visible light but do not convincingly show how this led to selective chemical transformations.<sup>97-100</sup>



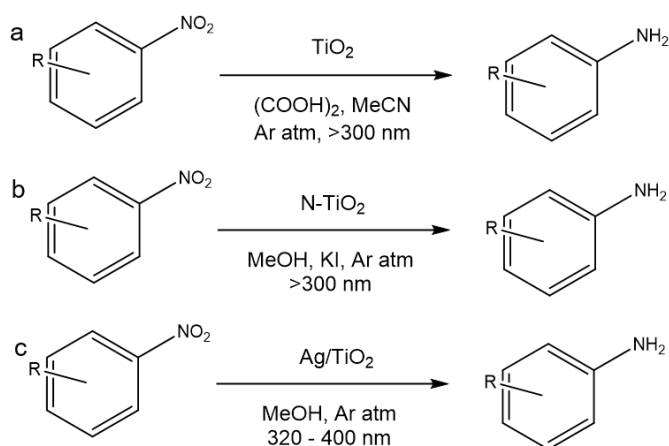
Scheme 1.6 – Visible light photocatalysis with titanium dioxide via substrate surface adsorption through a heteroatom ( $X = \text{N}, \text{O}, \text{S}$ ). Reprinted with permission from X. Chen, *Chem. Soc. Rev.*, 2014, **43**, 473-486. Published by Royal Society of Chemistry.<sup>3</sup>

Utilising substrate adsorption to achieve visible light absorption with titanium dioxide means that only a very small window of the solar light spectrum can be used. The use of other semiconducting photocatalysts that have smaller band gaps allows for more visible light absorption and so could be seen as better candidates for application as selective heterogeneous photocatalysts under solar irradiation. In addition, it has been shown that the use of other photocatalysts with valence and conduction band edge potentials that are not compatible with  $\bullet\text{O}^{2-}$  radical anion or  $\bullet\text{OH}$  radical formation helps to increase selectivity. The use of orthorhombic bismuth tungstate ( $\text{Bi}_2\text{WO}_6$ ) has a band gap appropriate for visible light absorption (2.8 eV, 440 nm) and has a valence band potential that is much less positive (+2.1 V vs NHE) than titania.<sup>24</sup> For an oxidation reaction to proceed, the band positions of the valence band edge must be more positive than the oxidation potential for the intended half reaction. The one electron oxidation potential of water into  $\bullet\text{OH}$  radicals is +2.7 V vs NHE<sup>124</sup> and so holes at the valence band edge of bismuth tungstate are not oxidising enough to form  $\bullet\text{OH}$  radicals. As a result, bismuth tungstate dispersed in water has been used to oxidise benzyl alcohol selectively to benzaldehyde (selectivity >99%) under visible light irradiation from a filtered Xe arc lamp (>420 nm) without the formation of  $\bullet\text{OH}$  radicals from water oxidation.

Electron paramagnetic resonance with a DMPO spin trap was used to show that no  $\bullet\text{OH}$  radicals were made when using visible light irradiated bismuth tungstate dispersed in water. Interestingly, the conduction band potential of bismuth tungstate (-0.7 V vs NHE) was shown to be more than capable of the formation of  $\bullet\text{O}^{2-}$  radical anions and it was stated that dioxygen reduction to  $\bullet\text{O}^{2-}$  radical anion was necessary to prevent electron hole recombination, however the formation of  $\bullet\text{O}^{2-}$  species did not impact the observed

benzaldehyde selectivity.<sup>24</sup> This could suggest that the formation of both  $\bullet\text{O}^{2-}$  radical anions from dioxygen reduction and  $\bullet\text{OH}$  radicals from water oxidation are needed for unselective degradation to occur. An aspect not discussed in this work was the reason for the lack of further oxidation to benzoic acid, although trace amounts of benzoic acids were observed.

There are several heterogeneous photocatalysis systems where the cause of selectivity has been associated to the chemoselective and strong adsorption of a substrate to the surface of a photocatalyst. Examples include the reduction of nitrobenzene derivatives selectively into anilines. Unmodified titania, irradiated by UV light and dispersed in ethanol, unselectively reduces nitrobenzene into a mixture of products; nitrosobenzene, *N*-hydroxylaniline and aniline.<sup>4</sup> However, other reports of the selective nitrobenzene reduction have been achieved through various modifications. 99% selectivity for a range of different aminobenzenes from the reduction of their corresponding nitrobenzenes was observed with the use of titania dispersed in acetonitrile irradiated by a Hg lamp (>300 nm) with an excess of oxalic acid used as a sacrificial reductant and hydrogen source, Scheme 1.7a.<sup>125</sup> Doping titania with nitrogen also enabled aminobenzene selectivity (yields between 90 and 99%) under UV and visible light irradiation; the sacrificial reductant and hydrogen source used was methanol, Scheme 1.7b.<sup>126</sup> In addition, silver nanoparticles photodeposited to the surface of titania enabled the selective reduction of nitrobenzene to aniline (achieving >99% selectivity) using UV irradiation from a Hg lamp ( $\lambda$  between 320 and 400 nm) and methanol present to act as the sacrificial reductant and hydrogen source, Scheme 1.7c.<sup>127</sup>



Scheme 1.7 – Selective aminobenzene formation via heterogeneous photocatalysis

The selectivity observed in some of the examples for nitroaromatics reduction to anilines has been associated to strong substrate adsorption as it has been suggested that the nitro

## Chapter 1

groups in these reactions had strong binding interactions with nitrogen species and silver metal found in N-doped and Ag/TiO<sub>2</sub> respectively.<sup>126, 127</sup> The direct adsorption of nitroaromatics will allow for effective charge transfer selectively to the desired functionality. The presence and oxidation of sacrificial reductants such as methanol, ethanol and KI were also fundamental in obtaining the conversion of nitroaromatics.<sup>126, 127</sup>

The work that utilised Ag/TiO<sub>2</sub> for selective nitrobenzene reduction used changes in the  $\lambda_{\text{max}}$  of the surface plasmon resonance band for silver, observed by electronic absorption spectra, to suggest that nitrobenzene binds strongly to silver in this system whereas aniline shows a much weaker binding interaction. Weak binding is consistent with effective desorption of the anilines from the surface of the photocatalyst. This is fundamental in the selectivity of these reactions. DFT was also used to investigate the binding of nitro groups to silver, Figure 1.9. It was found that strong nitrobenzene binding was due to the similar distances between Ag atoms and the O atoms in the nitro group and the electrophilic nature of nitrobenzene coupled with the electron donating nature of the Ag metal.<sup>104</sup> The reduction of nitrobenzene to aniline occurs via several intermediate products which would have different binding interactions to the surface of Ag/TiO<sub>2</sub>, however the binding interactions of these species were not reported and so more work could have been shown to explain the observed selectivity for aniline.

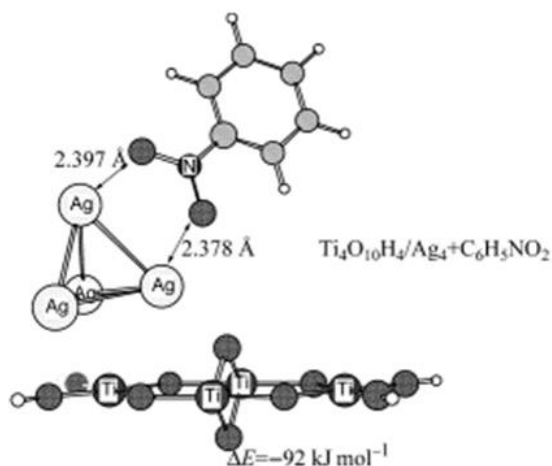


Figure 1.9 – Adsorption of nitrobenzene to silver metal supported by a titania photocatalyst. A model system of  $\text{Ti}_4\text{O}_{10}\text{H}_4/\text{Ag}_4+\text{C}_6\text{H}_5\text{NO}_2$  was used to generate this optimised structure via DFT. Reprinted with permission from H. Tada, *ChemPhysChem*, 2005, **6**, 1537 – 1543. Copyright 2005 John Wiley & Sons.<sup>104</sup>

### 1.4.3 Intermediate and product desorption

It has been said that product desorption is fundamental in achieving selectivity;<sup>1</sup> without desorption, substrates bound to the catalyst surface can undergo repeated redox reactions to mineralization. It has been claimed that various methods of photocatalyst surface modification has been effective in ensuring desorption from a photocatalytic surface by blocking some active redox sites. MoO<sub>x</sub> coated TiO<sub>2</sub> and irradiated by UV light in a flow gas-solid reactor, produced benzene selectivity (up to 65%) from cyclohexane oxydehydrogenation whereas unmodified titania resulted in cyclohexane mineralization.<sup>128</sup> It has been suggested that the addition of MoO<sub>x</sub> poisoned unselective sites at the TiO<sub>2</sub> photocatalytic surface. The reduction in cyclohexane conversion from unmodified TiO<sub>2</sub> (25% conversion) to the TiO<sub>2</sub> coated with the optimal amount of MoO<sub>x</sub> (7.6% Mo loaded by wt gives 15% conversion) partly supported this conclusion associated to catalyst poisoning but did not demonstrate how MoO<sub>x</sub> specifically reduced activity from the sites that unselectively converted cyclohexane and does not suggest what interactions result in effective desorption.

WO<sub>3</sub> coated TiO<sub>2</sub> has also been used to increase the selectivity of aerobic benzyl alcohol oxidation to benzaldehyde under UV irradiation in water, Scheme 1.9. Unmodified TiO<sub>2</sub> resulted in 13% benzaldehyde selectivity whereas a 7.6% (W loaded by weight) WO<sub>3</sub> coated TiO<sub>2</sub> resulted in 56% benzaldehyde selectivity.<sup>20</sup> The report claimed that WO<sub>3</sub> in this system was not an active oxidation catalyst and that holes generated by the absorption of light by WO<sub>3</sub> (2.80 eV band gap) were transferred to the valence band of titania as the top of the valence band of titania (+2.95 V vs. NHE) is higher in energy than that of tungsten oxide (+3.20 V vs. NHE), Figure 1.10c.<sup>20</sup>

However, a result that was reported but not discussed in depth was the benzaldehyde selectivity from only the use of an unmodified WO<sub>3</sub> photocatalyst; which was 61%.<sup>20</sup> This suggests that WO<sub>3</sub> could act as an active oxidation photocatalyst. Moreover, the benzaldehyde selectivity with the use of WO<sub>3</sub> was comparable to the optimised selectivity for the WO<sub>3</sub> coated TiO<sub>2</sub>; this could be used to tentatively suggest that similar amounts of over-oxidation processes could occur with the use of both photocatalytic materials. As the only other product discussed was CO<sub>2</sub>, formed in low quantities with the use of both WO<sub>3</sub> and 7.6 wt% W WO<sub>3</sub> coated TiO<sub>2</sub>, it is difficult to make any conclusions with regards to the identity of other products associated to the ca. 35-40% of unaccounted selectivity.<sup>20</sup>

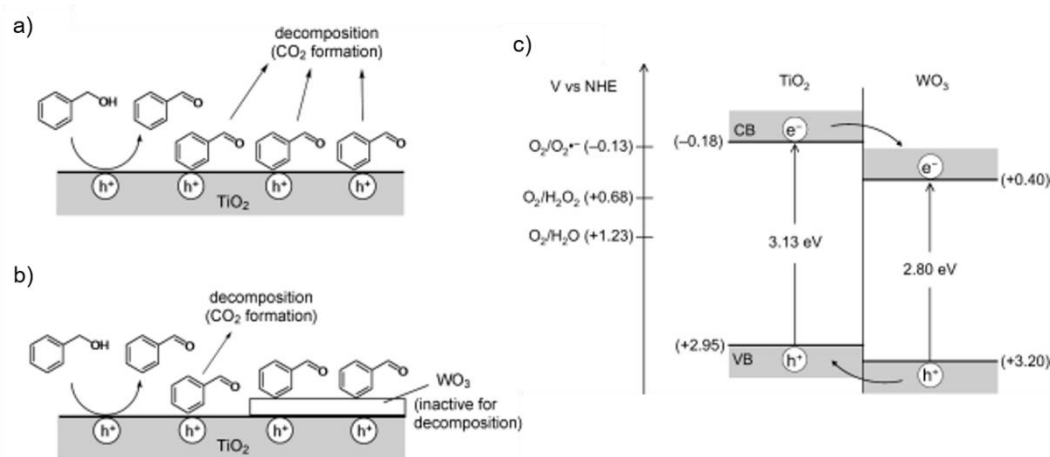


Figure 1.10 – (a) The ineffective desorption of benzaldehyde from TiO<sub>2</sub> which results in poor benzaldehyde selectivity (b) Effective desorption of benzaldehyde from WO<sub>3</sub> coated TiO<sub>2</sub> to ensure selective benzyl alcohol oxidation; (c) the suggested migration of charge showing the movement of photo-generated holes to titania and photoelectrons to WO<sub>3</sub>. Reprinted with permission from Y. Shiraishi, *Chem. Eur. J.*, 2011, **17**, 9816-9824. Copyright 2011 John Wiley & Sons.<sup>20</sup>

It is likely that over-oxidation to benzoic acid occurred. Benzoic acid has been known to bind strongly to the surface of metal oxides and can significantly inhibit other heterogeneous selective photocatalytic processes. The oxidation of toluene with UV irradiated titania in air was found to be inhibited by the formation and surface accumulation of benzoic acid.<sup>129</sup> If benzoic acid formed and bound strongly to the surface of WO<sub>3</sub> in the example above, then this interaction would inhibit the adsorption of benzyl alcohol and so slow the rate of reaction. In addition, this inhibition would also promote benzaldehyde selectivity by reducing the amount of benzaldehyde re-adsorption and so limiting the amount of further oxidation.

This theory was not discussed in the original report, is speculative and has been hypothesised by the author of this thesis. Benzoic acid adsorption and the subsequent impact on selectivity has not been studied in a wide range of systems. However, this kind of carboxylic acid inhibition could be important in achieving heterogeneous photocatalytic selectivity. Carboxylic acid inhibition could also be the reason for the increase in selectivity observed when oxalic acid is used as a sacrificial oxidant for the reduction of nitroaromatics to anilines using irradiated titania, Scheme 1.7a.

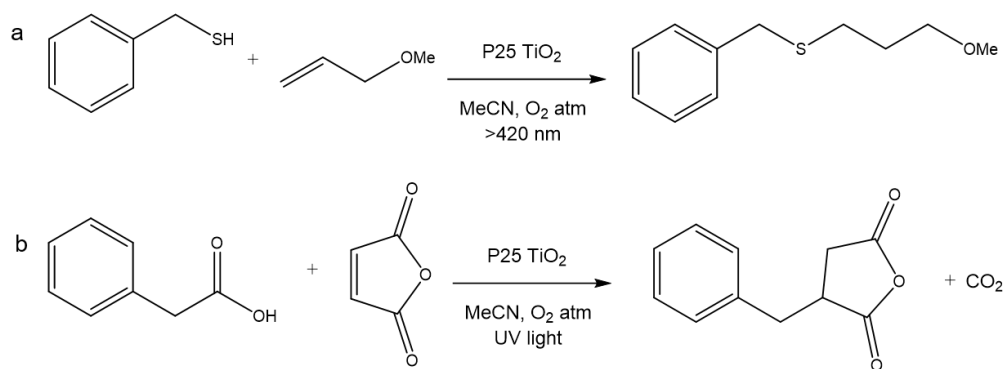
#### 1.4.4 Reactions in solution

Often a reactive species is able to undergo desorption from the photocatalyst surface after a redox reaction. In such systems, selective product formation can be achieved through

## Chapter 1

the reaction of such desorbed species with other compounds found at sufficient concentrations in solution. The best candidates for such compounds are those that are capable of fast reaction rates with the desorbed intermediates.

An example of such a system is the aerobic oxidation of benzyl mercaptans in the presence of titania dispersed in acetonitrile which showed the capacity for heterogeneous photocatalytic thiol-ene formation between benzyl mercaptans and a variety of different alkenes, Scheme 1.8a. Benzyl mercaptans are oxidised to form benzyl radicals which then form C-S bonds to alkenes in solution. Isolated yields as high as 90% were observed for the C-S coupled products formed by irradiation from a 20 W household bulb.<sup>33</sup> Similar radical chemistry has been observed with the use of UV irradiated titanium dioxide dispersed in acetonitrile for the decarboxylation of phenylacetic acid that resulted in the formation of a radical species used to cause C-C coupling to electron deficient alkenes found in molecules such as maleic anhydride, Scheme 1.8b.<sup>30</sup>



Scheme 1.8 – Thiol-ene and decarboxylative C-C bond coupling reactions using irradiated titania.<sup>30, 33</sup>

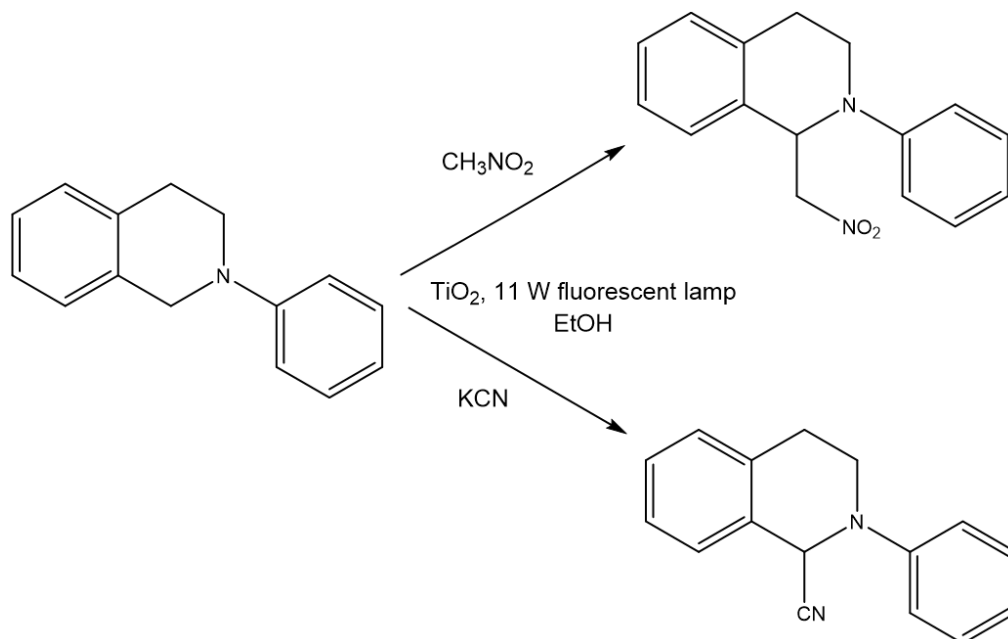
Titanium dioxide has also been applied to dehydrogenative coupling reactions similar to those observed with the use of homogeneous photocatalysts such as, Rose Bengal and Ru(bpy)<sub>3</sub>Cl<sub>2</sub>. The oxidation of tetrahydroisoquinoline derivatives allowed for activation of the carbon adjacent to nitrogen and subsequent nucleophilic attack from species in solution, Scheme 1.9. As a result, C-C bond forming reactions have been achieved between tetrahydroisoquinoline derivatives and CH<sub>3</sub>NO<sub>2</sub> and KCN which gave yields as high as 93% and 99% respectively; ethanol was used as a solvent and a 11 W fluorescent lamp was used for visible light irradiation.<sup>70</sup>

The use of ethanol was found to be optimal as a solvent which is surprisingly as alcohols are easily oxidised in heterogeneous photocatalytic systems. In addition, the high yields suggest that there was not a great amount of further oxidation or reduction even though the products contain functional groups which are capable of such reactions. It is possible



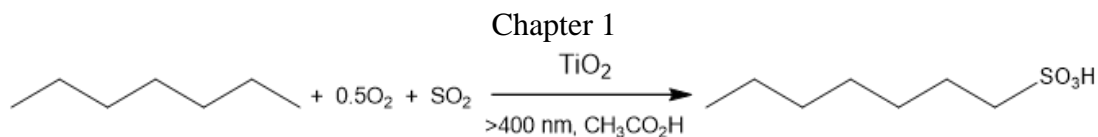
## Chapter 1

that the use of ethanol as solvent was optimal because ethanol could competitively bind and undergo oxidation which may have increased selectivity for the intended products by limiting re-adsorption and further redox reactions.



Scheme 1.9 – The use of visible light irradiated titanium dioxide for dehydrogenative coupling reactions of tetrahydroisoquinoline derivatives with  $\text{CH}_3\text{NO}_2$  and  $\text{KCN}$ .<sup>70</sup>

Alkanes adsorb very weakly to the surface of metal oxides such as titania and so their oxidation or reduction cannot be achieved by direct heterogeneous photocatalysis. However, the sulphoxidation of unactivated alkanes has been achieved via the oxidation of sulphur dioxide and reduction of dioxygen with anatase titania dispersed in acetic acid and irradiated with a 150 W Xe lamp through a  $>400$  nm filter, Scheme 1.10.<sup>130</sup> Low yields are obtained for the use of P25 titania in this reaction (ca. 20% in 10 h) and little discussion was given to selectivity. It is possible that selectivities were not discussed as the sulphoxidated product was able to adsorb to the photocatalyst surface which resulted in low product selectivity. It is also possible that the use of glacial acetic acid as solvent also mediated product selectivity through competitive binding to the surface of the photocatalyst. As discussed previously carboxylic acids have shown to bind strongly to the surface of metal oxides<sup>129</sup> and the hydrophobic nature of the long alkyl chain found in the product of sulphoxidation reduce the product's capacity for adsorption to the hydrophilic titania surface.



Scheme 1.10 – Sulfoxidation of alkanes and epoxidation of alkenes using irradiated titania.

## 1.5 Summary of selectivity and opportunities for investigation

It is clear from the discussion above that the selectivity of a heterogeneous photocatalytic reaction is dependent on a number of variables, such as: the irradiance wavelength range; solvent; the presence of sacrificial reagents; the presence of reagents capable of reacting with intermediate products in solution; the presence of compounds capable of competitive binding and photocatalyst modifications. However, the specific reasoning for the observed selectivity is not always clear. In many cases, it is possible to speculate that competitive binding and inhibition play a role in the observed selectivity of the heterogeneous photocatalytic systems. Further investigation is needed on a range of different systems in order to observe how significant competitive binding is to selectivity.

Other visible light absorbing heterogeneous photocatalysts that are capable of absorbing a much larger amount of visible light than titania have been used for selective chemical transformations. However, the specific interaction that guides selectivity is rarely investigated in depth.<sup>18, 22, 131-133</sup> A class of materials that provide a significant number of opportunities for exploration in the field of visible light heterogeneous photocatalysis are bismuth containing metal oxides. A number of different bismuth containing metal oxides can be synthesised and have shown the capacity for visible light absorption.<sup>24, 35, 92, 134-138</sup> In addition, several of these materials have been used in heterogeneous photocatalysis for selective chemical transformations.<sup>22, 24, 35, 139</sup> However, to my knowledge, there are several examples of reactions which have been shown to be possible with the use of irradiated titania that have not been investigated with some or any of the bismuth containing oxides.

## 1.6 Project aims

The primary aim of this project is to investigate bismuth containing semiconductors as potential heterogeneous photocatalysts for selective chemical transformations of value under visible light irradiation and, where selectivity is observed, to understand the reasons for this selectivity.

The principal objective of Chapter 2 will be to investigate which of the previously reported bismuth containing semiconductors is most successful in acting as a selective

## Chapter 1

photocatalyst for a particular chemical transformation of interest, namely in the oxidation of benzyl alcohol to benzaldehyde. The introduction of Chapter 2 will explore in more detail the attributes of bismuth containing semiconductors that allow these materials to be successful heterogeneous photocatalysts and will give reported examples of their use.

Having established which material is the best photocatalyst for selective benzyl alcohol under the conditions used in Chapter 2, the objective of Chapter 3 will be to explore this reaction system more extensively to be able to understand what causes benzaldehyde selectivity. The work will also attempt to draw conclusions associated to the role of dioxygen as an oxidant in this reaction as well as the causes of benzaldehyde selectivity; the value of achieving aldehyde selectivity from alcohol oxidation will also be discussed in the introduction of Chapter 3.

Having established the importance of dioxygen as an oxidant in the system described in Chapter 3, the objective of Chapter 4 will be to explore whether selective chemical transformations can be achieved using other oxidants, such as trifluoromethylation reagents, as a source of additional functionality. Chapters 3 and 4 will also investigate the role of various carboxylic acids in the heterogeneous photocatalytic systems used to see if the presence of these acids affects the product selectivity observed. With this in mind, the objective of Chapter 5 will be to investigate how the modification of the surface of previously used bismuth containing semiconductors affects how these materials behave in the presence of carboxylic acids, possibly allowing for the use of certain carboxylic acids as starting materials for another potentially selective reaction of interest, i.e. Photo-Giese coupled products.

The percentage conversion for starting materials and percentage selectivities for products will be the main metrics used to compare catalysts and different reaction systems. Quantum yield and quantum efficiency could be used for a similar purpose, however it was decided that these will not be used throughout this work as obtaining data on starting material conversion and product selectivity is operationally simpler and more relevant to achieving selective chemical transformations.

## 2 The Direct Comparison of Bismuth-Containing Semiconductors for the Heterogeneous Photocatalytic Oxidation of Benzyl Alcohol Selectivity into Benzaldehyde

### 2.1 Introduction

Many different binary transition metal oxides have been used as heterogeneous photocatalysts for a wide variety of applications.<sup>94, 140-146</sup> The most widely used material in heterogeneous photocatalysis, particularly in the field of selective chemical transformations is titanium dioxide.<sup>14, 16, 19, 21, 26, 147-153</sup> However, titania has not been able to absorb visible light without the formation of surface bound exciplexes which enabled visible light absorption.<sup>15, 17, 21</sup>

Other binary transition metal oxides have been utilised in heterogeneous photocatalysis. However, their use is limited by short charge carrier transport lengths before recombination within the bulk of the semiconducting material,<sup>154-156</sup> the average hole diffusion length of haematite ( $\text{Fe}_2\text{O}_3$ ) is ca. 10 nm.<sup>157-159</sup> However, the addition of bismuth to such binary metal oxides to form ternary metal oxides has been shown to provide a solution to this problem; this solution is discussed further in section 2.1.1.

#### 2.1.1 Bismuth containing semiconductors

The addition of bismuth to binary metal oxides to form ternary bismuth containing metal oxide semiconductors generally increases a material's ability to absorb visible light as the addition of Bi 6s orbitals to the top of the valence band narrows the materials band gap.<sup>160-163</sup> The addition of bismuth also allows for an increase in charge carrier mobility. It has been suggested that large bismuth 6s orbitals are capable of overlapping in these ternary metal oxides acting as effective charge carrier pathways,<sup>74, 164-166</sup> Figure 2.1.<sup>167, 168</sup> It has been found that the top of the valence band of bismuth containing semiconductors has a high amount of Bi 6s orbital character, Figure 2.2.<sup>160</sup> The density of states in this region in ternary bismuth containing metal oxide semiconductors is higher than in analogous binary metal oxide materials where the top of the valence band has a high amount of O 2p orbital character.<sup>74, 164-166, 160</sup> The result is that the average hole carrier distance for bismuth containing semiconductors is higher than that of corresponding binary metal oxides.<sup>169</sup> This means that more holes can react at the catalyst surface, become trapped and carry out redox chemistry.

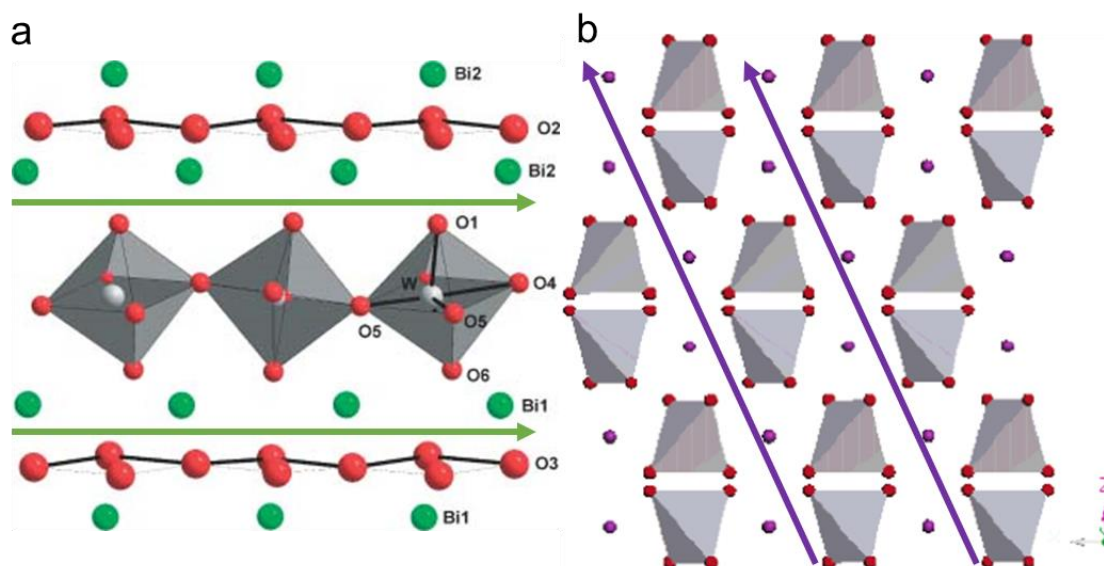


Figure 2.1 – The crystal structures of a) orthorhombic bismuth tungstate and b) monoclinic bismuth vanadate showing the channels of bismuth centres which can help charge carrier mobility through these materials. In a) green centres correspond to bismuth ions and in b) purple centres correspond to bismuth ions. Oxygen anions are in red and the grey colours show transition metal centred octahedra and tetrahedra in a) and b) respectively. a) Adapted with permission from M. Maczka, *J. Raman Spectrosc.*, 2010, **41**, 1059–1066. Published by John Wiley & Sons, Ltd.<sup>167</sup> b) Adapted with permission from M. Oshikiri, *J. Phys. Chem. B*, 2006, **110**, 9188–9194. Copyright 2006 American Chemical Society.<sup>168</sup>

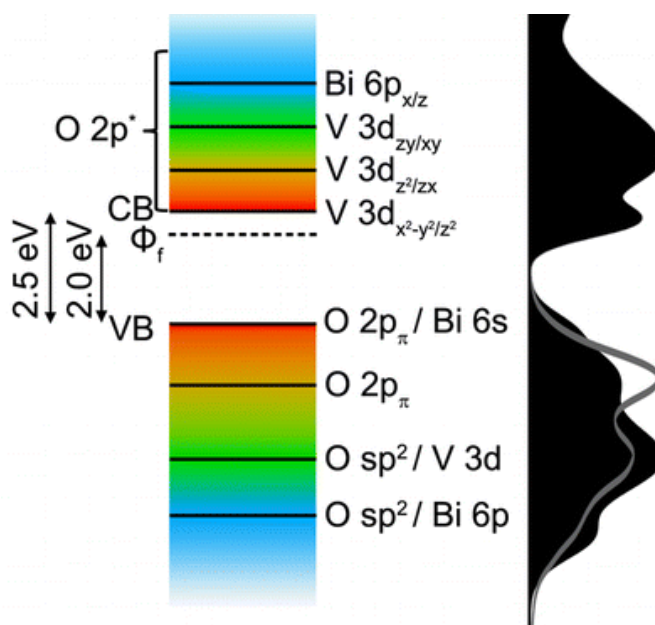
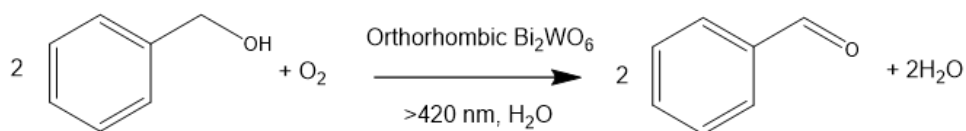


Figure 2.2 – The density of states (black trace from XPS and XAS, grey trace from XES) and orbital characteristics around the bandgap of monoclinic bismuth vanadate. Adapted with permission from I. D Sharp, *Chem. Mater.*, 2014, **26**, 5365–5373.<sup>160</sup> Copyright 2014 American Chemical Society.

Similar advantageous phenomena have been associated with the formation of other ternary metal oxides using heavy metals such as tin, lead or antimony.<sup>170-172</sup> It might be expected that the addition of such heavy metals would increase the toxicity of the semiconducting material. However, this has not been found to be the case with bismuth containing materials as they are surprisingly non-toxic.<sup>36, 173, 174</sup>

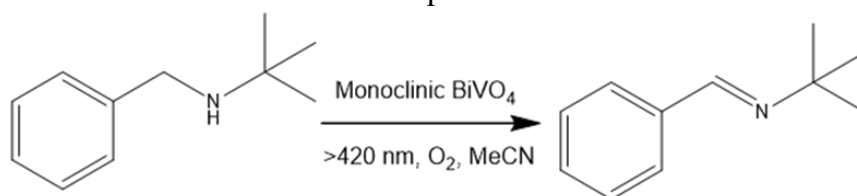
### 2.1.2 Photocatalytic application of bismuth containing semiconductors

Bismuth containing semiconductors have been used in a wide range of photocatalytic applications under visible light irradiation. In previously reported literature by Zhang et al., orthorhombic bismuth tungstate has been used as a selective photocatalyst for the oxidation of 0.1 mmol benzyl alcohol to benzaldehyde in 22 h<sup>24</sup> and for the oxidation of 0.1 mmol glycerol to dihydroxyacetone in 5 h<sup>175</sup> with the use of a 300 W Xe arc lamp along with 420 and 760 nm band pass filters, Scheme 2.1. These reactions were carried out in aqueous suspensions and it was claimed that the lack of •OH radical formation was fundamental in the selectivity observed.



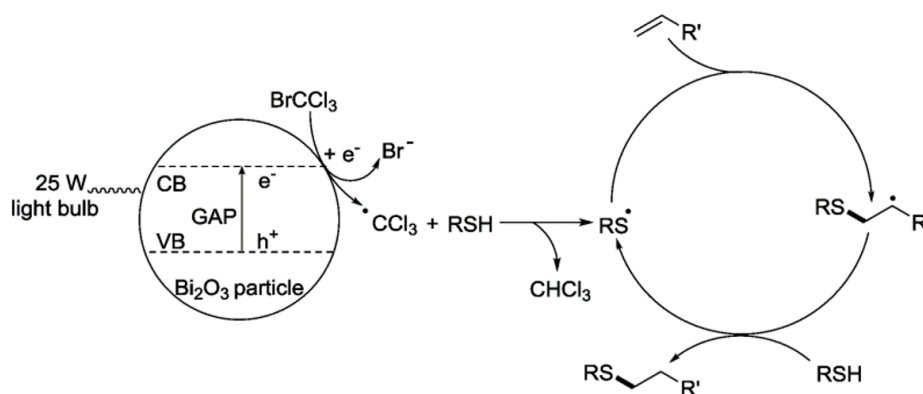
Scheme 2.1 – The oxidation of aerobic benzyl alcohol oxidation by visible light irradiated orthorhombic bismuth tungstate selectively into benzaldehyde.

Other literature, published by Yuan et al., has shown that monoclinic bismuth vanadate has been utilised in the selective aerobic oxidation of 0.1 mmol *N-t*-butylbenzyl amine to the corresponding imine in 7 h using a xenon arc lamp and a 420 nm band pass filter, Scheme 2.2.<sup>22</sup> Selectivities of >90% were achieved for a wide range of different benzyl amine substrates but no discussion was given as to the reason for the high selectivities achieved. It was suggested that differences in relative peak intensities between (040) and (110) peaks in the PXRD for different BiVO<sub>4</sub> samples could be linked to differences in conversion rates of benzyl amine. The authors of the report work have shown that the prepared BiVO<sub>4</sub> samples act as a better photocatalyst for the oxidation of benzyl amines than other bismuth containing semiconducting photocatalysts, such as bismuth tungstate, both in terms of benzyl amine conversion and benzyl imine selectivity. However, no data was given in relation to the morphologies, crystallinities or visible light absorption capacities of the other bismuth containing semiconductors used and so no conclusions could be made with regards to why there are differences in benzyl amine conversions and benzyl imine selectivities.



Scheme 2.2 – The aerobic oxidation of *N*-tertbutyl benzyl amine with visible light irradiated monoclinic bismuth vanadate

Binary bismuth oxides have also been shown to act as heterogeneous photocatalysts for selective organic transformations in previously reported work by Fadeyi et al. Catalytic amounts of bismuth oxide (1 mol%) have been used as a selective reductive radical initiator for C-S bond formation reactions between thiols and alkenes (0.5 mmol scale, >95% conversion in 12 h) via irradiation with a household 25 W bulb.<sup>35</sup> The proposed mechanism (Scheme 2.3) suggested that the irradiated bismuth oxide did not interact directly with the thiol or alkene but instead reduced  $\text{BrCCl}_3$  in order to produce a  $\cdot\text{CCl}_3$  radical via the loss of  $\text{Br}^-$ ; the  $\cdot\text{CCl}_3$  radical abstracted a hydrogen atom from the thiol in order to form a sulphur-centred radical which then couples to the alkene. Selectivity was not discussed in this work and the only comparison made was to the use of titanium dioxide as a heterogeneous photocatalyst for this thiol-ene reaction which was briefly discussed.



Scheme 2.3 – The mechanism for the irradiated  $\text{Bi}_2\text{O}_3$  initiated thiol-ene reaction. Reprinted with permission from O. O Fadeyi et al., *Org. Lett.*, 2015, **17**, 5756–5759.<sup>35</sup> Copyright 2015 American Chemical Society.

Another interesting bismuth containing semiconductor is bismuth ferrite ( $\text{BiFeO}_3$ ) which has also been reported as an effective heterogeneous photocatalyst with a band-gap capable of visible light absorption (2.2 eV, 560 nm).<sup>135, 176-180</sup> To date, bismuth ferrite has not been utilised as a photocatalyst for selective chemical transformations but has been used in the rapid degradation of phenolic compounds and of dyes such as methylene blue

under direct solar irradiation.<sup>178, 179</sup> Bismuth ferrite is of particular interest as it is an analogous bismuth containing semiconductor to the binary metal oxide haematite ( $\text{Fe}_2\text{O}_3$ ) which has been shown to be effective in the photoelectrochemical splitting of water for hydrogen evolution.<sup>181, 182</sup> The short charge carrier path length of haematite has limited the application of the material to use in mainly electrochemical systems,<sup>157-159</sup> however it is possible that the addition of bismuth could increase the charge carrier pathlength enough to allow for the wider application of iron containing semiconducting photocatalysts.

### 2.1.3 Comparing photocatalysts

Of the examples of the use of bismuth containing semiconductors in heterogeneous photocatalysis given, very little focus was given to comparing different semiconducting materials directly for their ability to act as effective and selective photocatalysts for the same reaction under analogous conditions. Only the example of benzyl amine oxidation discussed above involved any direct comparison of the use of bismuth containing semiconducting photocatalysts under analogous conditions.<sup>22</sup> Furthermore, their work only superficially compared the photocatalysts oxidative abilities without any discussion associated to the attributes of the various bismuth containing materials used that may affect the results observed. The lack of this information made it difficult to determine which materials provide the best avenues for advancement in the field.

In general, it was difficult to compare reactivity and selectivity of photocatalysts that have shown visible light photocatalytic activity, even when utilised for the same reaction. This was due to the high number of experimental variables between different heterogeneous photocatalytic reports. Differences in the irradiation source provided the most significant variables as spectral range and light intensity at specific wavelengths can vary dramatically, band pass filters provide additional confusion with regards to the wavelengths of light used. Furthermore, the catalyst loadings used across different studies range from 1 to 1250 mol% relative to the amount of starting material.<sup>15, 35</sup> Particle size and photocatalyst morphology also vary between different studies.<sup>136-138, 183</sup> These attributes affect surface area and so have an impact on the amount of substrate that can adsorb and react on the photocatalyst surface. These attributes also affect the proportion of charge carriers that can reach the surface of the photocatalyst and can therefore be used in the desired redox process.

In light of the number of variables across different photocatalytic studies, the number of different possible visible light absorbing bismuth containing photocatalysts and the lack



of studies that link differences in photocatalytic conversions and selectivities to physical or electronic attributes of different bismuth containing semiconductors, it was decided that different bismuth containing semiconductors of interest should be synthesised. These different materials were then compared as photocatalysts for the same reaction under analogous conditions in order to decide which materials were best for use in this selective heterogeneous photocatalytic system.

The heterogeneous photocatalytic conversion of several different starting materials was considered. Test reactions were carried out attempting to selectively transform benzyl mercaptan, benzyl chloride, benzyl bromide, benzyl carbamate, benzyl phosphonic acid and benzyl alcohol. However, the heterogeneous photocatalytic selective oxidation of benzyl alcohol appeared to be the most appropriate for the comparative study as it is the most highly studied reaction in the field of selective chemical transformations via heterogeneous photocatalysis. Many photocatalysts have been utilised for this reaction, such as  $\text{TiO}_2$ ,<sup>17</sup>  $\text{gC}_3\text{N}_4$ ,<sup>18</sup>  $\text{Bi}_2\text{WO}_6$ ,<sup>24</sup>  $\text{TiO}_2$  coated with  $\text{WO}_3$ ,<sup>20</sup>  $\text{CdS}$  coupled with amorphous  $\text{TiO}_2$ <sup>184</sup> and  $\text{Ru-O/BiVO}_4$ .<sup>185</sup> Studies such as these and the importance of selective alcohol oxidation to aldehydes are discussed further in chapter 3. The test reactions attempting to convert the starting materials other than benzyl alcohol listed above will not be discussed in this thesis.

### 2.1.4 Objectives

The objectives of this work were to:

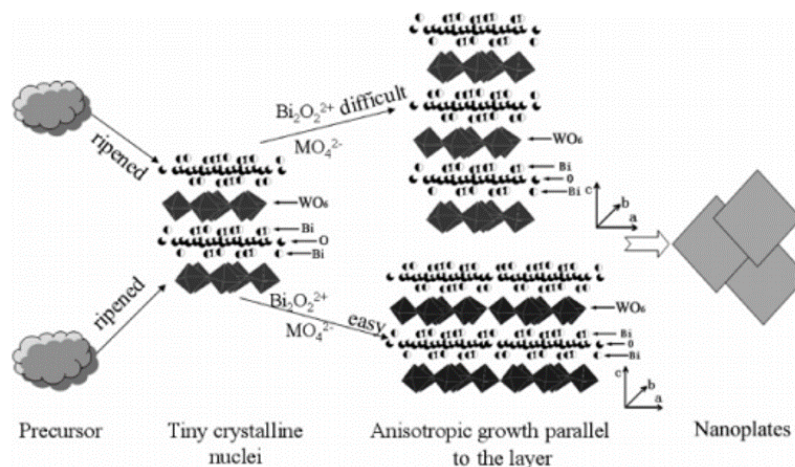
- Investigate which of the previously reported bismuth containing semiconductors is most successful in acting as a selective photocatalyst in the oxidation of benzyl alcohol to benzaldehyde; and
- Draw conclusions regarding which physical properties of the bismuth containing semiconductors are significant in the material's ability to act as a selective photocatalyst for benzyl alcohol oxidation.

## 2.2 Materials synthesis and characterisation

Electron-hole recombination reduces photocatalytic efficiency which can be linked to the diffusion length of holes and electrons. In addition, an increase in the surface area often gives an increase in activity due to the increasing availability of sites for substrate adsorption and chemical reaction. Therefore, the synthesis of particles of smaller dimension or materials with relatively high surface area were targeted to reduce the probability of bulk electron-hole recombination.<sup>134, 137, 177, 186</sup>

### 2.2.1 Bismuth tungstate ( $\text{Bi}_2\text{WO}_6$ )

Bismuth tungstate microflowers were synthesised hydrothermally from a reaction between bismuth nitrate and sodium tungstate without the presence of any templating reagent, adapted from a literature method.<sup>186</sup>  $\text{Bi}_2\text{WO}_6$  is the simplest of the Aurivillius materials which have a unique structure. The material is constructed from alternating  $(\text{Bi}_2\text{O}_2)_{n^{2n+}}$  layers and  $(\text{WO}_4)_{n^{2n-}}$  layers which allow for effective growth of the material along 2 dimensions; growth of the end of a layer is energetically more favourable than building a new layer. As a result, nanoflakes were synthesised by this method which aggregate together to form flower-like morphologies, Scheme 2.4.



Scheme 2.4 – The formation mechanism for orthorhombic  $\text{Bi}_2\text{WO}_6$  nanoplates. Reprinted with permission from C. Zhang and Y. Zhu., *Chem. Mater.*, 2005, **17**, 3537-3545.<sup>187</sup> Copyright 2005 American Chemical Society.

It has previously been shown that the flower-like bismuth tungstate species have an inherently high BET surface area, ca.  $10 \text{ m}^2\text{g}^{-1}$ , compared to other bismuth containing semiconductors that have been synthesised without a templating agent; the synthesis of bismuth vanadate without a templating agent has yielded materials with surface areas of ca.  $2 \text{ m}^2\text{g}^{-1}$ .<sup>188</sup> Other methods have been reported for the synthesis of other morphologies of bismuth tungstate. In previously reported work by Nithya et al., bismuth tungstate nanoparticles have been synthesised using a sonochemical synthetic method. However, this method requires a calcination step at  $500 \text{ }^\circ\text{C}$  in order to produce a crystalline material.<sup>189</sup> Such a step could result in particle sintering and therefore will reduce the surface area and photocatalytic activity of the material; no BET surface area is given but the average particle size for this method is  $60 \text{ nm}$ .<sup>189</sup> Other previously published work by Qamar et al. reported the synthesis of mesoporous bismuth tungstate through a soft templating hydrothermal method with the surfactant Pluronic F127.<sup>75</sup> Surface areas up to

$41 \text{ m}^2\text{g}^{-1}$  have been achieved from such a synthesis, however this increase in surface area did not translate to an increase in photocatalytic activity. In the reported work by Qamar et al., when the mesoporous bismuth tungstate catalyst was compared directly to an analogous non-mesoporous bismuth tungstate catalyst, in the visible light mediated degradation of Rhodamine B, a commonly used industrial dye, the increase in rate of degradation from the mesoporous bismuth tungstate sample over the non-mesoporous sample was only equivalent to ca. 10%.<sup>75</sup>

From the work contributing to this thesis, the  $\text{Bi}_2\text{WO}_6$  material synthesised appeared as an ivory coloured powder. Scanning electron microscopy of  $\text{Bi}_2\text{WO}_6$  showed agglomerated nanoflakes into flower-like morphologies, Figure 2.3. The agglomerates were ca.  $5 \mu\text{m}$  in diameter with nanoflakes that had a thickness in the order of nanometers.

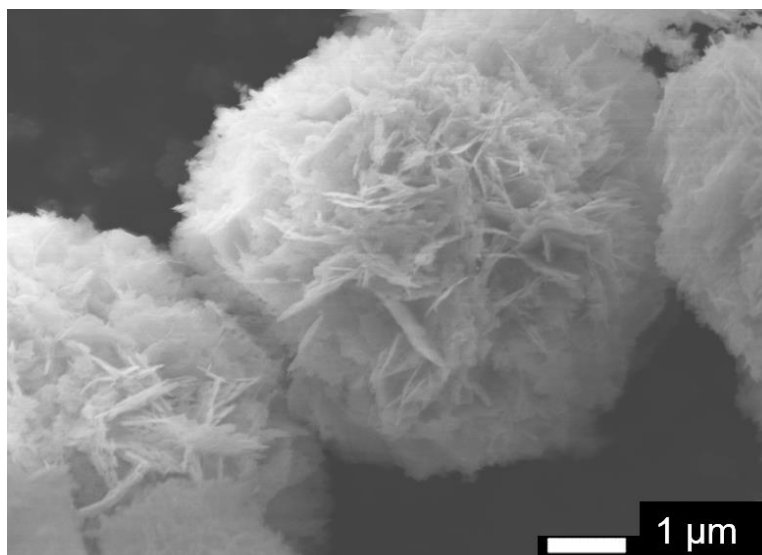


Figure 2.3 – SEM of  $\text{Bi}_2\text{WO}_6$

Powder X-ray diffraction data of  $\text{Bi}_2\text{WO}_6$  were consistent with crystalline orthorhombic  $\text{Bi}_2\text{WO}_6$  (JCPDS No. 39-0256), Figure 2.4. Minimum crystalline particle sizes can be estimated from the use of Scherrer's equation, Equation 2.1.

Equation 2.1

$$D = \frac{k_{sf}\lambda}{\beta_{fw}\cos(\theta)}$$

$D$  corresponds to the estimated minimum diameter of the crystalline particulate;  $k_{fw}$  is the shape factor = 0.89;  $\lambda$  corresponds to the wavelength of X-ray radiation (0.154046 nm for a Cu  $K\alpha$  emission source);  $\beta_{sf}$  corresponds to the full width at half maximum of the diffraction peak at  $2\theta$ ;  $\theta$  corresponds to the Bragg diffraction angle. This method only gives the minimum crystalline particle size as peak width is broadened both by the

instrument and particle shape effects; both of these factors are difficult to account for. For  $\text{Bi}_2\text{WO}_6$ , the minimum crystalline particle size was estimated to be 11.5 nm; the FWHM of the peak consistent with the diffraction from the (131) plane was used for this estimation.

The BET equation, Equation 2.2, was used to calculate the BET surface area of the materials from the nitrogen isotherms, values of relative pressure used for this calculation were consistently kept between 0.05 and 0.20, where the adsorption curve is closest to linearity.

$$\text{Equation 2.2} \quad \frac{p}{n_a(p_0 - p)} S_{total} = \frac{1}{n_m C} + \frac{(C-1)p}{n_m C p_0}$$

$p$  represents equilibrium pressure and  $p_0$  represents saturation pressure.  $n_a$  represents quantity of adsorbed gas and  $n_m$  represents the monolayer capacity.  $C$  is the BET constant and  $S_{total}$  represents total surface area. In Figure 2.5, it was noticed that the volume of nitrogen appears to decrease within this range. It is possible that the degassing of the  $\text{Bi}_2\text{WO}_6$  in this case was not effective enough meaning that adsorbates desorbed from the surface during this experiment. However, several repeats of this experiment could not avoid this phenomenon, suggesting that this is a sample dependant issue. The BET surface area of  $\text{Bi}_2\text{WO}_6$  was calculated as  $8.8 \text{ m}^2\text{g}^{-1}$ , there may be a significant error associated to this measurement due to the phenomenon discussed above. The nitrogen isotherm for  $\text{Bi}_2\text{WO}_6$  exhibited a type III isotherm typical of a non-porous material, Figure 2.5.

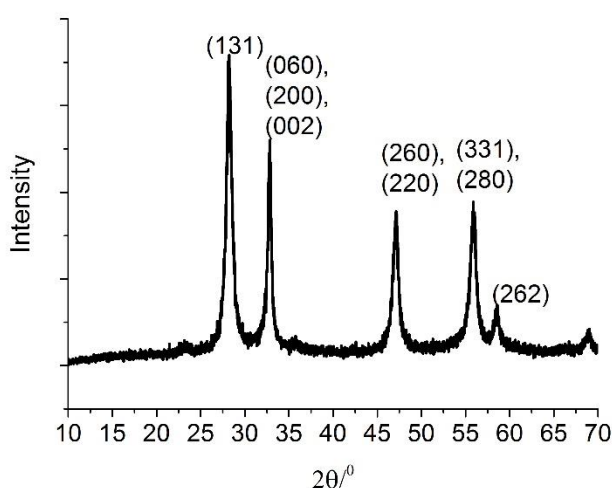


Figure 2.4 - PXRD of  $\text{Bi}_2\text{WO}_6$  consistent with crystalline orthorhombic  $\text{Bi}_2\text{WO}_6$  (JCPDS No. 39-0256).

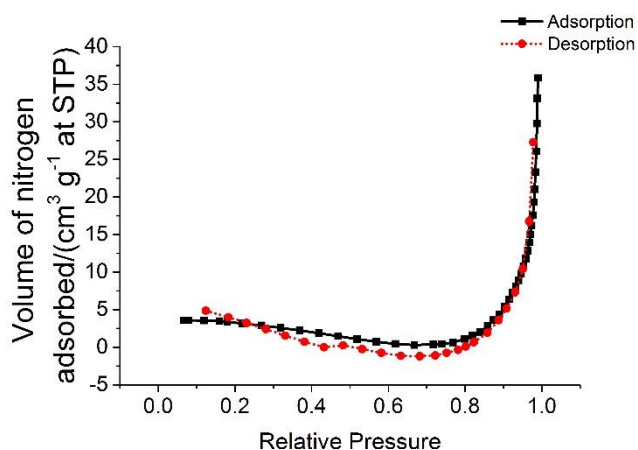


Figure 2.5 – N<sub>2</sub> isotherm for Bi<sub>2</sub>WO<sub>6</sub>

Diffuse reflectance UV-vis spectroscopy (DRUVS) was used to estimate the band gap of the Bi<sub>2</sub>WO<sub>6</sub> material. To be able to estimate the band gap for a semiconducting material, reflectance data must be converted using the Kubelka-Munk function, Equation 2.3 and Equation 2.4, and made into a Tauc plot by plotting this function against photon energy (E/eV).

Equation 2.3

$$F(R) \cdot E^r$$

Equation 2.4

$$F(R) = \frac{1-R^2}{2R}$$

R represents reflectance at a given photon energy (E); r gives the nature of the transition, for indirect semiconductors  $r = \frac{1}{2}$  and for direct semiconductors  $r = 2$ .

The Kubelka-Munk function was applied to the reflectance data to generate a Tauc plot giving an estimated band-gap of 2.80 eV (440 nm) for Bi<sub>2</sub>WO<sub>6</sub>, which was the same as the reported band gap of Bi<sub>2</sub>WO<sub>6</sub> (2.80 eV, 440 nm),<sup>75, 186, 187, 189</sup> Figure 2.6.

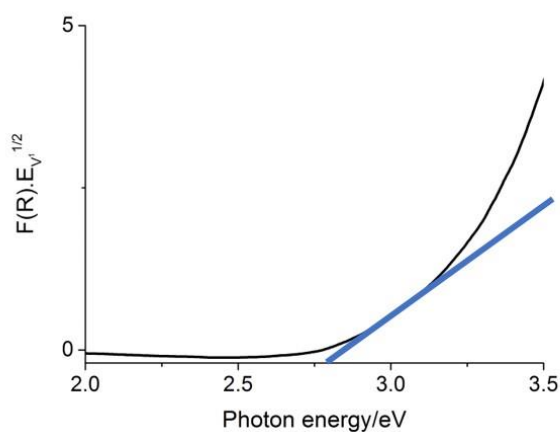
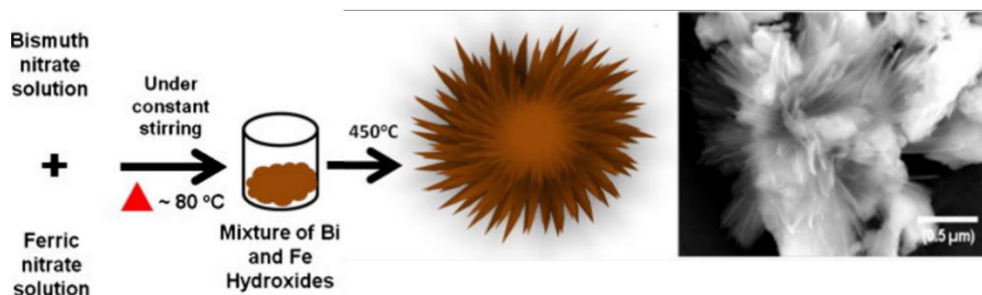


Figure 2.6 – The Tauc plot used to estimate the band-gap for the indirect semiconductor, Bi<sub>2</sub>WO<sub>6</sub>

### 2.2.2 Bismuth ferrite

In the work contributing to this thesis, bismuth ferrite was synthesised from the high temperature annealing of bismuth and iron hydroxides that were synthesised from bismuth and iron nitrate precursors. In the literature associated to this method from Sakar et al., solid-state annealing at 450 °C resulted in the formation of flower-like morphologies,<sup>177</sup> similar to those observed from the previously discussed bismuth tungstate synthesis. As mentioned above, high temperatures in bismuth-containing semiconductor synthesis have often been associated with bismuth diffusion and undesired particle sintering. However, bismuth diffusion was desired in this solid-state annealing synthesis in order to selectively form the desired material, BiFeO<sub>3</sub>. Other previously reported methods that required heating at lower temperatures caused unselective formation of bismuth ferrite, with evidence of significant amounts of Bi<sub>2</sub>O<sub>3</sub>, Fe<sub>2</sub>O<sub>3</sub> and Bi<sub>2</sub>Fe<sub>4</sub>O<sub>9</sub> found in the final material.<sup>176, 179, 180</sup> The flower-like morphology observed in the literature has been linked with dendritic growth of spherical particles which branch out as a result of metal diffusion between bismuth oxide and iron oxide, Scheme 2.5; high temperatures are needed for this metal diffusion to occur.



Scheme 2.5 – Literature method for the growth of BiFeO<sub>3</sub> with a flower-like morphology. Adapted with permission from Sakar et al., *Mater. Res Bull.*, 2013, **48**, 2878–2885.<sup>177</sup> Published by Elsevier.

Annealing to higher temperatures, such as 550 °C, led to the formation of large aggregates that are likely to have a low surface area and activity. The balancing of temperatures required to mediate material selectivity and particle sintering, limits the exploration of synthetic methods for the production of high surface area BiFeO<sub>3</sub>.<sup>177</sup> Combustion synthesis has been a method reported to achieve the high temperatures required for selective BiFeO<sub>3</sub> formation, but allows for a short reaction time which reduced the likelihood of significant particle sintering.<sup>60</sup> Combustion synthesis can however be dangerous as it required the mixing and drying of bismuth and iron precursors in the presence of nitric acid and an organic fuel to intentionally cause combustion.<sup>60</sup>

## Chapter 2

From the work contributing to this thesis, the synthesis of  $\text{BiFeO}_3$  at  $450\text{ }^\circ\text{C}$  resulted in the formation of a brown powder. Interestingly, scanning electron microscopy of bismuth ferrite did not show a flower-like morphology but instead showed a mixture of large agglomerated micrometer-sized spheres and larger plates that appear to be porous. Some exposed areas allowed for the observation of broken spheres and open plates where a highly connected porous material is visible, Figure 2.7.

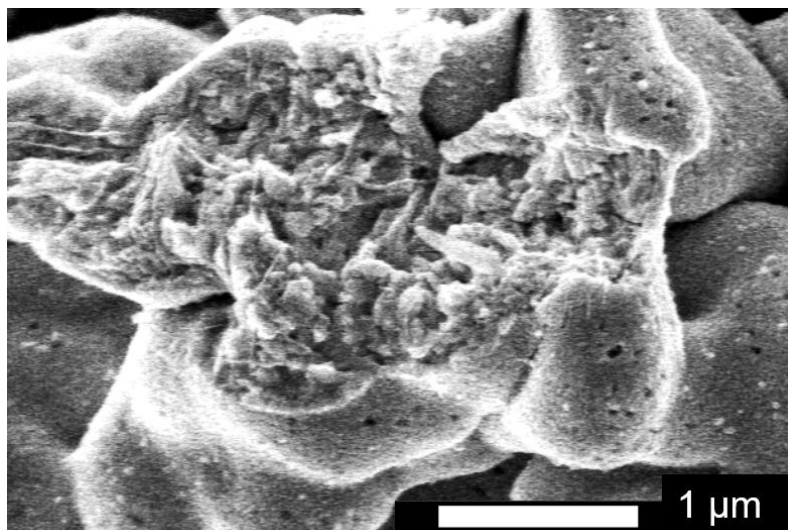


Figure 2.7 – SEM of synthesised  $\text{BiFeO}_3$

Powder X-ray diffraction data of  $\text{BiFeO}_3$  were consistent with rhombohedrally distorted perovskite bismuth ferrite (JCPDS No. 20-0169), Figure 2.8. There was no evidence of iron oxide or hydroxide or bismuth oxide or hydroxide species. Using Equation 2.1, the minimum crystalline particle size of  $\text{BiFeO}_3$  was estimated to be 13.8 nm; the FWHM of the peak consistent with the diffraction from the (021) plane was used for this estimation. The adsorption isotherm exhibited a type V isotherm typical of a porous material. The isotherm was also used to calculate the average pore diameter, 16 nm. The material can therefore be characterised as mesoporous, Figure 2.9. The BET surface area of  $\text{BiFeO}_3$  was calculated to be  $16.9\text{ m}^2\text{g}^{-1}$  using Equation 2.2.

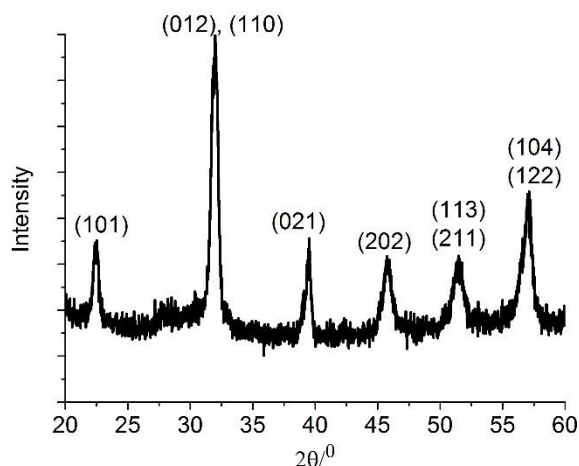


Figure 2.8 – PXRD of  $\text{BiFeO}_3$  consistent with rhombohedrally distorted perovskite bismuth ferrite (JCPDS No. 20-0169).

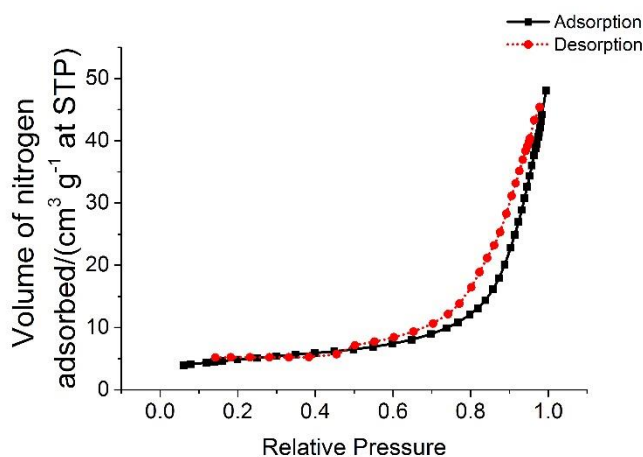


Figure 2.9 –  $\text{N}_2$  isotherm of  $\text{BiFeO}_3$

DRUVS was used to estimate the band gap of bismuth ferrite. The Kubelka-Munk function was applied to the reflectance data giving a band-gap of 1.7 eV (730 nm) for bismuth ferrite, which was significantly lower than the reported band gap of  $\text{BiFeO}_3$  (2.2 eV, 560 nm),<sup>135, 176-180</sup> Figure 2.10. In iron containing materials, absorption between 500 and 700 nm is often said to be consistent with d-d transitions between adjacent Fe centres.<sup>190, 191</sup> As a result, it may be said that the Tauc plot is consistent with d-d transitions and not with the excitement of an electron across a semiconducting band gap.



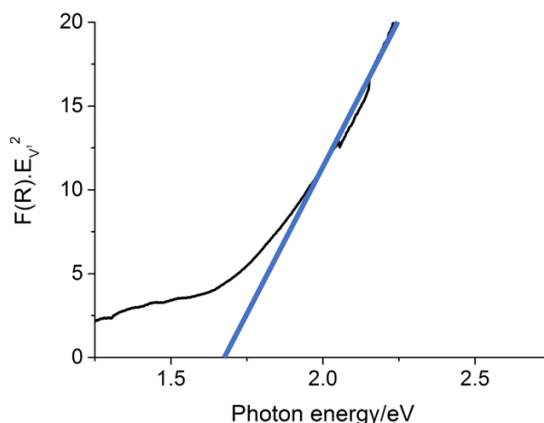


Figure 2.10 – The Tauc plot used to estimate the band-gap of the direct semiconductor,  $\text{BiFeO}_3$

An attempt to make small, spherical bismuth ferrite nanoparticles using a nebuliser and a tube furnace at high temperatures was attempted. The method proved effective in synthesising spherical nanoparticles, which were collected on a glass slide from the end of the tube furnace. However, only very small quantities of this material could be synthesised from an experiment. As a result, the bismuth ferrite made using this method shall not be discussed further in this thesis.

### 2.2.3 Bismuth oxide

The reproduction of  $\beta\text{-Bi}_2\text{O}_3$  nanoparticles from a previously reported solvothermal-calcination method by Xiao et al., was attempted. A bismuth-ethylene glycol complex was used to form bismuth metal nanoparticles by reduction from D-fructose at  $160\text{ }^\circ\text{C}$ . These particles were then calcined in order to form  $\beta\text{-Bi}_2\text{O}_3$  at  $300\text{ }^\circ\text{C}$ , Figure 2.11.<sup>134</sup> In a similar manner to the bismuth ferrite synthesis discussed above, specific calcination temperatures were required in order to completely oxidise the bismuth metal and to selectively form the most visible-light responsive polymorph of bismuth oxide which is  $\beta\text{-Bi}_2\text{O}_3$ .  $\alpha$ -,  $\beta$ -,  $\gamma$ - and  $\delta\text{-Bi}_2\text{O}_3$  are the various polymorphs of bismuth oxide and  $\alpha$ -,  $\beta$ - and  $\delta\text{-Bi}_2\text{O}_3$  are photo-responsive.<sup>134, 192</sup> Of these polymorphs,  $\beta\text{-Bi}_2\text{O}_3$  has the lowest band gap but has also been described as a metastable high temperature modification.<sup>134, 192</sup> Mixtures of various polymorphs of  $\text{Bi}_2\text{O}_3$ , that also include the  $\beta\text{-Bi}_2\text{O}_3$  polymorph, have been known to rapidly transform to the  $\alpha$ -polymorph at low temperatures.<sup>134, 192</sup> Therefore, the synthesis of pure phase  $\beta\text{-Bi}_2\text{O}_3$  was significantly important in optimising visible light absorption by avoiding the formation of the  $\alpha$ -polymorph.<sup>134</sup>

Other previously reported literature methods have shown nanoparticulate bismuth oxide produced from single sources. However, these methods required the degradation of

## Chapter 2

complex precursors such as  $[\text{Bi}_{38}\text{O}_{45}(\text{OMc})_{24}(\text{DMSO})_9]_2[\text{DMSO}_7]\text{H}_2\text{O}$  ( $\text{OMc} = \text{O}_2\text{CC}_3\text{H}_5$ ) and tris(*N*-furfuryl-*N*-(2-phenylethyl)dithiocarbamate)bismuth(III).<sup>193, 194</sup> Porous bismuth oxide has been synthesised using a sol-gel method with methoxyethanol and urea, but produced a mixture of polymorphs and surface areas no greater than  $10 \text{ m}^2\text{g}^{-1}$ .<sup>195</sup> Hollow  $\text{Bi}_2\text{O}_3$  spheres have also been synthesised by a solvothermal method in a mixed glycerol/ethanol solution but low BET surface areas were observed for this method, ca.  $3 \text{ m}^2\text{g}^{-1}$ .<sup>196</sup>

From the work contributing to this thesis,  $\beta\text{-Bi}_2\text{O}_3$  from the solvothermal calcination method appeared as a pale-yellow powder and the bismuth metal nanoparticles appeared as a grey powder. Scanning electron microscopy of  $\beta\text{-Bi}_2\text{O}_3$  showed a mixture of agglomerated plates and spheres which are roughly 100 nm in size, Figure 2.12. This was slightly larger than the 70 nm observed from the literature,<sup>134</sup> in addition, the literature reported SEM images showed spherical nanoparticles alone without the presence of the plates observed from the sample synthesised in this work.

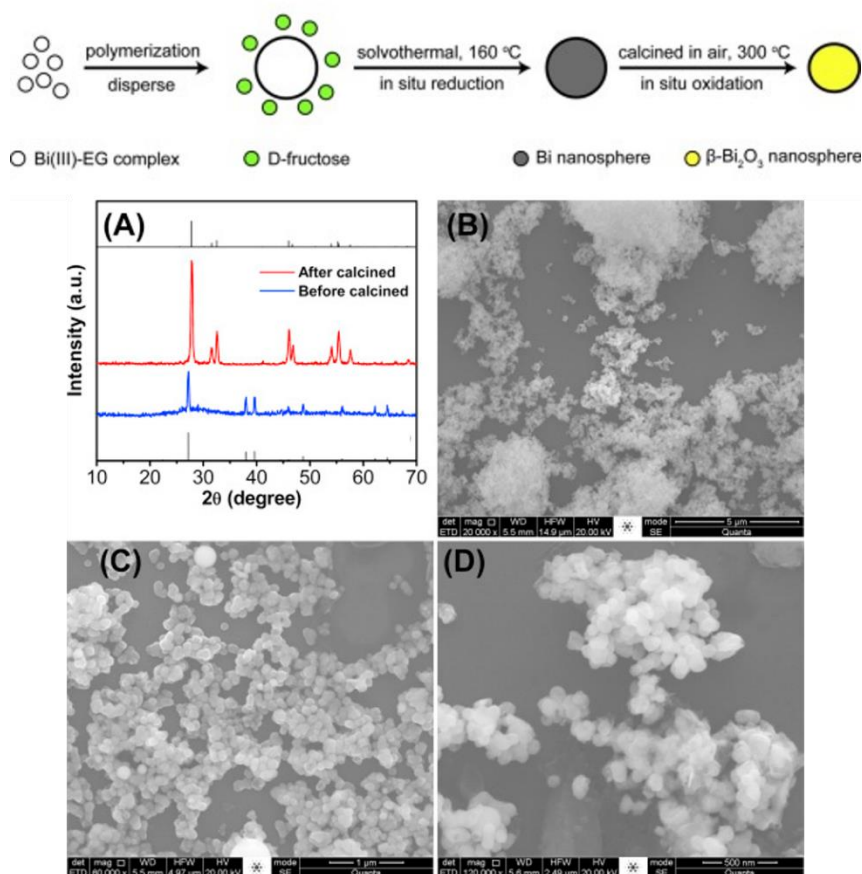


Figure 2.11 – An illustration for the synthesis of  $\beta\text{-Bi}_2\text{O}_3$  with literature characterisation data. A) PXRD of the final  $\beta\text{-Bi}_2\text{O}_3$  and the intermediate Bi metal product. B), C) and D) SEM images of the final  $\beta\text{-Bi}_2\text{O}_3$  nanosphere. Adjusted with permission from *J. Nan., Appl. Catal. B*, 2013, **140–141**, 433–443.<sup>134</sup> Printed by Elsevier.

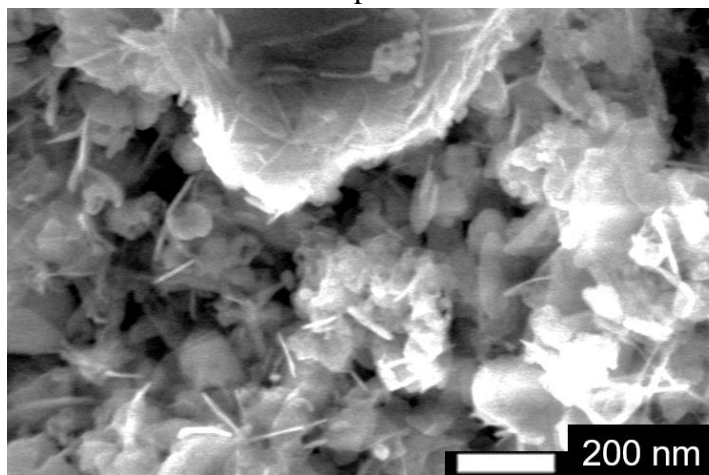


Figure 2.12 – SEM of  $\beta$ - $\text{Bi}_2\text{O}_3$  flakes

Powder X-ray diffraction data of  $\beta$ - $\text{Bi}_2\text{O}_3$  were consistent with crystalline tetragonal bismuth oxide (JCPDS No. 78-1793), Figure 2.13. Using Equation 2.1, the minimum crystalline particle size of  $\text{Bi}_2\text{O}_3$  was estimated to be 34.1 nm; the FWHM of the peak consistent with the diffraction from the (210) plane was used for this estimation. The nitrogen isotherm exhibited a type III isotherm typical of a non-porous material, Figure 2.14. The BET surface area of  $\beta$ - $\text{Bi}_2\text{O}_3$  was calculated to be  $6.2 \text{ m}^2\text{g}^{-1}$  using Equation 2.2.

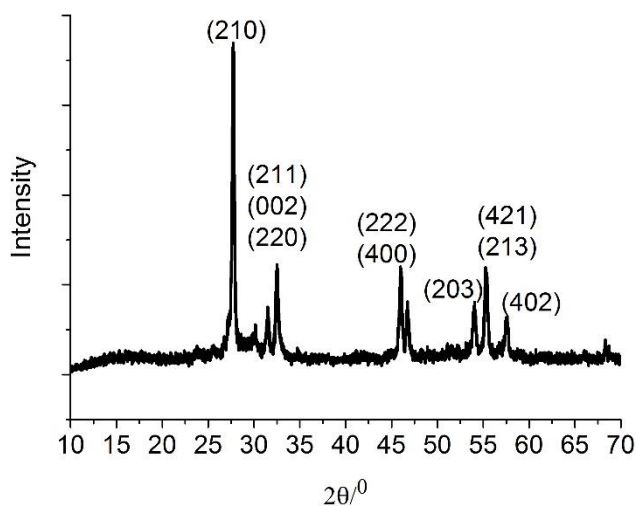


Figure 2.13 – PXRD of  $\beta$ - $\text{Bi}_2\text{O}_3$  consistent with crystalline tetragonal bismuth oxide (JCPDS No. 78-1793).

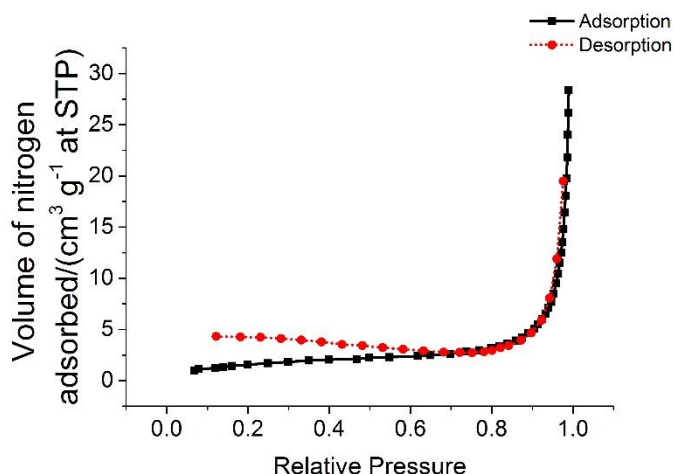


Figure 2.14 –  $N_2$  isotherm of  $\beta$ - $Bi_2O_3$

DRUVS was used to estimate the band gaps of the bismuth oxide. The Kubelka-Munk function was applied to the reflectance data giving a band-gap of 2.70 eV (460 nm), which was slightly higher than the reported band gap of  $\beta$ - $Bi_2O_3$  (2.4 eV, 520 nm),<sup>134, 193, 194</sup> Figure 2.15.

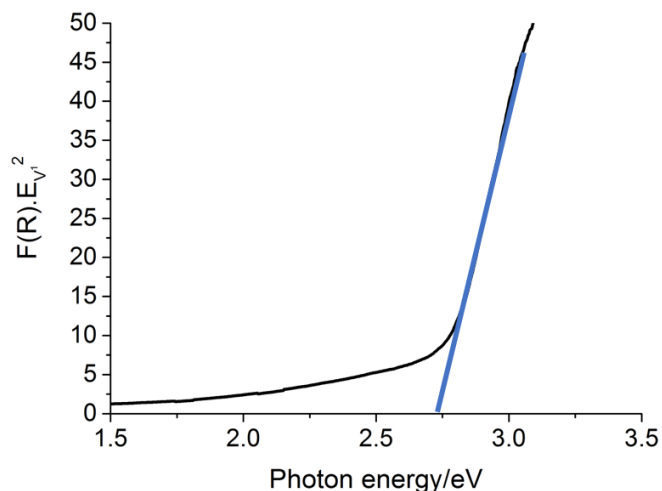


Figure 2.15 – The Tauc plot used to estimate the band-gap of the direct semiconductor,  $\beta$ - $Bi_2O_3$

#### 2.2.4 Bismuth vanadate

Bismuth vanadate nanoparticles (nan- $BiVO_4$ ) were synthesised from a reaction between  $[Bi(EDTA)]^-$  and  $(NH_4)VO_3$  under hydrothermal conditions using a modified literature procedure; the original method that this work was based on was published by Sun et al.<sup>137</sup> Other methods have been described to prepare  $BiVO_4$  to maximise surface area. These include the solvothermal synthesis of free hollow  $BiVO_4$  spheres,<sup>197</sup> combustion synthesis of  $BiVO_4$  nanoparticles,<sup>198</sup> spray pyrolysis to form  $BiVO_4$  thin films<sup>199</sup> and the synthesis

## Chapter 2

of nanoporous  $\text{BiVO}_4$  electrodes through electrochemical deposition of  $\text{BiOI}$  and a subsequent reaction with  $\text{VO}(\text{acac})_2$ .<sup>200</sup> These syntheses gave materials exhibiting surface areas in the range  $3.0 - 31.2 \text{ m}^2\text{g}^{-1}$ . However, to my knowledge, only the synthesis of  $\text{BiVO}_4$  electrodes, and not colloidal powders, have yielded materials with surface areas significantly higher than  $10 \text{ m}^2\text{g}^{-1}$ .

Visually, nan- $\text{BiVO}_4$  appeared as a yellow powder. Scanning electron microscopy of  $\text{BiVO}_4$  showed agglomerated particles with features that range in size from ca. 20 to 100 nm, Figure 2.16.

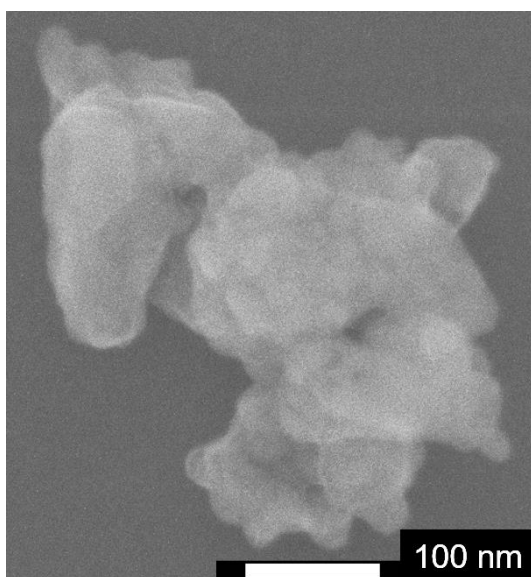


Figure 2.16 - SEM of nan- $\text{BiVO}_4$

Powder X-ray diffraction data of  $\text{BiVO}_4$  were consistent with crystalline monoclinic  $\text{BiVO}_4$  (JCPDS no. 14-0688), Figure 2.17. Using Equation 2.1, the minimum crystalline particle size of nan- $\text{BiVO}_4$  was estimated to be 15.7 nm; the FWHM of the peak consistent with the diffraction from the (121) plane was used for this estimation. The nitrogen isotherm exhibited a type III isotherm typical of a non-porous material, Figure 2.18. The BET surface area of nan- $\text{BiVO}_4$  was calculated as  $7.9 \text{ m}^2\text{g}^{-1}$  using Equation 2.2.

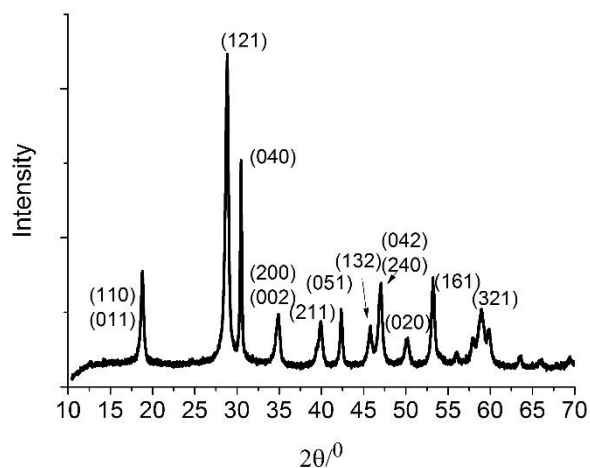


Figure 2.17 – PXRD for nan-BiVO<sub>4</sub> consistent with crystalline monoclinic BiVO<sub>4</sub> (JCPDS no. 14-0688)

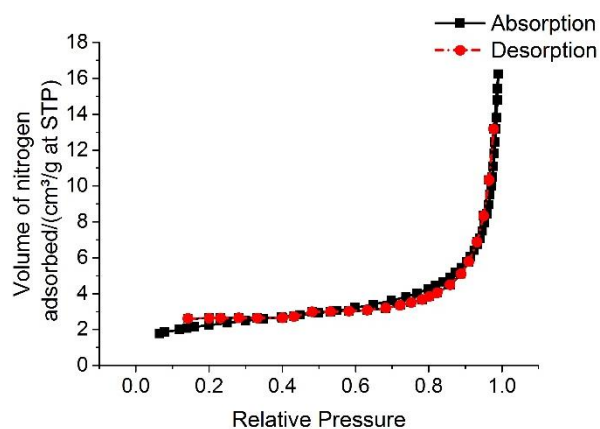


Figure 2.18 – N<sub>2</sub> isotherm for nan-BiVO<sub>4</sub>

DRUVS was used to estimate the band gaps of the BiVO<sub>4</sub> material. The Kubelka-Munk function was applied to the reflectance data giving an estimated band-gap of 2.25 eV (540 nm) for nan-BiVO<sub>4</sub>, which was slightly lower than the reported band gap of monoclinic BiVO<sub>4</sub> (2.4 eV, 520 nm), Figure 2.19.<sup>137, 197, 198</sup>

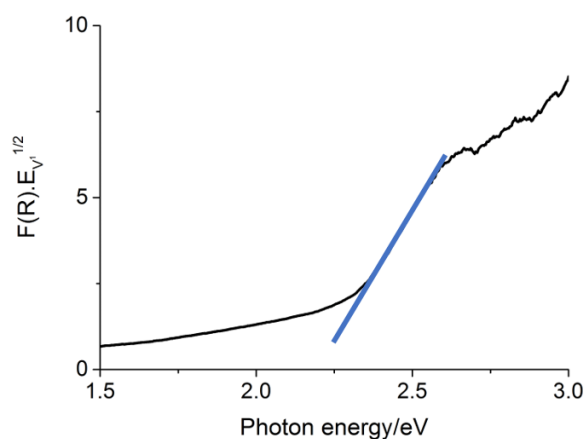


Figure 2.19 - The Tauc plot used to estimate the band-gap of the indirect semiconductor, nan-BiVO<sub>4</sub>

Several different methods of synthesising monoclinic bismuth vanadate with relatively high surface area were attempted; these included methods used to synthesise microporous and mesoporous materials.<sup>201, 202</sup> However, due to complex nature of these methods and the lack of any significant difference in surface areas obtained, these other methods of synthesising monoclinic bismuth vanadate will not be discussed in this thesis.

### 2.2.5 Photocatalyst comparison

Each material synthesised in section 2.2.1-4 was used in the aerobic oxidation of benzyl alcohol in acetonitrile under the irradiance of a 30 W blue LED array, Table 2.1. The power of this LED array was measured at 230 mWcm<sup>-2</sup>. The power of this blue LED array was tested at least every 3 months throughout this project to ensure that this power stayed relatively constant and measurements did not vary below 225 mWcm<sup>-2</sup> or above 257 mWcm<sup>-2</sup>.

In order to specifically observe the activity of the photocatalytic semiconductors under visible light irradiation, an adapted commercially available blue LED flood light was chosen as an irradiation source. LEDs are cheap, powerful, efficient and very easy to source. But most importantly the narrow emission range of LEDs mean that only visible light wavelengths were utilised in photocatalysis, Figure 2.20. Blue LEDs have been ubiquitously used in homogeneous photocatalysis but are much less commonly used in heterogeneous photocatalysis. Examples of blue LED use in homogeneous photocatalysis include: Ru(bpy)<sub>3</sub>Cl<sub>2</sub> and Ir(ppy)<sub>2</sub>(dtbbpy)PF<sub>6</sub> complexes under blue LED light irradiation being used in the coupling of *N*-aryltetrahydroisoquinoline and various Michael acceptors;<sup>203</sup> the *ortho*-alkylation of electron deficient heteroarenes, via alcohol

## Chapter 2

oxidation, which has been made possible by the irradiation of  $\text{Ir}(\text{ppy})_2(\text{dtbbpy})\text{PF}_6$  complexes with blue LEDs<sup>67</sup> and Ir complexes which have also been utilised as photo-initiators for the polymerisation of *N*-vinylcarbazole under blue or green LED light irradiation.<sup>204</sup>

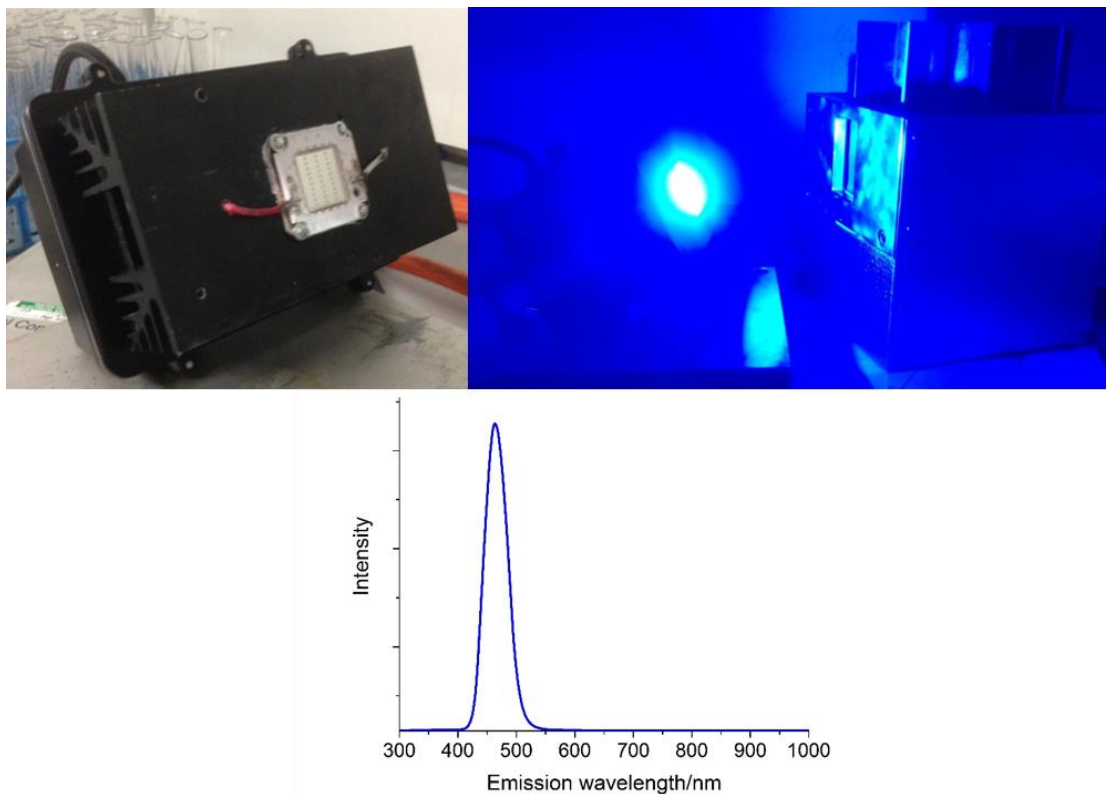


Figure 2.20 – The adapted commercially available blue LED flood light (both off and on) and its emission spectrum showing emission wavelengths consistent with blue light only (400 to 560 nm).

High power and low efficiency xenon or mercury arc lamps are often used in heterogeneous photocatalysis alongside band pass filters in order to control the wavelengths used to visible light only. However, it has been observed that band pass filters do not effectively filter all light below the cut-off wavelength quoted for a specific filter. In fact, it should be noted that for a 400 nm filter, 50% transmission occurs at 400 nm and 0% transmission occurs at roughly 380 nm, Figure 2.21. This is very significant in any work utilising anatase or rutile titania. With a band gap of 3.2 eV (390 nm), anatase titania cannot absorb photons with a wavelength of 400 nm but with the use of a 400 nm band pass filter, UV photons of 390 nm will still be able to bridge the bandgap in anatase titania. With a band gap of 3.05 eV (405 nm), rutile titania cannot absorb photons with a wavelength of 420 nm but with the use of a 420 nm band pass filter, photons with wavelengths as low as 405 nm will still be able to bridge the bandgap in rutile titania.



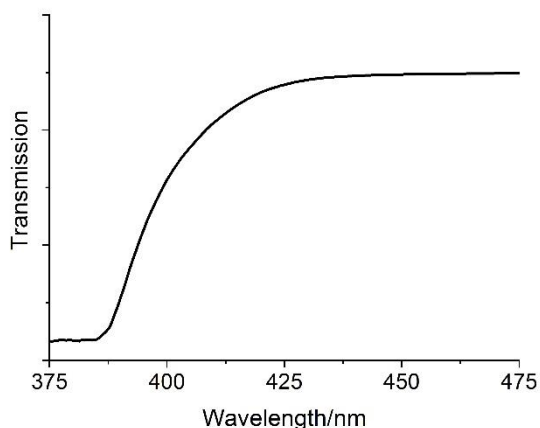


Figure 2.21 – The transmission of light through a >400 nm band pass filter, showing that light with wavelengths shorter than 400 nm pass through the filter. A 1 kW Hg[Xe] arc lamp was used as an emission source with a broad range of emission wavelengths in this region.

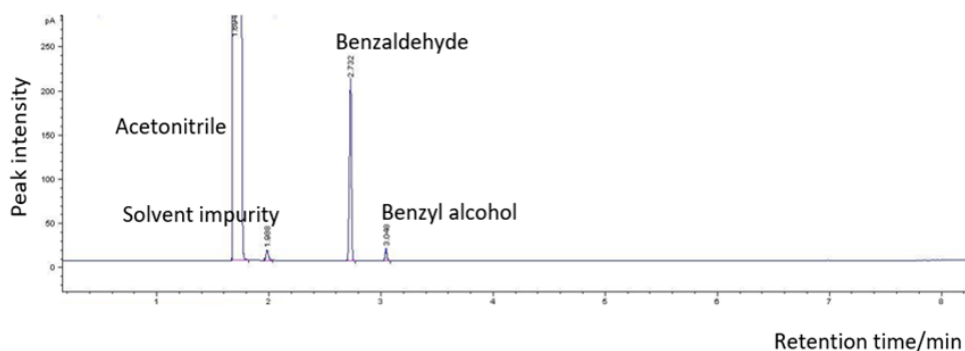


Figure 2.22 – Gas chromatograph for the reaction mixture from the oxidation of benzyl alcohol selectively to benzaldehyde with blue light irradiated nan-BiVO<sub>4</sub>

For analysis, an aliquot of each reaction mixture was taken and gas chromatography was used to study its contents, using a reverse phase column and heating from 90 to 300 °C with a heating rate of 20 °C min<sup>-1</sup>. The gas chromatograms showed peaks with retention times consistent with benzaldehyde and benzyl alcohol, 2.7 and 3.0 min respectively, Figure 2.22. No evidence was present for the formation of any other oxidation products such as benzoic acid (retention time of 2.5 min) or decarboxylated products such as benzene (retention time of 1.9 min). The formation of benzaldehyde selectively from these reactions was supported by <sup>1</sup>H NMR spectra (d<sub>6</sub>-DMSO, 400 MHz) which clearly showed a peak consistent with the presence of an aldehyde functionality at 9.98 ppm and 3 aromatic signals with integrations that were appropriately proportionate to the aldehyde peak; the only other signals present were consistent with the starting material benzyl alcohol (4.45 ppm consistent with the CH<sub>2</sub>OH functionality and corresponding aromatic signals in the ranges of 7.14-7.21 and 7.23-7.31 ppm). Calibration curves, Figure 2.23

## Chapter 2

and Figure 2.24, of known benzyl alcohol and benzaldehyde concentrations against GC peak area were used to quantify the yield of the reactions, defined in Equation 2.5, and determine benzyl alcohol conversions and benzaldehyde selectivities using Equation 2.6 and Equation 2.7. Calibration curves for all reactants and starting materials throughout this work can be found in the accompanying materials CD. All GC peak areas for all reactions throughout this work fell within the GC peak areas obtained for the relevant concentrations used to make the calibration curves for each study. Selectivity and yield calculations were adjusted accordingly when a reaction involved 2 molar equivalents of starting material forming 1 molar equivalent of product.

$$\text{Equation 2.5} \quad \% \text{ Yield} = \frac{C_p}{C_o} \times 100$$

$$\text{Equation 2.6} \quad \% \text{ Conversion} = \frac{(C_o - C_t)}{C_o} \times 100$$

$$\text{Equation 2.7} \quad \% \text{ Selectivity} = \frac{C_p}{(C_o - C_t)} \times 100$$

$C_o$  represents initial concentration of starting material (in  $\text{mmoldm}^{-3}$ );  $C_t$  represents concentration of starting material at time = t (in  $\text{mmoldm}^{-3}$ );  $C_p$  represents concentration of product at time = t (in  $\text{mmoldm}^{-3}$ ).

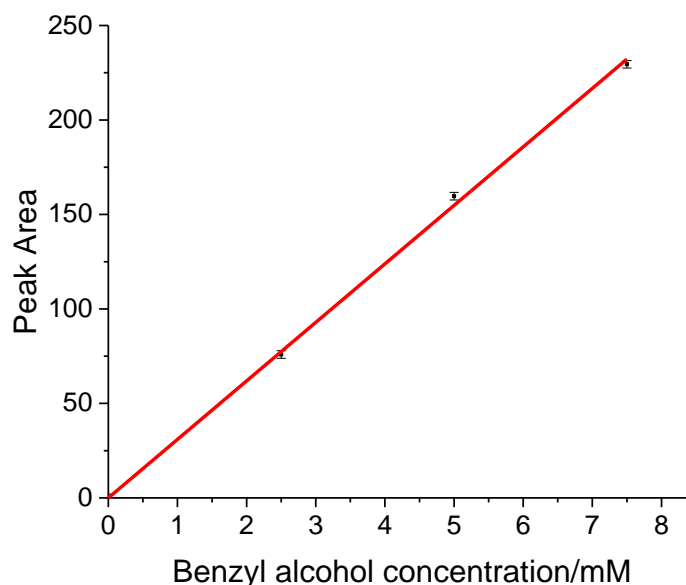


Figure 2.23 – Benzyl alcohol calibration curve of concentration against GC peak area at a retention time of 3.0 min. The standard error for this linear regression was used to calculate error from the average differences between the data points and the linear regression. The error in peak area on each data point was calculated as +/- 0.4.

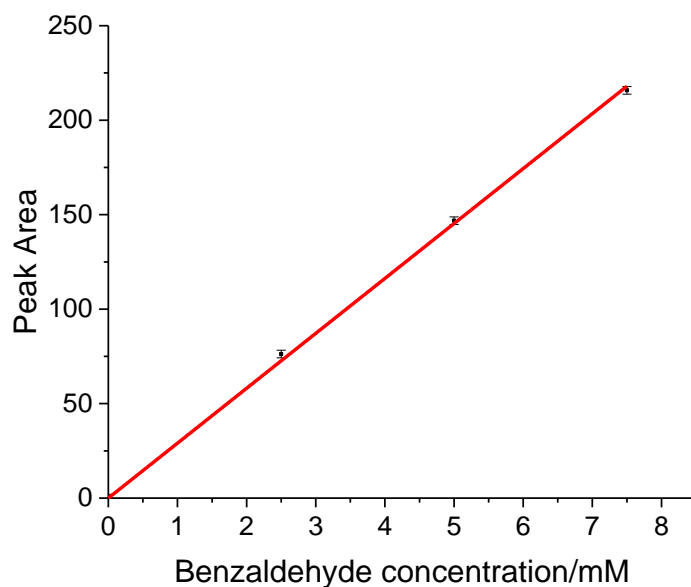
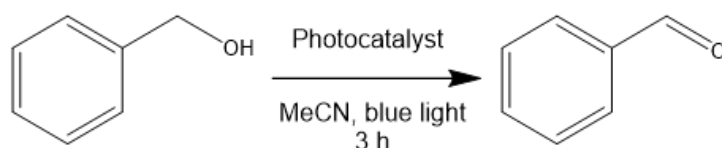


Figure 2.24 - Benzaldehyde calibration curve of concentration against GC peak area at a retention time of 2.7 min. The standard error for this linear regression was used to calculate error from the average differences between the data points and the linear regression. The error in peak area on each data point was calculated as +/- 0.3.

Table 2.1 – The results of the use of various blue light irradiated bismuth containing semiconductors in the aerobic oxidation of benzyl alcohol into benzaldehyde.



Photocatalyst (Band gap/eV, BET surface area/m <sup>2</sup> g <sup>-1</sup> , min. crystallite size/nm)	% benzyl alcohol conversion <sup>a,b</sup>	% benzaldehyde selectivity <sup>a,b</sup>	% benzaldehyde yield <sup>a,b</sup>
Bi <sub>2</sub> WO <sub>6</sub> (2.8, 8.8, 11.5)	27	94	25
BiFeO <sub>3</sub> (1.7, 16.9, 16.0)	13	0 <sup>c</sup>	0 <sup>c</sup>
β-Bi <sub>2</sub> O <sub>3</sub> (2.7, 6.2, 34.1)	9	91	8
nan-BiVO <sub>4</sub> (2.3, 7.9, 15.7)	88	95	84

<sup>a</sup>conditions: 0.1 mmol photocatalyst, 0.1 mmol benzyl alcohol, 10 mL acetonitrile, air atm, <sup>b</sup>The conversion, selectivity and yields were determined using GC. <sup>c</sup>Signal below detection limit.

Controls with the nan-BiVO<sub>4</sub> catalyst and no irradiation but heated to 40 °C resulted in 0% benzyl alcohol conversion. In addition, a control with no photocatalyst and irradiation

## Chapter 2

from the 30 W blue LED also resulted in 0% benzyl alcohol conversion. A control using irradiated nan-BiVO<sub>4</sub> with an argon atmosphere instead of dioxygen also resulted in no benzyl alcohol conversion. This suggested that the oxidation of benzyl alcohol was aerobic and proceeded by heterogeneous photocatalysis.

The use of the synthesised bismuth containing semiconducting photocatalysts for the oxidation of benzyl alcohol under blue light irradiation are given in Table 2.1. Interestingly, the material with the highest surface area, BiFeO<sub>3</sub>, had one of the lowest rates of benzyl alcohol conversion. In addition, oxidation of benzyl alcohol did not result in benzaldehyde formation, 13% benzyl alcohol conversion was observed but there was no selectivity for the formation of benzaldehyde. It is possible that a lack of crystallinity resulted in poor charge carrier transport. It is not possible to quantitatively state how much of a material is amorphous but a qualitative assessment can be made by comparing the minimum crystallite size obtained from PXRD to the particle sizes observed in the SEM. As the minimum crystallite size for BiFeO<sub>3</sub> (16.0 nm) is much smaller than that of the large particles observed in the SEM, it can be suggested that much of the material is amorphous and so does not have the charge carrier properties needed for effective heterogeneous photocatalysis. The minimum crystallite sizes for each of the other materials synthesised here are of the same order as the particle sizes observed in their respective SEMs and so it can be said that these materials are likely to be highly crystalline and therefore have the appropriate charge carrier properties needed to carry out effective heterogeneous photocatalysis. Bi<sub>2</sub>WO<sub>6</sub> provides an exception to this as its estimated minimum crystallite size is much lower than the size of the sheets observed in the corresponding SEMs for Bi<sub>2</sub>WO<sub>6</sub>. The reason for this can be associated to the shape of the Bi<sub>2</sub>WO<sub>6</sub> sheets as the arguably 2-dimension particles are not consistent with obtaining accurate estimations of minimum crystallite size from PXRD as the best estimations arise from spherical particles.

It can also be hypothesised that the lack of benzaldehyde formation with the use of BiFeO<sub>3</sub> was likely to be as a result of photo-Fenton chemistry leading to unselective degradation of organic compounds into volatile compounds such as carbon dioxide and water.<sup>205-207</sup> No work was carried out to try and detect the presence of carbon dioxide or water to confirm this as these were not the intended products of this work. The dioxygen and residual water are used as sources of •OH radical via redox reactions with surface iron cations which are the primary source of degradation in Fenton-chemistry. It can be suggested that the conversion between BiFeO<sub>3</sub> and the other materials used here should

## Chapter 2

not be compared as benzyl alcohol conversion is not due to oxidation from photolytically formed holes but was being degraded by photo-Fenton chemical processes.

It was observed that nan-BiVO<sub>4</sub> gave the greatest percentage conversion of benzyl alcohol, 88%, and also resulted in the highest selectivity for benzaldehyde, 95%. Bi<sub>2</sub>WO<sub>6</sub> and β-Bi<sub>2</sub>O<sub>3</sub> both yielded high benzaldehyde selectivities with 94% and 91% respectively. However, the benzyl alcohol conversions observed for Bi<sub>2</sub>WO<sub>6</sub> and β-Bi<sub>2</sub>O<sub>3</sub> were ca. 3 times lower and 9 times lower than that observed with the use of nan-BiVO<sub>4</sub> nanoparticles (27% and 9% respectively).

Explaining these trends was not simple as there could be many different factors that contribute to the overall activity of a heterogeneous photocatalyst for a specific reaction. However, the difference in band-gap energies could be a significant contributing factor in the difference in benzyl alcohol conversion between nan-BiVO<sub>4</sub> and Bi<sub>2</sub>WO<sub>6</sub>. The band gap for the nan-BiVO<sub>4</sub> was estimated at 2.30 eV (540 nm) whereas the band gap for Bi<sub>2</sub>WO<sub>6</sub> was estimated at 2.80 eV (435 nm). As the blue LED spectral range is between 400 and 560 nm, nan-BiVO<sub>4</sub> was able to absorb most of the light emitted by the LED (400 to 540 nm), whereas Bi<sub>2</sub>WO<sub>6</sub> was only able to absorb a much smaller portion (400 to 435 nm). This might also be a contributing factor to the lower conversion observed for β-Bi<sub>2</sub>O<sub>3</sub>, as the band gap for β-Bi<sub>2</sub>O<sub>3</sub> was estimated at 2.70 eV (460 nm), and therefore β-Bi<sub>2</sub>O<sub>3</sub> could only absorb photons between 400 and 460 nm.

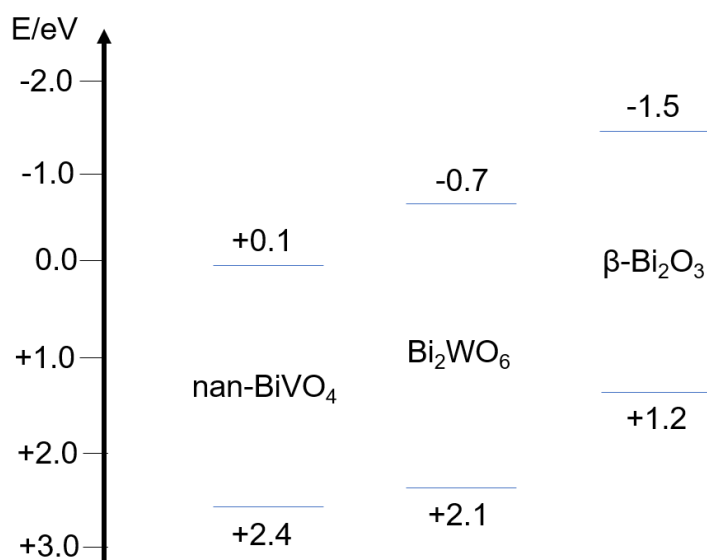


Figure 2.25 – Band positions for nan-BiVO<sub>4</sub>, Bi<sub>2</sub>WO<sub>6</sub> and β-Bi<sub>2</sub>O<sub>3</sub> vs NHE.

However, a much more pertinent factor when comparing the activity for photocatalytic oxidation of β-Bi<sub>2</sub>O<sub>3</sub>, Bi<sub>2</sub>WO<sub>6</sub> and nan-BiVO<sub>4</sub> was the oxidation potential for the valence

band edge of each of these materials, Figure 2.25. The valence band edge for  $\beta$ -Bi<sub>2</sub>O<sub>3</sub> (+1.2 V vs NHE)<sup>208</sup> have been found to be a lot less positive than that for Bi<sub>2</sub>WO<sub>6</sub> (+2.1 V vs NHE)<sup>209</sup> and nan-BiVO<sub>4</sub> (+2.4 V vs NHE)<sup>210</sup>. The oxidation potential of benzyl alcohol is ca. +0.85 V vs NHE,<sup>211</sup> so all 3 photocatalysts are capable of oxidising benzyl alcohol. However, there was less of a thermodynamic driving force for the holes found in the valence band of  $\beta$ -Bi<sub>2</sub>O<sub>3</sub> to oxidise benzyl alcohol than there was for the holes found in the VB of Bi<sub>2</sub>WO<sub>6</sub> or nan-BiVO<sub>4</sub>.

The control experiment without dioxygen showed that the presence of dioxygen was necessary for this reaction to take place. This was due to the need for extraction of photo-excited electrons that would otherwise recombine with holes at the photocatalyst surface. If the reduction of dioxygen was linked to the thermodynamic driving force for this system, it would be expected that  $\beta$ -Bi<sub>2</sub>O<sub>3</sub> would have the highest activity as  $\beta$ -Bi<sub>2</sub>O<sub>3</sub> has the most negative conduction band edge potential (-1.5 V vs NHE)<sup>208</sup>. However, as the material with the most positive valence band edge potential, nan-BiVO<sub>4</sub>, was the most active it can be suggested that the oxidation of benzyl alcohol was associated with the thermodynamic driving force of this system. Differences in surface area could also have an impact on conversion rates from the use of different photocatalysts, as a higher surface area material is able to adsorb more substrate which leads to a higher rate of conversion. However, as the BET surface areas of  $\beta$ -Bi<sub>2</sub>O<sub>3</sub>, Bi<sub>2</sub>WO<sub>6</sub> and nan-BiVO<sub>4</sub> are similar, it could be said that surface area was not a significant factor contributing to differences in benzyl alcohol conversion.

It could be suggested that nan-BiVO<sub>4</sub> proved to be the best semiconductor for photocatalytic benzyl alcohol oxidation due to a combination of the material's high oxidation potential and the material's ability to absorb a relatively high amount of visible light photons. However, various methods can be used to increase the photocatalytic activity of semiconductors by attempting to increase surface area or by minimising electron-hole recombination. Section 2.3 discusses the work done to attempt to increase the activity of nan-BiVO<sub>4</sub> as a photocatalyst for benzyl alcohol oxidation.

### 2.3 Modifying bismuth vanadate

As it has been observed that the use of nan-BiVO<sub>4</sub> results in the highest benzyl alcohol conversions of the materials used in section 2.2. It was decided that the modification of nan-BiVO<sub>4</sub> would be explored in an attempt to increase benzyl alcohol conversion.

### 2.3.1 Heterojunction synthesis by milling

When two semiconducting materials with different Fermi levels are joined together, a heterojunction forms.<sup>209, 212-218</sup> As the Fermi levels between these two materials are different, charge carriers pass over this interface in order to create one Fermi level across this junction. As a result, band-bending occurs between the valence and conduction bands of these materials. When irradiated the newly formed photoelectrons move to the material with the least negative conduction band edge and holes move to the material with the least positive valence band edge. This creates effective charge separation and therefore has been shown to give a greater photocatalytic activity over a single component semiconductor.

An attempt at synthesising a  $\text{BiVO}_4/\text{Bi}_2\text{WO}_6$  heterojunction was made by mixing a 1:1 molar ratio of nan- $\text{BiVO}_4$  and  $\text{Bi}_2\text{WO}_6$  together in a small amount of ethanol to form a paste and milling this paste with alumina spheres. The paste was milled for 4 h and the resulting material had a pale-yellow colour. Scanning electron microscopy of  $\text{BiVO}_4/\text{Bi}_2\text{WO}_6$  showed evidence of the microflower morphology of bismuth tungstate covered in nanoparticles that are roughly 20 to 100 nm in size, which are indicative of nan- $\text{BiVO}_4$ . Energy dispersive X-ray images indicate that vanadium and tungsten are found throughout the sample, Figure 2.26.

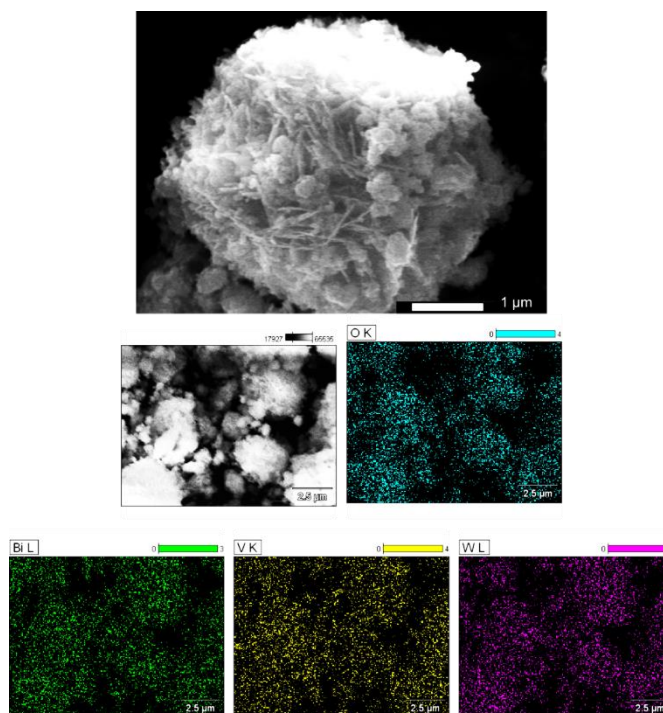


Figure 2.26 – An SEM image and EDX mapping of  $\text{BiVO}_4/\text{Bi}_2\text{WO}_6$ . The EDX mapping shows that V and W can be found throughout the sample.

## Chapter 2

Powder X-ray diffraction data of  $\text{BiVO}_4/\text{Bi}_2\text{WO}_6$  were consistent with a mixture of crystalline monoclinic  $\text{BiVO}_4$  (JCPDS no. 14-0688) and crystalline orthorhombic  $\text{Bi}_2\text{WO}_6$  (JCPDS No. 39-0256), Figure 2.27. Using Equation 2.1, the minimum crystalline particle size of  $\text{BiVO}_4$  species was estimated to be 16.6 nm and the minimum crystalline particle size of  $\text{Bi}_2\text{WO}_6$  species was estimated to be 11.5 nm; the FWHM of the peaks consistent with the diffractions from the  $\text{Bi}_2\text{WO}_6$  (131) plane and the  $\text{BiVO}_4$  (121) plane were used for this estimation. The particle sizes for  $\text{BiVO}_4/\text{Bi}_2\text{WO}_6$  are the same as those observed in nan- $\text{BiVO}_4$  and  $\text{Bi}_2\text{WO}_6$  respectively, suggesting that milling has no effect on particle size.

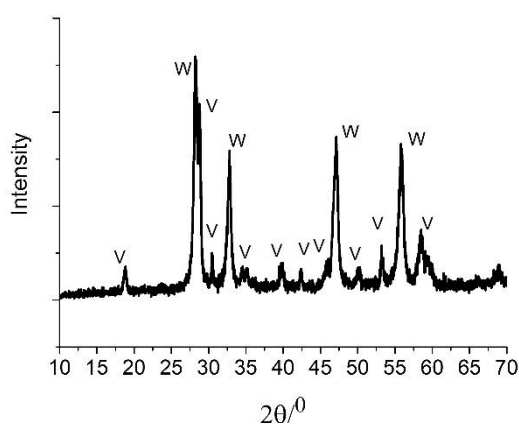


Figure 2.27 – PXRD for  $\text{BiVO}_4/\text{Bi}_2\text{WO}_6$ . The peaks labelled V are consistent with crystalline monoclinic  $\text{BiVO}_4$  (JCPDS no. 14-0688). The peaks labelled W are consistent with crystalline orthorhombic  $\text{Bi}_2\text{WO}_6$  (JCPDS No. 39-0256)

DRUVS was used to estimate the band gap of the  $\text{BiVO}_4/\text{Bi}_2\text{WO}_6$  material. The Kubelka-Munk function was applied to the reflectance data giving an estimated band-gap of 2.40 eV (520 nm) for  $\text{BiVO}_4/\text{Bi}_2\text{WO}_6$  which was the same as the reported band gap of monoclinic  $\text{BiVO}_4$  (2.4 eV, 520 nm) but slightly higher than that observed for nan- $\text{BiVO}_4$ , Figure 2.28.



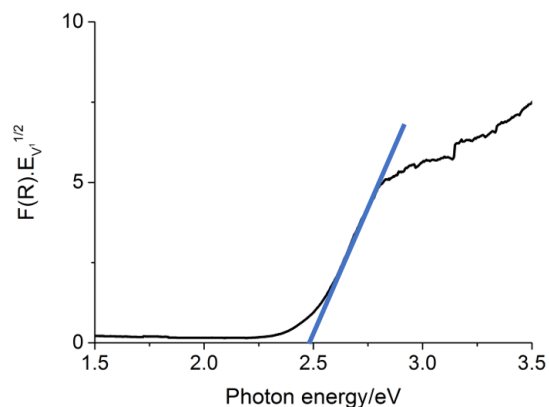


Figure 2.28 – The Tauc plot used to estimate the band gap of  $\text{BiVO}_4/\text{Bi}_2\text{WO}_6$  made up of indirect semiconductors

### 2.3.2 Doping

Extrinsic semiconductors have been doped by the addition of a small amount of another element and have inherently different properties to intrinsic or unmodified semiconductors.<sup>186, 219-221</sup> Doped semiconductors can be better photocatalysts than undoped analogues as doping creates a higher number of inter-band defect sites which require the absorption of lower energy photons in order to create photo-excited electrons and so a greater proportion of the visible light spectrum can be used in photocatalysis.

In separate reports from Song et al. and Shan et al., Mo and W doping has been found to have a beneficial impact on the photocatalytic activity of bulk  $\text{BiVO}_4$  in degrading dyes such as methylene blue and Rhodamine B.<sup>186, 220</sup> 1% Mo/W has also been found to be the optimal amount of dopant in order to generate optimal photocatalytic turnover.<sup>186, 220</sup> With this in mind, the hydrothermal synthesis of 1% Mo doped and 1% W doped  $\text{BiVO}_4$  was carried out using appropriate amounts of ammonium molybdate and sodium tungstate dihydrate. The hydrothermal temperature for this reaction was increased to 120 °C as no product was formed from a reaction at 90 °C. The products of these reactions have the same yellow colour as the bismuth vanadate nanoparticles.

Scanning electron microscopy of both Mo-doped and W-doped  $\text{BiVO}_4$  showed a very different morphology to that observed for unmodified nan- $\text{BiVO}_4$ . Instead of agglomerations of nanoparticles between 20 and 100 nm in size, large mostly spherical particles were observed ca. 10  $\mu\text{m}$  in size. The spheres appeared to be dendritic in nature, with a solid core that had rods that had grown out from the centre in all directions, Figure 2.29.

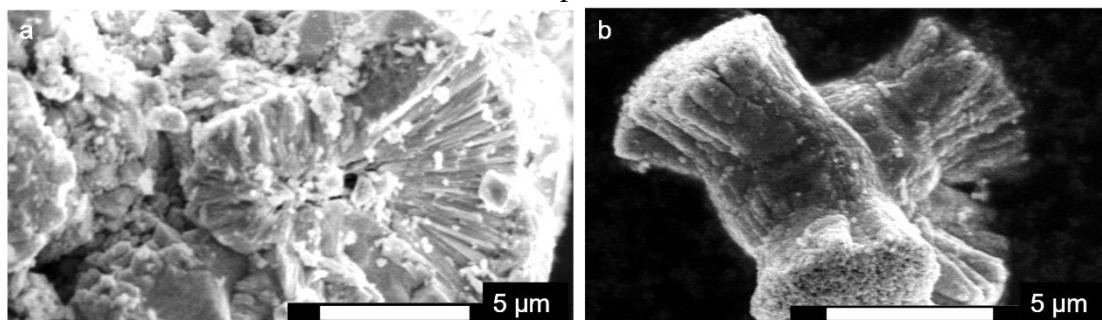


Figure 2.29 – SEM of a) Mo-doped  $\text{BiVO}_4$  and b) W-doped  $\text{BiVO}_4$

The increase in temperature is not responsible for the change in morphology observed as nanoparticles are synthesised utilising hydrothermal synthetic methods between 90 and 120 °C. It can be hypothesised that the dopants act as nucleation sites for fast uncontrolled growth which means that bismuth chelation with EDTA becomes an ineffective method of controlling particle size.

Powder X-ray diffraction data of Mo-doped and W-doped  $\text{BiVO}_4$  were consistent with crystalline monoclinic  $\text{BiVO}_4$  (JCPDS no. 14-0688), however the peak intensities of the Mo-doped  $\text{BiVO}_4$  material were very different to those observed in the PXRD of nan- $\text{BiVO}_4$  which suggested that the synthesis of Mo-doped  $\text{BiVO}_4$  involved the specific growth of particles with a preferred orientation that was very different to that of nan- $\text{BiVO}_4$ . The PXRD for W-doped  $\text{BiVO}_4$  also contained peaks consistent with crystalline tetragonal  $\text{BiVO}_4$  (JCPDS no. 14-0133), suggesting that W-doped  $\text{BiVO}_4$  was not entirely phase pure, Figure 2.30. Using Equation 2.1, the minimum crystalline particle size of the Mo-doped  $\text{BiVO}_4$  was estimated to be 26.0 nm and the minimum crystalline particle size of W-doped  $\text{BiVO}_4$  was estimated to be 33.8 nm; the FWHM of the peaks consistent with the diffractions from the (121) plane was used for this estimation.

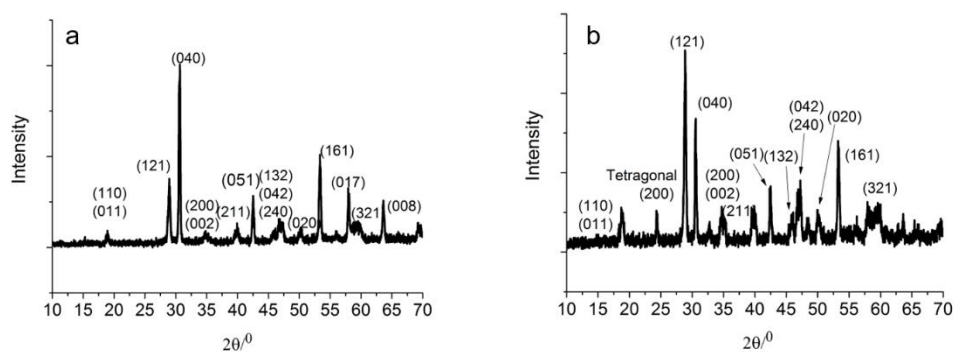


Figure 2.30 – PXRD of a) Mo-doped  $\text{BiVO}_4$  consistent with crystalline monoclinic  $\text{BiVO}_4$  (JCPDS no. 14-0688) and b) W-doped  $\text{BiVO}_4$  consistent with crystalline monoclinic  $\text{BiVO}_4$

(JCPDS no. 14-0688) but also showing evidence of crystalline tetragonal schellite  $\text{BiVO}_4$  (JCPDS no. 14-0133).

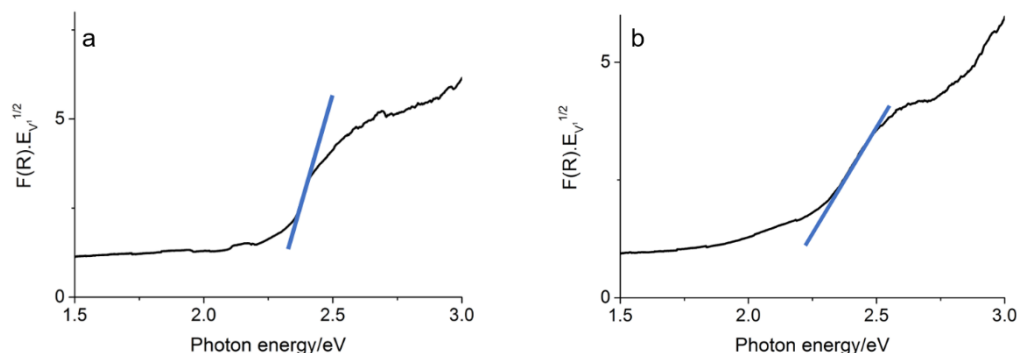


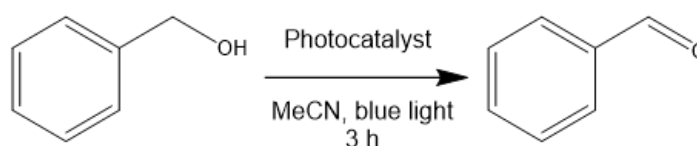
Figure 2.31 – The Tauc plots for used to estimate the band-gaps of a) Mo-doped  $\text{BiVO}_4$  and b) W-doped  $\text{BiVO}_4$

DRUVS was used to estimate the band gaps of the Mo-doped and W-doped  $\text{BiVO}_4$  materials. The Kubelka-Munk function was applied to the reflectance data giving estimated band-gaps of 2.30 eV (540 nm) and 2.25 eV (550 nm) for Mo-doped and W-doped  $\text{BiVO}_4$  respectively which were similar to the band gap calculated for nan- $\text{BiVO}_4$  (2.25 eV, 540 nm), Figure 2.31.

### 2.3.3 Modified bismuth vanadate catalyst comparison

These modified photocatalysts were used in analogous benzyl alcohol oxidation experiments to those described in section 2.2.5, Table 2.2.

Table 2.2 – The results of the use of blue light irradiated photocatalysts for the aerobic oxidation of benzyl alcohol selectively to benzaldehyde



Photocatalyst (Band gap/eV, min. crystallite size/nm)	% benzyl alcohol conversion <sup>a,b</sup>	% benzaldehyde selectivity <sup>a,b</sup>	% benzaldehyde yield <sup>a,b</sup>
$\text{BiVO}_4/\text{Bi}_2\text{WO}_6$ (2.4, 11.5)	42	86	36
W-doped $\text{BiVO}_4$ (2.3, 33.8)	32	79	25
Mo-doped $\text{BiVO}_4$ (2.3, 26.0)	52	86	45

<sup>a</sup>conditions: 0.1 mmol photocatalyst, 0.1 mmol benzyl alcohol, 10 mL acetonitrile, air atm, <sup>b</sup>The conversion, selectivity and yields were determined using GC.

It was observed that nan-BiVO<sub>4</sub> outperformed all modified bismuth vanadate materials, both in terms of benzyl alcohol conversion and benzaldehyde selectivity. The particle size of the doped semiconductors is reminiscent of bulk BiVO<sub>4</sub> which exhibit poor photocatalytic activity due to extensive electron-hole recombination in the bulk.<sup>136</sup> Therefore, to observe any photoactivity for the oxidation of benzyl alcohol was surprising and suggested that the doping has been successful in creating surface defect sites for charge carrier trapping that extends charge carrier lifetime in order to enable their use in redox chemistry. However, the morphological differences between the doped BiVO<sub>4</sub> materials and nan-BiVO<sub>4</sub> allowed for more substrate adsorption to nan-BiVO<sub>4</sub> and therefore a higher benzyl alcohol conversion rate.

Defect formation may also be the reason that the BiVO<sub>4</sub>/Bi<sub>2</sub>WO<sub>6</sub> material does not show the intended synergistic effect associated with heterojunctions. The point where 2 materials meet can also act as a defect site for recombination of charge carriers in irradiated semiconductors.<sup>222</sup> Methods often utilise calcination after mixing to thermally remove these interface defects,<sup>223</sup> however temperatures of greater than 200 °C have been required in other systems attempting to synthesise heterojunctions. As previously discussed, bismuth containing semiconductors with relatively high surface areas have been known to sinter at such temperatures and so it was decided that no calcination step should be included.

The lack of any increase in photoactivity on adaptation of the bismuth vanadate nanoparticles was disappointing. However, nan-BiVO<sub>4</sub> have shown increased photoactivity for benzyl alcohol oxidation over bismuth tungstate. Bismuth tungstate had previously been reported as a successful, cutting-edge, selective visible light photocatalyst for the oxidation of benzyl alcohol that is also simple to prepare.<sup>24</sup> Any attempt to use bulk bismuth vanadate for benzyl alcohol oxidation has required immobilised ruthenium photocatalysts or sacrificial cobalt reagent in a micellar system.<sup>27</sup><sup>224</sup> As a result, chapter 3 will explore the novel use of nan-BiVO<sub>4</sub>, described above, as a photocatalyst for the selective oxidation of benzyl alcohol to benzaldehyde.

## 2.4 Conclusions

The work outlined in this chapter met the objectives outlined by showing that of the bismuth containing semiconductors used as photocatalysts for the aerobic oxidation of benzyl alcohol, nan-BiVO<sub>4</sub> was capable of the highest benzyl alcohol conversion as well as the highest benzaldehyde selectivity. These are characteristics consistent with nan-BiVO<sub>4</sub> being the most effective photocatalyst. The work was also able to draw

## Chapter 2

conclusions about which physical properties of the bismuth containing semiconductors are important in a material being an effective photocatalyst by showing the importance of crystallinity, valence band energy, band gap and avoiding the formation of sites for where recombination is likely to occur internally. The importance of crystallinity was shown in the lack of benzyl alcohol conversion and benzaldehyde selectivity with the use of BiFeO<sub>3</sub>. The importance of balancing having a highly positive valence band energy and a small band gap was observed when comparing the amount of benzyl alcohol converted in the reactions using nan-BiVO<sub>4</sub>, Bi<sub>2</sub>WO<sub>6</sub> and β-Bi<sub>2</sub>O<sub>3</sub>. The importance of avoiding the formation of internal recombination sites was observed in the work using the milled BiVO<sub>4</sub>/Bi<sub>2</sub>WO<sub>6</sub> powder as a photocatalyst for benzyl alcohol oxidation.

This work is relevant to the overall aim of this thesis as it demonstrated that several bismuth containing semiconductors are capable of behaving as heterogeneous photocatalysts for selective benzyl alcohol oxidation in benzaldehyde under the conditions used. In addition, the use of bismuth oxide and bismuth vanadate for this purpose had not been previously reported and so expands the knowledge of this research area. This work also guided the rest of the work outlined in this thesis as it showed which material, of the one's used here, is most likely to behave as a heterogeneous photocatalyst in other reaction systems under the conditions used. This work also enabled the work outlined in Chapter 3 by providing a viable reaction system to study so that the selectivity of heterogeneous photocatalytic systems using bismuth containing semiconductors can be better understood.

## 3 Selective Benzyl Alcohol Oxidation and Product Inhibition using Bismuth Vanadate Nanoparticles

### 3.1 Introduction

#### 3.1.1 Heterogeneous photocatalytic benzyl alcohol oxidation

Aldehydes are used as food additives, fragrances and intermediates in several different synthetic routes and are often synthesised from the selective oxidation of corresponding alcohols.<sup>225-230</sup> Often these oxidations are achieved with the wasteful use of stoichiometric quantities of chromate or permanganate species.<sup>231-234</sup> Precious metal catalysts have also been used at elevated temperatures to achieve this oxidation.<sup>235, 236</sup>

Selective alcohol oxidation via heterogeneous photocatalysis utilises earth abundant materials, at room temperature, that can also be recycled with ease.<sup>4, 15, 16, 18, 24, 131-133, 147, 184, 224, 237-239</sup> A significant proportion of the work associated to selective alcohol oxidation with the use of a heterogeneous photocatalyst has involved the use of titanium dioxide.<sup>15, 16, 147, 184, 237, 238</sup> However, as the band gaps of rutile and anatase titania are 3.0 eV and 3.2 eV, UV light was required to achieve reasonable alcohol conversion rates, however the use of UV light has been shown to lead to over-oxidation of alcohols into corresponding carboxylic acids.<sup>237</sup>

In previously reported literature, it has been shown that a wide range of different materials have been used in order to increase the amount of visible light used in the heterogeneous photocatalytic oxidation of alcohols. As previously stated and shown in chapter 2, bismuth tungstate (band gap = 2.8 eV) was able to selectively oxidise benzyl alcohol into benzaldehyde.<sup>24</sup> However, it has been observed that nan-BiVO<sub>4</sub> produced a higher benzaldehyde yield under the same reaction conditions. In other previous reports, materials such as graphitic carbon nitride (band gap = 2.7 eV) have also shown the capacity for selective alcohol oxidation but at similarly slow rates to that observed with the use of bismuth tungstate.<sup>18</sup> Higher rates have been reported through the use of composite materials that were able to effectively separate charge carriers and thus avoid recombination. Examples of such materials found in literature include amorphous titania coated CdS,<sup>184</sup> bismuth tungstate-graphene oxide<sup>239</sup> and tungsten oxide coupled with a palladium oxide cocatalyst.<sup>133</sup> Other composites consist of precious metal complexes, such as ruthenium centred photocatalysts, bound to the surface of a solid support; the solid supports were not seen as photoactive by themselves.<sup>131, 224</sup> One particular example of interest is the adsorption of a ruthenium complex onto the surface of bismuth vanadate.

## Chapter 3

Bulk bismuth vanadate, with particles sizes larger than 1  $\mu\text{m}$ , were used in this literature example. The large particle size meant that the unmodified bismuth vanadate could not carry out photocatalysis due to high likelihood of bulk recombination events.<sup>224</sup> The synthesis of such composites often required complicated synthetic procedures, involving several more steps compared to the synthesis of a singular component semiconductor. The studies associated to the use of these photocatalysts did not often fully explore the mechanism of benzyl alcohol oxidation and provided insufficient discussion as to why these reactions are selective for benzaldehyde formation. In addition, in examples where an increase in activity was observed, reduced charge carrier recombination was often cited as the reason for this,<sup>73, 216, 218, 239-241</sup> however few studies attempted to observe this change in charge carrier recombination.

As nan-BiVO<sub>4</sub> produced the highest benzyl alcohol conversions and highest benzaldehyde selectivities amongst the photocatalysts used in the oxidation of benzyl alcohol in Chapter 2, it was decided that an extensive study of the use of nan-BiVO<sub>4</sub> for the oxidation of benzyl alcohols would be carried out with the aim of providing an understanding of the reaction mechanism, the cause of selectivity and the significance of charge carrier recombination.

### 3.1.2 Objectives

The objectives of this work were:

- To attempt to understand what causes benzaldehyde selectivity when nan-BiVO<sub>4</sub> is used to oxidise benzyl alcohol under visible light irradiation; and
- To attempt to understand the role and importance of various components of the reaction systems

## 3.2 Selective benzyl alcohol oxidation

### 3.2.1 Kinetics and comparison to bulk BiVO<sub>4</sub> and Degussa P25 TiO<sub>2</sub>

Reports of the heterogeneous photocatalytic oxidation of 4-methoxybenzyl alcohol selectively into 4-methoxybenzaldehyde include the use of titanium dioxide irradiated by a visible light LED lamp<sup>15</sup> and bismuth tungstate<sup>24</sup>, bismuth tungstate-reduced graphene oxide composites,<sup>239</sup> and bulk bismuth vanadate with an immobilised ruthenium photocatalyst,<sup>224</sup> irradiated under visible light using a 300 W Xe arc lamp. The bismuth tungstate-reduced graphene oxide composite provided the state of the art,<sup>239</sup> giving full conversion of 0.1 mmol 4-methoxybenzyl alcohol in 6.5 h using 20 mg (ca. 0.04 mmol) of catalyst, but involved the synthesis of a complex multicomponent photocatalyst that

required several fabrication steps. Of the singular component photocatalysts, titanium dioxide required 12.5 molar excess of catalyst irradiated for 4 h,<sup>15</sup> and bismuth tungstate required long irradiation times (22 h) from a Xe arc light source to give 4-methoxybenzyl alcohol conversion of ca. 95 %<sup>24</sup> and has already shown to give 3 times lower benzyl alcohol conversion than nan-BiVO<sub>4</sub> under the same conditions for the oxidation of benzyl alcohol.

Here, nan-BiVO<sub>4</sub> (0.1 mmol) was used in the oxidation of 4-methoxybenzyl alcohol (0.1 mmol) in acetonitrile (10 mL) with 1 atm of dioxygen and achieved completion in 3 h. This reaction was repeated several times with varying lengths of irradiation in order to observe the kinetics of the reaction, Figure 3.1. A zero-order rate constant of 5.4 mmol dm<sup>-3</sup> h<sup>-1</sup> can be associated to the data in Figure 3.1. This result is surprising as this is not in agreement with the kinetics associated to Langmuir-Hinshelwood or Eley-Rideal mechanisms. More kinetic work would be needed to be able to conclude the order of this reaction. Another 3 h reaction was used to fully convert 4-methoxybenzyl alcohol into 4-methoxybenzaldehyde; this reaction was used for product isolation and characterisation by <sup>1</sup>H, <sup>13</sup>C NMR and ESI-MS.

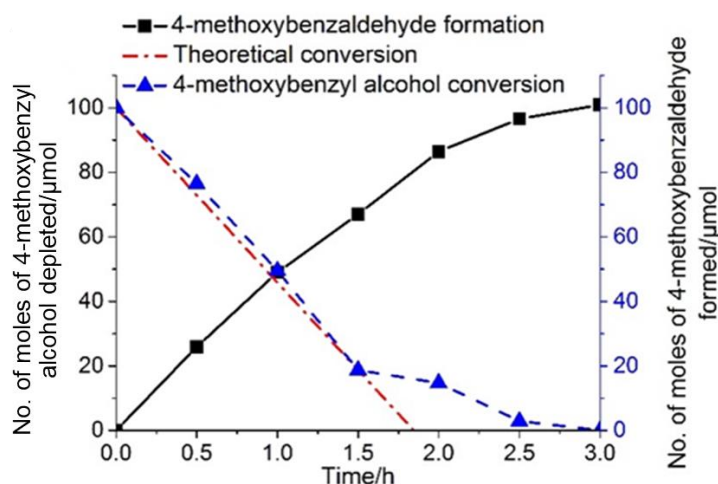


Figure 3.1 – The conversion of 4-methoxybenzyl alcohol into 4-methoxybenzaldehyde as a function of time. Number of moles of starting material and product were obtained using <sup>1</sup>H NMR peak intensities against a known amount of maleic acid as an internal calibrant. The line for theoretical conversion was derived from the zero-order rate constant,  $k_0 = 5.4 \text{ mmol dm}^{-3} \text{ h}^{-1}$ .

Catalyst comparison was carried out under analogous conditions to those used to generate the data in Figure 3.1. Unlike the bismuth containing semiconducting materials used in chapter 2, with features that were consistent with high activity under visible light irradiation,<sup>24, 134, 137, 177</sup> a synthesised bulk BiVO<sub>4</sub> material<sup>136</sup> and Degussa P25 Titania were also used to oxidise 4-methoxybenzyl alcohol under analogous conditions



### Chapter 3

to show the importance of a high surface area and an ability to absorb significant amounts of visible light under these conditions, Table 3.1.

To synthesise the bulk  $\text{BiVO}_4$ , a similar method to the synthesis of nan- $\text{BiVO}_4$  was used, however no EDTA was added and the hydrothermal temperature was raised to  $240\text{ }^\circ\text{C}$ .<sup>136</sup> This was done to ensure that large monoclinic crystallites would form. SEM of the bulk  $\text{BiVO}_4$  material show large, smooth  $\mu\text{m}$  sized crystallites, Figure 3.2. The BET surface area for bulk  $\text{BiVO}_4$  was below the level of detection ( $<0.1\text{ m}^2\text{ g}^{-1}$ ).

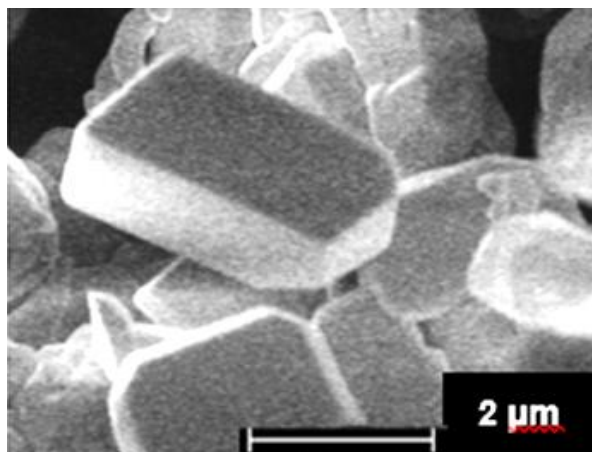


Figure 3.2 – SEM of bulk  $\text{BiVO}_4$

PXRD data of the bulk  $\text{BiVO}_4$  were consistent with crystalline monoclinic  $\text{BiVO}_4$  (JCPDS no. 14-0688), Figure 3.3, and DRUVS along with the Kubelka-Munk function showed that bulk  $\text{BiVO}_4$  has a similar band gap (2.25 eV) to that of nan- $\text{BiVO}_4$ , Figure 3.4. P25  $\text{TiO}_2$  is a mixture of 25% rutile (3.0 eV) and 75% anatase (3.2 eV) polymorphs. The surface area of this materials is  $50\text{ m}^2\text{ g}^{-1}$ <sup>242</sup> and particle sizes are in the range of 20 – 50 nm.<sup>243</sup>

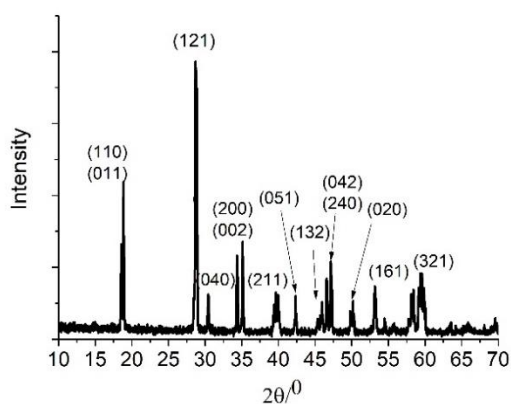


Figure 3.3 – PXRD for bulk  $\text{BiVO}_4$ . This data is consistent with crystalline monoclinic  $\text{BiVO}_4$  (JCPDS no. 14-0688)

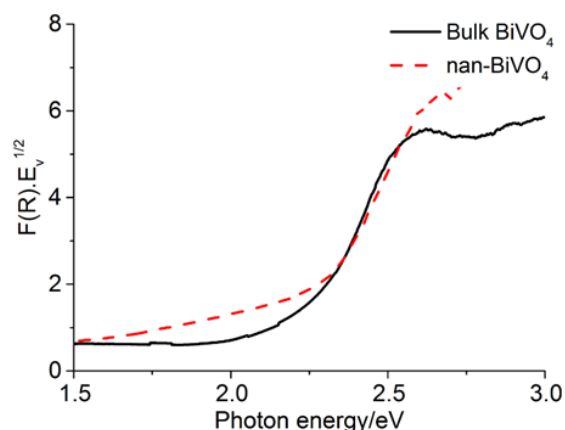
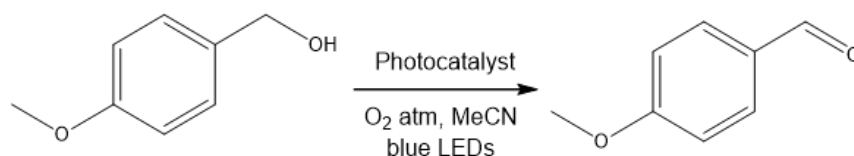


Figure 3.4 – Tauc plot showing the Kubelka-Munk function against photon energy for both bulk and nan-BiVO<sub>4</sub>

Table 3.1 – The comparison of nan-BiVO<sub>4</sub>, bulk BiVO<sub>4</sub> and P25 TiO<sub>2</sub> as photocatalysts for 4-methoxybenzyl alcohol oxidation



Photocatalyst <sup>a</sup> (Band gap/eV, BET surface area/m <sup>2</sup> g <sup>-1</sup> , SEM particle size/nm)	Conversion (%) <sup>b</sup>	Selectivity (%) <sup>b</sup>	Yield (%) <sup>b</sup>
nan-BiVO <sub>4</sub> (2.3, 7.9, 20-100)	97	> 99	96
bulk BiVO <sub>4</sub> (2.3, <0.1, >1000)	3	> 99	3
P25 TiO <sub>2</sub> (3.0, 50, 20-50)	10	> 99	10

<sup>a</sup>conditions: 0.1 mmol photocatalyst, 0.1 mmol 4-methoxybenzyl alcohol, 10 mL acetonitrile, 1 atm O<sub>2</sub>, blue LED irradiation for 2.5 h. <sup>b</sup>Determined by <sup>1</sup>H NMR.

It was apparent that nan-BiVO<sub>4</sub> was the best photocatalyst under these conditions, Table 3.1. The conversion of 4-methoxybenzyl alcohol with nan-BiVO<sub>4</sub> was 10 times higher than with the use of P25 TiO<sub>2</sub> and 30 times higher than with the use of bulk BiVO<sub>4</sub>. Regardless of the high surface area of P25 TiO<sub>2</sub>, the material's low capacity for visible light absorption limited oxidation. The ability to utilise some of the visible light wavelengths emitted from the blue LED arises from surface exciplex formation from the adsorption of 4-methoxybenzyl alcohol to the photocatalysts surface.<sup>19, 21, 151</sup> The higher alcohol conversion with the use of nan-BiVO<sub>4</sub> in comparison to bulk BiVO<sub>4</sub> can either be associated to higher numbers of charge carriers reaching the surface or the higher surface area of nan-BiVO<sub>4</sub> which allowed for a higher amount of adsorption to the

### Chapter 3

photocatalytic surface. Separate control experiments without the use of photocatalyst, blue LEDs and with an Ar atmosphere respectively all resulted in no alcohol conversion; this showed that the reaction is driven by aerobic heterogeneous photocatalysis. Although, equimolar amounts of photocatalysts and 4-methoxybenzyl alcohol were used in each reaction, it can be said that the oxidation of benzyl alcohol with nan-BiVO<sub>4</sub> was catalytic as nan-BiVO<sub>4</sub> is a solid material. A significant proportion of nan-BiVO<sub>4</sub> was bulk material that could not partake directly in the oxidation of 4-methoxybenzyl alcohol; a much smaller proportion of the material will be found at the surface meaning that catalytic turnover is essential in achieving total alcohol conversion.

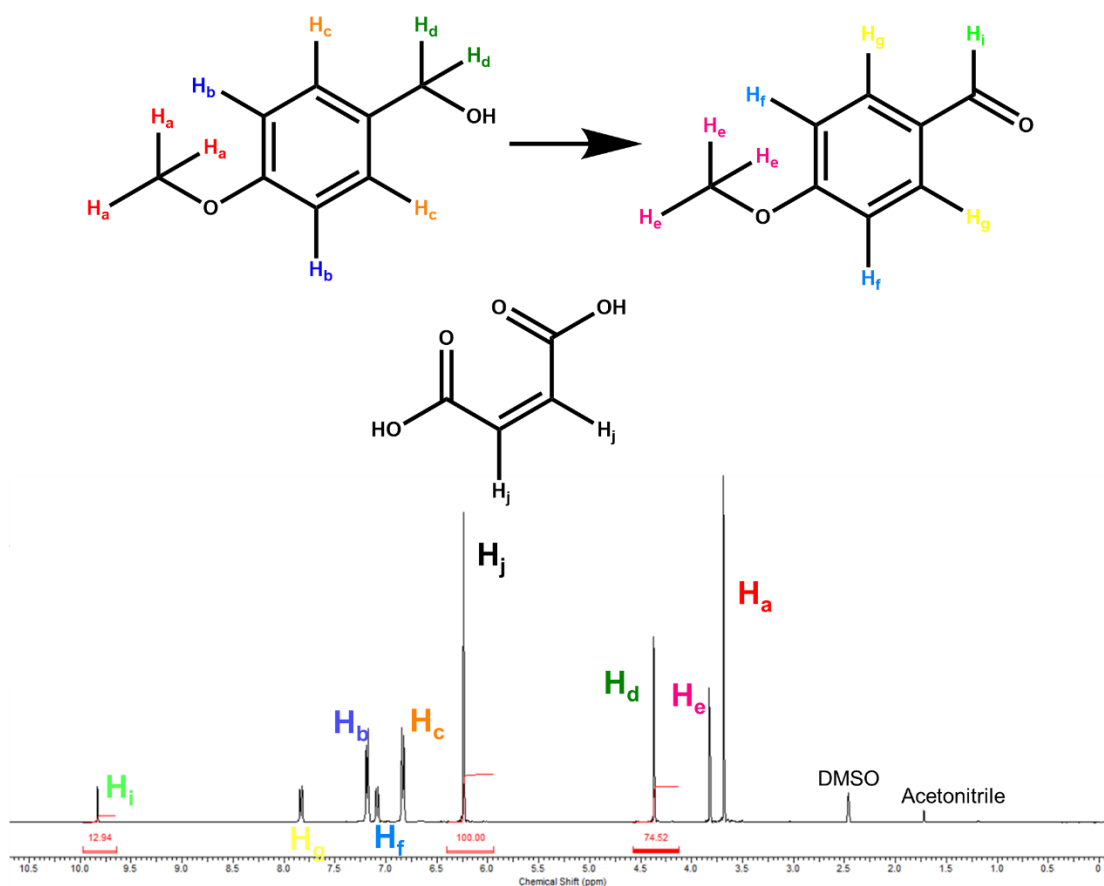


Figure 3.5 – An example <sup>1</sup>H NMR (*d*<sub>6</sub>-DMSO, 400 MHz) from the oxidation of 4-methoxybenzyl alcohol and method for calculating conversion and selectivity. Reaction conditions: 0.1 mmol nan-BiVO<sub>4</sub>, 0.1 mmol 4-methoxybenzyl alcohol, 10 mL acetonitrile, 1 atm O<sub>2</sub>, 30 min blue LED irradiation. 100 μmol maleic acid was added and used as an internal standard.

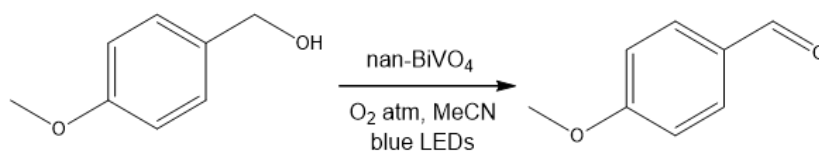
To quantify the amount of starting material and product present, a known amount of maleic acid was added to the *d*<sub>6</sub>-DMSO solvent as an internal standard, Figure 3.5. The yield of 4-methoxybenzaldehyde from the example given was 25.9 μmol as the ratio of the number of protons contributing to the aldehyde peak at 9.7 ppm to the number of protons contributing to the maleic acid alkene peak at 6.2 ppm is 1:2. Equation 2.5, Equation 2.6 and Equation 2.7 were used to determine yield, percentage 4-methoxybenzyl

## Chapter 3

alcohol conversion and percentage 4-methoxybenzaldehyde selectivity from these reactions respectively; from the example spectrum a 26% conversion and 102% (>99%) selectivity were calculated. It is possible to obtain values above 100% for selectivity due to errors in the addition of 4-methoxybenzyl alcohol at the start of the reaction and errors associated to the addition of deuterated solvent in preparation of the NMR sample.

More repeats of the oxidation of 4-methoxybenzyl alcohol by blue LED light irradiated nan-BiVO<sub>4</sub> under analogous conditions were carried out in order to determine the error on the percentage conversions obtained, Table 3.2. The data range for the percentage conversions of 4-methoxybenzyl alcohol after 2.5 h of irradiation, ranged from 90 to 100% about a mean of 95%. As a result, the error in conversion is estimated at +/- 5%. The 4-methoxybenzaldehyde selectivity achieved in these reactions was > 99% and no over oxidation to 4-methoxybenzoic acid was observed.

Table 3.2 – Repeats of 4-methoxybenzyl alcohol for error determination.



<u>Reaction number<sup>a</sup></u>	<u>Percentage 4-methoxybenzylalcohol conversion<sup>b</sup></u>
1	96
2	90
3	93
4	100
5	97
6	94

<sup>a</sup> conditions: 0.1 mmol nan-BiVO<sub>4</sub>, 0.1 mmol 4-methoxybenzyl alcohol, 10 mL acetonitrile, 1 atm O<sub>2</sub>, blue LEDs 2.5

h. <sup>b</sup>The percentage conversion of 4-methoxybenzyl alcohol were determined using <sup>1</sup>H NMR.

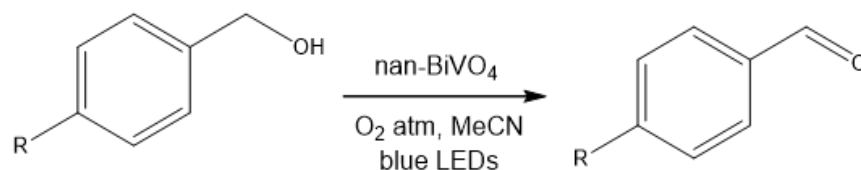
### 3.2.2 Steric and electronic effects

Nan-BiVO<sub>4</sub> was also used to oxidise a range of substituted benzyl alcohols selectively into their corresponding aldehydes, Table 3.3. It was observed that the presence of electron donating groups led to high conversions of benzyl alcohol; methoxy groups led to >99% conversion and methyl groups gave a 97% conversion. However, electron withdrawing groups result in much lower conversions; for CF<sub>3</sub> alcohol conversion was 48% and for NO<sub>2</sub> was 46%. From this, it could be suggested that the formation of an electron rich intermediate was part of the rate determining step for this reaction. The exception to this was found with a hydroxy substituent where only 30% conversion was

### Chapter 3

observed; this was coupled with a low selectivity of 52%. This outlier was most likely to be the result of competitive surface binding between the phenolic and benzylic hydroxyl groups. Good selectivities were seen across the reactions with most achieving >90% selectivity. Lower selectivities for the corresponding aldehyde were observed with the oxidation of 4-trifluoromethyl and 4-nitrobenzaldehyde; 83% and 84% respectively.

Table 3.3 – The photocatalytic oxidation of substituted benzyl alcohols using blue LED light irradiated nan-BiVO<sub>4</sub>.



R =	Conversion (%) <sup>a, b</sup>	Selectivity (%) <sup>a, b</sup>	Yield (%) <sup>a, b</sup>
Me	97	90	87
iPr	75	91	68
Ph	58	89	51
Cl	66	94	62
Br	91	91	83
I	50	96	48
CF <sub>3</sub>	48	83	39
NO <sub>2</sub>	46	84	38
C(O)OMe	60	95	57
NHC(O)Me	87	> 99	86
OMe	> 99	> 99	>99
OH	30	52	16
H	73	> 99	73

<sup>a</sup>conditions: 0.1 mmol photocatalyst, 0.1 mmol *para*-substituted benzyl alcohol, 10 mL acetonitrile, 1 atm O<sub>2</sub>, blue LED irradiation for 3 h. <sup>b</sup> Determined by <sup>1</sup>H NMR except for where R = H which was analysed by GC.

Steric effects had an impact on the oxidation of 4-methyl-, 4-isopropyl- and 4-phenylbenzyl alcohol which gave conversions of 97, 75 and 58%, respectively. This trend suggests that larger substituents limited alcohol adsorption to the catalyst surface and therefore limited the rate of oxidation; although the selectivity remains high in all cases. Halogen substitution appeared to show a balance of electronic and steric effects. The chloro substituent was the most electron withdrawing and contributed least to any electron rich intermediate which in turn resulted in a lower benzyl alcohol conversion. Whereas, the iodo substituent provided the largest steric clash and so limited the number of molecules found at the catalyst surface at any particular point in time. As a result, the presence of a bromo substituent resulted in the highest alcohol conversion (91%). The

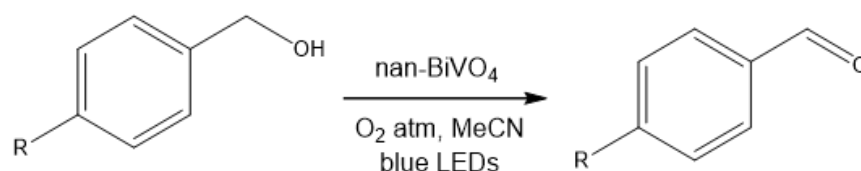
### Chapter 3

higher steric clash of the iodo substituent appeared to have a greater impact than the electron withdrawing effects of the chloro substituent as the conversion of chlorobenzyl alcohol was higher (66%) than the conversion of iodobenzyl alcohol (50%).

These trends are different to those observed with other single-component photocatalysts; in previously reported literature, titania and bismuth tungstate both showed no variation in alcohol conversion rate upon the use of a variety of different substituents.<sup>15, 24</sup> The use of a Bi<sub>2</sub>WO<sub>6</sub>-reduced graphene oxide composite<sup>239</sup> or a bulk BiVO<sub>4</sub> loaded with a ruthenium photocatalyst<sup>224</sup> have shown that electron donating substituent groups result in higher benzyl alcohol conversions. However, no mechanistic conclusions could be drawn from these systems as the role of each component in these composite catalysts was unclear.

In an attempt to observe significant increases in alcohol conversions, some reactions were repeated with longer irradiation times. Alcohols with isopropyl-, iodo- and phenyl-substituents all gave full conversion without loss in aldehyde selectivity, Table 3.4. The steric effect on each of these substituents would be significant and so each of these substituents would have a large impact on the number of molecules that can adsorb to the catalyst surface. However, the larger substituents may allow for effective benzaldehyde desorption away from the catalyst which in turn mediated catalytic turnover.

Table 3.4 - The extended photocatalytic oxidation of substituted benzyl alcohols using blue LED light irradiated nan-BiVO<sub>4</sub>



R =	Time/h	% Conversion <sup>a, b</sup>	% Selectivity <sup>a, b</sup>	% Yield <sup>a, b</sup>
iPr	8	> 99	94	93
COOMe	8	80	78	62
NO <sub>2</sub>	12	74	77	57
Cl	12	95	87	82
CF <sub>3</sub>	12	44	82	36
OH	22	36	65	23
I	24	> 99	90	89
Ph	24	> 99	97	96

<sup>a</sup>conditions: 0.1 mmol photocatalyst, 0.1 mmol para-substituted benzyl alcohol, 10 mL acetonitrile, 1 atm O<sub>2</sub>, blue LED irradiation for 3 h. <sup>b</sup> Determined by <sup>1</sup>H NMR.

However, in some cases the increase in conversion was less than expected. From an extra 9 h of irradiation, the conversion of 4-nitrobenzyl alcohol only increased from 46% to 74%. No increase in 4-trifluoromethylbenzyl alcohol conversion is observed upon irradiation for 12 h (44%) when compared to that observed for 3 h of irradiation (48%). These reactions indicated that benzyl alcohol oxidation with nan-BiVO<sub>4</sub> involved a reversible reaction, a photostationary state or product/by-product inhibition. 4-trifluorobenzaldehyde was irradiated in the presence of blue LED irradiated nan-BiVO<sub>4</sub> for several hours, however no 4-trifluorobenzyl alcohol was observed and so it can be said that there was no photostationary state and benzyl alcohol oxidation with nan-BiVO<sub>4</sub> was not a reversible reaction. As a result, the impact of catalyst poisoning and product inhibition was explored.

### 3.2.3 Inhibition

Various quantities of 4-methoxybenzaldehyde, 4-trifluorobenzaldehyde and 4-nitrobenzaldehyde were added to reaction mixtures for the oxidation of 4-methoxybenzyl alcohol by blue light irradiated nan-BiVO<sub>4</sub> and the associated impact on alcohol conversion was observed, Figure 3.6.

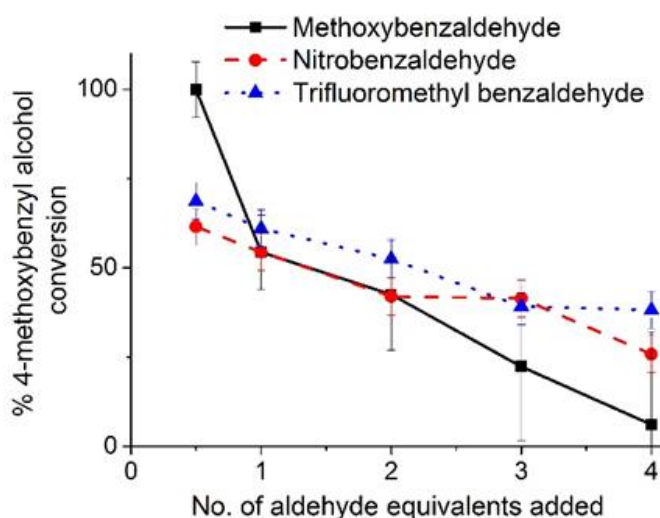


Figure 3.6 – The effect of the addition of para substituted benzaldehydes to the photooxidation of 4-methoxybenzyl alcohol by nan-BiVO<sub>4</sub>. Reaction conditions: 0.1 mmol nan-BiVO<sub>4</sub>, 0.1 mmol 4-methoxybenzyl alcohol, 10 mL acetonitrile and 1 atm dioxygen. Percentage conversions were calculated from <sup>1</sup>H NMR.

It was evident that the addition of these benzaldehydes had an impact on 4-methoxybenzyl alcohol oxidation. It was also evident that benzaldehydes with electron withdrawing substituents had a higher impact on alcohol oxidation at lower concentrations, whereas

### Chapter 3

methoxybenzaldehyde appeared to show the highest impact on alcohol conversion at higher concentrations; the addition of 4 equivalents of 4-methoxybenzaldehyde resulted in a reduction in 4-methoxybenzyl alcohol conversion from >99% to 6%.

The reactions that resulted in the highest amount of inhibition (3 and 4 equivalents of 4-methoxybenzaldehyde) were also the only reactions where 4-methoxybenzoic acid could be observed (ca. 1% and 2% respectively), Figure 3.7. The formation of 4-methoxybenzoic acid was as a result of the oxidation of 4-methoxybenzaldehyde and it was possible that 4-methoxybenzoic acid binding was the cause of inhibition.

In previously reported electrochemical work, the formation of benzaldehyde selectivity from the oxidation of benzyl alcohol has been difficult to achieve and over oxidation often occurred;<sup>211, 244, 245</sup> electrochemically using both gold and nickel electrodes it has been shown that both benzaldehyde and benzoic acid formed simultaneously from the oxidation of benzyl alcohol.<sup>211, 244, 245</sup> It was also known that carboxylic acids bind strongly to the surface of metal oxides<sup>246</sup> and could easily bind irreversibly to an active oxidation site which would stop catalytic turnover. It can be said that in these benzoic acid inhibited systems, aldehyde selectivity was achieved because acid binding and inhibition of surface oxidation sites stops the adsorption and oxidation of both alcohol and aldehyde molecules.



## Chapter 3

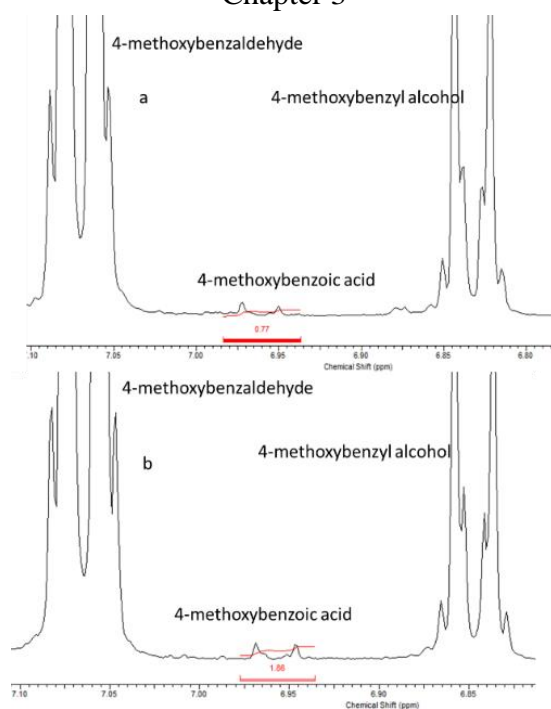


Figure 3.7 - A selection of the  $^1\text{H}$  NMR spectra (400 MHz,  $\text{d}_6\text{-DMSO}$ ) for the 4-methoxybenzyl alcohol inhibition reactions using: a) 3 equiv. 4-methoxybenzaldehyde and b) 4 equiv. 4-methoxybenzaldehyde containing a signal consistent with the meta-protons of 4-methoxybenzoic acid, at 6.97 ppm. The signals have been integrated against a known amount of maleic acid. Other expected signals at 3.78 ( $\text{CH}_3\text{O}$ ) and 7.86 ppm ( $o\text{-H}_{\text{Ar}}$ ) consistent with 4-methoxybenzoic acid cannot be used for quantification due to overlap with signals attributable to 4-methoxybenzaldehyde.

### 3.2.4 Ketone and carboxylic acid inhibition

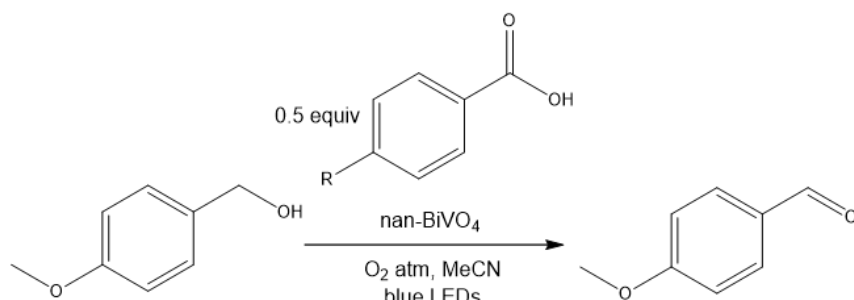
It was with the potential for either aldehyde product or carboxylic acid by-product inhibition in mind that further inhibition experiments were conducted. Initially, 0.5 equivalents of a range of different benzoic acids and acetophenones were added to reaction mixtures for the photocatalytic oxidation of 4-methoxybenzyl alcohol, Table 3.5 for benzoic acid inhibition and Table 3.6 for acetophenone inhibition. All reactions gave benzaldehyde selectivities  $>99\%$ .

If aldehydes significantly inhibited alcohol oxidation then it is likely that the surface binding interaction was via an acetal functionality.<sup>247</sup> If an acetal functionality was the binding interaction between inhibiting substrate and the metal oxide surface then acetophenones should be able to form a ketal functionality and also cause effective alcohol oxidation inhibition. Some significant inhibition was observed with the use of 0.5 equivalents of methoxyacetophenone; alcohol conversion was reduced by 23%. However, more electron withdrawing substituted acetophenones did not inhibit alcohol oxidation

### Chapter 3

effectively. As this was the opposite trend observed for inhibition with benzaldehydes at the same concentrations, this could be used to tentatively suggest that acetal formation was not a significant factor contributing to the inhibition effects observed.

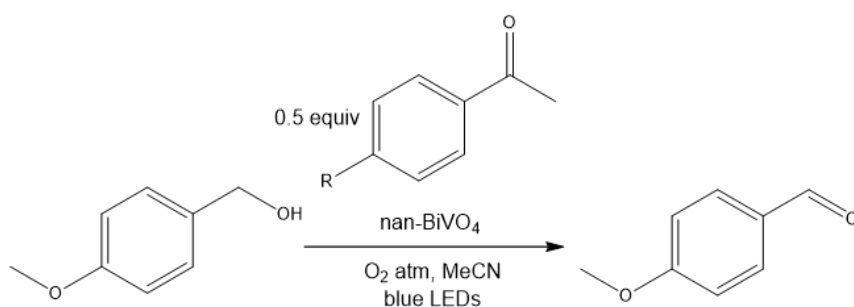
Table 3.5 – The effect of the addition of para substituted benzoic acids to the photooxidation of 4-methoxybenzyl alcohol by nan-BiVO<sub>4</sub>.



R <sup>a</sup>	% Conversion <sup>b</sup>	% Selectivity <sup>b</sup>
NO <sub>2</sub>	6	>99
COOMe	6	>99
iPr	12	>99
OMe	8	>99

<sup>a</sup>conditions: 0.1 mmol nan-BiVO<sub>4</sub>, 0.1 mmol 4-methoxybenzyl alcohol, 0.05 mmol *para*-substituted benzoic acid, 10 mL acetonitrile, 1 atm O<sub>2</sub>, blue LEDs 3 h. <sup>b</sup>The conversion and selectivity were determined using <sup>1</sup>H NMR.

Table 3.6 - The effect of the addition of para substituted acetophenone to the photooxidation of 4-methoxybenzyl alcohol by nan-BiVO<sub>4</sub>



R <sup>a</sup>	% Conversion <sup>b</sup>	% Selectivity <sup>b</sup>
NO <sub>2</sub>	>99	>99
COOMe	95	>99
iPr	96	>99
OMe	78	>99

<sup>a</sup>conditions: 0.1 mmol nan-BiVO<sub>4</sub>, 0.1 mmol 4-methoxybenzyl alcohol, 0.05 mmol *para*-substituted acetophenone, 10 mL acetonitrile, 1 atm O<sub>2</sub>, blue LEDs 3 h. <sup>b</sup>The conversion and selectivity were determined using <sup>1</sup>H NMR.

### Chapter 3

The addition of benzoic acids clearly had an inhibitory effect; alcohol conversions were reduced by ca. 90% regardless of substituent. However, from this data it cannot be said that over oxidation to 4-methoxybenzoic acid is the root cause of the inhibition observed as the concentrations of benzoic acids used to generate the data in Table 3.5 were much higher than any benzoic acid concentrations observed in the experiments that generated the data in Table 3.3, Table 3.4 and Figure 3.6. As a result, the 4-methoxybenzoic acid inhibition experiments were repeated with varying concentrations of 4-methoxybenzoic acid in order to examine whether significant inhibition can occur at low benzoic acid concentrations, Figure 3.8.

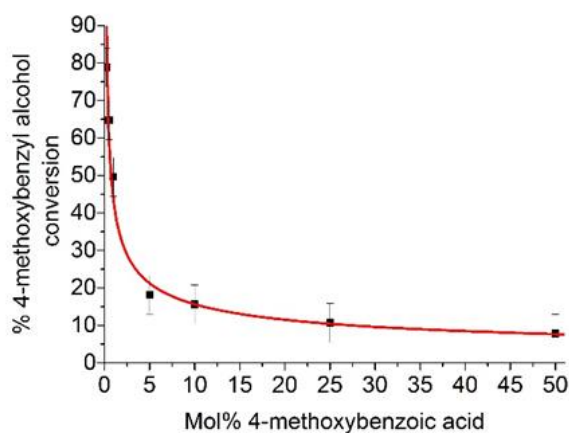


Figure 3.8 – Inhibition of 4-methoxybenzyl alcohol conversion with various amounts of 4-methoxybenzoic acid. Mol% is relative to the amount of 4-methoxybenzyl alcohol. Reaction conditions: 0.1 mmol nan-BiVO<sub>4</sub>, 0.1 mmol 4-methoxybenzyl alcohol, 10 mL acetonitrile and 1 atm dioxygen. Percentage conversions were calculated from <sup>1</sup>H NMR.

Significant inhibition was observed, with the addition of 1 mol% of 4-methoxybenzoic acid; 4-methoxybenzyl alcohol conversion was reduced by 50%. 5 mol% 4-methoxybenzoic acid resulted in a reduction in 4-methoxybenzyl alcohol conversion of over 80%. For reactions with the addition of 0.1, 0.5 or 1 mol% 4-methoxybenzoic acid, no 4-methoxybenzoic acid was observed in the final NMR spectrum after irradiation. This could suggest that repeated oxidation of this benzoic acid species resulted in complete degradation to volatile products. However, this could also suggest that all of the benzoic acid added to these reaction mixtures stayed irreversibly bound to the surface of nan-BiVO<sub>4</sub>. This could explain why no benzoic acid was observed in the NMR spectra for most of the data in Table 3.3, Table 3.4 and Figure 3.6 as the small amounts of benzoic acid formed from over-oxidation was strongly and irreversibly bound to the catalyst surface.

### Chapter 3

To test whether 4-methoxybenzoic acid could irreversibly bind to the catalyst surface and cause alcohol oxidation inhibition, a 10 mM solution of 4-methoxybenzoic acid in acetonitrile was stirred with nan-BiVO<sub>4</sub> (0.1 mmol) for several hours. The nan-BiVO<sub>4</sub> was centrifuged out of this solution and washed repeatedly with acetonitrile to remove any unbound substrate; after drying, the mass of nan-BiVO<sub>4</sub> remained the same as before the acid wash suggesting that the catalyst had not been degraded upon stirring in acid. This 4-methoxybenzoic acid washed nan-BiVO<sub>4</sub> was then used to oxidise 4-methoxybenzyl alcohol (0.1 mmol) with 3 h of irradiation from the blue LED array. Only 45% alcohol conversion was observed; this suggests that some sites were inhibited by irreversibly bound 4-methoxybenzoic acid. As some alcohol conversion did occur, this also suggests that more than one kind of oxidation site existed at the surface of nan-BiVO<sub>4</sub> at which substrates, such as 4-methoxybenzoic acid or 4-methoxybenzaldehyde, were able to reversibly inhibit alcohol oxidation.

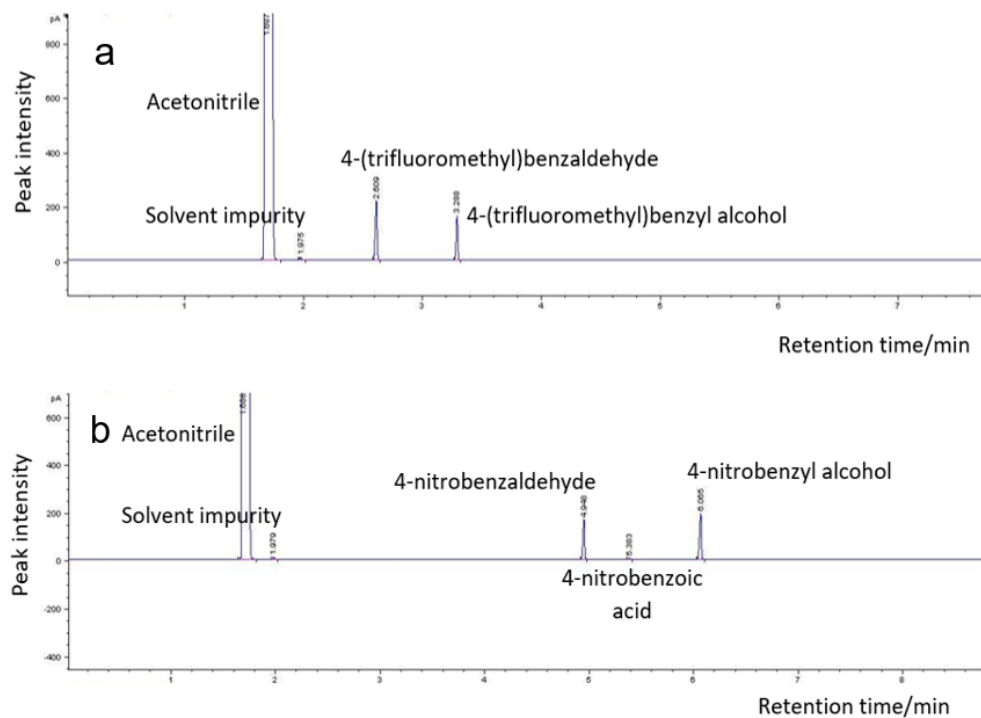


Figure 3.9 – Gas Chromatograms for the oxidation of: a) 0.1 mmol 4-(trifluoromethyl)benzyl alcohol and b) 4-nitrobenzyl alcohol by 0.1 mmol blue light irradiated nan-BiVO<sub>4</sub> with 1 atm O<sub>2</sub>, 10 mL acetonitrile. Reaction time = 3 h. Gas Chromatography was performed on an Agilent/HP 6890, with an injection volume of 1  $\mu$ L, using compressed air as a carrier gas at 1 mL min<sup>-1</sup>, a flame ionised detector at 250 °C, and Chrompack DB-5ms column between 90 and 300 °C with ramp rate 20 °C min<sup>-1</sup>.

The inhibition effects discussed here can be used to explain some of the trends observed throughout the benzyl alcohol experiments. The aldehyde selectivities of the oxidation of

trifluoromethylbenzyl alcohol and nitrobenzyl alcohol were relatively low; ca. 83% after 3 h of irradiation. Gas chromatography from these reaction mixtures only showed evidence for the presence of the corresponding alcohols, aldehydes and small quantities of acid, Figure 3.9. As a result, it could be suggested that strong binding of these acids to the surface of nan-BiVO<sub>4</sub> led to the repeated oxidation of these substrates, resulting in the formation of volatile, low molecular weight compounds, such as carbon dioxide and water. As carbon dioxide and water were not the intended products of this work and could be easily lost, no analysis was carried out to try and detect the presence of these compounds.

The electronic effect trends observed in Figure 3.6 could be explained through varying benzoic acid inhibition. At low concentrations of benzaldehyde, only small amounts of benzoic acid were formed. Benzoic acids with electron withdrawing substituent groups exhibited a greater inhibitory effect at these concentrations because these species are stronger acids than benzoic acids with electron donating substituents.<sup>248</sup> One possible binding mechanism for benzoic acid onto the surface of nan-BiVO<sub>4</sub> is via esterification; electron withdrawing substituted benzoic acids were more likely to provide the conditions necessary to initiate esterification with surface hydroxyl groups.<sup>249</sup> As the concentration of benzaldehyde increased, benzaldehyde analogues with electron donating groups were more easily oxidised than those with electron withdrawing groups<sup>17</sup> so more oxidation to the corresponding benzoic acid occurred for benzaldehyde analogues with an electron donating group. This higher concentration of benzoic acid, with electron donating substituents, was able to interact with more of the catalyst surface and is therefore capable of a greater inhibitory effect.

The results of these inhibition studies suggested that by-product inhibition had a significant impact on the use of nan-BiVO<sub>4</sub> for the photocatalytic oxidation of benzyl alcohols. Catalyst poisoning and reaction inhibition are prominent features of thermal heterogeneous catalysis;<sup>250-256</sup> examples include: the use of KCl to deactivate V<sub>2</sub>O<sub>5</sub>-WO<sub>3</sub>/TiO<sub>2</sub> used in the reduction of NO by NH<sub>3</sub>,<sup>251</sup> the poisoning of Pd based catalysts, used for methane oxidation,<sup>255, 256</sup> by sulphur dioxide and the CO inhibition of Pd-Pt/Al<sub>2</sub>O<sub>3</sub> catalysts used for the oxidation of CO. Inhibition has been rarely discussed in heterogeneous photocatalysis and could be a significant factor in any observed photocatalytic selectivity. Only one previous example of heterogeneous photocatalytic reaction inhibition with the use of organics could be found, the UV light mediated oxidation by titania was inhibited by the formation of the benzoic acid.<sup>129</sup> As a result, this

work provides a platform for further work investigating the effect of inhibition on reaction selectivity in order to gain a better understanding of how heterogeneous photocatalytic systems can be used for selective chemical transformations.

### 3.2.5 Catalyst recycling and stability

An important advantage of the use of a heterogeneous photocatalyst is the ability to easily separate the photocatalyst from a reaction mixture by centrifugation and then recycle said material in another photocatalytic reaction.<sup>28, 70, 71</sup> The stability and recyclability of nan-BiVO<sub>4</sub> was investigated over 4 repeat uses of the material as a photocatalyst for the oxidation of 4-methoxybenzyl alcohol, Figure 3.10. The first reaction resulted in the complete conversion of 0.1 mmol 4-methoxybenzyl alcohol to 4-methoxybenzaldehyde. After the first repeat use of the nan-BiVO<sub>4</sub>, a significant drop in conversion was observed; this percentage alcohol conversion was roughly maintained at ca. 75% throughout the oxidation repeats. It could be suggested that 4-methoxybenzoic acid formation was the cause of this reduction in conversion. However, after the final repeat oxidation, it was noted that mechanical losses of ca. 10% nan-BiVO<sub>4</sub> that would account for some of the reduction in alcohol conversion. PXRD, Figure 3.11 and SEM data, Figure 3.12 suggested that nan-BiVO<sub>4</sub> was unchanged after being used as an oxidation photocatalyst.

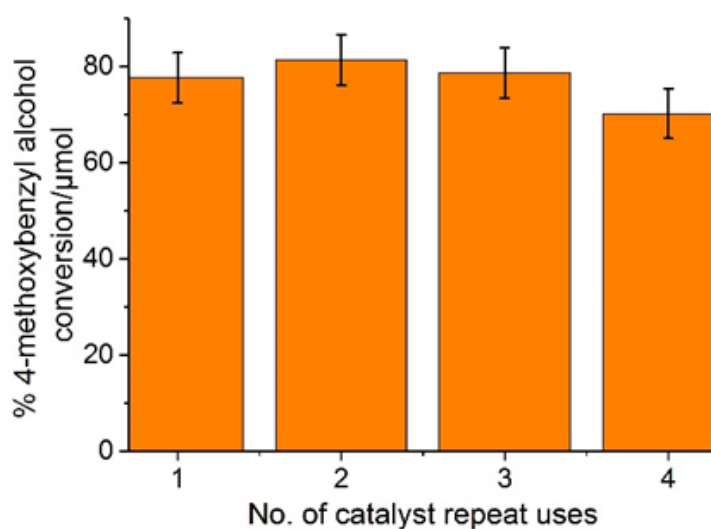


Figure 3.10 – Recycle of nan-BiVO<sub>4</sub> (0.1 mmol) for the selective photooxidation of 4-methoxybenzyl alcohol (0.1 mmol per repeat) into 4-methoxybenzaldehyde, blue LED irradiation for 3 h for each reaction, 1 atm O<sub>2</sub>, 10 mL acetonitrile.

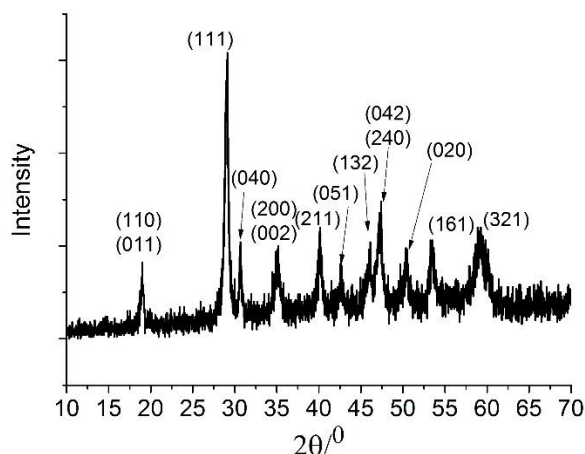


Figure 3.11 - PXRD for used nan-BiVO<sub>4</sub>. This data is consistent with crystalline monoclinic BiVO<sub>4</sub> (JCPDS no. 14-0688).

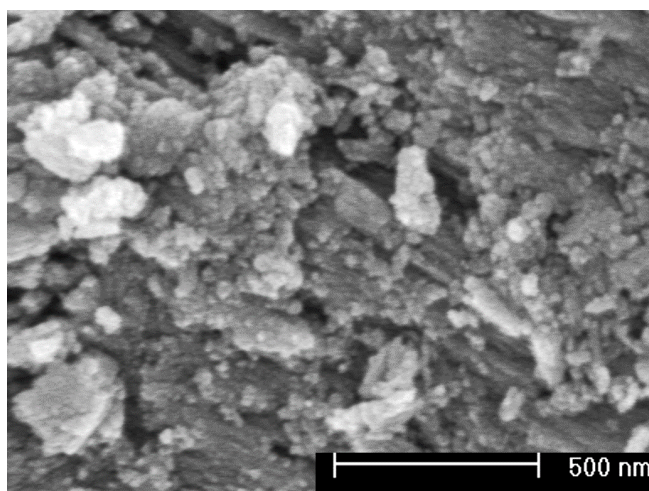


Figure 3.12 – SEM of used nan-BiVO<sub>4</sub>. The image shows agglomerated nanoparticles ca. 50 – 100 nm in size.

### 3.2.6 Mechanism

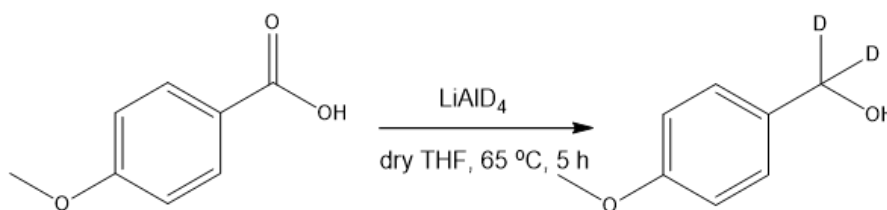
#### 3.2.6.1 Use of isotopically labelled benzyl alcohols

The use of isotopically labelled starting materials can help in furthering the understanding of the kinetic isotope effect for a particular reaction and can establish whether atom exchange occurs between reactive species.

Comparing the reaction rates of conversion of  $\alpha$ -D<sub>2</sub>-4-methoxybenzyl alcohol and  $\alpha$ -H<sub>2</sub>-4-methoxybenzyl alcohol can be useful in determining whether the cleavage of a C-H bond adjacent to the alcohol functionality is relevant to the rate determining step for alcohol oxidation<sup>15, 18</sup> with nan-BiVO<sub>4</sub>. Deuterium has twice the mass of hydrogen and bonds between carbon and heavier isotopes require more energy to break. C-D bonds

### Chapter 3

have a lower zero-point energy and a lower vibrational frequency than C-H bonds and so more energy is required to overcome the activation barrier for C-D bond cleavage.<sup>257</sup> As a result, if the cleavage of this C-H/D bond is relevant to the rate limiting step, the rate constant for the oxidation of  $\alpha$ -D<sub>2</sub>-4-methoxybenzyl alcohol ( $k_D$ ) will be significantly lower than the rate constant for the oxidation of  $\alpha$ -H<sub>2</sub>-4-methoxybenzyl alcohol ( $k_H$ );  $k_H/k_D \gg 1$  known as a primary kinetic isotope effect.<sup>15, 18</sup> If  $k_H/k_D \approx 1$ , then there is a secondary kinetic isotope effect and the cleavage of this C-H/D bond is not relevant to the rate determining step for benzyl alcohol oxidation with blue light irradiated nan-BiVO<sub>4</sub>.



Scheme 3.1 – The synthesis of  $\alpha$ -D<sub>2</sub>-4-methoxybenzyl alcohol via reduction with LiAlD<sub>4</sub>

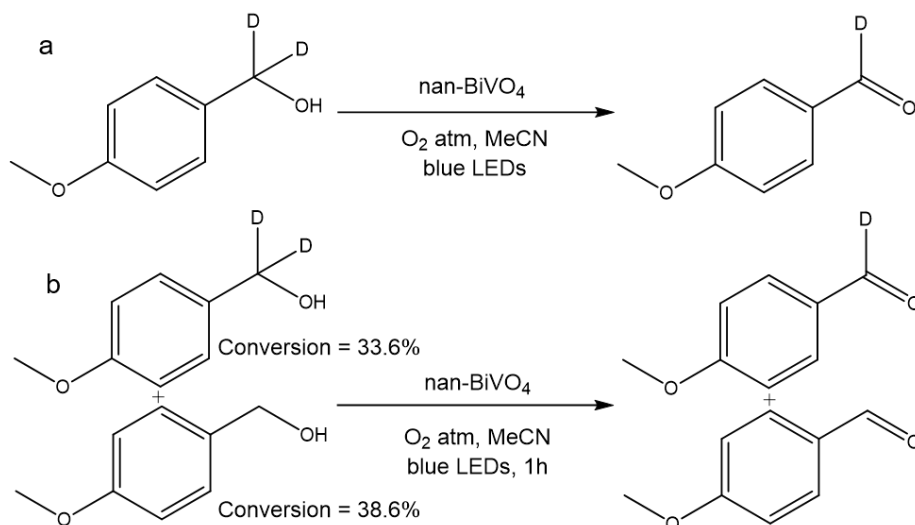
$\alpha$ -D<sub>2</sub>-4-methoxybenzyl alcohol was synthesised via the reduction of 4-methoxybenzoic acid with LiAlD<sub>4</sub> in dry THF, Scheme 3.1. <sup>1</sup>H NMR and ESI-MS were consistent with successful deuteration and reduction; <sup>1</sup>H NMR (CDCl<sub>3</sub>, 400 MHz) was consistent with that of 4-methoxybenzyl alcohol with only a trace signal (<1%) observable for the protons consistent with a methylene functionality adjacent to a hydroxyl group. ESI-MS of the isolated compound resulted in the observation of a sodiated molecular ion peak at 163.0691; the theoretical calculated mass/charge ratio for sodiated  $\alpha$ -D<sub>2</sub>-4-methoxybenzyl alcohol was 163.0699.

The photooxidation of  $\alpha$ -D<sub>2</sub>-4-methoxybenzyl alcohol with blue light irradiated nan-BiVO<sub>4</sub> over 3 hours resulted only in the formation of deuterated 4-methoxybenzaldehyde, Scheme 3.2a. <sup>1</sup>H NMR (CDCl<sub>3</sub>, 400 MHz) was consistent with that of 4-methoxybenzaldehyde with only a trace signal (<1%) observable for the proton consistent with the aldehyde functionality. ESI-MS resulted in the observation of a molecular ion peak at 138.0661; the theoretical calculated mass/charge ratio for deuterated 4-methoxybenzaldehyde was 138.0660. This suggested that no proton exchange occurred between the protons in the methylene group and the hydroxyl proton on oxidation. The oxidation of a 50/50 mixture of  $\alpha$ -D<sub>2</sub>-4-methoxybenzyl alcohol and  $\alpha$ -H<sub>2</sub>-4-methoxybenzyl alcohol by nan-BiVO<sub>4</sub> with 1 h of irradiation was used to calculate  $k_H/k_D$ , Scheme 3.2b. <sup>1</sup>H NMR peak integrations were used to show that  $\alpha$ -H<sub>2</sub>-4-methoxybenzyl



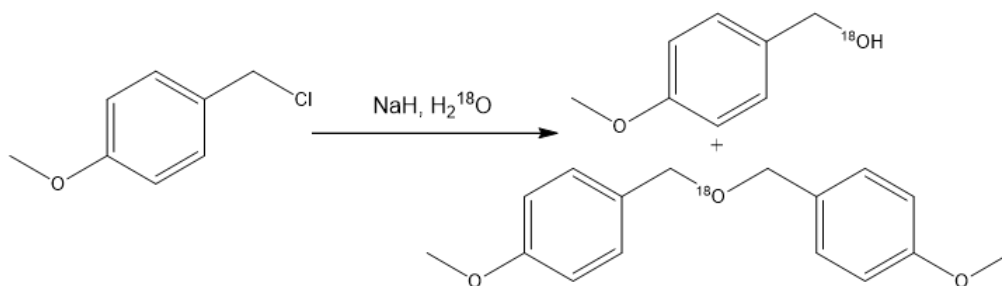
### Chapter 3

alcohol conversion was 39% and that  $\alpha$ -D<sub>2</sub>-4-methoxybenzyl alcohol conversion was 34%.



Scheme 3.2 – The use of  $\alpha$ -D<sub>2</sub>-4-methoxybenzyl alcohol to observe the lack of H atom exchange and a secondary kinetic isotope effect.

As the oxidation of 4-methoxybenzyl alcohol with nan-BiVO<sub>4</sub> proceeded with zero order kinetics and with >99% aldehyde selectivity, the conversion percentages given are proportional to the rate constants  $k_H$  and  $k_D$  respectively. Therefore  $k_H/k_D = 1.3$ ; this is consistent with a secondary kinetic isotope effect and so a C-H/D cleavage was not relevant to the rate determining step for this reaction. A secondary kinetic isotope effect that is greater than 1 is often consistent with a rate determining step that involves a change in hybridisation from  $sp^3$  to  $sp^2$ . This was different to the photocatalysis of benzyl alcohol with TiO<sub>2</sub> and gC<sub>3</sub>N<sub>4</sub> that have been previously reported in literature, where primary kinetic isotope effects were observed with  $k_H/k_D$  of 3.9 and 3.3, respectively.<sup>15, 18</sup>

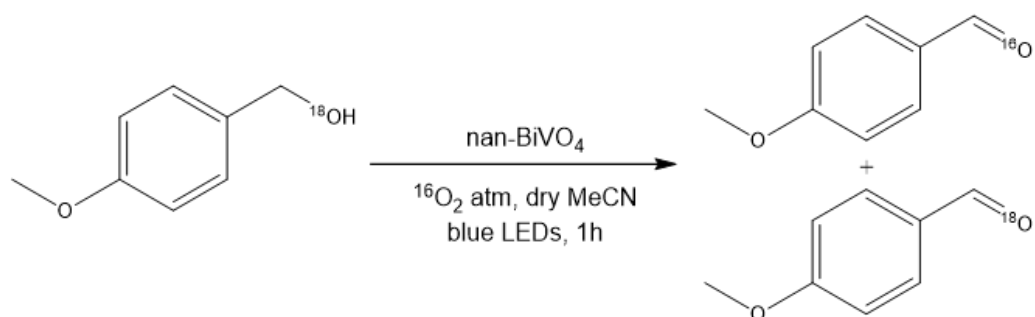


Scheme 3.3 – Synthesis of <sup>18</sup>O labelled 4-methoxybenzyl alcohol unselectively from the hydrolysis of 4-methoxybenzyl chloride with sodium hydride and H<sub>2</sub><sup>18</sup>O.

In order to explore the possibility of oxygen atom exchange between dioxygen and benzyl alcohol upon oxidation, <sup>18</sup>O labelled 4-methoxybenzyl alcohol was synthesised and

### Chapter 3

oxidised by nan-BiVO<sub>4</sub>. <sup>18</sup>O labelled 4-methoxybenzyl alcohol was synthesised from the hydrolysis of an excess of 4-methoxybenzyl chloride with H<sub>2</sub><sup>18</sup>O and sodium hydride, Scheme 3.3. The reaction resulted in the formation of <sup>18</sup>O labelled 4-methoxybenzyl alcohol and the corresponding ether product which formed from the nucleophilic attack of 4-methoxybenzyl oxide anion onto the electropositive carbon adjacent to a chlorine atom of 4-methoxybenzyl chloride. <sup>18</sup>O labelled 4-methoxybenzyl alcohol was separated from the crude reaction mixture by silica column using a 33% ethyl acetate in pet ether (40 – 60 °C) eluent. ESI-MS of the isolated product resulted in the observation of a potassiated molecular ion peak at 179.0358; the theoretical calculated mass/charge ratio for potassiated <sup>18</sup>O labelled 4-methoxybenzyl alcohol was 179.0360. <sup>1</sup>H NMR (CDCl<sub>3</sub>, 400 MHz) of the isolated product was consistent with 4-methoxybenzyl alcohol.



Scheme 3.4 – Oxidation of <sup>18</sup>O labelled 4-methoxybenzyl alcohol to observe oxygen atom exchange. Ratio of <sup>16</sup>O:<sup>18</sup>O observed was 2:1 by ESI-MS.

0.1 mmol <sup>18</sup>O labelled 4-methoxybenzyl alcohol was oxidised by 0.1 mmol nan-BiVO<sub>4</sub> irradiated by blue LEDs in the presence of 1 atm <sup>16</sup>O<sub>2</sub>, Scheme 3.4. Acetonitrile dried with calcium hydride and distilled over molecular sieves was used as solvent and nan-BiVO<sub>4</sub> was dried by heating at 80 °C *in vacuo* to minimise exposure to water. ESI-MS of the reaction mixture after irradiation showed the presence of both <sup>16</sup>O and <sup>18</sup>O labelled 4-methoxybenzaldehyde. A sodiated molecular ion peak for <sup>18</sup>O labelled 4-methoxybenzaldehyde was observed at 161.0456; the theoretical calculated mass/charge ratio for sodiated <sup>18</sup>O labelled 4-methoxybenzaldehyde was 161.0459. A sodiated molecular ion peak for <sup>16</sup>O labelled 4-methoxybenzaldehyde was observed at 159.0405; the theoretical calculated mass/charge ratio for sodiated <sup>16</sup>O labelled 4-methoxybenzaldehyde was 159.0417. The ratio of <sup>16</sup>O to <sup>18</sup>O labelled product in the ESI-MS was 2:1. This data suggested that there was some oxygen atom exchange in this reaction, however it was not conclusively possible to specify what interaction led to this atom exchange. It is possible that oxidation of 4-methoxybenzyl alcohol and reduction of dioxygen occurring at the surface of nan-BiVO<sub>4</sub> led to the exchange of O atoms or that

exchange with residual  $\text{H}_2^{16}\text{O}$  occurred with the aldehyde forming an acetal functionality, either at the photocatalyst surface, in solution or upon exposure to the atmosphere (which was limited but unavoidable for injection into the ESI-MS). In previously reported literature, analogous work has explored oxygen atom exchange in the aerobic photooxidation of benzyl alcohol on titania which concluded that full oxygen exchange does occur via a 5-membered metallocycle.<sup>258, 259</sup>

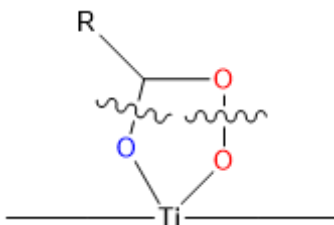


Figure 3.13 – The breaking of the 5 membered metallocycle proposed in literature that mediated O atom exchange in alcohol oxidation. O atoms coloured red were from a dioxygen molecule and O atoms coloured blue were from an alcohol molecule.<sup>258, 259</sup>

### 3.2.6.2 Time resolved photoluminescence

Time resolved photoluminescence spectroscopy can be used to detect electron-hole recombination in an irradiated semiconductor through the observation of luminescence. Intensity of emission is linked to the likelihood of electron hole recombination and so the effectiveness of a photocatalyst can be examined through the comparison of emission intensity.<sup>132, 241, 260-264</sup> Electron-hole recombination is often discussed as a limiting factor in photocatalysis,<sup>63-67</sup> however other attributes of a photocatalyst can also prove to be limiting. An example of a potentially limiting attribute that is relevant to this work is the surface area available for substrate adsorption. Therefore, the use of time resolved photoluminescence spectroscopy can be very illuminating with regards to what is the rate limiting step for a particular photocatalytic system. The analysis of decay curves for characteristic emission wavelengths can be used to examine charge carrier lifetimes. These lifetimes can be used to compare the likelihood that a charge carrier will go onto carry out a redox reaction at the catalyst surface; the longer the lifetime, the more likely it is that the charge carrier will cause a redox reaction. The relevance of these lifetimes to a photocatalytic reduction or oxidation of interest can also be examined through observing changes in lifetime associated to the addition of different substrates.

The photoluminescence spectrum of bulk and nan- $\text{BiVO}_4$  were recorded after excitation with a 380 nm picosecond pulse LED, Figure 3.14a. 2 overlapping peaks were observed with  $\lambda_{\text{max}1} = 445 \text{ nm}$  and  $\lambda_{\text{max}2} = 475 \text{ nm}$ . Emission decay curves, Figure 3.14b, at various

### Chapter 3

emission wavelengths were recorded and Edinburgh photonics F980 software was used to analyse these curves by fitting bi-exponential curves to the data obtained. These curves fit to Equation 3.1.

$$\text{Equation 3.1} \quad I = Ae^{-t/\tau_1} + Be^{-t/\tau_2} + c$$

I - signal intensity at a given time (t).  $\tau_1$  - lifetime associated to the emission peak with  $\lambda_{\text{max}} = 445$  nm.  $\tau_2$  - lifetime associated to the emission peak with  $\lambda_{\text{max}} = 475$  nm. c - arbitrary constant. A and B are proportionality constants which allow for the calculation of percentage contributions from the emission peaks at  $\lambda_{\text{max}} = 445$  nm and  $\lambda_{\text{max}} = 475$  nm,  $\%C_{\tau_1}$  and  $\%C_{\tau_2}$  respectively. Equation 3.2 and Equation 3.3 were used for the calculation of these percentage contributions.

$$\text{Equation 3.2} \quad \%C_{\tau_1} = \frac{A\tau_1}{(A\tau_1 + B\tau_2)} \times 100$$

$$\text{Equation 3.3} \quad \%C_{\tau_2} = \frac{B\tau_2}{(A\tau_1 + B\tau_2)} \times 100$$

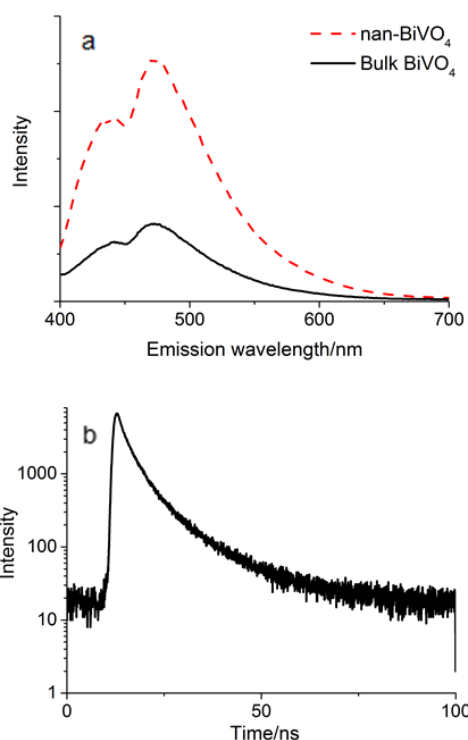
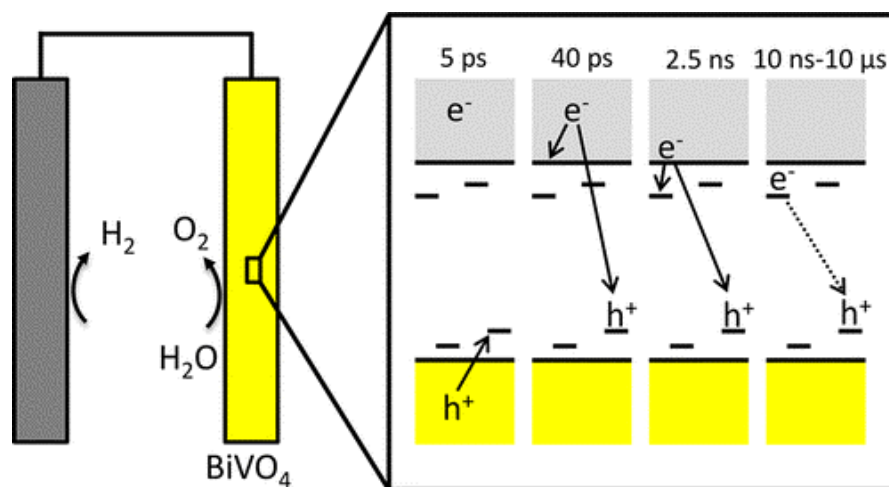


Figure 3.14 – a) Emission spectrum for a  $1 \text{ mg mL}^{-1}$  dispersion of  $\text{BiVO}_4$  dispersed in dry, nitrogen degassed acetonitrile, excitation wavelength = 380 nm. b) Decay curve for nan- $\text{BiVO}_4$ , excitation wavelength = 380 nm, emission wavelength = 440 nm.

Lifetimes under a range of different conditions are given in Table 3.7. Data was collected at the emission wavelengths of 420 and 500 nm as this allows for the assignment of

lifetimes to the emission peaks in Figure 3.14. The shorter lifetime of ca. 3 ns is derived from the peak with  $\lambda_{\text{max}1} = 445$  nm and the lifetime of ca. 10 ns is derived from the peak with  $\lambda_{\text{max}2} = 475$  nm.

Characterising these emissions was challenging as the emission spectrum of  $\text{BiVO}_4$  appeared to be vary significantly based upon a wide number of variables including but not limited to sample preparation method, excitation wavelengths and the presence of different defect sites.<sup>137, 224, 229, 250, 265-267</sup> In literature by Kennis et al., other methods such as transient absorption spectroscopy have been used to assignment charge carrier lifetimes to transitions in photoelectrochemical water splitting systems using  $\text{BiVO}_4$ .<sup>268</sup>



Scheme 3.5 – The charge carrier dynamics of bismuth vanadate as shown by transient absorption. Reprinted with permission from J. T. M. Kennis, *J. Phys. Chem. C*, 2014, **118**, 27793–27800.<sup>268</sup> Copyright 2014 American Chemical Society.

Photoelectron trapping at defect sites below the conduction band and the recombination of photoelectrons in the conduction band and holes trapped in states with energies just above the valence band were found to have lifetimes of roughly 2.5 ns and electrons trapped at defect sites recombining with holes found at defect sites were found to have lifetimes of ca. 10 ns, Scheme 3.5. These lifetimes were similar to those observed in this work. It is also possible to use published computationally derived DFT data to establish the formation energies of defect sites for n-type  $\text{BiVO}_4$ ,<sup>269</sup> Figure 3.15 and then use this to characterise the emission peaks seen in Figure 3.14.

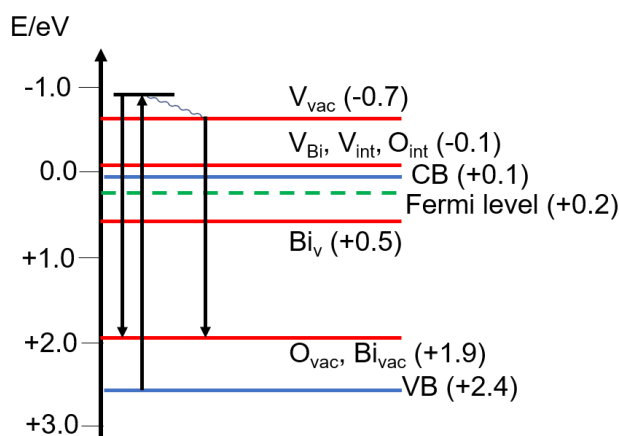


Figure 3.15 – Formation energies for defect sites calculated using a model for n-type  $\text{BiVO}_4$  and the transitions that lead to the emissions observed in Figure 3.14 energies quoted vs NHE.  $V_{\text{vac}}$  – V vacancy;  $V_{\text{Bi}}$  – V at a Bi site;  $V_{\text{int}}$  – V in an interstitial site;  $O_{\text{int}}$  – O in an interstitial site;  $\text{Bi}_V$  – Bi at a V site;  $O_{\text{vac}}$  – Bi vacancy;  $\text{Bi}_{\text{vac}}$  – Bi vacancy.<sup>269</sup>

Excitation of an electron to 3.3 eV (380 nm) above the valence band potential could have recombined with holes found at O or Bi vacancies ( $O_{\text{vac}}$  and  $\text{Bi}_{\text{vac}}$  respectively) and emitted a photon with an energy of 2.80 eV (445 nm); it can be suggested that this transition was consistent with the emission peak at 445 nm with a lifetime of ca. 3 ns. After excitation, electrons could also undergo thermal relaxation and become trapped at intra-conduction band defect states centred on V vacancies ( $V_{\text{vac}}$ ). After this, recombination with holes found in O or Bi vacancies would result in the emission of a photon with an energy of 2.60 eV (475 nm); it can be suggested that this transition was consistent with the emission peak at 475 nm with a lifetime of ca. 10 ns. These assignments were also in agreement with those made using transient absorption spectroscopy.<sup>268</sup>

Table 3.7 – Excited state lifetimes for  $\text{BiVO}_4$  in acetonitrile

Sample <sup>a</sup>	$\tau_1/\text{ns}$ (A/%); $\tau_2/\text{ns}$ (B/%) <sup>b</sup>	$\tau_1/\text{ns}$ (A/%); $\tau_2/\text{ns}$ (B/%) <sup>c</sup>
nan- $\text{BiVO}_4$ , $\text{N}_2$	3.02±0.10 (56.2); 10.86±0.47 (43.8)	3.52±0.10 (45.1); 11.91±0.37 (54.9)
nan- $\text{BiVO}_4$ , $\text{O}_2$	2.94±0.09 (58.1); 11.19±0.43 (41.9)	3.45±0.11 (46.8); 11.29±0.34 (53.2)
nan- $\text{BiVO}_4$ , $\text{N}_2$ , BnOH	2.25±0.04 (53.0); 8.31±0.15 (47.0)	3.41±0.10 (45.2); 10.13±0.22 (54.8)
nan- $\text{BiVO}_4$ , $\text{O}_2$ , BnOH	2.29±0.06 (52.8); 8.39±0.22 (47.2)	3.08±0.09 (42.5); 9.59±0.20 (57.5)
<u>Bulk <math>\text{BiVO}_4</math>, <math>\text{N}_2</math></u>	<u>3.63±0.27 (47.3); 11.94±0.92 (52.7)</u>	<u>4.18±0.34 (38.1); 12.85±0.78 (61.9)</u>

<sup>a</sup> 1 mg mL<sup>-1</sup> dispersion in MeCN, under 1 atm of  $\text{N}_2$  or  $\text{O}_2$ , 0.1 mmol (10 mM) of benzyl alcohol (BnOH) <sup>b</sup>Excited state lifetimes and % contribution in brackets obtained from excitation at 380 nm and emission at 420 nm, <sup>c</sup>Analogous data from excitation at 380 nm and emission at 500 nm.

### Chapter 3

Comparing emission spectra for bulk and nan-BiVO<sub>4</sub> yielded some unexpected conclusions. The higher intensity of the emission spectrum for nan-BiVO<sub>4</sub> suggested that more electron-hole recombination occurred in the nan-BiVO<sub>4</sub> photocatalyst and so the bulk BiVO<sub>4</sub> should be the more effective photocatalyst. In addition, the longer charge carrier lifetimes observed at both emission wavelengths for bulk BiVO<sub>4</sub> also suggested that the charge carriers were more likely to avoid electron-hole recombination and undergo a redox reaction in the bulk BiVO<sub>4</sub> photocatalyst; this supported the conclusion made when comparing emission spectra that bulk BiVO<sub>4</sub> should be a more effective photocatalyst than nan-BiVO<sub>4</sub>. However, it has already been observed that nan-BiVO<sub>4</sub> converted 30 times more 4-methoxybenzyl alcohol than bulk BiVO<sub>4</sub> after 3 h of blue light irradiation and so nan-BiVO<sub>4</sub> was a significantly more effective photocatalyst than bulk BiVO<sub>4</sub>. As a result, it can be suggested that electron-hole recombination was not rate limiting in the use of nan-BiVO<sub>4</sub> as a photocatalyst. Instead, it can be proposed that the significantly higher surface area of nan-BiVO<sub>4</sub> (7.9 m<sup>2</sup> g<sup>-1</sup>) in comparison to bulk BiVO<sub>4</sub> (<0.1 m<sup>2</sup> g<sup>-1</sup>) allowed for a higher amount of substrate adsorption to nan-BiVO<sub>4</sub>, and so the capacity for substrate adsorption was more rate limiting than electron-hole recombination.

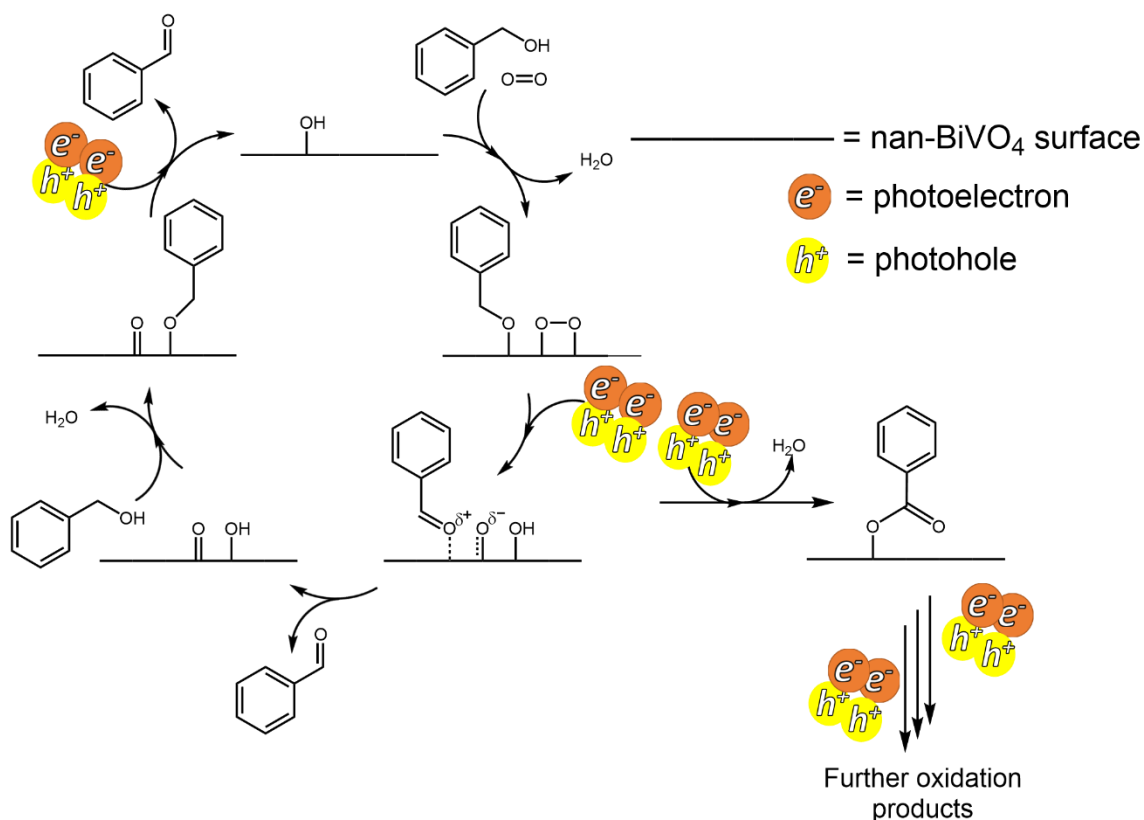
Benzyl alcohol and dioxygen were added to the nan-BiVO<sub>4</sub> dispersion to observe the effect on charge carrier lifetime. The addition of benzyl alcohol resulted in a significant reduction in charge carrier lifetime across all lifetimes measured at both wavelengths the addition of dioxygen only resulted in a reduction in  $\tau_2$  derived from decay curves at an emission wavelength of 500 nm. A reduction in nearly all lifetimes observed with the addition of benzyl alcohol were consistent with the emission assignments as all emissions were associated with the recombination of electrons with holes found in trapped states and surface trapped holes were used in benzyl alcohol oxidation.

No conclusions based upon the changes in lifetime associated to dioxygen reduction could be made as the data associated to changes in  $\tau_2$  does not show a consistent trend; possibly due to the limited solubility of dioxygen in acetonitrile. However, due to the significant changes observed upon the addition of benzyl alcohol, it can be said that the lifetimes observed were associated to charge carriers that are relevant to the aerobic oxidation of benzyl alcohol into benzaldehyde.

#### 3.2.6.3 *Proposed mechanism*

The results are consistent with the mechanism given in Scheme 3.6. Blue light photons were absorbed by nan-BiVO<sub>4</sub> and caused electron hole separation. These charge carriers

became trapped at surface defect sites where the photoexcited electron reduced surface bound dioxygen and the corresponding hole oxidised surface bound benzyl alcohol. Benzaldehyde was formed which liberated protons and enabled the formation of water as the final reduction product. Benzaldehyde could have either undergone desorption from the surface or be oxidised further to form benzoic acid and then stay bound irreversibly to inhibit further oxidation. The surface retained benzoic acid could then be oxidised further.



Scheme 3.6 – Proposed mechanism for the oxidation of benzyl alcohol with nan-BiVO<sub>4</sub>

### 3.3 Conclusions

The work outlined in this chapter met the objectives given and is also directly contributing to the overall aim of this thesis. This is because an understanding of what causes benzaldehyde selectivity was found in that small amounts of benzoic acids were capable of significantly inhibition benzyl alcohol conversion. It could be concluded that strong, and possibly irreversibly, binding of benzoic acids to the surface of nan-BiVO<sub>4</sub> inhibited any further oxidation of benzaldehyde resulting in high benzaldehyde selectivities. This interaction could be key in the development of effective heterogeneous photocatalytic systems into the future as it could possibly lead to the formation of purposefully and controlled inhibition to ensure selectivity for a desired product.



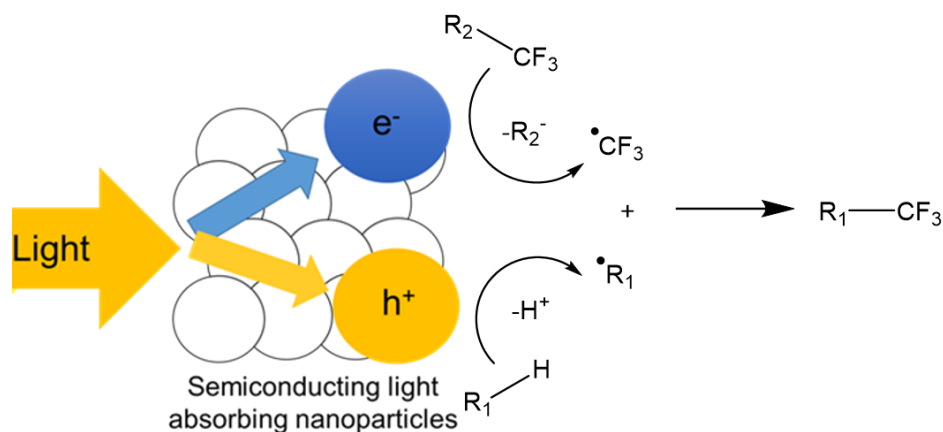
### Chapter 3

The role and importance of various other components of this reaction system was also explored. It was confirmed that a dioxygen oxidant is needed in order to carry out the complementary reduction reaction which limits electron-hole recombination. Even though oxygen exchange was observed, it could not be confirmed whether oxygen exchange occurred between benzyl alcohol and dioxygen via a surface bound intermediate. However, the observation of any oxygen exchange is encouraging with regards to attempting to incorporate useful functionality of an oxidant into the final organic product obtained from a heterogeneous photocatalytic reaction system.

## 4 Heterogeneous Photocatalytic Trifluoromethylation

### 4.1 Introduction

In chapters 2 and 3, it was observed that benzyl alcohols can be selectively oxidised into corresponding benzaldehydes using blue light irradiated semiconducting bismuth containing photocatalysts. With the use of nan-BiVO<sub>4</sub>, it was observed that dioxygen was needed in order to act as an oxidant, however isotope labelling experiments could not specifically conclude whether photocatalytic O atom exchange occurred between dioxygen and benzyl alcohol in this reaction. If O atom exchange did occur during this reaction, then this was an example where part of an oxidant molecule has been incorporated into an oxidised final product of value, through heterogeneous photocatalysis.<sup>259</sup> The incorporation of functionalities found in oxidants into the selectively formed final product provided inspiration for the work in this chapter. It is possible to consider that the single electron reduction of a range of different oxidants by an irradiated heterogeneous photocatalyst could produce radical species which gives access to a range of synthetically important radical addition reactions. One group of oxidants that could be utilised for this purpose are trifluoromethylation reagents, Scheme 4.1.



Scheme 4.1 – The reduction of a trifluoromethylated compound to enable the functionalisation of reductants to provide products of interest.

#### 4.1.1 Trifluoromethylation reagents

Fluorinated hydrocarbons have been used for a wide range of different applications. Fluorinated polymers are used in non-stick coatings due to their hydrophobic nature;<sup>270-272</sup> fluorinated molecules have proven to be useful in altering the properties of liquid crystal displays<sup>273, 274</sup> and fluorination of pharmaceuticals has been known to transform

the stability and barrier permeability of such compounds when compared to their unmodified analogues.<sup>275-278</sup> The late stage fluorination and trifluoromethylation of pharmaceutical compounds has been seen as an opportunity to use existing drug candidates and easily create new pharmaceutically relevant and potentially more active drugs.<sup>279-281</sup> As a result, the use of trifluoromethylation reagents has become a growing research area of interest.<sup>62, 282-288</sup>

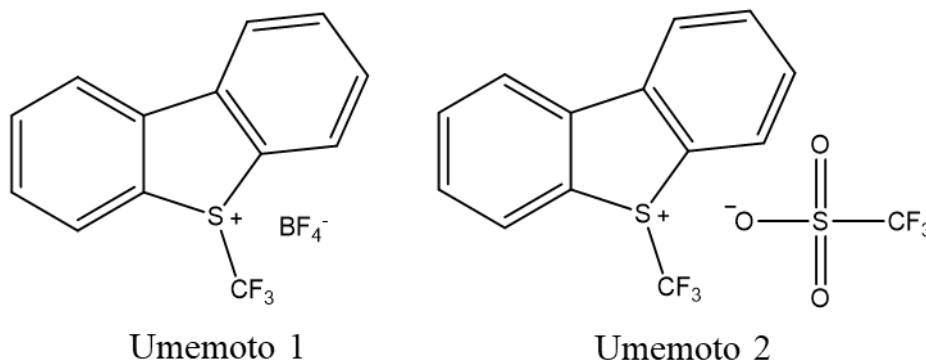


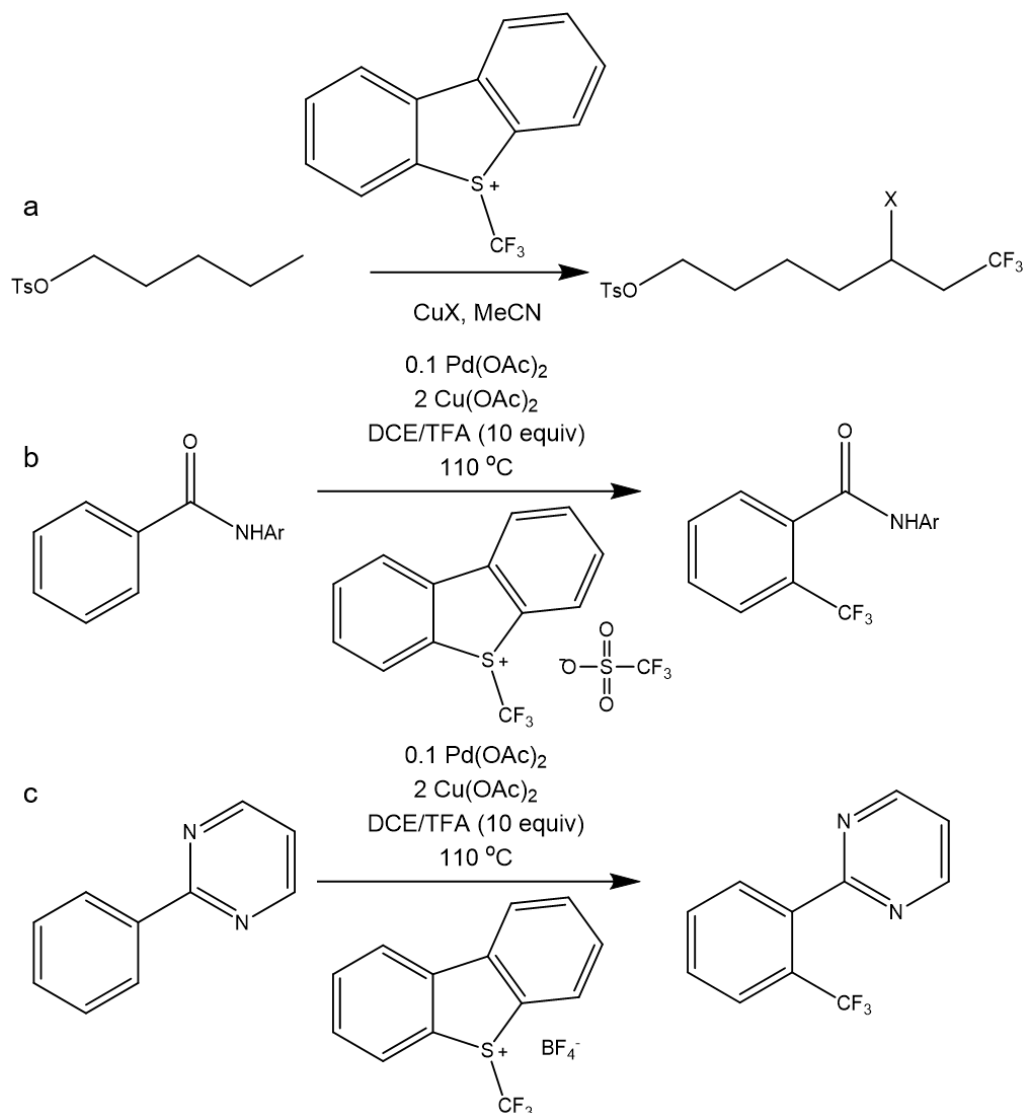
Figure 4.1 – The structures of trifluoromethylating reagents Umemoto 1 and Umemoto 2.

Umemoto's reagents are a series of *S*-trifluoromethyl diarylsulfonium salts which act as electrophilic trifluoromethylation reagents, Figure 4.1. Umemoto 1 and 2 are shelf-stable and have been shown to have low reduction potentials (ca. 0.0 V vs. NHE)<sup>283</sup> and as a result have found utility in the trifluoromethylation of alkenes, alkynes and aromatic rings, Scheme 4.2.

#### 4.1.2 Thermal trifluoromethylation with copper

Stoichiometric amounts of copper halide salts ( $\text{Cu}^{\text{I}}\text{X}$ ) have been used, in previously reported literature by An et al., in the reduction of Umemoto 1 which results in the formation of trifluoromethyl radicals. These radicals subsequently enabled the halotrifluoromethylation of terminal alkene functionalities bound to long chain aliphatics, Scheme 4.2a.<sup>284</sup> Miura et al. used stoichiometric quantities of copper acetate alongside catalytic quantities of palladium in order to achieve the direct thermal trifluoromethylation of aromatic rings. The *ortho* directed trifluoromethylation has been shown to occur via electrophilic addition of a formal  $\text{CF}_3^+$  species. This system has been used for the trifluoromethylation of benzyl amines (up to 83% yield) and phenyl amides (up to 94% yield) through the use of 10 mol% palladium ( $\text{Pd}^{\text{II}}$ ) acetate and 2 equivalents of copper ( $\text{Cu}^{\text{II}}$ ) acetate heated to 110 °C, Scheme 4.2b.<sup>287</sup> In addition, a similar system has been reported to trifluoromethylate the benzyl ring of phenyl-pyrimidines (up to 88% yield), Scheme 4.2c.<sup>286</sup> Although successful, these systems generally required elevated

temperatures and the excess use of copper species as well as the use of palladium catalysts that are expensive and difficult to recover and reuse from reaction mixtures.



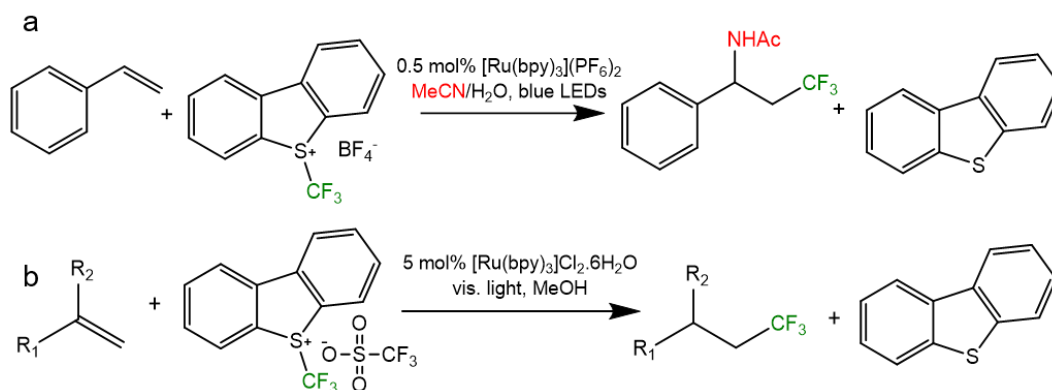
Scheme 4.2 – Literature examples of thermal trifluoromethylation reactions of alkenes and aromatics using Umemoto reagents.<sup>284, 286, 287</sup>

### 4.1.3 Photolytic trifluoromethylation

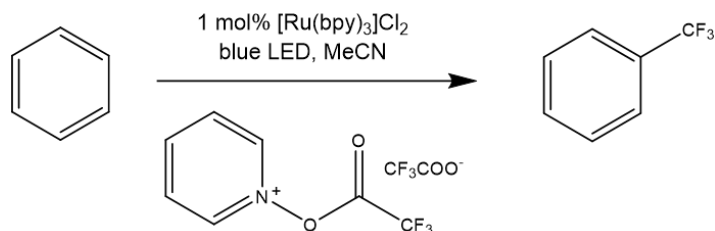
Homogeneous photocatalytic radical trifluoromethylation of alkenes has shown that it is possible to replace the high quantities of copper needed, in the thermally activated examples discussed, with catalytic amounts (often <1 mol%) of iridium and ruthenium photocatalysts, Scheme 4.3. Umemoto 1 was reduced by *fac*-[Ir(ppy)<sub>3</sub>] irradiated by blue LEDs in the presence of alcohols to achieve oxy-trifluoromethylation of alkenes, the alcohol acted as solvent, reductant and reactant in this reaction.<sup>283</sup> Styrenes have been amino-trifluoromethylated through the reduction of Umemoto 1 by blue LED light irradiated [Ru(bpy)<sub>3</sub>](PF<sub>6</sub>)<sub>2</sub> in an acetonitrile:water solvent mixture, acetonitrile also acted as a reactant in this system, Scheme 4.3a.<sup>62</sup> Unactivated alkenes have also been

## Chapter 4

hydrotrifluoromethylated by visible light irradiated  $[\text{Ru}(\text{bpy})_3]\text{Cl}_2 \cdot 6\text{H}_2\text{O}$  where the oxidation of methanol acted as a hydrogen source, Scheme 4.3b.<sup>288</sup>



Scheme 4.3 – Ruthenium centred photocatalysts used in trifluoromethylation reactions of alkenes with visible light and Umemoto reagents.<sup>62, 288</sup>



Scheme 4.4 – Trifluoromethylation of benzene with a ruthenium photocatalyst, irradiated with blue LED light, and a pyridinyl trifluoroacetyl ester.<sup>32</sup>

$[\text{Ru}(\text{bpy})_3](\text{PF}_6)_2$  irradiated with blue LED light has also been used to reduce a pyridinyl trifluoroacetyl ester made *in situ* from trifluoroacetic anhydride and pyridine-N-oxide,<sup>32</sup> Scheme 4.4. This system was used to trifluoromethylate a wide range of alkenes, alkynes, aromatic and heteroaromatic substrates and utilised a CF<sub>3</sub> source made from precursors that are significantly cheaper than commercially available Umemoto reagents. The use of these homogeneous photocatalysts has removed the need for high quantities of a copper initiator, however these reactions still required the use of rare and expensive metals such as ruthenium and iridium. These photocatalysts also cannot be easily recycled or reused. One example of a potentially recyclable, visible light active, heterogeneous photocatalyst used in trifluoromethylation was gC<sub>3</sub>N<sub>4</sub>, irradiated by a commercial Philips cool daylight energy-saving 60 W bulb, Scheme 4.5. This system was shown to reduce CF<sub>3</sub>SO<sub>2</sub>Cl (ca. +0.05 V vs NHE) in order to trifluoromethylate benzene and *N*-methylpyrrole; a 65 % yield was obtained for the trifluoromethylation of benzene in 60 h.<sup>72</sup>



Scheme 4.5 – The use of graphitic carbon nitride in the trifluoromethylation of benzene with  $\text{CF}_3\text{SO}_2\text{Cl}$  and visible light.

The use of a heterogeneous photocatalyst made of abundant elements such as those found in  $\text{gC}_3\text{N}_4$  in the radical trifluoromethylation of challenging substrates such as benzene with a cheap source of  $\text{CF}_3$ , such as  $\text{CF}_3\text{SO}_2\text{Cl}$  provides the state of the art for heterogeneous photocatalytic trifluoromethylation. However, the study of this slow trifluoromethylation reaction did not include the recycling of the photocatalyst used; used a light source without quoting the wavelength range or emission power and gave little mechanistic detail. Comparisons were made with other photocatalysts for this reaction and showed that  $\text{BiVO}_4$  was not active for the photocatalytic trifluoromethylation of benzene with  $\text{CF}_3\text{SO}_2\text{Cl}$  under the conditions used. However, no discussion was given with regards to the morphology and surface area of the  $\text{BiVO}_4$  used; which were shown to be significant factors in the heterogeneous photooxidation of benzyl alcohols in chapter 3.

Trifluoromethylating reagents such as pyridyl trifluoroacetyl ester or trifluoromethane sulfonyl chloride are significantly cheaper and therefore more viable in larger scale trifluoromethylations than the use of reagents such as Umemoto 1 and 2.<sup>32, 72</sup> However, both trifluoroacetic anhydride and trifluoromethane sulfonyl chloride react violently with water<sup>32, 72</sup> and so are both much less stable than the Umemoto reagents:<sup>289</sup> great care is needed in the use of these reagents. The ideal trifluoromethylating starting material would be trifluoroacetic acid, the oxidation of which could generate  $\text{CF}_3$  radicals through decarboxylation.<sup>32</sup> However, the oxidation potential of trifluoroacetic acid is  $>2.5$  V vs. NHE.<sup>22</sup> This oxidation potential is even more positive than the valence band of bismuth vanadate ( $+2.4$  V vs NHE)<sup>210</sup> which is one of the most oxidising semiconductors. As a result, it is unlikely that heterogeneous photocatalysis would be able to achieve trifluoromethylation through the oxidation of trifluoroacetic acid.

The lack of the extensive use and study of different heterogeneous photocatalysts in the trifluoromethylation of a range of substrates provides an opportunity. Bismuth containing semiconducting photocatalysts, such as  $\text{Bi}_2\text{WO}_6$  and nan- $\text{BiVO}_4$ , have the capacity to absorb large amounts of visible-light irradiation and have conduction band potentials

which suggest that these materials are capable of reducing trifluoromethylating reagents such as Umemoto's reagents with the purpose of selective trifluoromethylation. The use of heterogeneous photocatalysts in trifluoromethylation reactions is currently largely unexplored, and as such, it was of interest to investigate whether bismuth containing semiconducting photocatalysts could be employed for this application.

#### 4.1.4 Objectives

The objective of the work discussed in this chapter is:

- To explore whether selective chemical transformations can be achieved using other oxidants, such as trifluoromethylation reagents, as a source of additional functionality

## 4.2 Trifluoromethylation

### 4.2.1 Reduction of Umemoto 1 for the trifluoromethylation of styrene

To examine whether it was possible to reduce Umemoto's reagents with bismuth containing semiconductors, both  $\text{Bi}_2\text{WO}_6$  and nan- $\text{BiVO}_4$  (0.1 mmol) were dispersed in methanol (10 mL) and irradiated with blue LED light for 12 h in the presence of styrene (0.1 mmol) and Umemoto 1 (0.2 mmol). Styrene was chosen as a substrate for  $\text{CF}_3$  radical detection as the phenyl ring adjacent to the alkene functionality provided an electron rich environment that reacts rapidly with a  $\text{CF}_3$  radical.<sup>62, 283, 288</sup> Centrifugation was used to remove the photocatalysts and reaction mixtures and products were extracted into DCM; this DCM solvent was later removed *in vacuo*. The remaining mixtures was taken into  $\text{CDCl}_3$  for NMR analysis, a known amount of fluorobenzene was also added to be used as a standard in quantifying yields. From both reactions,  $^1\text{H}$  and  $^{19}\text{F}$  NMR were consistent with the presence of trifluoromethylated products suggesting that both photocatalysts were able to reduce Umemoto 1 and therefore generate  $\text{CF}_3$  radicals. The spectra suggested that compound **4.1**, Figure 4.2, was the major product with both the use of nan- $\text{BiVO}_4$  and  $\text{Bi}_2\text{WO}_6$ . This characterisation was consistent with that reported in literature by Novak et al. for compound **4.1**.<sup>290</sup>

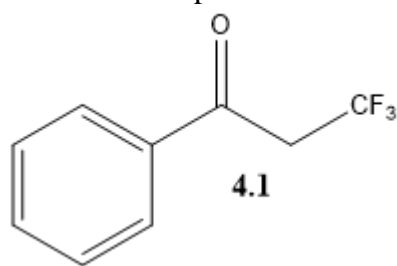


Figure 4.2 – The major product of the oxytrifluoromethylation of styrene using blue light irradiated nan-BiVO<sub>4</sub> or Bi<sub>2</sub>WO<sub>6</sub> and Umemoto 1.

A triplet in the <sup>19</sup>F NMR spectrum at a chemical shift of -62.0 ppm and a quartet in the <sup>1</sup>H NMR spectrum at a chemical shift of 3.80 ppm both with the same coupling constants,  $J = 10.1$  Hz, were consistent with a methylene group adjacent to a trifluoromethyl group. The chemical shift of the methylene group has also been shifted downfield due to the presence of the adjacent carbonyl group. Peaks with chemical shifts of 7.52, 7.62 and 7.92 ppm respectively were consistent with an aryl ring adjacent to a carbonyl functionality; these peaks show proportionate peak integrations compared to the quartet at 3.80 ppm. The presence of other triplets in the <sup>19</sup>F NMR spectra of the reaction mixtures, split by similar coupling constants to those observed in the major product, suggested that other trifluoromethylated compounds with adjacent methylene groups were formed during these reactions. The chemical shifts of these triplets were -63.8, -63.4, and -63.5 ppm and were observed with both the use of irradiated nan-BiVO<sub>4</sub> and Bi<sub>2</sub>WO<sub>6</sub>. These signals were consistent with the previous literature data by Yang et al. for compounds **4.2**, **4.3** and **4.4**, respectively, Figure 4.3.<sup>291</sup> The 2 chiral centres identified in the scheme below (\*) result in the formation of diastereoisomers, which was why 2 separate triplets are observed in the <sup>19</sup>F NMR.

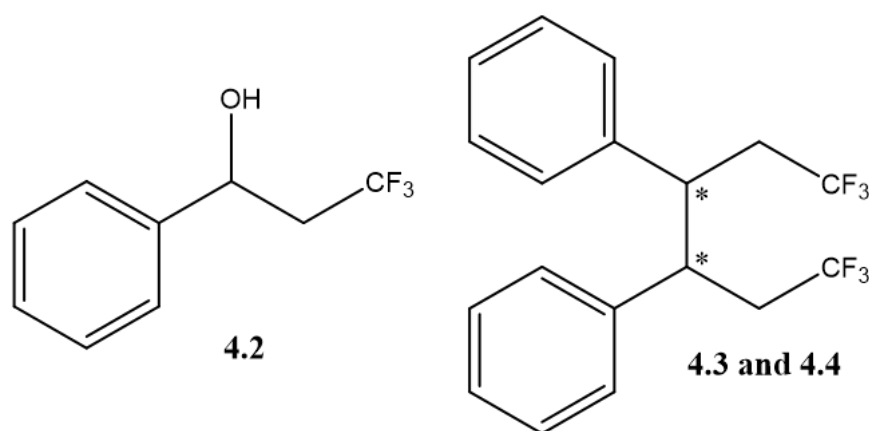
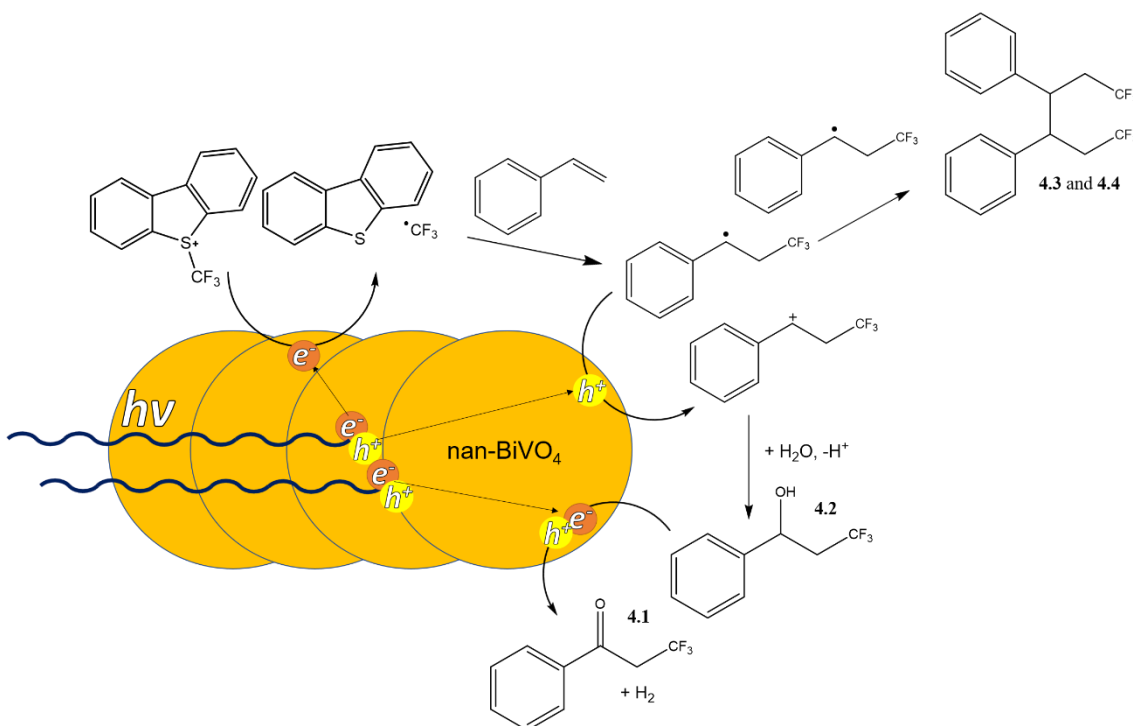


Figure 4.3 – Structures of compounds **4.2**, **4.3** and **4.4** that are byproducts in the formation of compound **4.1**.



## Chapter 4

The high amounts of coupling interactions between proton environments in compounds **4.2**, **4.3** and **4.4** and the low integrations for these compounds in the  $^{19}\text{F}$  NMR meant that signals consistent with these compounds were not detectable in the  $^1\text{H}$  NMR spectra. With the use of nan- $\text{BiVO}_4$ , the yields for **4.2**, **4.3** and **4.4** were 3%, 7% and 7% respectively, calculated against a known concentration of fluorobenzene used as a standard in the  $^{19}\text{F}$  NMR. Yields throughout this work were calculated using Equation 2.5. The observation of these signals in the  $^{19}\text{F}$  NMR presence was useful when proposing a mechanism for the formation of **4.1**, Scheme 4.6. The reduction of Umemoto 1, by photoelectrons generated through the absorption of visible light photons in the semiconductor, released a  $\text{CF}_3$  radical which bound onto the terminal carbon of the alkene group in styrene. This resulted in the formation of a secondary radical adjacent to the phenyl ring; the dimerization of this intermediate resulted in the formation of **4.3** and **4.4**. This intermediate could be oxidised again to form a cation which was then capable of reacting with water (present in the reaction mixture either from adsorption to the catalyst surface or from residue amounts found in the methanol solvent) to form the alcohol **4.2** and this alcohol was then oxidised again, by holes trapped at the surface of the irradiated photocatalyst, to form the ketone **4.1**.



Scheme 4.6 – Proposed mechanism for the formation of products observed in the trifluoromethylation of styrene via the reduction of Umemoto 1 with blue LED light irradiated nan- $\text{BiVO}_4$

## Chapter 4

As nan-BiVO<sub>4</sub> produced the highest yield for **4.1** (31% in comparison to 22% with the use of Bi<sub>2</sub>WO<sub>6</sub>, these were NMR yields obtained against a fluorobenzene standard), the reaction with nan-BiVO<sub>4</sub> was repeated with a 9:1 methanol:deionised water solvent mixture. This reaction supported the proposed mechanism as the increased concentration of water resulted in only the formation of the major product **4.1**; NMR yield of **4.1** against fluorobenzene = 88%; only traces of products **4.2**, **4.3** or **4.4** was observed. It may be expected that the addition of water would also increase the yield of compound **4.2**. However, it can be suggested that the addition of water could have increased the number of hydroxyl groups on the surface of nan-BiVO<sub>4</sub>.<sup>292</sup> This could have decreased the likelihood of alcohol desorption as the alcohol would have strong hydrogen-bonding interactions with these hydroxyl groups.<sup>292</sup> The decreased alcohol desorption would allow for effective oxidation to the corresponding ketone, **4.1**.

Control experiments also supported the proposed mechanism as none of the products discussed above were evidenced in the absence of irradiation or the absence of a photocatalyst suggesting that both light and photocatalyst were required for this photocatalytic trifluoromethylation to occur.

To the knowledge of this author, no other photocatalytic trifluoromethylation of alkenes has resulted in the selective formation of products containing a ketone functionality such as that observed in the formation of compound **4.1**. The selective formation of alcohol products similar to compound **4.2** was observed with the use of 5 mol% *fac*-Ir(ppy)<sub>3</sub> and [Ru(bpy)<sub>3</sub>](PF<sub>6</sub>)<sub>2</sub> irradiated with blue LEDs with the presence of water and Umemoto's reagent.<sup>283</sup> The only known work that resulted in the formation of trifluoromethylated products that also contained adjacent ketone functionalities, similar to compound **4.1**, involved the trifluoromethylation of  $\alpha$ -haloketones with a nucleophilic Cu<sup>I</sup>CF<sub>3</sub> species.<sup>290</sup> Unlike the work described above, the ketone functionality was not synthesised in the trifluoromethylation reaction. In addition, the Cu<sup>I</sup>CF<sub>3</sub> species needed for this work was synthesised with the use of strong bases to cuperate fluoroform (CHCF<sub>3</sub>).<sup>293</sup> As a result, it can be said that there are many advantages to the heterogeneous photocatalytic oxytrifluoromethylation described in this thesis over previous work that resulted in the selective formation of compound **4.1**.

The work described above has shown that it was possible to carry out heterogeneous photocatalytic trifluoromethylation via the reduction of an Umemoto reagent using visible light irradiated bismuth containing semiconductors. However, as it has been reported that trifluoromethylation reactions of alkenes have been carried out by the use of cheap and

widely available reagents such as copper salts,<sup>284,285</sup> it was decided that this work should be extended to trifluoromethylation of more challenging substrates.

#### 4.2.2 Reduction of Umemoto 1 for the trifluoromethylation of aromatics

The trifluoromethylation of benzene was attempted using stoichiometric quantities of Umemoto 1 and 10 mol% nan-BiVO<sub>4</sub>, dispersed in methanol and irradiated by blue LEDs. After irradiation for 24 h, centrifugation to remove photocatalyst, a DCM extraction and a subsequent flash silica column in pet ether to remove unreacted Umemoto 1, the products were taken up in CDCl<sub>3</sub> for <sup>1</sup>H and <sup>19</sup>F NMR analysis. The <sup>19</sup>F NMR gave 4 singlet peaks of similar intensities,  $\delta = -62.9, -61.6, -61.4$  and  $-60.7$  ppm and the <sup>1</sup>H NMR spectra showed a complicated mixture of peaks in the aromatic region. These data suggested that trifluoromethylation of aromatics had occurred, however none of the peaks in the <sup>1</sup>H NMR were consistent with the desired trifluorotoluene product.<sup>294</sup>

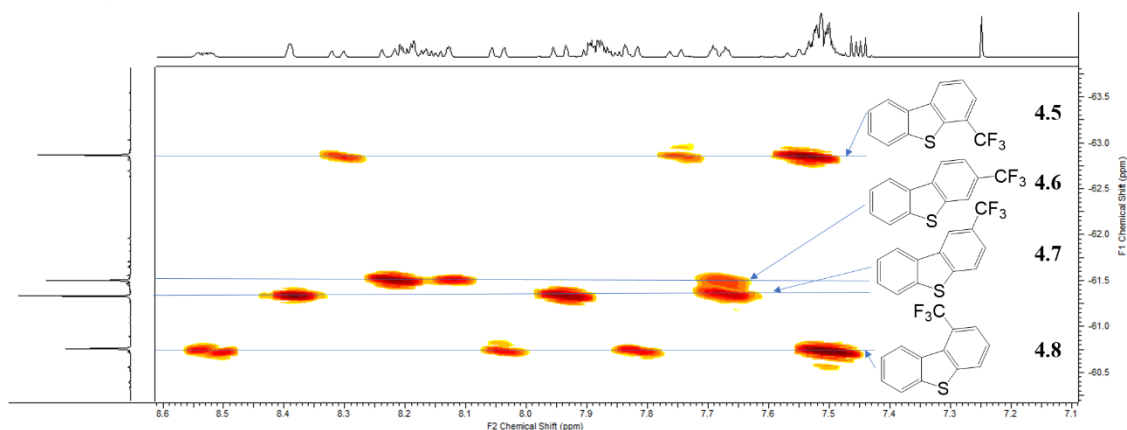
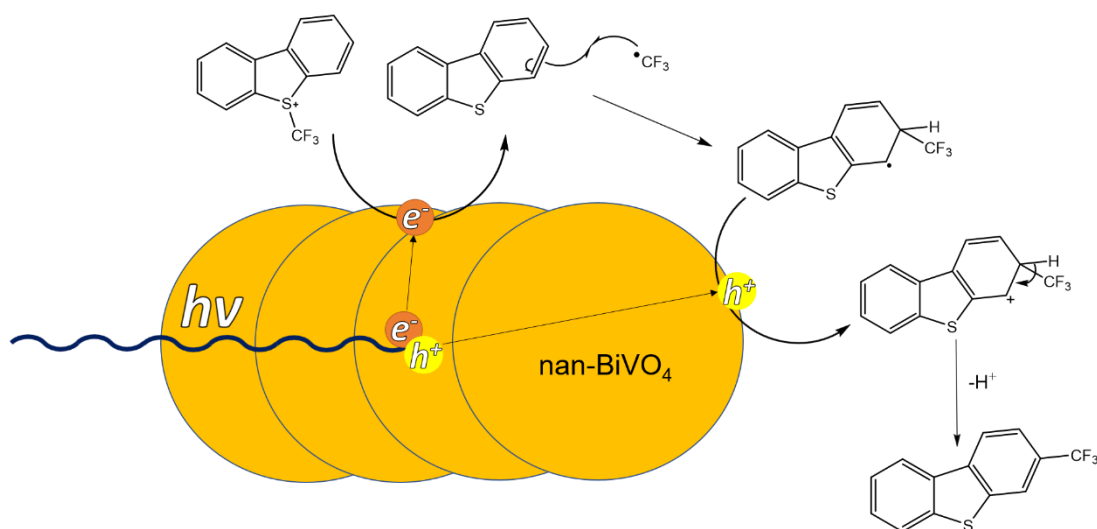


Figure 4.4 – H-F HMBC (500 MHz, CDCl<sub>3</sub>) for a mixture of compounds **4.5**, **4.6**, **4.7** and **4.8** formed from the reduction and rearrangement of Umemoto **1** by blue LED light irradiated nan-BiVO<sub>4</sub>

To try and characterise the <sup>1</sup>H NMR peaks, a <sup>1</sup>H-<sup>19</sup>F 2D HMBC experiment was carried out, Figure 4.4. It was found that coupling interactions existed between the aromatic proton environments and the fluorine environments, showing that trifluoromethylation of aromatic species had occurred. In addition, it was possible to use these coupling interactions to suggest compounds whose structures were consistent to each of the fluorine environments. It was found that the 4 fluorine environments were consistent with each of the possible isomers of mono-substituted trifluoromethyl dibenzothiophene, i.e. reduced and rearranged Umemoto reagent, compounds **4.5** – **4.8**.<sup>295</sup> Very few previously reported examples of the formation of compounds **4.5** – **4.8** could be found.<sup>295, 296</sup>

Compounds **4.5** – **4.8** were observed as minor by-products from the photocatalytic direct trifluoromethylation of glycals using *fac*-Ir(ppy)<sub>3</sub> and visible light by B. Wang et al.<sup>295</sup>

These trifluoromethylated compounds formed in this reaction because the reduction of Umemoto 1, by photoelectrons in the semiconductor, led to the formation of an electron rich aromatic species, dibenzothiophene. This dibenzothiophene reacted more rapidly with an electron deficient trifluoromethyl radical than benzene, Scheme 4.7. It could also be suggested that adsorption of dibenzothiophene via the S atom to the surface of nan-BiVO<sub>4</sub> accelerated the formation of compounds **4.5** – **4.8**.



Scheme 4.7 – Proposed mechanism for the trifluoromethylation of dibenzothiophene from the reduction of Umemoto's reagent by blue light irradiated nan-BiVO<sub>4</sub>. The formation of compound **4.6** is given here as an example.

It was decided that the quantification of these product yield would not be attempted as these products were considered as by-products different to the desired product from the reaction system. As the reduction of Umemoto's reagents would always produce this electron rich aromatic species, it was decided that trifluoromethylation of aromatics should be attempted with other trifluoromethylating reagents that contain an electron deficient aromatic species that is unlikely to react with electron deficient trifluoromethyl radicals.

#### 4.2.3 Attempted reduction of pyridyl trifluoroacetyl ester for the trifluoromethylation of aromatics

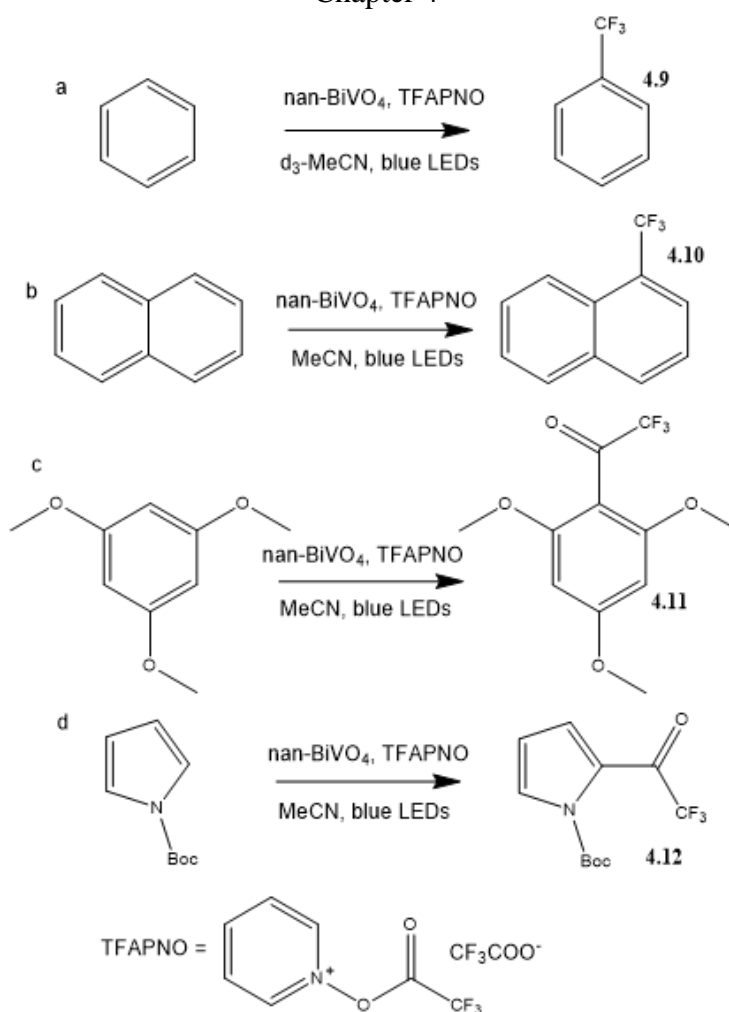
It has been shown that pyridyl trifluoroacetyl ester acts as a trifluoromethylating reagent that can be made from readily available and cheap reagents; trifluoroacetic anhydride and

pyridine-*N*-oxide.<sup>32</sup> In contrast to Umemoto's reagents, the reduction of this pyridyl trifluoroacetyl ester produced pyridine, carbon dioxide and a CF<sub>3</sub> radical. As an electron deficient pyridine was produced, in contrast to the electron rich dibenzothiophene, the by-product pathway involving the addition of the CF<sub>3</sub> radical into the aromatic species formed from oxidant reduction should be much less competitive than the addition of the CF<sub>3</sub> radical into aromatics such as benzene.

As a result, the use of pyridyl trifluoroacetyl ester, made *in situ* from pyridine-*N*-oxide and trifluoroacetic anhydride, for the reductive trifluoromethylation of benzene was attempted using blue light irradiated nan-BiVO<sub>4</sub> dispersed in dry deuterated acetonitrile, Scheme 4.8a. Deuterated solvent was used so that the reaction could be analysed without workup. A four times excess of benzene, relative to the amount of pyridyl trifluoroacetyl ester, was also used. After 20 h irradiation, <sup>1</sup>H and <sup>19</sup>F NMR spectra both gave peaks consistent with the formation of the desired product, trifluorotoluene (**4.9**).<sup>297</sup> The percentage yield of trifluorotoluene (**4.9**) was found to be ca. 30%, obtained using the aromatic <sup>1</sup>H NMR peak consistent with benzene and assuming selective trifluorotoluene formation. Analogous control experiments run in the dark at 40 °C and with irradiation but no photocatalyst resulted in 0% and trace trifluorotoluene formation respectively, suggesting that both light and nan-BiVO<sub>4</sub> were essential for this trifluoromethylation reaction.

To explore the scope of this reaction, other electron rich aromatic species were used as substrates in this trifluoromethylation reaction. Stoichiometric amounts of electron rich aromatic substrates were used, relative to the amount of pyridyl trifluoroacetyl ester, with 20 mol% nan-BiVO<sub>4</sub> dispersed in dry acetonitrile; each reaction was irradiated for 24 h. The trifluoromethylation of naphthalene resulted in the formation of 26% of compound **4.10**, Scheme 4.8b.<sup>298</sup> However, the attempted trifluoromethylation reactions of 2,4,6-trimethoxybenzene and *N*-*boc*-pyrrole did not give the expected trifluoromethylated products as the formation of the corresponding Friedel-Crafts products were out-competing the formation of the desired products. The major products of these reactions were compounds **4.11**, Scheme 4.8c, and **4.12**, Scheme 4.8d, respectively,<sup>299-301</sup> the yield of compound **4.11** was 77% and the yield of compound **4.12** was 14%. These products were as a result of trifluoroacylation and could simply be described by a Friedel-Crafts reaction mechanism.

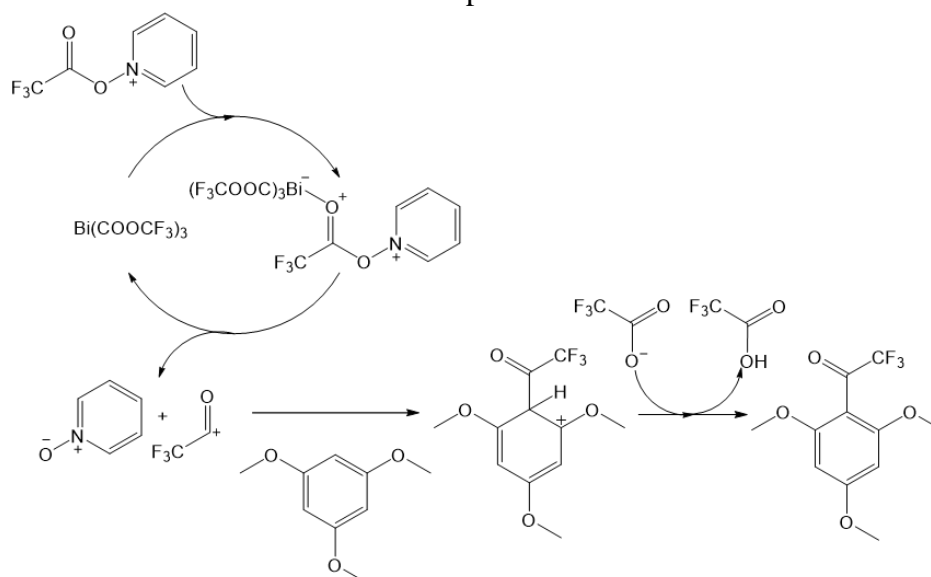
## Chapter 4



Scheme 4.8 – The use of irradiated nan-BiVO<sub>4</sub> in trifluoromethylation and trifluoroacylation of aromatics

### 4.2.4 Catalyst degradation

Bi(III) has been previously reported to act as a Lewis acidic homogeneous catalyst for Friedel-Crafts reactions.<sup>302, 303</sup> It was reported that bismuth triflate can catalyze the benzoylation of aromatics with benzoic anhydride.<sup>302</sup> Bismuth triflate has also been used in the intramolecular Friedel-Crafts cyclisation of tertiary alcohols.<sup>303</sup> It is possible that bismuth leached into solution during these reactions as a result of the degradation of the nan-BiVO<sub>4</sub> and was therefore been able to carry out Friedel-Crafts acylation, Scheme 4.9.



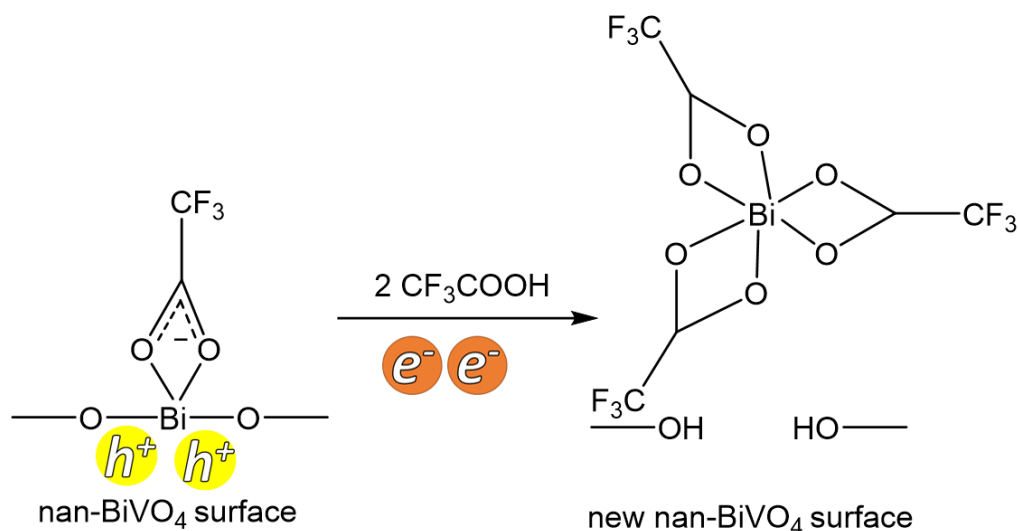
Scheme 4.9 – The proposed mechanism for bismuth catalyzed Friedel-Crafts acylation of 2,4,6-trimethoxybenzene to form compound **4.10**

The colours of the reaction mixtures after irradiation suggested that catalyst degradation had occurred as each reaction was a colour consistent with vanadium solutions in various oxidation states.<sup>304, 305</sup> The trifluoromethylation of benzene and naphthalene resulted in a green coloured solution consistent with  $\text{V}^{3+}$  and the trifluoroacylation of trimethoxybenzene and *N*-*boc*-pyrrole resulted in dark blue (consistent with  $\text{V}^{4+}$ ) and dark red (consistent with  $\text{V}^{5+}$ ) coloured solutions respectively. ICP-MS confirmed the presence of vanadium and bismuth in the reaction mixtures from the attempted trifluoromethylation of naphthalene and also found that bismuth was present in concentrations ca. 7 times that of vanadium ( $[\text{}^{209}\text{Bi}] = 10,000 \text{ ppm}$ ,  $[\text{}^{51}\text{V}] = 1,500 \text{ ppm}$ ). XRF showed a higher ratio of V:Bi (3:2) present at the nan- $\text{BiVO}_4$  surface after use in these attempted trifluoromethylation reactions when compared to unused photocatalyst suggesting that more bismuth had been removed from the catalyst than vanadium.

These data suggested that removal of bismuth from the photocatalytic material was the principal reason for catalyst degradation during this reaction. It can be suggested that the trifluoroacetate anions, that formed as the counterion to the pyridyl fluoroacetyl ester, played a significant role in the degradation of nan- $\text{BiVO}_4$  as these anions could bind strongly to  $\text{Bi}^{3+}$  cationic centres.<sup>306</sup> The dark control experiment discussed above showed no evidence of photocatalyst degradation, so it could also be suggested that the photocatalyst only degrades under irradiation.

A proposed mechanism, Scheme 4.10, for photolytic degradation involves hole accumulation at the surface will leads to charge build up. This charge builds up can be

relieved by the loss of  $\text{Bi}^{3+}$ . However, the loss of bismuth does not occur without the presence of trifluoroacetic acid in solution. Trifluoroacetic acid provides protons to hydrolyse Bi-O bonds and then binds to free bismuth once in solution; this results in the formation of a stable  $\text{Bi}^{3+}(\text{CH}_3\text{COO}^-)_3$  complex. The presence of vanadium in solution could be simply as a result of significant bismuth loss resulting in complete destabilisation of the surface of nan- $\text{BiVO}_4$ .



Scheme 4.10 – An illustration showing a scheme for the photolytic degradation of nan- $\text{BiVO}_4$  into the Bi centred Friedel-Craft catalyst

As the fluorination of substrates was probably driven by a Friedel-Crafts reaction and not through redox chemistry associated to electron-hole separation in an irradiated semiconductor, no more work was carried out with regards to attempted trifluoromethylation using the pyridyl trifluoroacetyl ester, including the isolation of previously discussed products. Other simple trifluoromethylation reagents, such as trifluoromethanesulfonyl chloride and sodium triflate, were also used alongside nan- $\text{BiVO}_4$  and  $\text{Bi}_2\text{WO}_6$  in attempted photocatalytic trifluoromethylation reactions. However, the lack of observation of any fluorinated products, via  $^{19}\text{F}$  NMR, indicated that these reactions were unsuccessful and so no further work was carried out on these reactions.

For future work into the successful trifluoromethylation of aromatic substrates through the use of visible light absorbing bismuth containing semiconductors, an appropriate trifluoromethylating reagent will be needed that: has an appropriate reduction potential relative to the semiconducting materials used; does not contain electron rich aromatic rings that can also be trifluoromethylated and also is compatible with the maintenance of the catalyst surface. Future work could also explore adapting the semiconductor surface to make the photocatalyst more tolerant to degradation. Beyond this, semiconductor



adaptation can provide more opportunities to achieve selective chemical transformations, it was with this in mind that the work described in chapter 5 was carried out.

### **4.3 Conclusions**

The work outlined in this chapter met the objective set to explore whether it is possible to use bismuth containing semiconductors to reduce oxidants and therefore incorporate valuable functionality from these oxidants into the structure of a useful desired product. This was successfully achieved using simple systems involving the trifluoromethylation of electron rich alkenes, but was less successful at forming desired trifluoromethylated aromatic compounds.

This contributed to the overall aim of this thesis by broadening the scope for bismuth containing semiconductors within the field of heterogeneous photocatalysis by showing that these materials can be used in trifluoromethylation reactions. This work also contributes to developing our understanding of how strongly acidic carboxylic acids interact and degrade the surface of bismuth vanadate. This guides further work in this field as it leads to the exploration of methods that can be used to avoid this and, as it will be seen in Chapter 5, can also lead to opportunities to use these bismuth containing heterogeneous photocatalysts in currently unexplored reaction systems.

## 5 Photo-Kolbe and Photo-Giese Chemistry with Platinised Bismuth-containing Semiconductors

### 5.1 Introduction

#### 5.1.1 Photocatalyst adaptation

As previously observed in chapters 2, 3 and 4, visible light absorbing bismuth-containing semiconductors such as  $\text{BiVO}_4$  and  $\text{Bi}_2\text{WO}_6$  were capable of carrying out benzyl alcohol oxidation and the trifluoromethylations upon visible light irradiation. Literature, from Zhang et al. and from Yuan et al. separately, has also shown that these catalysts can be used for benzyl amine oxidation.<sup>22, 24</sup> However, the number of species that can adsorb to these unmodified photocatalysts, undergo a redox reaction and then desorb effectively without further reaction and result in the formation of one product with high selectivity is limited. The modification of a semiconducting surface with a cocatalyst can allow for substrates to adsorb to this surface differently. This change in binding can drastically alter selectivity as these different interactions provide opportunities to exploit different reaction pathways.<sup>133, 307-312</sup> In addition, a cocatalyst at the surface of a material can have a significant impact on charge transfer which can drastically improve conversion rates when compared to an unmodified photocatalyst.<sup>210, 313, 314</sup>

In the field of water splitting for the generation of solar fuels, the addition of a catalytic amount of  $\text{CoP}_1$  to a  $\text{BiVO}_4$  electrode increased the amount of oxygen production and photocurrent by ca. 15 times over the bare  $\text{BiVO}_4$  electrode (from  $0.2 \text{ mA cm}^{-2}$  to  $3.0 \text{ mA cm}^{-2}$  and from ca.  $8 \mu\text{mol O}_2$  produced to  $100 \mu\text{mol O}_2$  produced after 6 h) at 1.23 V vs. NHE under AM1.5 irradiation ( $400 \text{ mW cm}^{-2}$ ), Figure 5.1.<sup>314, 315</sup> A nanoporous bismuth vanadate electrode coupled with  $\text{FeOOH}$  and  $\text{NiOOH}$  achieved stoichiometric  $\text{O}_2$  formation with 90% photocurrent to  $\text{O}_2$  conversion and a photocurrent of  $2.7 \text{ mA cm}^{-2}$  at 0.6 V vs RHE under AM1.5 irradiation, the electrode without the iron and nickel oxy hydroxide produced a photocurrent of roughly  $0.2 \text{ mA cm}^{-2}$  under analogous conditions.<sup>316</sup>

Adding a cocatalyst to the surface of a semiconducting material have been successful in changing the efficiencies and selectivities of photocatalysts for a wide range of applications.<sup>210, 313, 314</sup> However, the addition of metal nanoparticles to a semiconducting surface is the technique most used in improving a photocatalyst for use in selective chemical transformations.

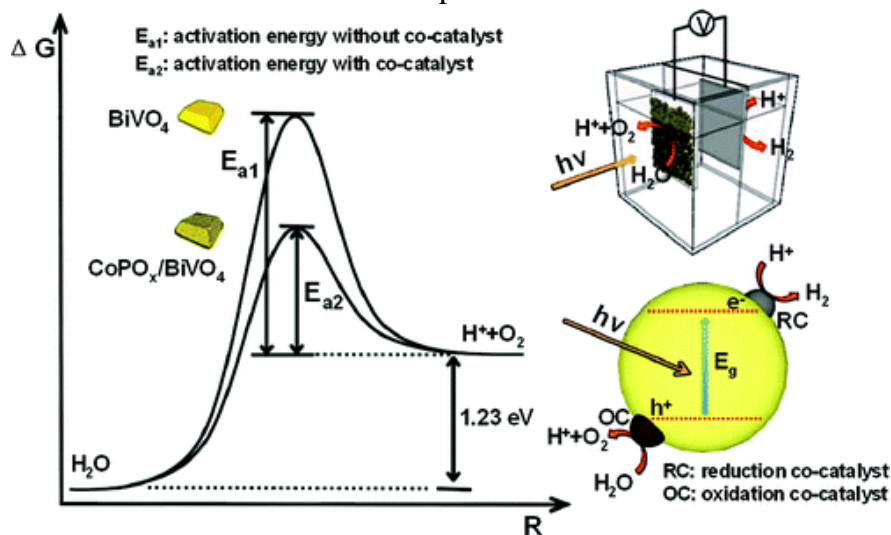


Figure 5.1 – Representation of the CoPi:BiVO<sub>4</sub> electrodes synthesised by Wang, Li et al. Reprinted with permission from C. Li, *J. Phys. Chem. C.*, 2012, **116**, 5082-5089. Copyright 2012 American Chemical Society.<sup>4</sup>

The interface between metal to a semiconductor creates a Schottky barrier due to the pinned Fermi level of the metal. Upon irradiation, this Schottky barrier ensures the one directional movement of photoexcited electrons to the surface bound metal species and therefore minimises electron-hole recombination, Figure 5.2. As a result, photocatalysts with surface bound metal nanoparticles have been reported to be more effective than unmodified photocatalysts in systems that are already capable of achieving selective chemical transformation.<sup>75, 317</sup>

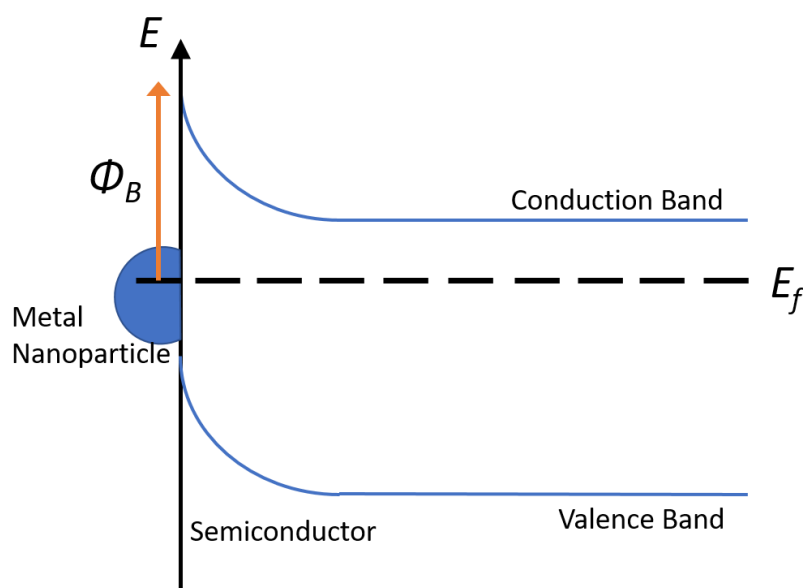


Figure 5.2 – An illustration of the Schottky barrier that forms at the interface of a semiconductor and a metal nanoparticle.

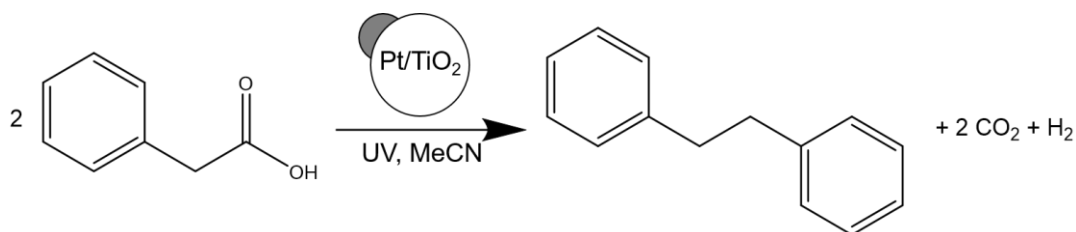
## Chapter 5

In previously reported work, noble metal nanoparticle deposition has been shown to have a significant impact of the selectivity of photocatalysts.<sup>84, 255, 311, 312, 318, 319</sup> Platinum nanoparticles on the surface of titania have both been used to synthesise nitroso compounds with up to 90% selectivity from amines upon irradiation with visible light from a Xe arc lamp and a >450 nm filter; without the presence of platinum, azo compounds were synthesised selectively.<sup>312</sup> In addition, platinised titania has been utilised in selective dehalogenation and cyclization reactions using visible light irradiation. 0.2% Pt on titania was found to be optimal for the dehalogenation of iodobenzene derivatives under irradiation from a Luzchem solar simulator with a 375 nm filter, diisopropylethylamine was needed as a sacrificial hole acceptor for this reductive chemistry to occur. The same photocatalytic systems were then used to achieve the cyclisation of alkenyl iodide compounds.<sup>311</sup> Visible light irradiated titania (>405 nm) coupled with palladium nanoparticles have been used to photocatalyse the C-C bond cross coupling of aromatics and acetonitrile to form benzyl cyanide compounds with high selectivities (92%).<sup>318</sup> Unmodified titania resulted in the unselective degradation of the starting materials. C-H bond activation of ethers and subsequent aryl C-C cross coupling reactions have been reported, by Tyagi et al., with similar Pd(0) nanoparticles supported by a titanium dioxide photocatalyst irradiated with a Xe lamp with a >350 nm filter, all coupled products were generated with a 99% selectivity.<sup>319</sup>

### 5.1.2 Photo-Kolbe chemistry

One particularly interesting example of achieving selectivity with platinised titania is in Photo-Kolbe chemistry. Kolbe chemistry was first utilised as an electrochemical method to decarboxylate carboxylic acids yielding alkyl radicals that then dimerise.<sup>320</sup> The platinum electrodes drove the reduction of protons to form dihydrogen which allowed for oxidative decarboxylation of carboxylic acids, loss of carbon dioxide then subsequent dimerization. It has been shown that Photo-Kolbe chemistry, using photocatalysis with platinum nanoparticles deposited onto the surface of titanium dioxide under UV irradiation, to dimerise a wide range of different carboxylic acids is possible, Scheme 5.1.<sup>321</sup> Titania under UV irradiation (emitted from UVA sunlamp arrays, 8 x 15 W,  $\lambda_{\text{max}} \approx 350$  nm) has been used to oxidise carboxylate anions of phenylacetic acid to a radical anion. Carbon dioxide was lost from the radical anion to form benzyl radicals that subsequently add to electron deficient alkenes, such as maleic anhydride.<sup>30</sup> Titania was not a selective photocatalyst for a wide range of substrates and is only capable of oxidising oxyacetic acids to give moderate yields (>40%) of the products derived from

decarboxylative coupling to electron deficient alkenes. The attempted dimerization of other carboxylic acids with unmodified titania resulted in unselective mineralization.<sup>30</sup>



Scheme 5.1 – Photo-Kolbe dimerization of phenylacetic acid to bibenzyl, carbon dioxide and hydrogen by UV light irradiated platinumised titanium dioxide.

Like in Kolbe electrochemical systems, the platinum nanoparticles catalysed the selective formation of dihydrogen in dimerization reactions, this reduced the formation of species associated to mineralization such as  $\bullet\text{OH}$  radicals. Carboxylate anions are therefore allowed to be oxidised on the surface of titania selectively forming benzyl radicals. This showed that platinumised titania was able to act as a selective photocatalyst for Photo-Kolbe reactions.

Alternative methods of achieving similar C-C coupling reactions can be found in homogenous thermal palladium catalysed cross coupling which significantly expanded the variety of organic products that could be synthesised with relative ease.<sup>322-325</sup> However, nucleophilic coupling reagents that are capable of binding to the Pd centre are required for these reactions, these reagents include Grignards, stannanes and boronic acids.<sup>326</sup> Photo-Kolbe chemistry provides a method of achieving C-C bond formation without such reagents and instead requires simple carboxylic acids. Other methods of generating radicals from carboxylic acids exist for use in a thermally activated homogeneous system. However, these methods involve the use of harmful and difficult to prepare precursors including diacyl peroxides, Hunsdieker salts<sup>327</sup> or Baron esters.<sup>30, 328</sup>

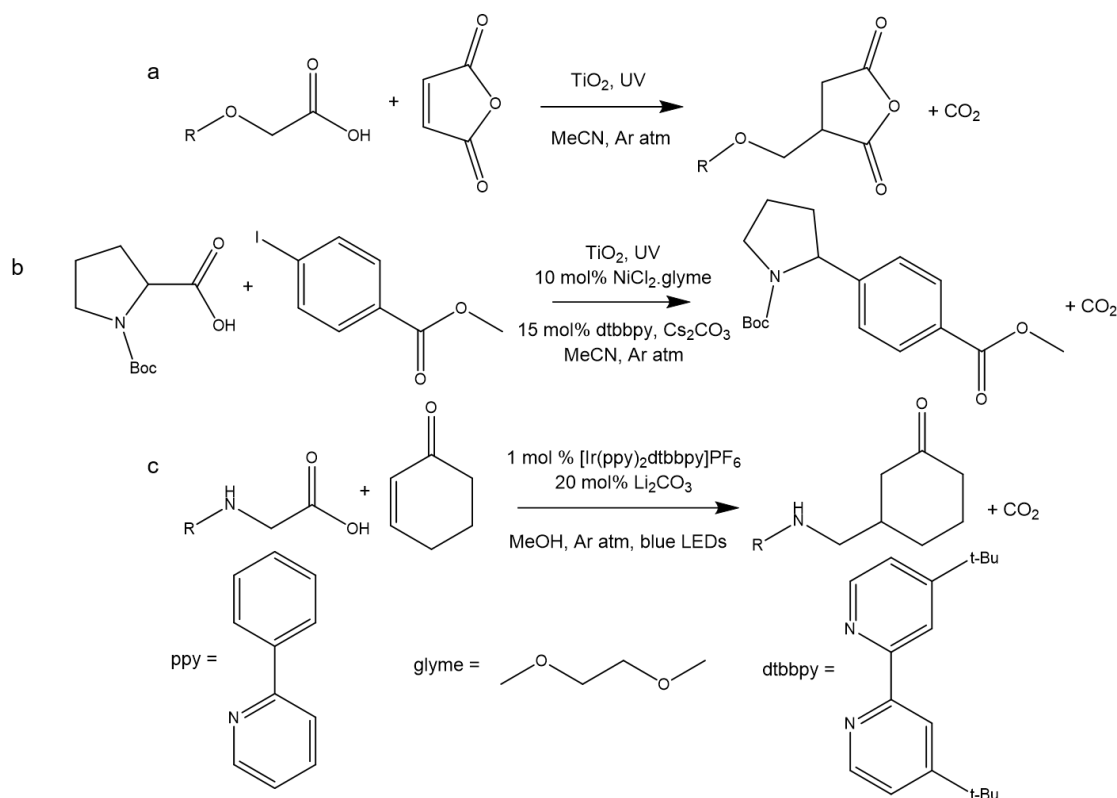
### 5.1.3 Visible light absorption and Photo-Giese chemistry

Visible light irradiation of platinumised titania does not lead to decarboxylation of carboxylic acids in the presence of this platinumised titania photocatalyst. No solely heterogeneous photocatalytic system irradiated with visible light has been utilised for Kolbe-like chemistry. Successful platinumization of a bismuth containing semiconductor could utilise visible light to achieve this Photo-Kolbe chemistry. Although the dimerised products of

## Chapter 5

Photo-Kolbe chemistry are not of particular interest, the creation of carbon centred radicals could be utilised further in other more interesting coupling reactions.

The decarboxylative oxidation of phenylacetic acid forms an electron rich benzyl radical.<sup>321</sup> Giese reactions involve an addition reaction between an electron rich radical species, such as a benzyl radical, and an electron deficient functionality, such as alkenes with adjacent electron withdrawing groups.<sup>329</sup> The first reported radical Giese reactions were typically initiated using AIBN and required tributyltin hydride as a radical mediator,<sup>330</sup> however investigating tin-free alternatives that initiate this radical reaction photochemically became a growing area of research that aims to replace highly toxic tin containing initiators.<sup>331</sup> In previously reported work by Ryu et al., UV irradiation and stoichiometric amounts of cyanoborohydride have been utilised to achieve Photo-Giese reactions between iodohydrocarbons and various acrylate species.<sup>331</sup>



Scheme 5.2 – Literature examples of photochemical Giese reactions initiated through decarboxylation of carboxylic acids.<sup>30, 326, 332</sup>

In other previously reported work by Manley et al., an excess of titanium dioxide and hard UV irradiation has been used to couple oxyacetic acids to various maleic anhydride and maleimide derivatives, Scheme 5.2a.<sup>30</sup> Further to this, the use of UV and titania P25 has been reported by McTiernan et al. in a semi-heterogeneous photocatalysis system with a homogeneous nickel catalyst to decarboxylate various carboxylic acids in order to

achieve coupling to iodoaromatics, Scheme 5.2b.<sup>326</sup> The only example of the use of visible light to date has required the use of homogeneous iridium photocatalysts which were used to decarboxylate various glycine analogues to form  $\alpha$ -amino radicals which subsequently reacted with electron deficient alkenes such as cyclohexanone, Scheme 5.2c,<sup>332</sup> 11 W blue LED stripes were used to encase the reaction vessel. Each of these reactions required a source of hydrogen in order to produce a saturated final product. In each of these systems, the reduction of the radical addition intermediate led to the formation of an anion which was then protonated. Platinum metal on the surface of a bismuth containing semiconductor irradiated by visible light has the potential to act as a good catalytic surface for this reduction reaction. It was with the potential for visible light mediated heterogeneous Photo-Kolbe and Photo-Giese reactions in mind that the aims of this work were set.

### 5.1.4 Objectives

The objectives of this work were:

- To investigate how the modification of the surface of previously used bismuth containing semiconductors affects how these materials behave in the presence of carboxylic acids; and
- To investigate the potential for such modified semiconductors to act as Photo-Giese photocatalysts

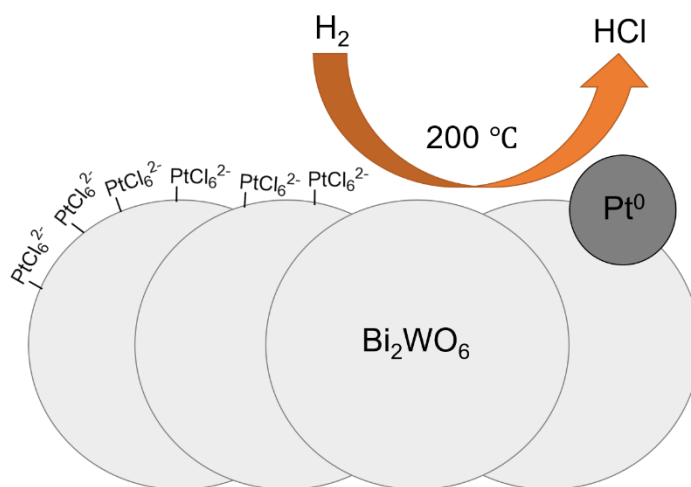
## 5.2 Results and Discussion

### 5.2.1 Platinization and Characterisation

Several methods can be used to platinise semiconductors. In previously reported work by Mills, small platinum nanoparticles have been synthesised by heating  $\text{Pt}^{4+}$  under reflux at 100 °C in the presence of sodium citrate which acted as a reducing and surface stabilising agent.<sup>321</sup> The addition of semiconducting material to this solution triggered precipitation of these Pt metal nanoparticles onto the surface of said semiconducting material. This method has been shown to be successful in the platinization of titanium dioxide.<sup>321</sup> It has been hypothesised that upon the addition of the semiconducting material the citrate-protected platinum nanoparticles are destabilised,<sup>321</sup> presumably due to the strong interaction between metal oxide surfaces and carboxylate anions. Adsorption of the platinum nanoparticles follows this destabilisation. The advantages of the use of this method are that it is very simple and is unlikely to affect the morphology of the semiconductor as the platinization takes place at room temperature. However,

platinization via the adsorption of citrate protects platinum nanoparticles may not always be guaranteed with materials that have low zeta potentials.

Another method for platinum nanoparticle formation has been reported where platinum reduction occurred via the addition of a reducing agent such as sodium borohydride.<sup>333</sup> In addition, it has been possible to use a flow of dihydrogen at high temperatures to reduce  $\text{Pt}^{4+}$  to  $\text{Pt}^0$  thermally on the surface of metal oxides in order to form metal platinum nanoparticles,<sup>317</sup> Scheme 5.3. This thermal method could guarantee adsorption as a chloroplatinic acid solution was dried onto the surface of the semiconductor and then heated under a hydrogen flow to reduce platinum species at the catalyst surface. However, the use of thermal treatment under a hydrogen flow and the use of reagents such as sodium borohydride can result in undesired sample contamination and doping,<sup>334</sup> which can destabilise the semiconductor or increase electron-hole recombination in the bulk and thus reducing photocatalytic efficiency.<sup>335</sup> In addition, and as previously state, the heating of bismuth containing semiconductors to 200 °C is known to have an effect on semiconductor morphology due to Bi migration.<sup>136</sup>



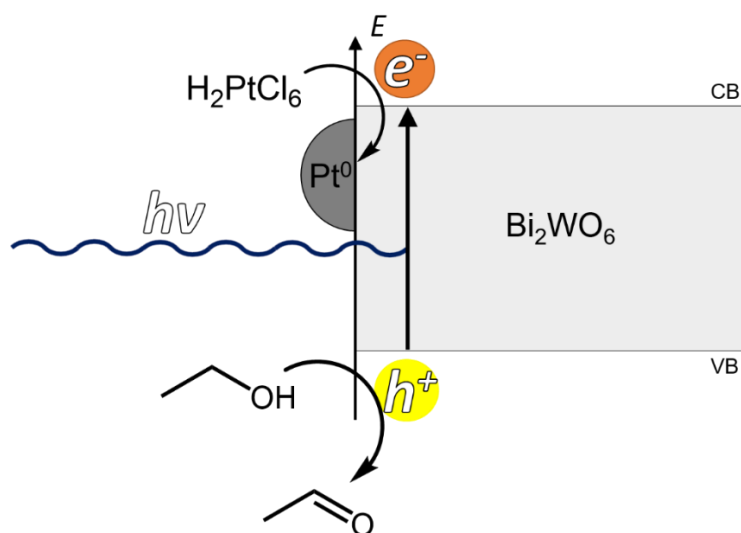
Scheme 5.3 - The formation of Pt NPs thermally through the reduction a platinum precursor at elevated temperature under a flow of dihydrogen gas.

Examples where surface adsorbed platinum nanoparticles have formed from the photochemical reduction of  $\text{Pt}^{4+}$  by an irradiated semiconducting metal oxide have also been reported. These systems often required alcohols to act as a sacrificial reductant and an appropriate irradiation source. UV irradiation (365 nm from a 300 W Osram Ultra-Vitalux lamp) of a titania suspension in a chloroplatinic acid and isopropanol solution has been reported, by Vaiano et al., to result in the formation of 5 nm Pt nanoparticles.<sup>336</sup> In addition, the synthesis of platinum nanoparticles roughly 10 nm in size has been reported



by Gholipour et al. from the reduction of chloroplatinic acid on graphitic carbon nitride under UV irradiation using a solar simulator in the presence of triethanolamine reductant.<sup>337</sup> In work by Wu et al., bismuth tungstate has been platinised by irradiating a  $\text{Bi}_2\text{WO}_6$  suspension in a chloroplatinic acid, ethanol and water mixture with UV light,<sup>108</sup> the material was used for the effective photodegradation of an antibiotic, ciprofloxacin.<sup>108</sup> Advantages of this method include the formation of well-defined platinum nanoparticles specifically at reduction active sites utilising the photochemical method.<sup>109</sup> Photochemical platinization also guarantees an interaction between the metal nanoparticle and semiconducting substrate, unlike platinization through the use of a Pt-citrate deposition method. Moreover, photochemical platinization occurs at low temperature meaning that detrimental phenomena such as particle sintering or migration, that are often associated with thermal treatment, are avoided. As a result of the various advantages and the broad application of this method with a number of different photocatalysts, it was decided that the platinization of nan- $\text{BiVO}_4$  and  $\text{Bi}_2\text{WO}_6$ , synthesised and characterised in chapter 2, was to be attempted using the photochemical deposition method.

Platinization was attempted utilising blue light from a 30 W LED array, irradiating nan- $\text{BiVO}_4$  and  $\text{Bi}_2\text{WO}_6$  in a 20% ethanol solution containing chloroplatinic acid, Scheme 5.4. The amount of chloroplatinic acid used was chosen so that the final semiconductors would contain 0.15% Pt by weight as several reports have shown that a Pt loading of between 0.1% and 0.2% by weight is optimal for high conversion and high selectivity for selective heterogeneous photocatalysis.<sup>311, 312</sup>



Scheme 5.4 – The photochemical platinization of blue LED light irradiated bismuth tungstate in an ethanol:water solvent mixture.

## Chapter 5

The platinumization of  $\text{Bi}_2\text{WO}_6$  resulted in a colour change from ivory to grey. In addition, the reaction solution turned from an orange colour, consistent with a chloroplatinic acid solution, to a colourless solution. These colour changes suggested that chloroplatinate anions were removed from solution and deposited onto the surface of  $\text{Bi}_2\text{WO}_6$  in the form of  $\text{Pt}^0$  metal and so suggested that platinumization was successful. The dark grey material formed shall be referred to as  $0.15\text{-Pt-Bi}_2\text{WO}_6$ . Powder X-ray diffraction data of  $0.15\text{-Pt-Bi}_2\text{WO}_6$  were consistent with crystalline orthorhombic  $\text{Bi}_2\text{WO}_6$  (JCPDS No. 39-0256), Figure 5.3. Diffuse reflectance UV-vis spectroscopy (DRUVS) was used to estimate the band gaps of the  $0.15\text{-Pt-Bi}_2\text{WO}_6$  material. The Kubelka-Munk function was applied to the reflectance data to generate a Tauc plot giving an estimated band-gap of 2.85 eV (435 nm) for  $0.15\text{-Pt-Bi}_2\text{WO}_6$ , Figure 5.4.

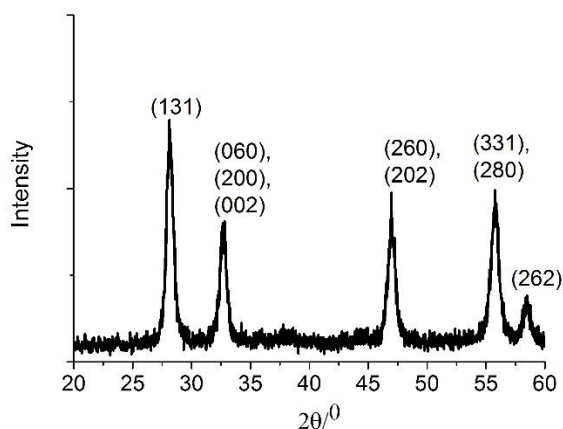


Figure 5.3 - PXRD of  $0.15\text{-Pt-Bi}_2\text{WO}_6$  consistent with crystalline orthorhombic  $\text{Bi}_2\text{WO}_6$  (JCPDS No. 39-0256).

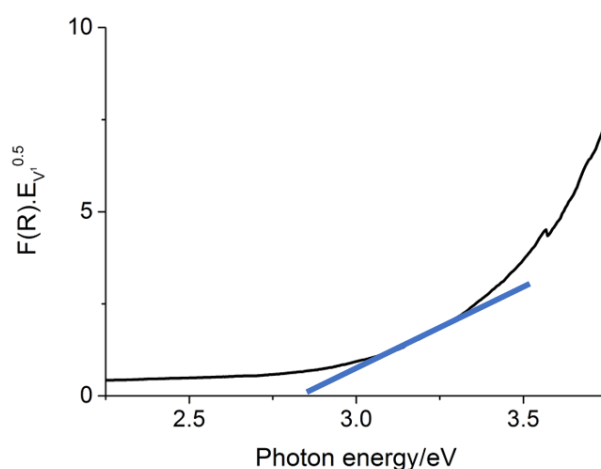


Figure 5.4 - The Tauc plot used to estimate the band-gap for the indirect semiconductor,  $0.15\text{-Pt-Bi}_2\text{WO}_6$

## Chapter 5

Transmission electron microscopy images showed thin, agglomerated plates that are roughly square or rectangular in shape, Figure 5.5. The length of the edge of these plates was ca. 50 – 200 nm. On the surface of these plates, well defined spherical nanoparticles that were between 3 and 5 nm in diameter were observed. Specific area electron diffraction of 0.15-Pt-Bi<sub>2</sub>WO<sub>6</sub>, Figure 5.6, yielded diffraction spots that correspond to the orthorhombic Bi<sub>2</sub>WO<sub>6</sub> (Miller indices (131), (200), (202) and (133)) and platinum metal (Miller indices (111), (200) and (220)). This characterisation suggested that photodeposition of platinum was successful and that platinum formed into 3 – 5 nm diameter nanoparticles on the surface of Bi<sub>2</sub>WO<sub>6</sub> under the conditions used. It also suggested that photo-deposition does not change the crystallinity, morphology or visible light absorption of Bi<sub>2</sub>WO<sub>6</sub>. To establish the amount of Pt on the surface of 0.15-Pt-Bi<sub>2</sub>WO<sub>6</sub>, inductively coupled plasma mass spectrometry (ICP-MS) was used. The results were consistent with the full conversion of chloroplatinic acid to platinum nanoparticles ([Pt] = 1560 ppm) and so it can be said that Pt content on 0.15-Pt-Bi<sub>2</sub>WO<sub>6</sub> was 0.15% by weight.

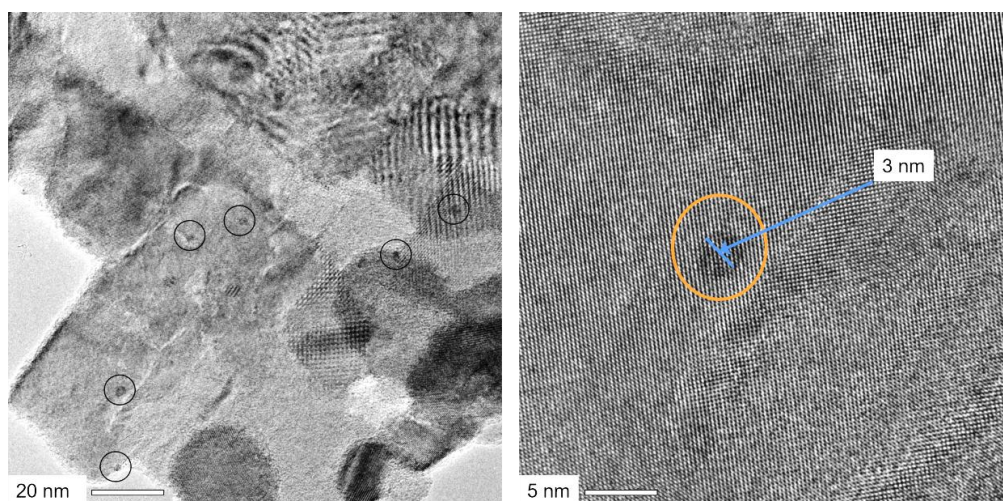


Figure 5.5 – TEM images showing spherical nanoparticles on the surface of 0.15-Pt-Bi<sub>2</sub>WO<sub>6</sub>

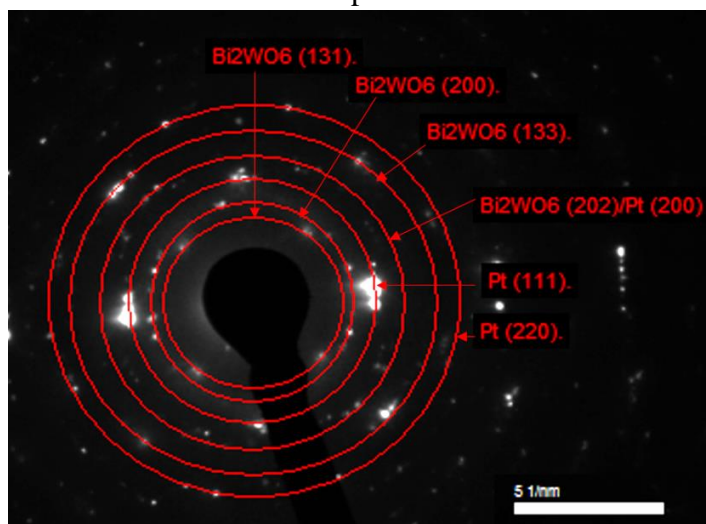


Figure 5.6 – SAED of 0.15-Pt-Bi<sub>2</sub>WO<sub>6</sub> showing diffraction patterns of orthorhombic Bi<sub>2</sub>WO<sub>6</sub> and Pt metal.

The platinization of nan-BiVO<sub>4</sub> resulted in a colour change from yellow to a dark green. In addition, the reaction solution turned from an orange colour, consistent with a chloroplatinic acid solution, to a colourless solution. These colour changes suggested that chloroplatinate anions were removed from solution and deposited onto the surface of nan-BiVO<sub>4</sub> in the form of Pt metal. This tentatively suggested that platinization has been successful. The dark green material shall be referred to as 0.15-Pt-nan-BiVO<sub>4</sub>. Powder X-ray diffraction data of 0.15-Pt-nan-BiVO<sub>4</sub> were consistent with crystalline monoclinic BiVO<sub>4</sub> (JCPDS no. 14-0688), Figure 5.7. DRUVS was used to estimate the band gaps of the 0.15-Pt-nan-BiVO<sub>4</sub> material. The Kubelka-Munk function was applied to the reflectance data giving an estimated band-gap of 2.40 eV (520 nm) for 0.15-Pt-nan-BiVO<sub>4</sub>, Figure 5.8.

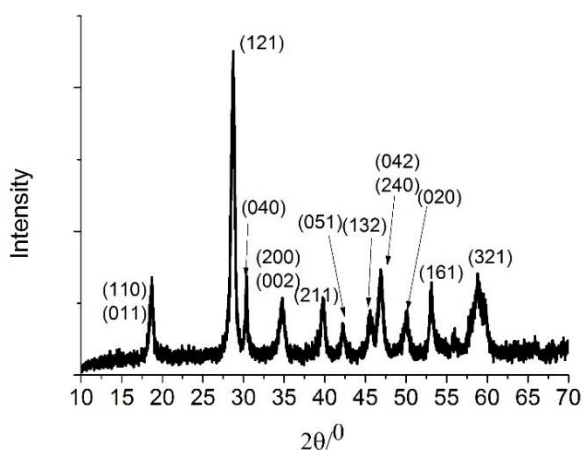


Figure 5.7 - PXRD of 0.15-Pt-BiVO<sub>4</sub> consistent with crystalline monoclinic BiVO<sub>4</sub> (JCPDS No. 14-0688).

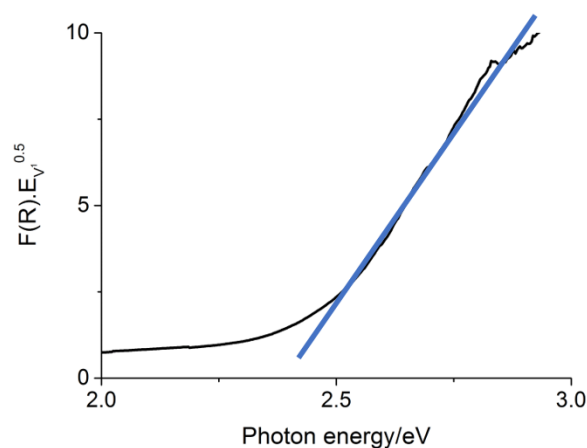


Figure 5.8 - The Tauc plot used to estimate the band-gap for the indirect semiconductor, 0.15-Pt-BiVO<sub>4</sub>

Transmission electron microscopy showed agglomerated particles with features that range in size from ca. 20 to 100 nm, Figure 5.9. However, no evidence could be found for the formation of Pt metal nanoparticles on the surface of nan-BiVO<sub>4</sub>. Although there was a lack of evidence from the TEM of the presence of well-defined spherical nanoparticles, like those observed in the TEM of 0.15-Pt-Bi<sub>2</sub>WO<sub>6</sub>, it was not possible to carry out further analysis to explore Pt content. This characterisation suggested that the process of photo-deposition of Pt on the surface of nan-BiVO<sub>4</sub> resulted in no changes to nan-BiVO<sub>4</sub> with regards to semiconducting particle morphology, crystallinity or visible light absorption. Even though characteristic colour changes were observed, no conclusive argument could be made with regards to the success of platinization of nan-BiVO<sub>4</sub>.

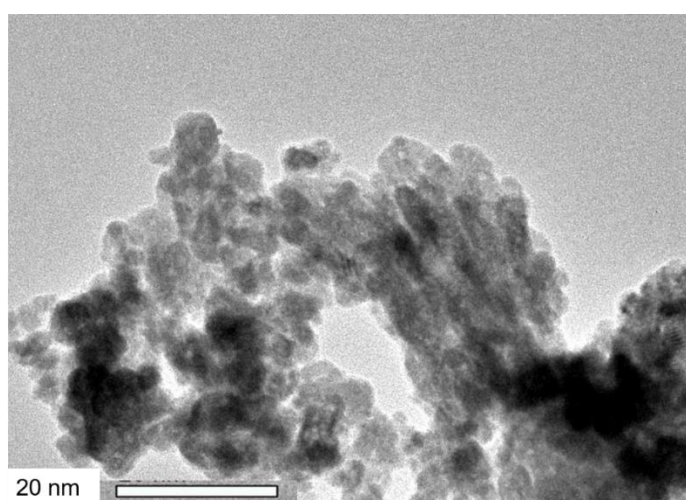


Figure 5.9 – TEM images of 0.15-Pt-BiVO<sub>4</sub>

### 5.2.2 Attempted Photo-Kolbe dimerization

0.15-Pt-Bi<sub>2</sub>WO<sub>6</sub> was used to oxidise phenylacetic acid, Table 5.1, with the aim of forming bibenzyl as a result of radical dimerization. 0.15-Pt-BiVO<sub>4</sub> was also used for this reaction even though conclusive evidence could be found that showed successful platinumization. Reaction conditions are given in Table 5.1 and gas chromatography was used to analyse the reaction mixtures after irradiation with the blue LED array and a mixture of unexpected oxidation products were observed, an example GC is given in Figure 5.10.

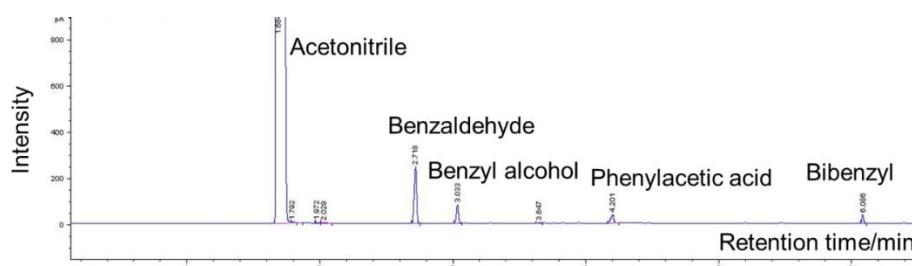
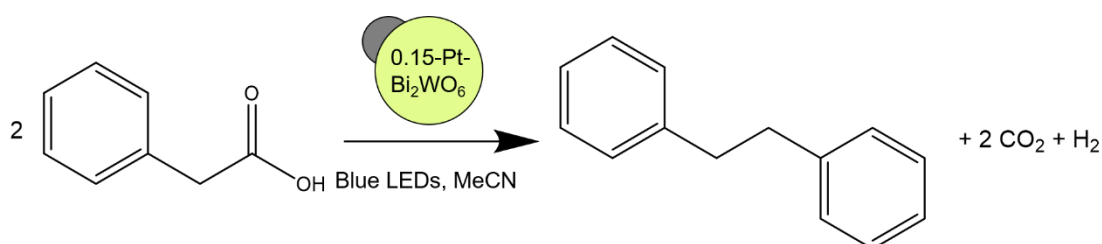


Figure 5.10 – Example gas chromatogram of the reaction mixture from the attempted dimerization of phenylacetic acid with blue LED light irradiated 0.15-Pt-BiVO<sub>4</sub>

Table 5.1 – Results of the attempted Photo-Kolbe dimerizations with 0.15-Pt-Bi<sub>2</sub>WO<sub>6</sub> and 0.15-Pt-BiVO<sub>4</sub>



	Irradiation time/h	<sup>a,b</sup> Percentage phenylacetic acid conversion	<sup>a,b</sup> Percentage bibenzyl selectivity	<sup>a,b</sup> Percentage benzyl alcohol selectivity	<sup>a,b</sup> Percentage benzaldehyde selectivity
0.15-Pt-Bi <sub>2</sub> WO <sub>6</sub>	6	>99	0	6	87
0.15-Pt-BiVO <sub>4</sub>	6	96	12	20	67

<sup>a</sup>conditions: 0.15 mmol photocatalyst, 0.1 mmol phenylacetic acid, 10 mL dry acetonitrile, N<sub>2</sub> atm, blue LED irradiation. <sup>b</sup>The conversion and selectivity were determined using GC.

Apart from bibenzyl, benzyl alcohol and benzaldehyde were detected in the reactions catalysed by 0.15-Pt-Bi<sub>2</sub>WO<sub>6</sub> and 0.15-Pt-BiVO<sub>4</sub>. Calibration curves of concentration against peak area were constructed using stock solutions of benzyl alcohol, benzaldehyde, phenylacetic acid and bibenzyl in acetonitrile in order to quantify the phenylacetic acid conversion and the selectivities of the various products, Figure 5.11. Equation 2.5,



## Chapter 5

Equation 2.6 and Equation 2.7 were used to calculate yield, phenylacetic acid conversion and product selectivities respectively.

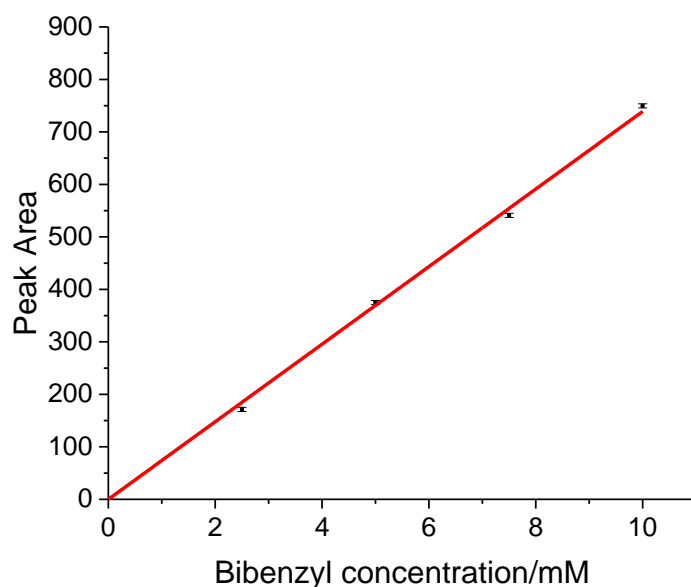


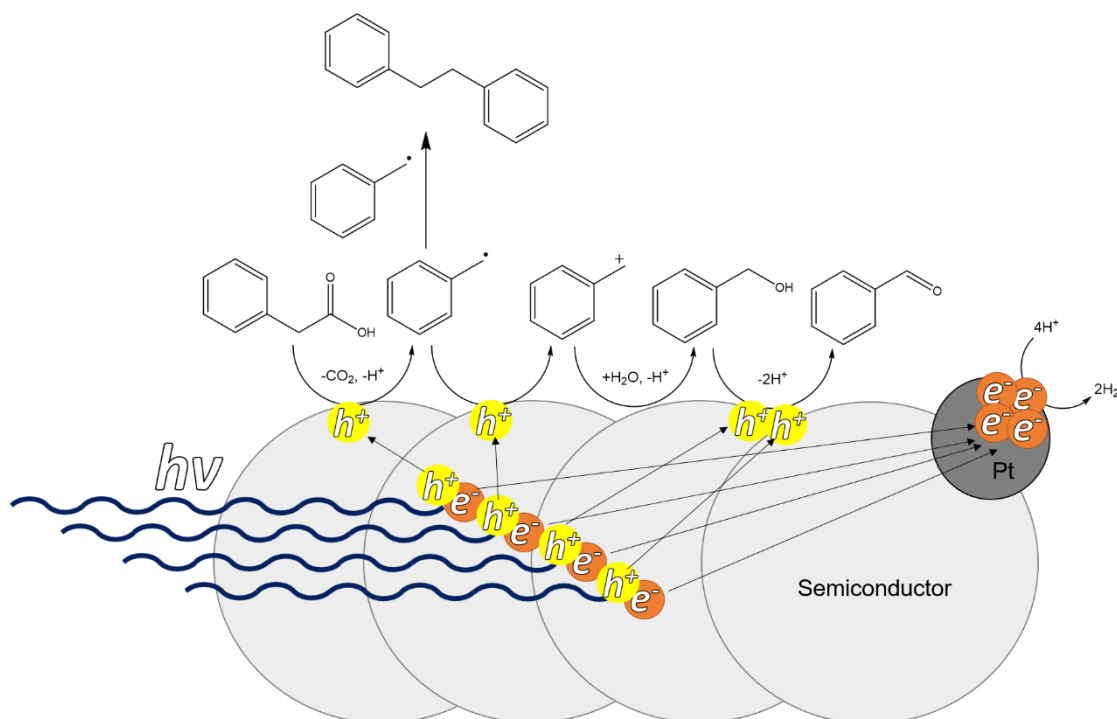
Figure 5.11 – An example calibration curve for bibenzyl concentration against GC peak area for the peak with  $R_t = 6.1$  min that is characteristic of the presence of bibenzyl. The standard error for this linear regression was used to calculate error from the average differences between the data points and the linear regression. The error in peak area on each data point was calculated as  $\pm 0.8$ .

Controls were carried out to ensure that the Photo-Kolbe reaction required 0.15-Pt- $\text{Bi}_2\text{WO}_6$  and light. A dark control, stirring the reaction mixture at 40 °C for 20 h resulted in no product formation. In addition, the irradiation of the reaction mixture without any of the 0.15-Pt- $\text{Bi}_2\text{WO}_6$  for 20 h also resulted in no product formation. These results indicate that the conversion of phenylacetic acid into oxidised products is the result of heterogeneous photocatalysis from irradiation of 0.15-Pt- $\text{Bi}_2\text{WO}_6$ .

The thermal and the Pt-citrate deposition methods described above were also attempted for the platinization of both nan- $\text{BiVO}_4$  and  $\text{Bi}_2\text{WO}_6$ . However, the materials platinised using the thermal and Pt-citrate methods showed poor phenylacetic acid conversions when used under analogous conditions to those used with 0.15-Pt- $\text{Bi}_2\text{WO}_6$  and so it was decided that the study of these materials shall not be included in this thesis. It should be noted that the range of products observed was the same as that observed with the use of 0.15-Pt- $\text{Bi}_2\text{WO}_6$ .

## Chapter 5

It can be proposed that benzyl alcohol and benzaldehyde are formed as a result of multiple oxidations of a phenylacetic acid molecule, Scheme 5.5. After phenylacetic acid adsorbed to the surface of an irradiated semiconductor, holes oxidised phenylacetic acid molecules which led to deprotonation and decarboxylation to yield benzyl radicals and carbon dioxide. If these benzyl radicals persisted at the surface of the semiconductor, holes oxidised these benzyl radicals to cations which then reacted with surface bound water molecules or hydroxyl groups to yield benzyl alcohol. Benzyl alcohol can then be retained at the catalyst surface and oxidised further by more holes to benzaldehyde. Corresponding photoexcited electrons produced by the formation of electron-hole pairs migrate to platinum metal at the catalyst surface and are used in the reduction of protons to dihydrogen.



Scheme 5.5 – An illustration of the proposed mechanism for bibenzyl, benzyl alcohol and benzaldehyde formation from the oxidation of phenylacetic acid with a blue LED light irradiated platinised semiconductor.

Semiconducting metal oxides such as bismuth tungstate are known to be highly hygroscopic and can retain high amounts of surface bound water.<sup>338</sup> To remove as much surface bound water without severely affecting particle morphology, 0.15-Pt-Bi<sub>2</sub>WO<sub>6</sub> were heated to 100 °C *in vacuo* for 2 h before use in Photo-Kolbe dimerization, however, this heated catalyst did not cause phenylacetic acid conversion. As no morphological

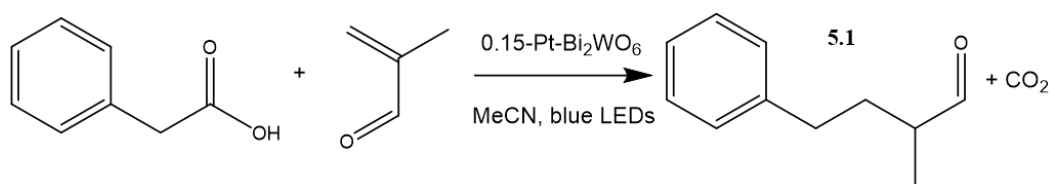


changes would be expected to the catalyst or surface bound nanoparticles under these conditions,<sup>186, 317</sup> it can be suggested that water molecules or hydroxyl groups found at the surface of the photocatalyst are necessary to mediate the adsorption of phenylacetic acid to the catalyst surface through hydrogen bonding.

Considering the proposed mechanism given in Scheme 5.5 and the data in Table 5.1, it can be suggested that 0.15-Pt-Bi<sub>2</sub>WO<sub>6</sub> was the more active photocatalyst in these reaction as 0.15-Pt-Bi<sub>2</sub>WO<sub>6</sub> was able to carry out more oxidation reactions than 0.15-Pt-BiVO<sub>4</sub> in order to give a higher selectivity for benzaldehyde. The attempted Photo-Kolbe reaction using blue light irradiated 0.15-Pt-Bi<sub>2</sub>WO<sub>6</sub> did not result in the formation of the desired bibenzyl product, however the formation of other valuable oxidation products such as benzaldehyde with high amounts of selectivity was encouraging. As a result, Photo-Giese reactions were attempted using 0.15-Pt-Bi<sub>2</sub>WO<sub>6</sub>.

### 5.2.3 Photo-Giese C-C cross coupling

0.15-Pt-Bi<sub>2</sub>WO<sub>6</sub> was used to attempt the coupling between phenylacetic acid and methacrolein, Scheme 5.6. After 10 h of irradiation by a 30 W blue LED array, the presence of the desired coupled product, **5.1**, was observed via <sup>1</sup>H NMR alongside phenylacetic acid. A reaction over 24 h of irradiation resulted in the full conversion of phenylacetic acid and from this reaction, **5.1** could be fully characterised by <sup>1</sup>H NMR, Figure 5.13, <sup>13</sup>C NMR, ESI-MS and GC, the characterisation via NMR and MS are in full agreement with the synthesis of **5.1** reported in literature by Mazet et al.<sup>339, 340</sup>



Scheme 5.6 – The Photo-Giese reaction between phenylacetic acid and methacrolein for the formation of **5.1** and carbon dioxide facilitated by 0.15-Pt-Bi<sub>2</sub>WO<sub>6</sub> irradiated by blue LEDs.

Evidence of coupling between the 2 starting materials was found in the presence of a multiplet at 2.66 ppm which was consistent with the benzyl methylene group coupled to another diastereotopically split methylene group, Figure 5.12a. This suggested that once formed a benzyl radical coupled to the terminal end of the alkene group of methacrolein. The presence of this diastereotopically split methylene group can be observed by complex multiplets at 2.06 ppm and 1.66 ppm, Figure 5.12b. Evidence of hydrogenation of the previously quaternary carbon present in methacrolein was found in the multiplet present

## Chapter 5

at 2.36 ppm, Figure 5.12c, which showed coupling to the methyl CH<sub>3</sub> found at 1.14 ppm, the adjacent methylene group found at 2.06 ppm and 1.66 ppm and the CHO signal at 9.62 ppm consistent with the retained aldehyde functionality. The <sup>13</sup>C NMR for **5.1** showed the presence of an aldehyde functionality with a peak at 205.0 ppm. No evidence could be found for the presence of an alkene functionality with peaks not present in the alkene region in either <sup>1</sup>H or <sup>13</sup>C NMR. Instead, peaks in the <sup>13</sup>C NMR spectrum at 32.2 and 45.7 ppm were found to be consistent with a saturated carbon in an aliphatic chain and a saturated carbon adjacent to a carbonyl group respectively. More evidence of coupling between phenylacetic acid and methacrolein was found in the integration of the aromatic signals at 7.27 ppm and 7.19 ppm that showed integrations equivalent to 2 and 3 protons respectively against an integration of 2 for the multiplet at 2.66 ppm. ESI-MS also provided evidence of the formation of **5.1** providing a m/z peak at 185.0942; [C<sub>11</sub>H<sub>14</sub>O]+Na<sup>+</sup> had a calculated m/z value of 185.0937. A stock solution of **5.1** with a known concentration in acetonitrile was used to generate a GC calibration curve of concentration of **5.1** vs. peak area, Figure 5.14. An example GC spectrum of a reaction mixture for the formation of **5.1** is given in Figure 5.15. From the calibration curve, the yields of **5.1** were found to be 64% and 94% for the 10 h and 24 h reactions respectively.

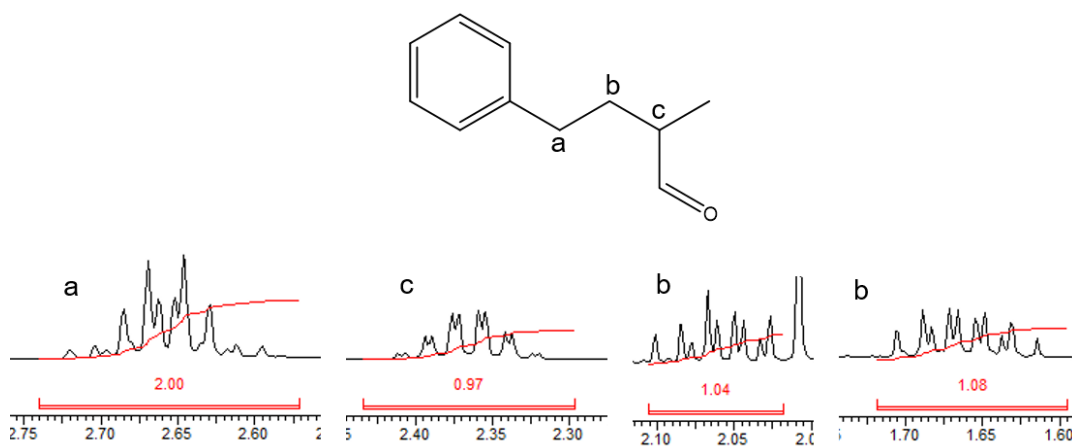


Figure 5.12 – Examples of the <sup>1</sup>H NMR peaks, recorded at 400 MHz in CDCl<sub>3</sub>, that give evidence of the successful coupling of a benzyl radical to methacrolein to form product **5.1**. a – the peak consistent with the methylene group adjacent to the phenyl group and another methylene group that is diastereotopically split. b – the peaks consistent with the diastereotopically split methylene group adjacent to functionalities b and c. c – the peak consistent with a methine group coupled to protons in methylene group, methyl group and the aldehyde proton. The peak given between 2.00 and 2.10 ppm also contains a singlet at 2.01 ppm consistent with an acetonitrile solvent impurity.

## Chapter 5

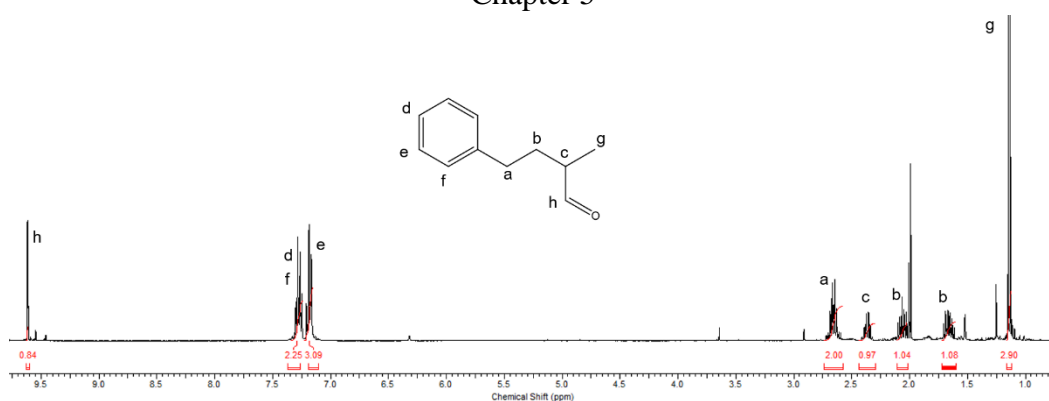


Figure 5.13 – Full  $^1\text{H}$  NMR spectrum ( $\text{CDCl}_3$ , 400 MHz) of the crude reaction mixture of the 24 h Photo-Giese reaction of phenylacetic acid and methacrolein resulting in **5.1** formation. Other observable peaks present in this spectrum can be associated to trace starting materials (methacrolein - 6.3 ppm and phenylacetic acid – 3.6 ppm), products (bibenzyl - 2.8 ppm) and solvent impurity (acetonitrile – 2.0 ppm and water – 1.5 ppm).

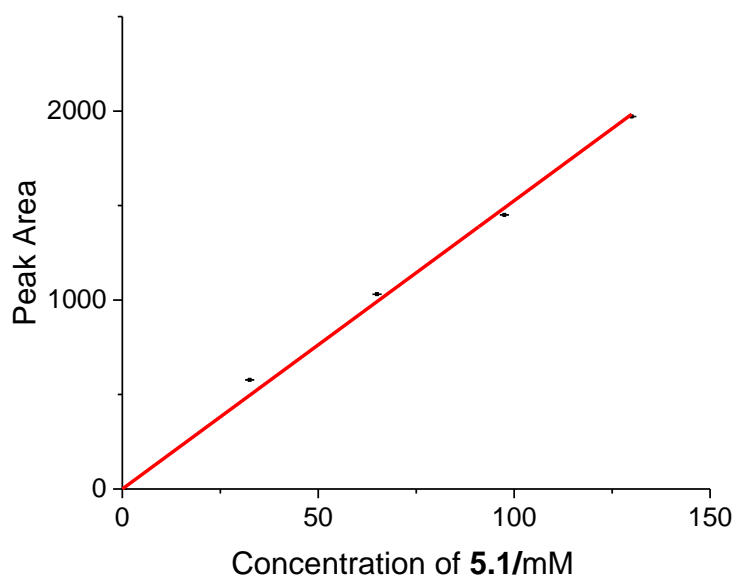


Figure 5.14 – GC calibration curve for Photo-Giese product **5.1** showing concentration of product against peak area at  $R_t = 4.8$  min. The standard error for this linear regression was used to calculate error from the average differences between the data points and the linear regression. The error in peak area on each data point was calculated as  $\pm 0.3$ .

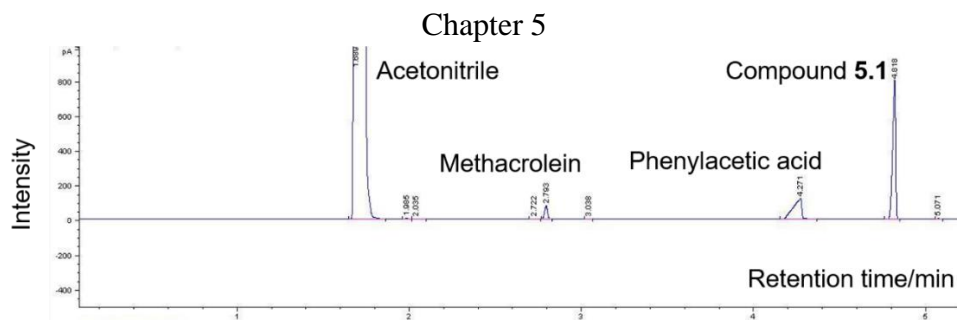
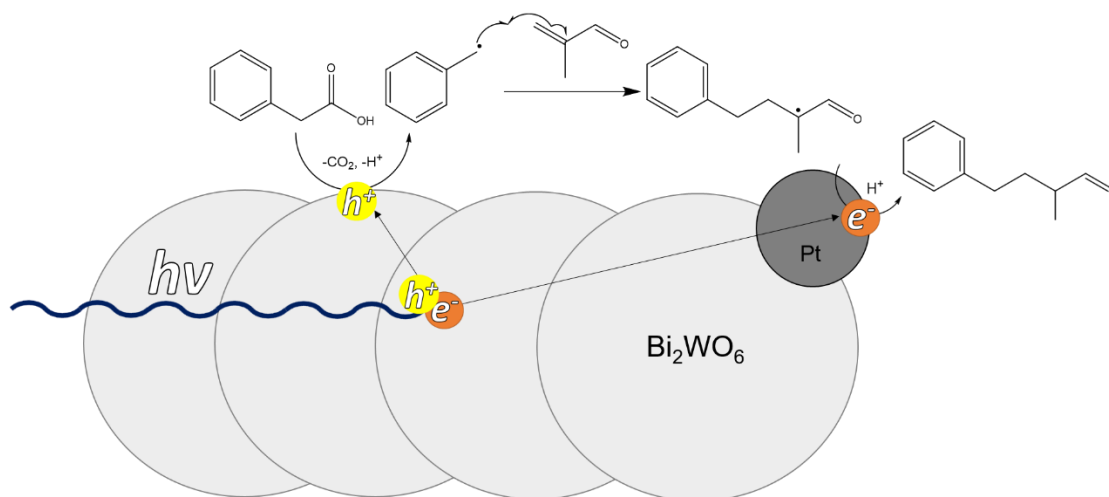


Figure 5.15 – An example gas chromatogram from a Photo-Giese reaction mixture coupling phenylacetic acid with methacrolein to form compound **5.1** with blue light irradiated 0.15-Pt-Bi<sub>2</sub>WO<sub>6</sub>

A proposed mechanism for the Photo-Giese formation of **5.1** using blue light irradiated 0.15-Pt-Bi<sub>2</sub>WO<sub>6</sub> is given in Scheme 5.7. 0.15-Pt-Bi<sub>2</sub>WO<sub>6</sub> absorbed a photon of visible light and generated electrons and holes which travel to the surface. The photolytically generated hole then travelled to an adsorbed phenylacetic acid molecule and caused oxidation which generated a benzyl radical, a carbon dioxide molecule and a proton. The electron rich benzyl radical coupled into the electron deficient alkene of methacrolein resulting in the formation of a carbon centred radical adjacent to the aldehyde and methyl group in the coupled intermediate. The addition product was then reduced by electrons at a Pt nanoparticle to form an anion which is subsequently protonated to give the final coupled product.



Scheme 5.7 – Proposed mechanism for the Photo-Giese reaction initiated by the decarboxylative photooxidation of phenylacetic acid by irradiated 0.15-Pt-Bi<sub>2</sub>WO<sub>6</sub>

#### 5.2.4 Optimisation

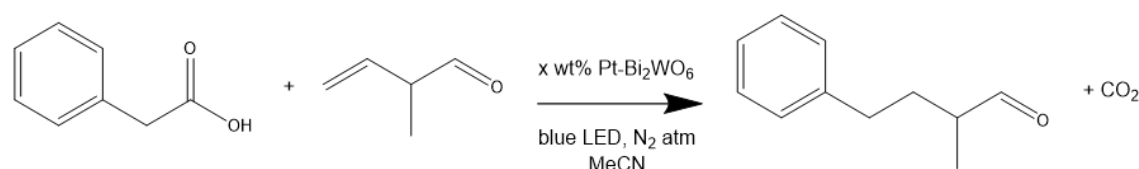
Catalyst optimisation was carried out to determine the amount of platinum that would result in the highest phenylacetic acid conversion and product selectivity, Table 5.2.

## Chapter 5

Different concentrations of chloroplatinic acid were employed in different photodeposition reactions. As the ICP-MS of 0.15-Pt-Bi<sub>2</sub>WO<sub>6</sub> showed complete adsorption of platinum via the photodeposition method, it was assumed that all platinum in solution was adsorbed to the Bi<sub>2</sub>WO<sub>6</sub> surface in each photodeposition reaction. This assumption was justified as the liquor for each photo-deposition reaction changed from orange to colourless. In addition, it was observed that higher concentrations of chloroplatinic acid resulted in the formation of darker photocatalysts upon photodeposition. These colour changes were consistent with full conversion of chloroplatinic acid to surface adsorbed Pt nanoparticles.

From the use of these photocatalysts with differing amounts of Pt, it was evident that after 10 h of irradiation the 0.15 wt% Pt on the surface of bismuth tungstate was optimal both with regards to phenylacetic acid conversion (68 %) and product selectivity (94 %). This was consistent with other reports that have shown an optimal platinum loading of between 0.1 and 0.2% Pt by weight.<sup>312,311</sup>

Table 5.2 - Photocatalyst optimisation. Results of Photo-Giese reactions with varying amounts of platinum on bismuth tungstate



x	% Phenylacetic acid conversion <sup>a,b</sup>	% Selectivity for compound <b>5.1</b> <sup>a,b</sup>	% Yield of compound <b>5.1</b> <sup>a,b</sup>
0.015	57	70	40
0.05	62	64	40
0.15	68	94	64
0.5	34	70	24
0	41	31	13

<sup>a</sup>conditions: 0.15 mmol photocatalyst, 0.1 mmol phenylacetic acid, 0.25 mmol methacrolein, 3 mL dry acetonitrile, N<sub>2</sub> atm, blue LED irradiation for 10 h. <sup>b</sup>The conversion, selectivity and yields were determined using GC.

The conversion of phenylacetic acid increased with increased Pt content from 0.015 wt% to 0.15 wt% Pt (57% and 62%, respectively). As the amount of surface platinum metal increased, more electrons were able to migrate to Pt nanoparticles in order to carry out hydrogen reduction.<sup>8,9</sup> This affected phenylacetic acid oxidation because fewer electrons were involved in electron-hole recombination events meaning that more holes can be used for the oxidation reaction. At 0.5 wt% Pt, a significant proportion of the photolytically produced holes were unable to interact with surface adsorbed phenylacetic acid due to the relatively high amount of platinum found at active sites, this platinum provided a partial

hole blocking layer.<sup>8,9</sup> This meant that electrons and holes had an increased probability of recombination in the 0.5 wt% Pt catalyst when compared to the 0.15 wt% Pt bismuth tungstate sample. However, the high amount of platinum in the 0.5 wt% Pt bismuth tungstate catalyst resulted in a high selectivity for compound **5.1** (70%). Another explanation for the reduced phenylacetic acid conversion observed with the use of 0.5 wt% Pt was the growth of larger platinum nanoparticles. Larger Pt nanoparticles are consistent with lower catalytic activities as more platinum is found in the bulk and so less catalytically active material was available for substrate adsorption and catalysis.<sup>8,9</sup>

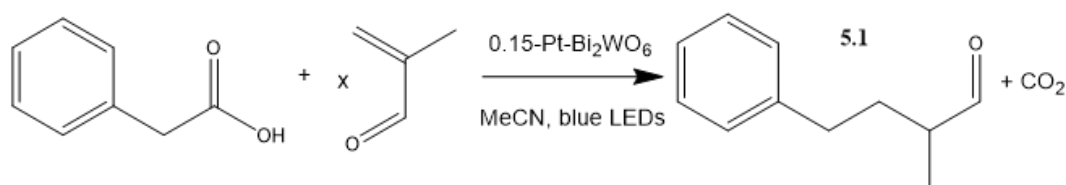
A reaction was carried out using bare bismuth tungstate and interestingly, the percentage phenylacetic acid conversion was not insignificant (41%). This shows that the presence of platinum was not necessary for the decarboxylation of carboxylic acids. In addition, some of the desired product was observed showing that bismuth tungstate was able to carry out the appropriate reduction processes. However, the percentage selectivity was the lowest of the catalysts used (31%) and so showed that any amount of platinum aided Photo-Giese reaction selectivity.

After platinum optimisation, the quantity of methacrolein used was optimised, Table 5.3. 1, 2.5 and 10 equivalents of methacrolein were used in separate Photo-Giese coupling reactions with phenylacetic acid. The conversions of phenylacetic acid for each reaction were similar. However, a decrease in selectivity for **5.1** was observed upon the addition of more methacrolein; 94% with the use of 2.5 equivalents of methacrolein and 74% with the use of 10 equivalents of methacrolein. It is not clear what the cause of this change in selectivity was upon the increased concentration of methacrolein. It is possible that a higher amount of methacrolein adsorption to the photocatalyst surface led to the competitive oxidation of methacrolein. Methacrolein oxidation products could include methacrylic acid. Further oxidation would result in the formation of allylic radicals via decarboxylation<sup>341</sup> which could react with benzyl radicals if present in a significant concentration. Due to time constraints, evidence of the presence of products associated to the radical termination of a benzyl radical and an allylic radical was not investigated.

When comparing the Photo-Giese reactions to the Photo-Kolbe reaction, it was of note that in all of the Photo-Giese reactions discussed here, significant amounts of benzaldehyde and benzyl alcohol were not observed. This is in stark contrast to the Photo-Kolbe dimerization attempted above, where only benzyl alcohol and benzaldehyde are observed as products from the use of 0.15-Pt-Bi<sub>2</sub>WO<sub>6</sub>. It can be suggested that the presence of the alkene, methacrolein, in high concentrations accelerated the reaction

pathway for the Photo-Giese reaction, enabling the fast addition of the benzyl radical and so made the formation of the corresponding alcohol and aldehyde much less competitive. There is also a possibility that methacrolein or even methacrylic acid, if formed via oxidation, bound to the photocatalyst surface reducing the likelihood of further oxidation of the benzyl radical. This would allow for effective benzyl radical desorption and selective formation of the desired Photo-Giese product. The interaction suggested here is a similar inhibitory interaction to that proposed in chapter 3, where a surface adsorbed substrate provides a blocking interaction to reduce further oxidation and therefore increase selectivity. The slower conversion of phenylacetic acid observed for the Photo-Giese reaction (68% in 10 h of irradiation) compared to that observed for the Photo-Kolbe reaction (>99% in 6 h of irradiation) could be used to tentatively support the concept of methacrolein related inhibition.

Table 5.3 – Photo-Giese reaction optimisation. Results of Photo-Giese reactions varying the quantity of methacrolein used



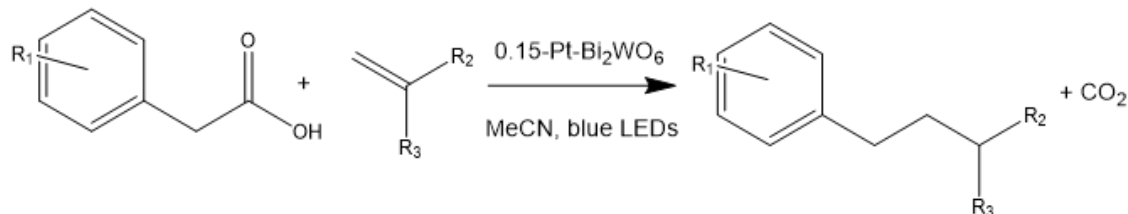
x	%Phenylacetic acid conversion <sup>a,b</sup>	%Selectivity for compound <b>5.1</b> <sup>a,b</sup>	% Yield of compound <b>5.1</b> <sup>a,b</sup>
1	74	62	45
2.5	68	94	64
10	76	74	56

<sup>a</sup>conditions: 0.15 mmol photocatalyst, 0.1 mmol phenylacetic acid, x mmol methacrolein, 3 mL dry acetonitrile, N<sub>2</sub> atm, blue LED irradiation for 10 h. <sup>b</sup>The conversion, selectivity and yields were determined using GC.

### 5.2.5 Substrate scope and inhibition

A variety of different acids and alkenes were used to assess the scope of Photo-Giese chemistry initiated by 0.15-Pt-Bi<sub>2</sub>WO<sub>6</sub>, Table 5.4. Initially substituted phenylacetic acid analogues were coupled with methacrolein by irradiated 0.15-Pt-Bi<sub>2</sub>WO<sub>6</sub>. Comparing data from 10 h of irradiation, it was evident that electronic effects had an impact on the observed percentage acid conversion. Electron donating para-methoxy groups resulted in a percentage acid conversion of 40%, whereas electron withdrawing para-chloro groups result in a higher percentage yield, 85%. Steric effects appear to be minimal; the use of 2-methoxyphenylacetic acid and 4-methoxyphenylacetic acid appeared to give similar acid conversions (45% and 40% respectively for 10 h of irradiation).

## Chapter 5

Table 5.4 – Photo-Giese reaction scope – Results of Photo-Giese reactions between phenylacetic acids and electron deficient alkenes initiated by blue light irradiated 0.15-Pt-Bi<sub>2</sub>WO<sub>6</sub>

R <sub>1</sub>	R <sub>2</sub>	R <sub>3</sub>	% Acid conversion <sup>a,b</sup>	% Giese product selectivity <sup>a,b</sup>	% Yield <sup>a,b</sup> (irradiation time)	Normalised % yield/h <sup>-1</sup>
H	Me	CHO	68	94	64 (10 h) <sup>d</sup>	6.4
			99	95	94 (24 h) <sup>c</sup>	3.9
2-MeO	Me	CHO	45	82	37 (10 h) <sup>d</sup>	3.7
4-MeO	Me	CHO	40	81	33 (10 h) <sup>d</sup>	3.3
			88	75	66 (30 h) <sup>c</sup>	2.2
4-Cl	Me	CHO	82	80	65 (10 h) <sup>d</sup>	6.5
			96	83	80 (20 h) <sup>c</sup>	4.0
H	H	CHO	67	92	62 (10 h) <sup>d</sup>	6.2
H	Me	COOMe	56	75	42 (10 h) <sup>d</sup>	4.2
			84	64	54 (30 h) <sup>c</sup>	1.8
H <sup>e</sup>			67	89	59 (10 h) <sup>d</sup>	5.9
			75	99	75 (20 h) <sup>c</sup>	3.8

<sup>a</sup>conditions: 0.15 mmol photocatalyst, 0.1 mmol acid, 0.25 mmol alkene, 3 mL dry acetonitrile, N<sub>2</sub> atm, blue LED irradiation. <sup>b</sup>The conversion, selectivity and yields were determined using GC. <sup>c</sup>Product structures were characterised by <sup>1</sup>H, <sup>13</sup>C and MS from reactions >10 h. <sup>d</sup><sup>1</sup>H NMR of 2 mL of the reaction mixture was confirm the presence of product in reactions = 10 h. <sup>e</sup>The product of the last entry in the table is compound **5.4**.

Higher acid conversions with electron withdrawing substituents was an unexpected trend as electron donating groups allow for easier oxidation of phenylacetic acid. However, the acid inhibition observed in the benzyl alcohol oxidation work described in chapter 3 suggested that electron withdrawing substituents increased the acidity of carboxylic acid groups meaning that acids with electron withdrawing substituents were more competitive binders.<sup>342</sup> It could be suggested that a similar phenomenon is being observed here, where phenylacetic acid compounds with electron withdrawing substituents were stronger acids and so had a better binding affinity to the surface of the photocatalyst which results in a faster oxidation reaction.



## Chapter 5

Methacrolein was not the only alkene used in these Photo-Giese reactions. The use of acrolein gave similar acid conversions (67 %) and percentage selectivities for the desired Photo-Giese product, **5.2** (92 %) to the use of methacrolein suggesting that the extra stabilisation of any radical species afforded by the additional methyl group in methacrolein has no significant effect on the Photo-Giese reaction. The only observable difference between these reaction mixtures was that a broad  $^1\text{H}$  NMR signal (2.05 – 2.35 ppm) consistent with polymer formation was observed in the  $^1\text{H}$  NMR after workup from the reaction using acrolein, Figure 5.16. With the use of acrolein, 0.15-Pt-Bi<sub>2</sub>WO<sub>6</sub> has acted as a radical initiator for polymerisation in creating a benzyl radical which then reacted with a molecule of acrolein to form another radical species. The secondary nature of this newly formed radical meant that instead of being selectively reduced and protonated, as was the case with the ternary radical formed with the use of methacrolein, a polymerising propagation step became competitive, Scheme 5.9. It was difficult to assign a structure to this polymer from this limited information. It could however be suggested that although the absence of a methyl group in acrolein doesn't affect the rate of formation of intended product, it did affect the number of side products observed.

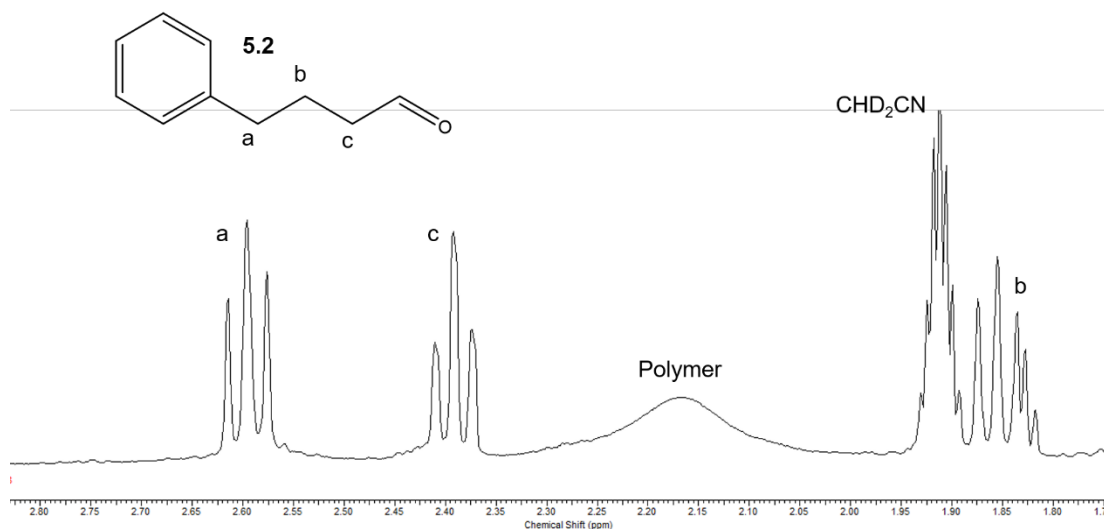
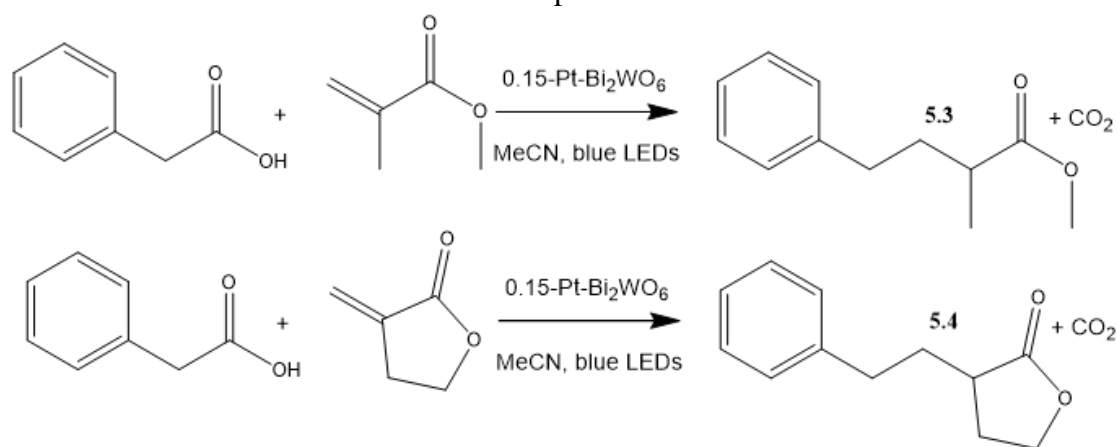


Figure 5.16 – A section of the  $^1\text{H}$  NMR (400 MHz,  $\text{d}_3\text{-MeCN}$ ) of the crude reaction mixture from the Photo-Giese coupling reaction between phenylacetic acid and acrolein, showing peaks consistent with aliphatic proton environments found in **5.2** and a broad peak consistent with polymer formation.



Scheme 5.8 – Photo-Giese reactions between phenylacetic acid and methyl methacrylate for the formation of compound **5.3** and between phenylacetic acid and  $\alpha$ -methylene- $\gamma$ -butyrolactone for the formation of compound **5.4**.

The use of methyl methacrylate and  $\alpha$ -methylene- $\gamma$ -butyrolactone gave coupled Photo-Giese products, **5.3** and **5.4**, in moderate to good yields (yield of **5.3** = 54% and yield of **5.4** = 75%), Scheme 5.8. **5.3** and **5.4** were isolated and characterised by <sup>1</sup>H, Figure 5.17 and Figure 5.18, <sup>13</sup>C NMR and ESI-MS. The NMR spectra were consistent with literature by Sammis et al. and Breit et al. describing the synthesis of both compound **5.3**<sup>343</sup> and **5.4**<sup>344</sup> respectively.

Evidence of coupling between phenylacetic acid and methyl methacrylate was found in the presence of a triplet at 2.60 ppm, Figure 5.17a, which was consistent with the benzyl methylene group coupled to another methylene group. This provided evidence that once formed a benzyl radical coupled to the terminal end of the alkene group of methyl methacrylate. Evidence of protonation of the previously quaternary carbon present in methyl methacrylate was found in a hextet present at 2.47 ppm, Figure 5.17c, which showed coupling to the methyl CH<sub>3</sub> found as a doublet at 1.18 ppm, Figure 5.17g, and the adjacent methylene group found at 2.00 ppm and 1.71 ppm, Figure 5.17b; the chemical shift of the hextet at 2.47 ppm was consistent with a hydrogen environment adjacent to a carbonyl group. The singlet at 3.66 ppm was consistent with a methyl group adjacent to an O atom of an ester functionality, Figure 5.17h. The presence of an ester was supported by the <sup>13</sup>C NMR for **5.3** which showed the presence of an ester functionality with a peak at 177.0 ppm. Evidence for saturation during this Photo-Giese reaction was also found in the <sup>13</sup>C NMR where no peaks were consistent with the alkene found in the methyl methacrylate starting material. Instead, peaks in the <sup>13</sup>C NMR at 33.6 and 39.0 ppm were consistent with a saturated carbon in an aliphatic chain and a saturated carbon adjacent to a carbonyl group respectively. ESI-MS also provided evidence of the formation of **5.3**

## Chapter 5

providing a  $m/z$  peak at 215.1035;  $[C_{12}H_{16}O_2]+Na^+$  had a calculated  $m/z$  value of 215.1048.

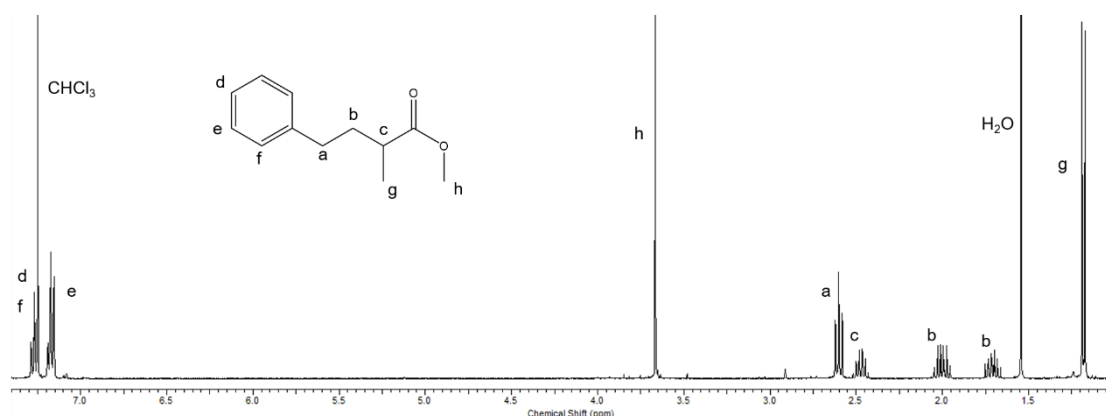


Figure 5.17 – The  $^1H$  NMR spectrum of compound **5.3** ( $CDCl_3$ , 400 MHz).

Interesting spectral features in the  $^1H$  NMR spectrum were evident from data acquired for **5.4**, Figure 5.18. Coupling interactions between diastereotopically split methylene groups, Figure 5.18a and Figure 5.18d, found in the aliphatic 5-membered ring and a newly formed  $^1H$  environment associated to a methine group adjacent to the carbonyl of the ester functionality, Figure 5.18c, led to the presence of complex multiplets. In addition, coupling interactions between the methylene groups found in-between the phenyl and 5 membered aliphatic ring, Figure 5.18b and Figure 5.18e, also produced complicated multiplets. These complex splitting patterns were consistent with the coupling of phenylacetic acid and  $\alpha$ -methylene- $\gamma$ -butyrolactone.<sup>344</sup>

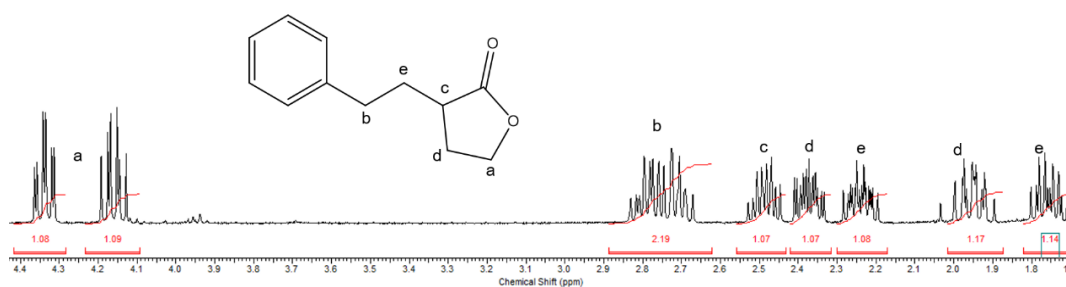
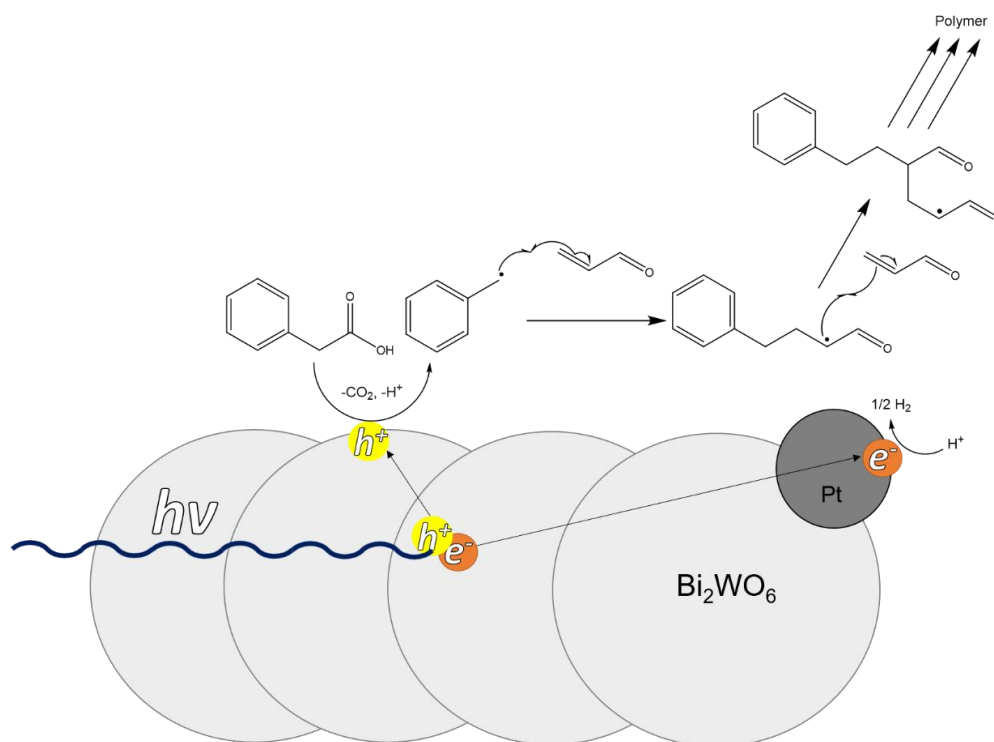


Figure 5.18 – Aliphatic region of the  $^1H$  NMR spectrum of compound **5.4** ( $CDCl_3$ , 400 MHz) showing the complex multiplets that are characteristic of coupling of phenylacetic acid and  $\alpha$ -methylene- $\gamma$ -butyrolactone and subsequent reduction and protonation.

The moderate yield obtained for the reaction between phenylacetic acid and methyl methacrylate (42% after 10 h of irradiation) could be attributed to hydrolysis using surface bound water or hydroxyl groups to form methacrylic acid which subsequently could be photolytically oxidised resulting in the formation of alternative coupling products. In

addition, the formation of methacrylic acid may result in further reaction inhibition as previously suggested.



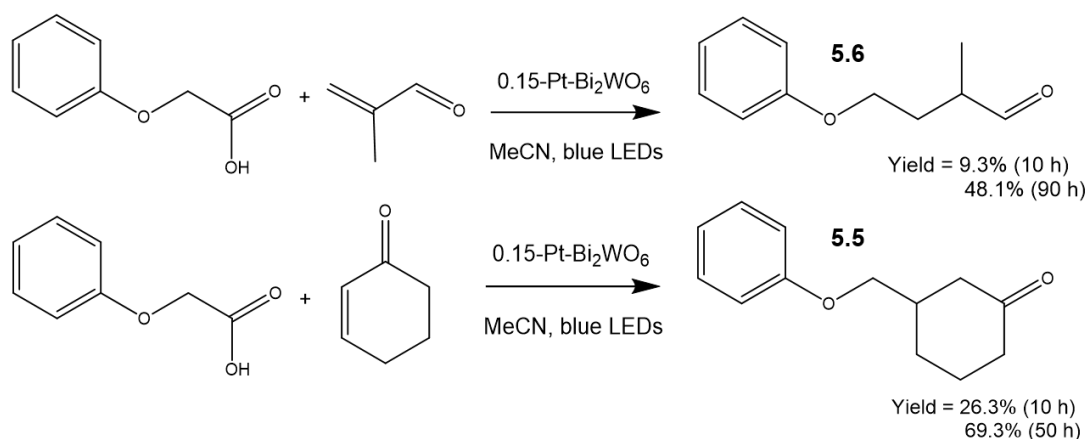
Scheme 5.9 – An illustration showing the capacity for a benzyl radical to propagate into a polymer through repeated reaction with molecules of acrolein.

To test whether carboxylic acid inhibition could be associated to the use of 0.15-Pt-Bi<sub>2</sub>WO<sub>6</sub> for the Photo-Giese chemistry discussed, a coupling reaction between methacrylic acid and phenyl acetic acid was attempted. Electronically, methacrylic acid should behave similarly to methyl methacrylate and so a Photo-Giese coupling product would be expected for an attempted reaction between methacrylic acid and phenylacetic acid. Interestingly, when methacrylic acid was used as an electron-deficient alkene to couple to phenylacetic acid, no conversion of phenylacetic acid to the desired Photo-Giese product was observed. In addition, no conversion to other previously detected products such as bibenzyl, benzyl alcohol or benzaldehyde were observed. This suggested that methacrylic acid was capable of Photo-Giese reaction inhibition. It must be stated that methacrylic acid was not directly observed as a product of any reaction. However, it could be suggested that if any carboxylic acid, other than phenylacetic acid, was able to bind strongly and irreversibly to the surface of 0.15-Pt-Bi<sub>2</sub>WO<sub>6</sub>, even small quantities of these other carboxylic acids could be capable of significant reductions in phenylacetic acid conversion. Further investigation of the impact of the addition of smaller quantities of methacrylic acid were not carried out due to time constraints.

## Chapter 5

Coupling reactions between phenylacetic acid and methacrylamide as well as between phenylacetic acid and cyclohexenone also resulted in no Photo-Giese product formation. It is possible that methacrylamide was able to bind to the surface of 0.15-Pt-Bi<sub>2</sub>WO<sub>6</sub> in a similar fashion to that suggested with in the attempted reaction with methacrylic acid, and therefore caused significant reaction inhibition. This suggestion was supported by the conversion of phenylacetic acid to bibenzyl (yield = 6%); other previously identified oxidation products could not be observed such as benzyl alcohol or benzaldehyde. The formation of bibenzyl also supports the conclusion that methacrylamide was capable of inhibiting oxidation. Unlike the Photo-Kolbe reaction using 0.15-Pt-Bi<sub>2</sub>WO<sub>6</sub> where no bibenzyl was observed, benzyl radicals were able to desorb from the catalyst surface and dimerise. It can be suggested that methacrylamide was bound to oxidation sites which reduced the likelihood of further benzyl radical oxidation.

The lack of Photo-Giese product formation between phenylacetic acid and cyclohexenone was as a result of the extra methylene group bonded to the alkene inductively donating electron density meaning that the alkene was too electron rich for coupling. Some phenylacetic acid conversion (43%) was observed in the attempted Photo-Giese reaction between phenylacetic acid and cyclohexenone; selectivities of 46%, 7% and 22% for bibenzyl, benzyl alcohol and benzaldehyde respectively were observed. The low selectivities for benzyl alcohol and benzaldehyde may have suggested that the carbonyl group of cyclohexenone was able to interact with the photocatalytic surface in order to limit further oxidation of benzyl radicals.



Scheme 5.10 – The decarboxylative photooxidation of phenoxyacetic acid and subsequent Photo-Giese reactions with electron deficient alkenes, to form **5.5** and **5.6**, initiated by blue light irradiation of 0.15-Pt-Bi<sub>2</sub>WO<sub>6</sub>.

When phenoxyacetic acid was oxidised by 0.15-Pt-Bi<sub>2</sub>WO<sub>6</sub> in the presence of cyclohexenone, the desired coupling product **5.5** was observed in a 69% yield after 50 h

of irradiation with blue LED light, Scheme 5.10. **5.5** was isolated and characterised by  $^1\text{H}$ ,  $^{13}\text{C}$  NMR and ESI-MS. The characterisation of **5.5** has not been previously reported, however the data was comparable to the data found for the synthesis of a similar compound formed from the addition of an aniliny methyl radical to cyclohexanone to form the corresponding saturated product.<sup>37</sup>

Evidence of coupling between phenoxyacetic acid and cyclohexene was found in the presence of a doublet at 3.86 ppm, Figure 5.19a, which was consistent with the methylene group adjacent to an O atom coupled to methine environment. The 5.5 Hz coupling constant of this doublet was not observed in the peaks that were furthest downfield within Figure 5.19b; this coupling constant would be observed in these peaks if  $\alpha$ -carbon addition had occurred. In addition, the region consistent with methylene groups adjacent to carbonyl groups and methine groups adjacent to other aliphatic groups gave an integration equivalent to 5 protons. These data support the conclusion that the addition to the  $\beta$ -carbon of cyclohexene had occurred. Complex multiplets in the aliphatic region for the  $^1\text{H}$  NMR of **5.5** were observed as a result of the diastereotopic nature of the methylene groups in the cyclohexanone ring, Figure 5.19b and Figure 5.19c. The relative integrations of the aliphatic peaks in comparison to the aromatic peaks present in the  $^1\text{H}$  NMR spectrum were also consistent with the formation of the desired coupling product. The  $^{13}\text{C}$  NMR spectrum of **5.5** was consistent with the presence of a ketone functionality with a peak at 211.3 ppm. In addition, the  $^{13}\text{C}$  spectrum supported the proposition that the addition of the phenoxy methyl radical is to the  $\beta$ -carbon of cyclohexanone as there are 2 peaks with chemical shifts consistent with carbons adjacent to a carbonyl group (44.9 and 41.3 ppm) and another peak consistent with the carbon environment of an aliphatic CH adjacent to other CH<sub>x</sub> groups (39.0 ppm); this combination would not have been observed upon  $\alpha$ -carbon addition. ESI-MS also provided evidence of the formation of **5.5** providing a m/z peak at 227.1034;  $[\text{C}_{13}\text{H}_{16}\text{O}_2]+\text{Na}^+$  had a calculated m/z value of 227.1043.

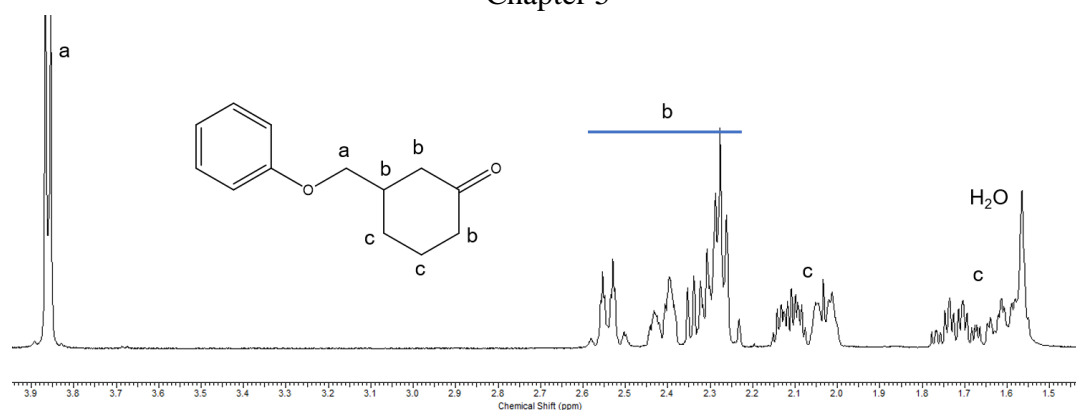
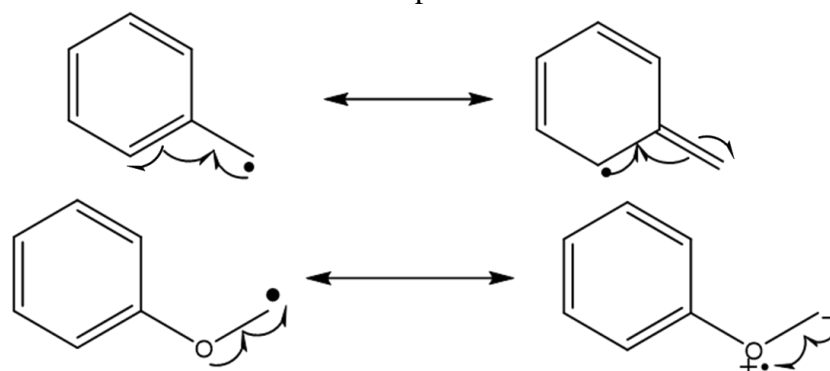


Figure 5.19 - Aliphatic region of the  $^1\text{H}$  NMR spectrum of compound **5.5** ( $\text{CDCl}_3$ , 400 MHz) showing the complex multiplets that are characteristic of coupling of phenoxyacetic acid and cyclohexenone and subsequent reduction and protonation. Solvent impurity (water in  $\text{CDCl}_3$  – 1.6 ppm) is also observed in this spectrum.

Slow coupling between phenoxyacetic acid and methacrolein was also observed; a 48 % yield of product **5.6**, characterised by  $^1\text{H}$ ,  $^{13}\text{C}$  NMR and ESI-MS, was obtained after 90 h of irradiation with blue LED light. The coupling of phenoxyacetic acid to methacrolein was significantly slower than the coupling of methacrolein to phenylacetic acid with yields ca. 7 times lower for the coupling of phenoxyacetic acid and methacrolein after 10 h of irradiation.

It has been previously observed that when dimerising phenylacetic acid and phenoxyacetic acid with platinumised titanium dioxide irradiated by UV, higher yields are obtained for phenylacetic acid (81 % in 19 h) than for phenoxyacetic acid (52 % in 21 h).<sup>30</sup> The reasoning for these phenomena is not obviously clear. However, it could be suggested that the ability of phenoxyacetic acid to undergo C-C coupling, where phenylacetic acid could not, could be attributed to the mesomeric effects that impact on the radical formed from oxidation, Scheme 5.11. The electron donation from the oxygen adjacent to the methylene group has a greater stabilising effect on the phenoxy-methylenyl radical when compared to the stabilising effect from the phenyl ring on the benzyl radical formed from phenylacetic acid oxidation.<sup>345</sup>



Scheme 5.11 – Comparison of electronic effects between a benzyl radical and a phenoxy methyl radical formed from the decarboxylation of phenylacetic acid and phenoxyacetic acid respectively.

The more stable phenoxy methylenyl radical persists for longer and is also more electron rich than a benzyl radical.<sup>345</sup> This stabilisation therefore allows for coupling with the less electron deficient alkene found in cyclohexenone. However, phenoxy methylenyl radicals should be more nucleophilic and this would suggest that phenoxy methyl radicals should be able to react more quickly with methacrolein than with cyclohexanone; in fact, the opposite trend was observed. The inhibition previously observed with methacrylic acid could provide an explanation. If phenoxyacetic acid was a poorly competitive binder to the photocatalyst surface, then phenoxyacetic acid would be oxidised less quickly in the Photo-Giese reaction with methacrolein than in the Photo-Giese reaction with cyclohexenone.

### 5.2.6 Catalyst recycling

A significant advantage of the use of heterogeneous catalysts is the ability to effectively separate the catalyst from the reaction mixture and reuse the material several times. With this in mind, a sample of 0.15-Pt-Bi<sub>2</sub>WO<sub>6</sub> was used in several repeats of the coupling of phenylacetic acid and methacrolein, Figure 5.20. It can be observed that the yield of Photo-Giese product **5.1** decreased each time the catalyst was reused. 90% yield was achieved during the first run, by the fifth run the yield had reduced to 26%. No mechanical mass loss of 0.15-Pt-Bi<sub>2</sub>WO<sub>6</sub> was observed during this experiment that would account for the reduction in phenylacetic acid conversion. In addition, no colour changes were observed that would suggest that elements such as W were dissolved in solution, this suggested that the use of phenylacetic acid does not degrade the photocatalyst.

In order to investigate the steady decline in phenylacetic acid conversion, the used catalyst was studied by DRUVS, PXRD and ATR-IR analysis in order to detect any changes that



## Chapter 5

can account for the loss of activity observed. No significant changes could be observed by PXRD, Figure 5.21a, and the Tauc plot generated from the DRUVS data, Figure 5.21b, which were consistent with crystalline orthorhombic  $\text{Bi}_2\text{WO}_6$  (JCPDS No. 39-0256) and gave an estimated band-gap of 2.85 eV (435 nm) for the material respectively.

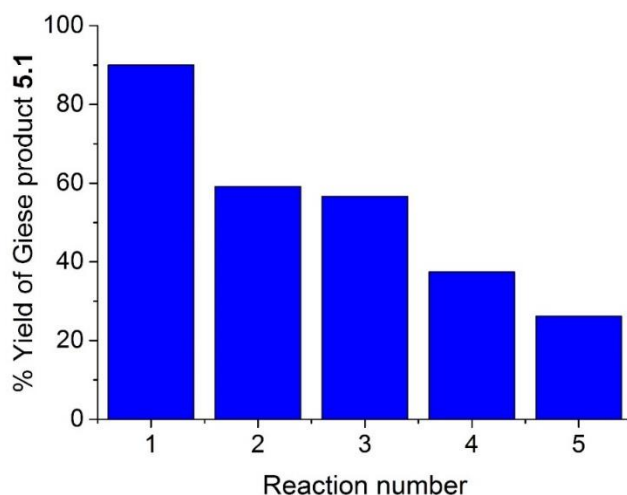


Figure 5.20 – A graph showing the results of the catalyst recycling experiment for the Photo-Giese reaction between phenylacetic acid (0.1 mmol) and methacrolein (0.25 mmol) photocatalysed by blue LED irradiated 0.15-Pt- $\text{Bi}_2\text{WO}_6$ . Irradiation time was 15 h for each reaction, other conditions for each reaction include 3 mL dry acetonitrile and a  $\text{N}_2$  atmosphere.

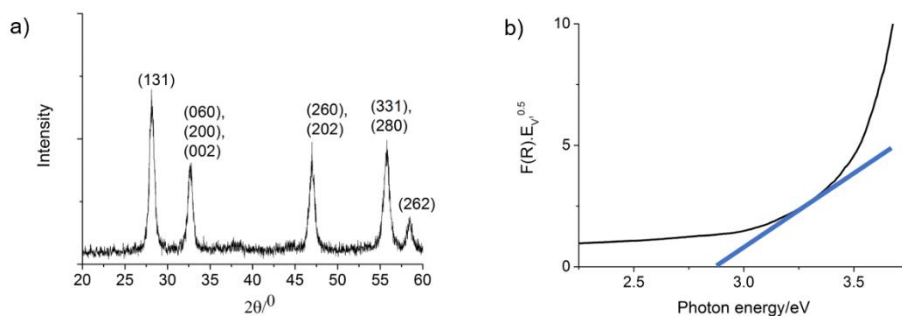


Figure 5.21 – a) PXRD of 0.15-Pt- $\text{Bi}_2\text{WO}_6$  consistent with crystalline orthorhombic  $\text{Bi}_2\text{WO}_6$  (JCPDS No. 39-0256); b) The Tauc plot used to estimate the band-gap for the indirect semiconductor, 0.15-Pt- $\text{Bi}_2\text{WO}_6$ .

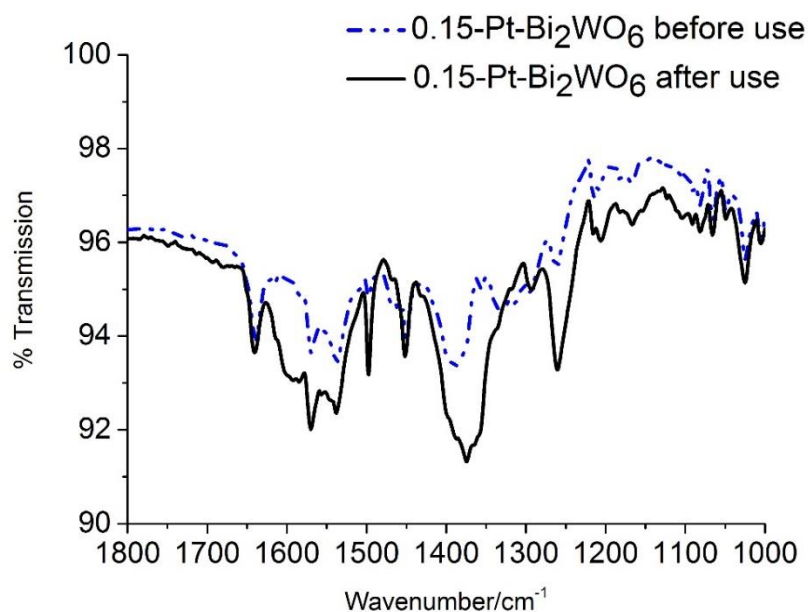


Figure 5.22 – Section of ATRIR for the 0.15-Pt-Bi<sub>2</sub>WO<sub>6</sub> photocatalyst before and after use in 5 Photo-Giese reactions coupling phenylacetic acid and methacrolein and inhibit the binding of phenylacetic acid and subsequently slow the rate of the intended Photo-Giese reaction.

Absorbance bands in the ATR-IR spectrum, Figure 5.22, for the used 0.15-Pt-Bi<sub>2</sub>WO<sub>6</sub> suggested the presence of organic material in the used photocatalyst sample. The sharp band at 1260 cm<sup>-1</sup> was consistent with C-H bending in methyl groups. A broad band between 1330 cm<sup>-1</sup> and 1450 cm<sup>-1</sup> could be attributed to C-O stretches. A sharp band at 1500 cm<sup>-1</sup> could be consistent with C-H bends in methylene groups and a broad band between 1520 cm<sup>-1</sup> and 1633 cm<sup>-1</sup> can be attributed to the presence of carboxylate functionalities, Figure 5.22. This data is consistent with the presence of a carboxylic acid which has irreversibly bound to the surface of the 0.15-Pt-Bi<sub>2</sub>WO<sub>6</sub> photocatalyst. It could be suggested that as more methacrolein is being added in each repeat reaction, more methacrolein can be oxidised at the catalyst surface and so have a greater impact on the inhibition of phenylacetic acid decarboxylative oxidation. It is also possible that the build-up of other carboxylic acids at the surface of the catalyst is responsible for inhibition and the associated reduction of phenylacetic acid conversion.

It can be concluded that substrate inhibition limits both the scope and the viability of 0.15-Pt-Bi<sub>2</sub>WO<sub>6</sub> as a visible light heterogeneous photocatalyst for the Photo-Giese coupling of carboxylic acids and electron deficient alkenes. However, it can be suggested that inhibition was also important for the selectivity of these systems. Therefore, future work related to the use of visible light heterogeneous photocatalysts should focus on understanding and diminishing the detrimental effects of inhibitory interactions between

metal oxide surfaces and substrates that have the potential to form carboxylic acid functionalities whilst maintaining the selectivity observed.

### 5.3 Conclusion

The work outlined here met the objectives outlined as the photochemical platinization of bismuth tungstate allowed for the more effective decarboxylation of phenylacetic acid when compared to bare bismuth tungstate. It was suggested that the addition of platinum significantly increased the selectivity for dihydrogen formation which was also a driving force behind decarboxylation and the formation of further oxidation products. The objective to investigate the potential of such materials in Photo-Giese reactions was also realised because 0.15-Pt-Bi<sub>2</sub>WO<sub>6</sub> was also found to be a successful photocatalyst used to generate Giese coupled products between electron rich bibenzyl radicals and electron deficient Michael acceptors. However, the platinization of bismuth tungstate did not entirely change the interaction between carboxylic acids and the surface as evidence of aldehyde selectivity from this reaction could be aligned with the formation of small amounts of various carboxylic acids. Further work is needed to assess which acid was present as the major inhibitor to further oxidation for the reaction systems explored in Chapter 5.

This work contributes to the overall aim of this thesis by broadening the scope of the chemistries that are possible with the use of bismuth containing semiconducting systems as heterogeneous photocatalyst to Giese coupling reactions and adds to the work in this thesis which shows their use as alcohol oxidation and trifluoromethylation photocatalysts. It can also be said that work in Chapter 5 supports conclusions made with regards to carboxylic acid inhibition controlling selectivity in these systems, as the work provides 2 more reaction systems in which aldehyde selectivity was achieved (i.e. benzaldehyde selectivity after phenylacetic acid decarboxylation and aldehyde product selectivity after Giese coupling).

## 6 Conclusions and Future Work

### 6.1 Conclusions

It can be concluded that this thesis advances the knowledge within the field of heterogeneous photocatalysis by demonstrating how bismuth containing semiconductors, namely bismuth vanadate and bismuth tungstate, can be used in a wide range of different selective chemical transformations that are initiated by visible light only. Previously the investigation of the potential for bismuth containing semiconductors acting as heterogeneous photocatalysis was limited to alcohol oxidation by bismuth tungstate and amine oxidation by bismuth vanadate or using these materials as supports for the immobilisation of homogeneous photocatalytic complexes.

However, the major addition to the knowledge within the area of heterogeneous photocatalysis that this thesis contributes is the concept that carboxylic acid inhibition is the cause of aldehyde selectivity across a number of different reactions and a number of different materials. This is possibly the most major contribution to this research field as this information can be used to optimise the surfaces of heterogeneous photocatalysts in order to balance selectivity and the ability to reuse and recycle these photocatalysts without seeing a decline in conversion rate.

The work in this thesis meets all the objectives set and each objective contributes to the principal aim of investigating bismuth containing semiconductors as potential heterogeneous photocatalysts for selective chemical transformations of value under visible light irradiation and, where selectivity is observed, understanding the reasons for this selectivity. How this was achieved is outlined in the conclusions of each individual chapter.

The connectivity between the different chapters of this thesis highlight how the objectives contribute to the overall aim. The objective of Chapter 2 was to establish which of the previously reported bismuth containing semiconductors could act as a suitable photocatalyst for selective benzyl alcohol oxidation and also make connections between the physical properties of these materials and the alcohol conversions and aldehyde selectivities observed. Nan-BiVO<sub>4</sub> was the best of the photocatalysts used and inspired the main objective of Chapter 3 which was to gain a better understanding of the effects resulting in benzaldehyde selectivity and also a better understanding of the role of other components in this reaction system, such as the need for dioxygen.

## Chapter 6

The inconclusive results from Chapter 3 with regards to the source of oxygen exchange observed in the benzyl alcohol oxidation inspired the work in Chapter 4 which was focussed upon attempting to conclusively observe the incorporation of a functional group into the desired, organic product using a bismuth containing semiconductor as a heterogeneous photocatalyst.

The interactions between surface and the carboxylic acids discussed in Chapters 3 and 4 (i.e. inhibition to enhance selectivity in Chapter 3 and binding and eventual degradation in Chapter 4) inspired the desire to modify these bismuth containing semiconductors in order to investigate how this changed the interaction between the catalyst and carboxylic acid which was a major objective of Chapter 5 and eventually led to the successful use of the photochemically platinised bismuth tungstate irradiated by blue light as a heterogeneous photocatalyst for Photo-Giese coupling reactions.

It can be said that with each step through this thesis outlined above, either the work shows how bismuth containing semiconductors can be used in heterogeneous photocatalytic systems which have not been explored or the work advances our understanding of the role of different components within these systems. Therefore, each of these steps contributes to the overall aim of this work given above.

### **6.2 Future Work**

There are many opportunities for further work that expand upon the results described in Chapter 4. Nan-BiVO<sub>4</sub> and Bi<sub>2</sub>WO<sub>6</sub> could be used in the oxytrifluoromethylation of a wide range of different alkenes using Umemoto's reagents. It was decided that this work would not form part of this thesis in order to explore more challenging trifluoromethylation reactions. It was also noted that similar reactions are possible with the use of abundant and cheap copper salts in solution. However, the use of a heterogeneous photocatalyst for trifluoromethylation of alkenes could be considered more sustainable as it may be easier to recover and reuse a heterogeneous photocatalyst in this system. It is also possible that the use of a metal oxide semiconductor coupled with a hydrogen evolution catalyst, such as 0.15-Pt-Bi<sub>2</sub>WO<sub>6</sub> synthesised in chapter 5, could be used to trifluoromethylate alkenes which are then reduced and protonated. This work would be of interest as it would widen the product scope of heterogeneous photocatalytic trifluoromethylation by avoiding the further oxidation and oxygenation reported in chapter 4.

## Chapter 6

In chapter 4, it was concluded that photodegradation of nan-BiVO<sub>4</sub> occurred, subsequently leading to the trifluoromethylation and trifluoroacylation of aromatics via a Friedel-Crafts mechanism. It was claimed that photodegradation was mediated by trifluoroacetic acid. It is likely that the trifluoroacetate anion of the pyridyl trifluoroacetate ester formed from the reaction between pyridine-*N*-oxide and trifluoroacetic anhydride was the source of the trifluoroacetic acid molecules necessary for photodegradation. Conducting ion exchange with a less basic counter anion may result in the formation of a pyridyl trifluoroacetate ester which can be used alongside a bismuth containing semiconducting material in the photocatalytic trifluoromethylation of aromatics.

In chapter 3, it was concluded that inhibition from small amounts of carboxylic acids capable of strong adsorption to the surface of the respective photocatalysts was important in achieving selectivity for benzaldehyde as the further oxidation was limited. It could be suggested that a similar phenomenon could be used to explain the high selectivity observed in the Photo-Giese reactions in chapter 5. However, it could also be said that significant quantities of carboxylic acids such as methacrylic acid can severely restrict the viability of the photocatalysts used.

More work is needed in relation to several aspects of these Photo-Giese reactions. Firstly, the specific identification of the side products of these reactions is important in understanding what specific interaction is causing inhibition in these systems. It could be speculated that methacrylic acid, benzoic acid and the corresponding carboxylic acid to the final Photo-Giese coupling products could all be present. It is possible that the decarboxylation of these species leads to the formation of other radical species which were also capable of forming coupled products with the electron deficient alkenes; the discovery of the presence of such products could prove to be useful. In addition, an assessment of the inhibition effects on this Photo-Giese reaction from the addition of small amounts of the various potential carboxylic acid inhibiting reagents could provide useful information with regards to understanding the effect of different substituents on inhibition. This work could also support any conclusions reached in the investigation of by-products in this Photo-Giese reaction.

With regards to the general direction of research into the use of heterogeneous photocatalysis for selective chemical transformations, the method of binding of these inhibiting species needs to be fully characterised. However, characterisation is difficult especially on the surface of bismuth-containing semiconductors. The capacity to only

## Chapter 6

synthesise relatively low surface areas bismuth-containing materials limits substrate adsorption and so a highly sensitive technique would be needed. In addition, different binding sites could have different interactions with the same substrates. This furthers the need for a highly sensitive technique that yields data with high levels of resolution. High resolution is necessary in order to allow for analysis of distinct but similar surface binding interactions. It may be possible to support this experimental work with DFT calculations of binding interactions between model metal oxide surfaces and simple compounds.

Once the binding interaction is better characterised, this information could be used to synthesise an ideally inhibited system that can be used repeatedly in selective heterogeneous photocatalysis. If an optimal quantity of substrate could permanently bind to the surface of a photocatalyst so that, under irradiation, an intended redox process progressed with a sufficient rate, without the formation of any additional inhibiting by-product, then high selectivities could be achieved with sufficient but more importantly sustainable conversion rates. It should be an aim of future work in the field of heterogeneous photocatalysis to achieve such a system.

Much work would be needed in order to achieve such a system. Analysis of the surface of visible light absorbing semiconducting materials would be needed in order to understand which sites need to be inhibited. Identification of such sites could also be used to determine what compounds would achieve strong and selective adsorption to these sites. However, the most challenging aspect of achieving such a system could be finding an inhibiting compound that adsorbs strongly but does not become mineralised at the surface of the irradiated photocatalyst.

## 7 Experimental

### 7.1 Characterisation

#### 7.1.1 Semiconductor characterisation

Powder X-ray Diffraction (PXRD) allows for the characterisation of crystalline materials using X-rays diffracted around atoms on characteristic planes. A material (ca. 1g) was placed on an alumini disk and spread out in the central disk so that the material lines up with the top of the disk. Data was acquired using a Bruker-AXS D8 Advance instrument fitted with a Lynxeye detector and acquired with Cu K $\alpha$  radiation between 10- 70° 2 $\theta$  and angles were moved through in 0.014° steps. The EVA software package was used for initial characterisation. Minimum crystallite size was also calculated using the FWHM and Scherrer's equation.

UV-vis Diffuse Reflectance Spectra (DRUVS) was used to build Tauc plots to establish the band gap for the materials used. A material (ca. 1g) was pressed between 2 cleaned quartz plates. Collection time was 10 s per collection; 10 spectra were combined and average; data was smoothed using a boxcar width of 30. Spectra were recorded on an Ocean Optic Inc. HR2000+ High Resolution Spectrometer after dark background and light background spectra were collected and subtracted from the acquired data to obtain reflectance from the sample. A SiO<sub>2</sub> white disk was used to collect the light background spectrum.

Scanning Electron Microscopy (SEM) was performed on a FEI Sirion scanning electron microscope or a Schottky field emission scanning electron microscope, at an accelerating voltage of 15 kV. Samples were prepared by spreading a small amount of powder onto carbon tape mounted on an aluminium stub or by dispersion in ethanol which was dropped onto a copper TEM grid and dried at room temperature in air. Energy dispersive x-ray (EDX) was used to determine the composition for the samples using an EDAX Phoenix EDS X-ray spectrometer. A voltage of 15 keV was used to analyse samples with a 30 second exposure time.

TEM images and electron diffraction patterns were obtained using a JEOL 2011 transmission electron microscope operated at 200 kV accelerating voltage. CCD images were extracted using Gatan Digital Micrograph software. Prior to analysis, solid samples for TEM imaging were ground in methanol and sonicated for 15 minutes to disperse. One drop of the dispersion was deposited onto 3 mm holey carbon coated copper grids and allowed to dry in air.



## Chapter 7

N<sub>2</sub> isotherms were generated using 100 mg (measured in triplicate) of samples dried under nitrogen for 6 h at 80 °C, and nitrogen adsorption isotherms were measured at 78 K on a Micromeritics Tristar 3000. Brunauer, Emmett and Teller (BET) N<sub>2</sub> surface area analysis was performed subsequently using P/P<sub>0</sub> range between 0.05 and 0.2 where curve linearity can be observed.

Attenuated total reflectance Infra-Red (ATR-IR) spectra were used to analyse organic adsorbates on the surface of catalysts and were recorded on a Perkin Elmer Spectrum Spectra. Before use methanol was used to wash the ATR-IR plate and allowed to evaporate. Background spectra were then collected from 650 to 4000 cm<sup>-1</sup> over an average of 4 scans. The sample (ca. 100 mg) was then placed on the plate for collection and compressed to form a disk. Data were recorded from 650 to 4000 cm<sup>-1</sup> over an average of 4 scans and backgrounds subtracted to generate the final spectrum.

X-ray fluorescence (XRF) was used to observe characteristic secondary emissions for specific elements to examine semiconductor content. Data collection was carried out on a Horiba XGT-7000 spectrometer, the X-ray gun tube diameter was 1.2 mm, the X-ray tube voltage was 30 kV, with a current of 0.025 mA. Acquisition time was 120 s. Less than 1 mg of sample could be used using this technique and data was collected in triplicate and averaged to give the final analysis.

The inductively coupled plasma mass spectrometry instrument is an Agilent 7700x ICP-MS. Samples (ca. 10 mg) were digested using a Milestone Ethos UP microwave digestion system fitted with an SK 15 rotor, which also involving destruction of the sample with dissolution in concentrated acid. The machine was calibrated using standards ranging from 0 to 1000 ppb. Measurements for vanadium were obtained using the [no gas] sampling mode, and [He] mode (gas collision mode) for bismuth.

Diffuse light scattering (DLS) and zeta potential measurements use light scattering to assess particle size and surface charge. Data were recorded on a Zetasizer instrument and analysed using the DTS v. 5.1 provided by Malvern. Semiconductor (ca. 10 mg) was dispersed in acetonitrile (10 mL, 1 mgmL<sup>-1</sup>) and placed in a quartz U-bend cell. The samples were measured at 25 °C and measurements were carried out in triplicate with 10-15 runs per single measurement.

### 7.1.2 Organic molecule characterisation

<sup>1</sup>H, <sup>19</sup>F, <sup>13</sup>C Nuclear magnetic resonance (<sup>1</sup>H NMR 400 MHz, <sup>19</sup>F NMR 376.3 MHz, <sup>13</sup>C NMR 100.6 MHz) spectra were recorded on a JEOL ECX400 and ECS400 spectrometers at room temperature. Chemical shifts are referenced to the deuterium lock of residual

## Chapter 7

solvent. A sample (minimum 10 mg) was dissolved in deuterated solvent, which contained a known concentration of internal calibrant for quantification when necessary. <sup>1</sup>H spectra were collected between -1 and 14 ppm and the number of scans was controlled so that data collection took ca. 1 min. <sup>19</sup>F spectra were collected between -200 and 250 ppm and the number of scans controlled so that data collection took ca. 1 min. <sup>13</sup>C spectra were collected between -20 and 220 ppm and the number of scans controlled so that data collection took at least 1 h.

Gas Chromatography (GC) was performed on an Agilent/HP 6890 (which contained a reverse phase column), with an injection volume of 1  $\mu$ L, using compressed air as a carrier gas at 1 mL min<sup>-1</sup>, a flame ionised detector at 250 °C, Chrompack DB-5ms column between 90 and 300 °C with ramp rate 20 °Cmin<sup>-1</sup>. Data collection would take 11.5 min, the oven took 5 min between runs to cool to the starting temperature. Samples were always dissolved in acetonitrile and made to a minimum concentration of 1 mM.

Mass spectrometry measurements were performed on a Bruker micrOTOF MS (ESI). A minimum of 5 mg of sample were submitted for analysis. Air sensitive samples were submitted using sealed vials made up in a glove box. The most frequently suggested solvent for dissolution before analysis was methanol.

CHN analysis of solid samples was obtained from the departmental service using an Exeter Analytical CE-440 analyser. Samples were heated to 1500 °C under He, and the elemental composition was determined from the combustion products. A minimum of 5 mg was supplied for organic samples. When observing surface coverage of a semiconductor a minimum of 100 mg was supplied for analysis.

### 7.1.3 Blue LED calibration

The irradiance at a distance of 2 cm from the 30 W blue LED used throughout this work was measured on a regular basis and at least every 3 months throughout the course of this project. The irradiance measured was 250 mWcm<sup>-2</sup> on average, the lowest irradiance was 245 mWcm<sup>-2</sup> and the highest was 257 mWcm<sup>-2</sup>.

Table 7.1 – The irradiance obtained from 2 cm away from the 30W blue LED array

Date (Month-Year)	Irradiance/mWcm <sup>-2</sup>
February-2015	249
May-2015	253
July-2015	257
October-2015	248
January-2016	249
April-2016	245
June-2016	245
September-2016	252
December-2016	253
January-2017	253
March-2017	247

#### 7.1.4 Control experiments

For each reaction control experiments were carried out assessing the need for photocatalyst, light and the impact of an O<sub>2</sub> atmosphere.

For each control assessing the need for photocatalyst, the reaction was carried out under irradiation from the 30 W blue LED array for the same length of time as the initial reaction attempt but simply without photocatalyst present. All other addition steps were carried out in the order given in their corresponding experimental. Analysis was carried out in the same way as detailed in the experimental section for each reaction.

For each control assessing the need for light, the reaction was prepared in the same way as stated in the experimental below. However, experiments were carried out in the absence of light using a blackout screen and heated to 40 °C which is the same as the

temperature reached after irradiation with the 30 W blue LED array (the temperature of reaction mixture did not increase above 40 °C regardless of irradiation time or solvent). The heated control experiments were carried out over 20 h. Analysis was carried out in the same way as detailed in the experimental section for each reaction.

For each control assessing the need for dioxygen, reactions mixtures were made on a Schlenk line using dry solvents. An Ar atmosphere was used in place of the dioxygen and was obtained using the gas line of the Schlenk apparatus. Analysis was carried out in the same way as detailed in the experimental section for each reaction.

## 7.2 Chapter 2 Experimental

### 7.2.1 Materials and Reagents

Bismuth nitrate pentahydrate (98%), iron nitrate nonahydrate (99%), D-fructose (99%), ethylene glycol (99%), sodium tungstate dihydrate (99%), ethylenediaminetetraacetic acid (98.5%), benzyl alcohol (99%) and *d*<sub>6</sub>-DMSO (99.5%) were purchased from Sigma Aldrich. Nitric acid (70%), sodium hydroxide and acetonitrile were purchased from Fisher Scientific. Ethanol was purchased from VWR. Ammonium metavanadate (98%) was purchased from Riedel-de-Haen. Maleic acid and ammonium molybdate were purchased from Fisons. P25 titania was purchased from Degussa. All chemicals were used as received.

### 7.2.2 Bismuth ferrite (BiFeO<sub>3</sub>) synthesis<sup>177</sup>

Bismuth nitrate pentahydrate (2.42 g, 5 mmol) and iron nitrate nonahydrate (2.02 g, 5 mmol) were added to distilled water (25 mL) and concentrated nitric acid (2 mL). Solvent was removed *in vacuo* at 95 °C; the precursors dissolve on heating. Once a paste forms the mixture was heated to 130 °C for a further 30 minutes. The resulting solid was heated at 450 °C for 3 h with a heating rate of 5 °C min<sup>-1</sup>. After cooling to room temperature, the resulting brown powder was washed with deionised water (50 mL) and left to dry overnight at 60 °C. Powder X-ray diffraction data of BiFeO<sub>3</sub> were consistent with rhombohedrally distorted perovskite bismuth ferrite (JCPDS No. 20-0169).

### 7.2.3 Bismuth oxide nanoparticle (β-Bi<sub>2</sub>O<sub>3</sub>) synthesis<sup>134</sup>

D-fructose (0.27 g, 1.5 mmol) was dissolved in ethylene glycol (35 mL). To this solution, bismuth nitrate pentahydrate (0.73 g, 1.5 mmol) was added and stirred for 30 minutes to give a colourless solution. The solution was divided and placed into two 23 mL Teflon-lined autoclaves and heated to 160 °C for 15 h with a heating rate of 5 °C min<sup>-1</sup>. After

cooling to room temperature, the material was washed with a 1:1 mixture of ethanol (20 mL) and distilled water (20 mL), three times and then dried overnight at 60 °C to yield a grey powder. The powder was then heated at 300 °C for 1 h to yield a pale-yellow powder with a heating rate of 5 °C min<sup>-1</sup>. This powder was washed with distilled water then dried overnight at 60 °C. Powder X-ray diffraction data of  $\beta$ -Bi<sub>2</sub>O<sub>3</sub> were consistent with crystalline tetragonal bismuth oxide (JCPDS No. 78-1793).

#### **7.2.4 Bismuth tungstate nanoflower (Bi<sub>2</sub>WO<sub>6</sub>) synthesis<sup>186</sup>**

Sodium tungstate dihydrate (1.32 g, 4 mmol) was dissolved in deionised water (45 mL) to give a colourless, transparent solution. Bismuth nitrate pentahydrate (3.88 g, 8 mmol) was added and stirred vigorously for 2 h. The remaining white dispersion was shared equally into 3 x 23 ml Teflon autoclaves and heated to 180 °C for 12 h with a heating rate of 5 °C min<sup>-1</sup>. The resulting solid was centrifuged out of suspension at 4000 rpm for 30 minutes using an Eppendorf Centrifuge 5702. The resulting ivory coloured pellet was washed with deionised water (50 mL) and left to dry overnight at 60 °C. Powder X-ray diffraction data of Bi<sub>2</sub>WO<sub>6</sub> were consistent with crystalline orthorhombic Bi<sub>2</sub>WO<sub>6</sub> (JCPDS No. 39-0256).

#### **7.2.5 Ethylenediaminetetraacetic acid (EDTA) mediated bismuth vanadate nanoparticle (nan-BiVO<sub>4</sub>) synthesis<sup>137</sup>**

Bismuth nitrate pentahydrate (4.85 g, 10 mmol) and EDTA (2.93 g, 10 mmol) were added to 100 mL 2M nitric acid and stirred for 30 mins until clear. Ammonium metavanadate (1.17 g, 10 mmol) was added to this solution and stirred for 2 h giving a green-yellow solution. The solution was heated at 90 °C for 6 h in a Teflon-lined autoclave with a heating rate of 5 °C min<sup>-1</sup> and after cooling to room temperature the resulting mixture was centrifuged at 4000 rpm for 30 min to yield a yellow powder, which was washed alternately with distilled water and ethanol and then dried overnight at 60 °C. Powder X-ray diffraction data of BiVO<sub>4</sub> were consistent with crystalline monoclinic BiVO<sub>4</sub> (JCPDS no. 14-0688).

#### **7.2.6 Bulk bismuth vanadate synthesis**

Bismuth nitrate pentahydrate (5.53 g, 12 mmol) was dissolved in 70% aqueous nitric acid (20 mL). Ammonium metavanadate (1.41 g, 12 mmol) was also dissolved in 5 M sodium hydroxide (20 mL). After stirring for 30 minutes, these solutions were mixed to give an orange precipitate. After stirring for a further 30 minutes, this solution was then decanted into Teflon lined autoclaves and heated at 240 °C for 16 h with a heating rate of 5 °C min<sup>-1</sup>. Centrifugation at 4000 rpm for 1 h settles out the orange ppt using an Eppendorf 5702

centrifuge. The solid was washed 3 times with distilled water and dried overnight at 60 °C. Powder X-ray diffraction data of BiVO<sub>4</sub> were consistent with crystalline monoclinic BiVO<sub>4</sub> (JCPDS no. 14-0688).

### 7.2.7 Benzyl alcohol aerobic oxidation utilising blue light irradiated semiconducting photocatalysts

A known amount of semiconducting photocatalyst (100 μmol) was added to a Schlenk flask containing benzyl alcohol stock solution (1 mL, 0.1 mmol in acetonitrile) and 9 mL of acetonitrile. The mixture was left to stir vigorously for 30 min to disperse the catalyst. The mixture was then irradiated with a 30 W blue LED array at a distance of 2 cm with an irradiance of 230 mW/cm<sup>2</sup>. The mixture reached ca. 40 °C by the end of the reaction and after irradiation, the catalyst was removed using centrifugation at 4000 rpm for 30 min. For GC analysis, 1 mL of supernatant was taken and 1 μL injected. For NMR analysis, the supernatant was reduced in volume using a rotary evaporator at 65 mbar at 20 °C, and the residue dissolved in d<sub>6</sub>-DMSO containing maleic acid as an internal standard.

**<sup>1</sup>H NMR:** (d<sub>6</sub>-DMSO, 400 MHz) δ<sub>H</sub>

Benzyl alcohol – 7.23-7.31 (4H, m, o/m-H<sub>ar</sub>), 7.14-7.21 (1H, m, p-H<sub>ar</sub>) 4.45 (2H, s, CH<sub>2</sub>OH)

Benzaldehyde – 9.98 (1H, s, CHO), 7.87 (2H, d, J = 7.3 Hz, o-H<sub>ar</sub>), 7.68 (1H, t, J = 7.3 Hz, p-H<sub>ar</sub>), 7.57 (2H, t, J = 7.3 Hz, m-H<sub>ar</sub>)

**GC:**

Benzyl alcohol, R<sub>t</sub> = 3.04 min

Benzaldehyde, R<sub>t</sub> = 2.72 min

## 7.3 Chapter 3 Experimental

### 7.3.1 Materials and Reagents

4-Methoxybenzyl alcohol (98%), 4-methylbenzyl alcohol (98%), 4-ethylbenzyl alcohol (99%), 4-isopropylbenzyl alcohol (97%), biphenyl-4-methanol (98%), 4-chlorobenzyl alcohol (99%), 4-bromobenzyl alcohol (99%), 4-iodobenzyl alcohol (97%), 4-trifluoromethylbenzyl alcohol (98%), 4-nitrobenzyl alcohol (99%), 4-hydroxybenzyl alcohol (99%), 4-nitrobenzaldehyde (99%), methyl 4-formylbenzoate (99%), 4-methoxybenzaldehyde (98%) and cuminaldehyde (98%) 4-nitrobenzoic acid (98%), 4-nitroacetophenone (98%), mono-methyl terephthalate (97%), 4-isopropylbenzoic acid

## Chapter 7

(98%), *p*-acetanisole (98%), *p*-anisic acid (99%), lithium aluminium deuteride (98%), deuterium oxide (99%), sodium hydride (95%), 4-methoxybenzyl chloride (99%) and silica were purchased from Sigma Aldrich. Methyl (4-hydroxymethyl) benzoate (99%), 4-acetamido benzyl alcohol (97%), methyl 4-acetylbenzoate (99%) and 4-isopropylacetophenone (97%) were purchased from Alfa Aesar. Tetrahydrofuran, dichloromethane, ethyl acetate and petroleum ether (40 – 60 °C) were purchased from VWR. Magnesium sulfate was purchased from Fisher scientific. 18-labelled water (99%) was purchased from Cambridge Isotope Laboratories. Dioxygen (99%) was purchased from BOC gases. All chemicals were used as received with the exception of tetrahydrofuran which was dried by distillation from sodium/benzophenone. Sodium metal (99%) and benzophenone (99%) were purchased from Sigma Aldrich.

### 7.3.2 Synthesis of $\alpha$ -D<sub>2</sub>-(4-methoxy)benzyl alcohol

Lithium aluminium deuteride (388mg, 9.23 mmol) was dispersed in dry THF (20 mL) and 4-methoxybenzoic acid (850 mg, 5.59 mmol) was dissolved in dry THF (10 mL) separately. The 4-methoxybenzoic acid solution was slowly added to the lithium aluminium deuteride dispersion and then the mixture was refluxed at 65 °C for 5 h. Once cooled to room temperature, D<sub>2</sub>O (15 mL) was added slowly and the mixture was refluxed again for 15 minutes. Once cooled to room temperature, THF (50 mL) was added and heated to 50 °C for 15 minutes. Once cooled, the dispersion was filtered and dried with MgSO<sub>4</sub>. After further filtration, solvent was removed *in vacuo*.

**<sup>1</sup>H NMR:** (CDCl<sub>3</sub>, 400 MHz)  $\delta_{\text{H}}$

$\alpha$ -D<sub>2</sub>-(4-methoxy)benzyl alcohol - 7.18 (2H, d, J = 9.2 Hz, 2-H<sub>ar</sub>), 6.84 (2H, d, J = 9.2 Hz, 3-H<sub>ar</sub>), 3.68 (3H, s, CH<sub>3</sub>O)

**ESI-MS:**

$\alpha$ -D<sub>2</sub>-(4-methoxy)benzyl alcohol

Calc for [C<sub>8</sub>H<sub>8</sub>D<sub>2</sub>O<sub>2</sub>]+Na<sup>+</sup> = 163.0699 Found 163.0691 (4.8 ppm error)

### 7.3.3 Synthesis of <sup>18</sup>O-labelled (4-methoxy)benzyl alcohol

Sodium hydride (12 mg, 0.5 mmol) was added to <sup>18</sup>O labelled water (250 mg) and was stirred for 15 minutes. 4-Methoxybenzyl chloride (136.5  $\mu$ L, 0.75 mmol) was added to the solution and the mixture was stirred overnight. The organic products were taken up in DCM and column chromatography was used to obtain only the labelled alcohol product; a 33% ethyl acetate in pet. ether (40 – 60 °C) solvent mixture was used, R<sub>f</sub> of alcohol = 0.15.

**<sup>1</sup>H NMR:** (CDCl<sub>3</sub>, 400 MHz) δ<sub>H</sub>

<sup>18</sup>O-labelled (4-methoxy)benzyl alcohol - 7.18 (2H, d, J = 9.2 Hz, 2-H<sub>ar</sub>), 6.84 (2H, d, J = 9.2 Hz, 3-H<sub>ar</sub>), 4.37 (2H, s, CH<sub>2</sub>OH), 3.68 (3H, s, CH<sub>3</sub>O)

**ESI-MS:**

<sup>18</sup>O-labelled (4-methoxy)benzyl alcohol

Calc for [C<sub>8</sub>H<sub>10</sub>O<sup>18</sup>O]<sup>+</sup>K<sup>+</sup> = 179.0360 Found 179.0358 (-1.1 ppm error)

### 7.3.4 Benzyl alcohol aerobic oxidation utilising blue light irradiated semiconducting nan-BiVO<sub>4</sub>

Nan-BiVO<sub>4</sub> (32.3 mg, 100 μmol) was added to a Schlenk flask containing benzyl alcohol stock solution (1 mL, 0.1 mmol in acetonitrile) and 9 mL of acetonitrile. The mixture was left to stir vigorously for 30 min to disperse the catalyst under an oxygen atmosphere via a balloon. The mixture was then irradiated with a 30 W blue LED array at a distance of 2 cm with an irradiance of 230 mW/cm<sup>2</sup>. The mixture reached ca. 40 °C by the end of the reaction and after irradiation, the catalyst was removed using centrifugation at 4000 rpm for 30 min. The supernatant was reduced in volume using a rotary evaporator at 65 mbar at 20 °C, and the residue dissolved in d<sub>6</sub>-DMSO containing maleic acid as an internal standard.

**<sup>1</sup>H NMR:** (CDCl<sub>3</sub>, 400 MHz) δ<sub>H</sub>

4-methoxybenzaldehyde – 9.86 (1H, s, CHO), 7.81 (2H, d, J = 8.4Hz, 2-H<sub>ar</sub>), 6.98 (2H, d, J = 8.4Hz, 3-H<sub>ar</sub>), 3.87 (3H, s, CH<sub>3</sub>O)

**<sup>13</sup>C NMR:** (CDCl<sub>3</sub>, 100.6 MHz) δ<sub>H</sub>

4-methoxybenzyl alcohol – 191.0, 164.8, 132.1, 130.0, 114.4, 55.6

**<sup>1</sup>H NMR:** (d<sub>6</sub>-DMSO, 400 MHz) δ<sub>H</sub>

4-methoxybenzyl alcohol - 7.18 (2H, d, J = 9.2 Hz, 2-H<sub>ar</sub>), 6.84 (2H, d, J = 9.2 Hz, 3-H<sub>ar</sub>), 4.37 (2H, s, CH<sub>2</sub>OH), 3.68 (3H, s, CH<sub>3</sub>O)

4-methoxybenzaldehyde – 9.83 (1H, s, CHO), 7.83 (2H, d, J = 8.4Hz, 2-H<sub>ar</sub>), 7.08 (2H, d, J = 8.4Hz, 3-H<sub>ar</sub>), 3.82 (3H, s, CH<sub>3</sub>O)

4-methylbenzyl alcohol - 7.18 (2H, d, J = 7.8 Hz, 2-H<sub>ar</sub>), 7.11 (2H, d, J = 7.8 Hz, 3-H<sub>ar</sub>), 4.39 (2H, s, CH<sub>2</sub>OH), 2.45 (3H, s, CH<sub>3</sub>)

4-methylbenzaldehyde - 9.91 (1H, s, CHO), 7.74 (2H, d, J = 8.4Hz, 2-H<sub>ar</sub>), 7.36 (2H, d, J = 8.4Hz, 3-H<sub>ar</sub>), 2.35 (3H, s, CH<sub>3</sub>)



## Chapter 7

4-ethylbenzyl alcohol - 7.18 (2H, d,  $J = 7.8$  Hz, 2- $H_{ar}$ ), 7.11 (2H, d,  $J = 7.8$  Hz, 3- $H_{ar}$ ), 4.41 (2H, s,  $CH_2OH$ ), 2.81 (2H, q,  $J = 7.8$  Hz,  $CH_2CH_3$ ), 1.17 (6H, d,  $J = 7.8$  Hz,  $CH(CH_3)_2$ )

4-ethylbenzaldehyde - 9.93 (1H, s,  $CHO$ ), 7.77 (2H, d,  $J = 8.4$ Hz, 2- $H_{ar}$ ), 7.41 (2H, d,  $J = 8.4$ Hz, 3- $H_{ar}$ ), 2.66 (2H, q,  $J = 7.8$  Hz,  $CH_2CH_3$ ), 1.12 (6H, d,  $J = 7.8$  Hz,  $CH(CH_3)_2$ )

4-isopropylbenzyl alcohol - 7.10-7.21 (4H, m,  $H_{ar}$ ), 4.40 (2H, s,  $CH_2OH$ ), 2.81 (1H, dq,  $J = 7.8$  Hz,  $CH(CH_3)_2$ ), 1.13 (6H, d,  $J = 7.8$  Hz,  $CH(CH_3)_2$ )

4-isopropylbenzaldehyde - 9.93 (1H, s,  $CHO$ ), 7.80 (2H, d,  $J = 8.4$ Hz, 2- $H_{ar}$ ), 7.44 (2H, d,  $J = 8.4$ Hz, 3- $H_{ar}$ ), 2.94 (1H, dq,  $J = 6.9$  Hz,  $CH(CH_3)_2$ ), 1.18 (6H, d,  $J = 6.9$  Hz,  $CH(CH_3)_2$ )

biphenyl-4-methanol - 7.27-7.64 (9H, m,  $H_{ar}$ ), 4.50 (2H, s,  $CH_2OH$ )

biphenyl-4-methanal - 10.01 (1H, s,  $CHO$ ), 7.95 (2H, d,  $J = 8.4$ Hz, 2- $H_{ar}$ ), 7.86 (2H, d,  $J = 8.4$ Hz, 3- $H_{ar}$ ), 7.34-7.52 (5H, m,  $H_{ar}$ )

4-chlorobenzyl alcohol - 7.31 (4H, m,  $H_{ar}$ ), 4.43 (2H, s,  $CH_2OH$ )

4-chlorobenzaldehyde - 9.96 (1H, s,  $CHO$ ), 7.89 (2H, d,  $J = 8.4$ Hz, 3- $H_{ar}$ ), 7.64 (2H, d,  $J = 8.4$ Hz, 2- $H_{ar}$ )

4-bromobenzyl alcohol - 7.46 (2H, d,  $J = 9.2$  Hz, 2- $H_{ar}$ ), 7.22 (2H, d,  $J = 9.2$  Hz, 3- $H_{ar}$ ), 4.55 (2H, s,  $CH_2OH$ )

4-bromobenzaldehyde - 9.94 (1H, s,  $CHO$ ), 8.08 (4H, m,  $H_{ar}$ )

4-iodobenzyl alcohol - 7.62 (2H, d,  $J = 9.2$  Hz, 2- $H_{ar}$ ), 7.09 (2H, d,  $J = 9.2$  Hz, 3- $H_{ar}$ ), 4.40 (2H, s,  $CH_2OH$ )

4-iodobenzaldehyde - 9.92 (1H, s,  $CHO$ ), 7.97 (2H, d,  $J = 8.4$ Hz, 2- $H_{ar}$ ), 7.62 (2H, d,  $J = 8.4$ Hz, 3- $H_{ar}$ )

4-trifluoromethylbenzyl alcohol - 7.62 (2H, d,  $J = 9.2$  Hz, 3- $H_{ar}$ ), 7.49 (2H, d,  $J = 9.2$  Hz, 2- $H_{ar}$ ), 4.55 (2H, s,  $CH_2OH$ )

4-trifluoromethylbenzaldehyde - 10.07 (1H, s,  $CHO$ ), 8.08 (2H, d,  $J = 8.4$ Hz, 3- $H_{ar}$ ), 7.92 (2H, d,  $J = 8.4$ Hz, 2- $H_{ar}$ )

4-nitrobenzyl alcohol - 8.15 (2H, d,  $J = 9.2$  Hz, 3- $H_{ar}$ ), 7.52 (2H, d,  $J = 9.2$  Hz, 2- $H_{ar}$ ), 4.37 (2H, s,  $CH_2OH$ )

4-nitrobenzaldehyde - 10.11 (1H, s,  $CHO$ ), 8.38 (2H, d,  $J = 8.4$ Hz, 3- $H_{ar}$ ), 8.11 (2H, d,  $J = 8.4$ Hz, 2- $H_{ar}$ )

## Chapter 7

4-hydroxybenzyl alcohol - 7.04 (2H, d,  $J = 8.2$  Hz, 2- $H_{ar}$ ), 6.66 (2H, d,  $J = 8.2$  Hz, 3- $H_{ar}$ ), 4.31 (2H, s,  $CH_2OH$ )

4-hydroxybenzaldehyde - 9.74 (1H, s,  $CHO$ ), 7.71 (2H, d,  $J = 8.7$  Hz, 2- $H_{ar}$ ), 6.88 (2H, d,  $J = 8.7$  Hz, 3- $H_{ar}$ )

Methyl (4-hydroxymethyl) benzoate - 7.88 (2H, d,  $J = 9.2$  Hz, 3- $H_{ar}$ ), 7.41 (2H, d,  $J = 9.2$  Hz, 2- $H_{ar}$ ), 4.54 (2H, s,  $CH_2OH$ ), 3.79 (3H, s,  $CH_3O$ )

Methyl 4-formylbenzoate - 10.06 (1H, s,  $CHO$ ), 8.10 (2H, d,  $J = 8.4$  Hz, 3- $H_{ar}$ ), 8.00 (2H, d,  $J = 8.4$  Hz, 2- $H_{ar}$ ), 3.85 (3H, s,  $CH_3O$ )

4-acetamido benzyl alcohol - 7.48 (2H, d,  $J = 8.7$  Hz, 3- $H_{ar}$ ), 7.18 (2H, d,  $J = 8.7$  Hz, 2- $H_{ar}$ ), 4.38 (2H, s,  $CH_2OH$ ), 2.02 (3H, s,  $CH_3CO$ )

4-acetoamido benzaldehyde - 9.82 (1H, s,  $CHO$ ), 7.76 (4H, m,  $H_{ar}$ ), 2.06 (3H, s,  $CH_3CO$ )

### ESI-MS:

4-methoxybenzaldehyde

Calc for  $[C_8H_8O_2]+H^+$  = 137.0597 Found 137.0589 (5.2 ppm error)

Calc for  $[C_8H_8O_2]+Na^+$  = 139.0640 Found 139.0636 (2.8 ppm error)

Deuterated (4-methoxy)benzaldehyde

Calc for  $[C_8H_7DO_2]+H^+$  = 138.0660 Found 138.0661 (-1.1 ppm error)

Calc for  $[C_8H_7DO_2]+Na^+$  = 160.0479 Found 160.0477 (1.3 ppm error)

$^{18}O$ -labelled (4-methoxy)benzaldehyde

Calc for  $[C_8H_8O^{18}O]+H^+$  = 159.0417 Found 159.0405 (5.6 ppm error)

Calc for  $[C_8H_8O^{18}O]+Na^+$  = 161.0459 Found 161.0456 (0.2 ppm error)

### 7.3.5 Time resolved photoluminescence spectroscopy

Time resolve photoluminescence was performed on an Edinburgh Photonics FLS 980 spectrometer, irradiating a 1 mg/mL dispersion with an Edinburgh instruments picosecond pulse light emitting diode,  $\lambda = 380$  nm.

## 7.4 Chapter 4 Experimental

### 7.4.1 Materials and Reagents

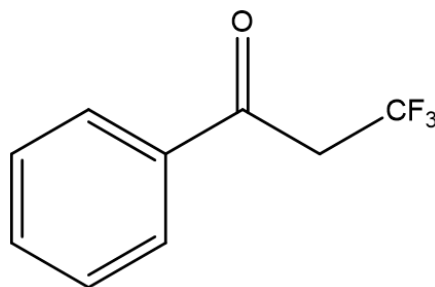
Naphthalene (99%), *N*-Boc-pyrrole (98%), 1,3,5-trimethoxybenzene (99%), Styrene, 5-(trifluoromethyl)dibenzothiophenium tetrafluoroborate (97%),  $CDCl_3$  (99%),

fluorobenzene (99%), pyridine-*N*-oxide (95%) and trifluoroacetic anhydride (99%) were purchased from Sigma Aldrich. Hydrochloric acid (37%), sodium hydrogen carbonate and sodium chloride were purchased from Fisher Scientific. Methanol was purchased from VWR. All chemicals were used as received.

#### 7.4.2 Photocatalytic synthesis of 3,3,3-trifluoro-1-phenyl-propan-1-one (4.1) using blue light irradiated bismuth vanadate nanoparticles and Umemoto's reagent (5-(trifluoromethyl)dibenzothiophenium tetrafluoroborate)

Nan-BiVO<sub>4</sub> (32.3 mg, 100 μmol) and 5-(trifluoromethyl)dibenzothiophenium tetrafluoroborate (68.0 mg, 200 μmol) were added to 10 mL of a 9:1 methanol and distilled water solution in a sealed Schlenk tube. Stryene (11.5 μL, 100 μmol) was subsequently added. The mixture was stirred vigorously for 90 minutes to disperse the catalyst under an argon atmosphere via a balloon. The mixture was then irradiated with a 30 W blue LED array at a distance of 2 cm with an irradiance of 230 mW/cm<sup>2</sup> for 150 minutes. The mixture reached ca. 40 °C by the end of the reaction and after irradiation, the catalyst was removed using centrifugation at 4000 rpm for 30 min. The organic products were extracted from the reaction liquor with dichloromethane which was subsequently dried with magnesium sulfate. For NMR analysis, the supernatant was reduced in volume using a rotary evaporator at 60 mbar at 20 °C, and the residue dissolved in CDCl<sub>3</sub> containing fluorobenzene as an internal standard.

#### 3,3,3-trifluoro-1-phenyl-propan-1-one (4.1)

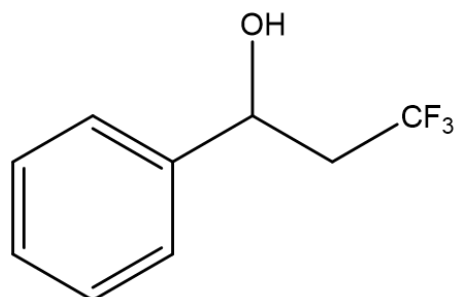


<sup>1</sup>H NMR: (CDCl<sub>3</sub>, 400 MHz) δ<sub>H</sub>

7.92 (2H, d, J = 7.3 Hz, o-H<sub>ar</sub>), 7.13 (1H, t, J = 7.3 Hz, p-H<sub>ar</sub>), 7.06 (2H, t, J = 7.3 Hz, m-H<sub>ar</sub>), 3.78 (2H, q, J = 10.1 Hz, CH<sub>2</sub>CF<sub>3</sub>)

<sup>19</sup>F NMR: (CDCl<sub>3</sub>, 376.3 MHz) δ<sub>F</sub>

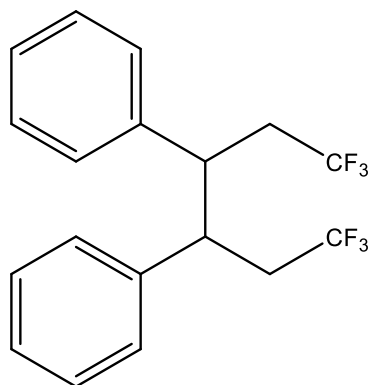
-61.9 (3F, t, J = 10.1 Hz, CF<sub>3</sub>)



**$^{19}\text{F}$  NMR:** ( $\text{CDCl}_3$ , 376.3 MHz)  $\delta_{\text{F}}$

-63.8 (3F, t,  $J = 10.0$  Hz,  $\text{CF}_3$ )

## 4.3 and 4.4



**$^{19}\text{F}$  NMR:** ( $\text{CDCl}_3$ , 376.3 MHz)  $\delta_{\text{F}}$

-63.4 (3F, t,  $J = 10.1$  Hz,  $\text{CF}_3$ ), -63.5 (3F, t,  $J = 9.9$  Hz,  $\text{CF}_3$ )

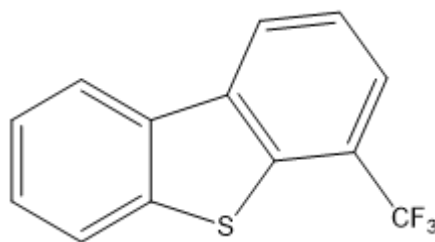
**7.4.3 Photocatalytic synthesis of trifluoromethylated dibenzothiophene (4.5-4.8) using blue light irradiated bismuth vanadate nanoparticles (nan-BiVO<sub>4</sub>) and Umemoto's reagent (5-(trifluoromethyl)dibenzothiophenium tetrafluoroborate)**

Nan-BiVO<sub>4</sub> (32.3 mg, 100  $\mu\text{mol}$ ) and 5-(trifluoromethyl)dibenzothiophenium tetrafluoroborate (680 mg, 2 mmol) were added to 10 mL of a 9:1 methanol and distilled water solution in a sealed Schlenk tube. Benzene (90  $\mu\text{L}$ , 1 mmol) was subsequently added. The mixture was stirred vigorously for 90 minutes to disperse the catalyst under an argon atmosphere via a balloon. The mixture was then irradiated with a 30 W blue LED array at a distance of 2 cm with an irradiance of 230 mW/cm<sup>2</sup> for 24 h. The mixture reached ca. 40 °C by the end of the reaction and after irradiation, the catalyst was removed using centrifugation at 4000 rpm for 30 min. The organic products were extracted from the reaction liquor with dichloromethane which was subsequently dried with magnesium sulfate. For NMR analysis, the supernatant was reduced in volume using a rotary

## Chapter 7

evaporator at 60 mbar at 20 °C, and the residue dissolved in  $\text{CDCl}_3$  containing fluorobenzene as an internal standard.

### 4.5



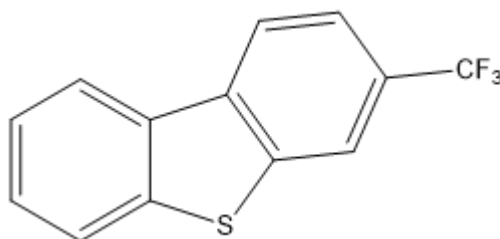
**$^1\text{H NMR}$ :** ( $\text{CDCl}_3$ , 400 MHz)  $\delta_{\text{H}}$

8.31 (1H, d,  $J = 8.2$  Hz,  $\text{H}_{\text{ar}}$ ), 8.21-8.14 (1H, m,  $\text{H}_{\text{ar}}$ ), 7.91-7.84 (2H, m,  $\text{H}_{\text{ar}}$ ), 7.69 (1H, d,  $J = 7.4$  Hz,  $\text{H}_{\text{ar}}$ ), 7.58-7.45 (2H, m,  $\text{H}_{\text{ar}}$ )

**$^{19}\text{F NMR}$ :** ( $\text{CDCl}_3$ , 376.3 MHz)  $\delta_{\text{F}}$

-62.9 (3F, s,  $\text{CF}_3$ )

### 4.6

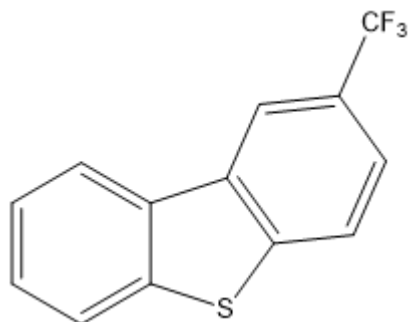


**$^1\text{H NMR}$ :** ( $\text{CDCl}_3$ , 400 MHz)  $\delta_{\text{H}}$

8.24 (1H, d,  $J = 8.2$  Hz,  $\text{H}_{\text{ar}}$ ), 8.21-8.17 (1H, m,  $\text{H}_{\text{ar}}$ ), 8.12 (1H, s,  $\text{H}_{\text{ar}}$ ), 7.92-7.86 (1H, m,  $\text{H}_{\text{ar}}$ ), 7.68 (1H, d,  $J = 8.2$  Hz,  $\text{H}_{\text{ar}}$ ), 7.56-7.47 (2H, m,  $\text{H}_{\text{ar}}$ )

**$^{19}\text{F NMR}$ :** ( $\text{CDCl}_3$ , 376.3 MHz)  $\delta_{\text{F}}$

-61.6 (3F, s,  $\text{CF}_3$ )



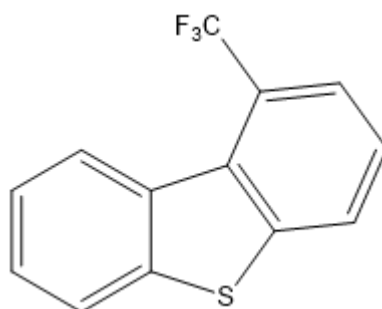
**<sup>1</sup>H NMR:** (CDCl<sub>3</sub>, 400 MHz) δ<sub>H</sub>

8.39 (1H, s, H<sub>ar</sub>), 8.24-8.19 (1H, m, H<sub>ar</sub>), 7.95 (1H, d, J = 8.2 Hz, H<sub>ar</sub>) 7.91-7.84 (1H, m, H<sub>ar</sub>), 7.68 (1H, dd, J = 8.2, 2.4 Hz, H<sub>ar</sub>), 7.56-7.47 (2H, m, H<sub>ar</sub>)

**<sup>19</sup>F NMR:** (CDCl<sub>3</sub>, 376.3 MHz) δ<sub>F</sub>

-61.5 (3F, s, CF<sub>3</sub>)

## 4.8



**<sup>1</sup>H NMR:** (CDCl<sub>3</sub>, 400 MHz) δ<sub>H</sub>

8.54-8.49 (1H, m, H<sub>ar</sub>), 8.04 (1H, d, J = 8.2 Hz, H<sub>ar</sub>) 7.91-7.86 (2H, m, H<sub>ar</sub>), 7.81 (1H, d, J = 8.0, H<sub>ar</sub>), 7.54-7.46 (2H, m, H<sub>ar</sub>)

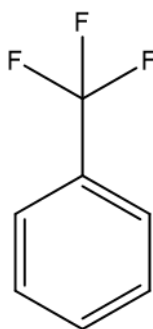
**<sup>19</sup>F NMR:** (CDCl<sub>3</sub>, 376.3 MHz) δ<sub>F</sub>

-60.7 (3F, s, CF<sub>3</sub>)

#### 7.4.4 Trifluoromethylation of aromatics utilising blue light irradiated bismuth vanadate nanoparticles (nan-BiVO<sub>4</sub>) and pyridyl trifluoroacetyl ester

Nan-BiVO<sub>4</sub> (14.0 mg, 40 μmol) and pyridine-N-oxide (38.0 mg, 400 μmol) were placed in a sealed Schlenk tube which was subsequently purged and backfilled with argon. 3 mL dry, degassed acetonitrile was added via cannula transfer. The aromatic substrate (400 μmol) and trifluoroacetic anhydride (56 μL, 400 μmol) were subsequently added and the reaction mixture stirred for 120 minutes to ensure catalyst dispersion. The mixture was

then irradiated with a 30 W blue LED array at a distance of 2 cm with an irradiance of 230 mW/cm<sup>2</sup> for 24 h. The mixture reached ca. 40 °C by the end of the reaction and after irradiation, the catalyst was removed using centrifugation at 4000 rpm for 30 min. The organic products were extracted from the reaction liquor with dichloromethane which was subsequently washed with 1M HCl, saturated sodium hydrogen carbonate and saturate brine before drying with magnesium sulfate. For analysis, the supernatant was reduced in volume using a rotary evaporator at 60 mbar at 20 °C, and the residue dissolved in CDCl<sub>3</sub>.

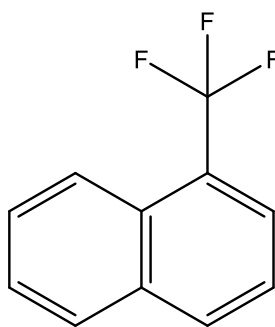
**Trifluoromethylbenzene (4.9)**

**<sup>1</sup>H NMR:** (*d*<sub>3</sub>-MeCN, 400 MHz) δ<sub>H</sub>

7.67 (2H, d, *J* = 7.6 Hz, o-H<sub>ar</sub>), 7.62 (1H, t, *J* = 7.6 Hz, p-H<sub>ar</sub>), 7.54 (2H, t, *J* = 7.6 Hz, m-H<sub>ar</sub>)

**<sup>19</sup>F NMR:** (*d*<sub>3</sub>-MeCN, 376.3 MHz) δ<sub>F</sub>

-63.0 (3F, s, CF<sub>3</sub>)

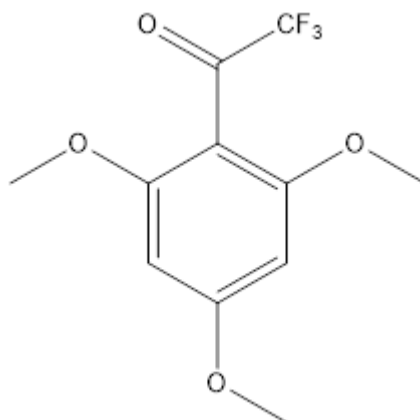
**1-Trifluoromethylnaphthalene (4.10)**

**<sup>1</sup>H NMR:** (CDCl<sub>3</sub>, 400 MHz) δ<sub>H</sub>

8.20 (1H, d, *J* = 8.2 Hz), 8.02 (1H, d, *J* = 8.2 Hz), 7.92 (1H, d, *J* = 7.3 Hz), 7.87 (1H, d, *J* = 7.3 Hz), 7.53-7.67 (3H, m)

**<sup>19</sup>F NMR:** (CDCl<sub>3</sub>, 376.3 MHz) δ<sub>F</sub>

-59.6 (3F, s, CF<sub>3</sub>)

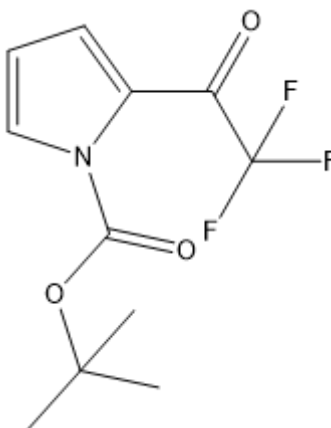
**1-Trifluoroacetyl-(2,4,6-trimethoxy)benzene (4.11)**

**$^1\text{H NMR}$ :** ( $\text{CDCl}_3$ , 400 MHz)  $\delta_{\text{H}}$

6.09 (2H, s, m- $\text{H}_{\text{ar}}$ ), 3.83 (3H, s, p- $\text{OCH}_3$ ), 3.79 (6H, s, o- $\text{OCH}_3$ )

**$^{19}\text{F NMR}$ :** ( $\text{CDCl}_3$ , 376.3 MHz)  $\delta_{\text{F}}$

-76.2 (3F, s,  $\text{COCF}_3$ )

**4.12**

**$^1\text{H NMR}$ :** ( $\text{CDCl}_3$ , 400 MHz)  $\delta_{\text{H}}$

7.56 (1H, m,  $\text{H}_{\text{ar}}$ ), 7.30 (1H, t,  $J = 3.2$  Hz,  $\text{H}_{\text{ar}}$ ), 6.17 (1H, m,  $\text{H}_{\text{ar}}$ ), 1.57 (9H, s,  $\text{CH}(\text{CH}_3)_3$ )

**$^{19}\text{F NMR}$ :** ( $\text{CDCl}_3$ , 376.3 MHz)  $\delta_{\text{F}}$

-72.7 (3F, s,  $\text{COCF}_3$ )



## 7.5 Chapter 5 Experimental

### 7.5.1 Materials and Reagents

Chloroplatinic acid hydrate (98%), nickel(II) acetate tetrahydrate (99%), phenoxyacetic acid (98%), 4-methoxyphenylacetic acid (99%), 2-methoxyphenylacetic acid (98%), cyclohexanone (95%), methacrolein (95%), acrolein (90%), methyl methacrylate (99%) and  $\alpha$ -methylene- $\gamma$ -butyrolactone (97%) were purchased from Sigma Aldrich. Phenylacetic acid (99%), 4-chlorophenylacetic acid (98%) and 4-nitrophenylacetic acid (98%) were purchased from Alfa Aesar. Sodium citrate was purchased from Fisons. Dihydrogen gas (99%) was purchased from BOC gases. D<sub>3</sub>-MeCN (99%) was purchased from VWR. Acetonitrile was purchased from Fisher Scientific. All chemicals were used as received with the exception of acetonitrile which was stirred with calcium hydride for 72 h and distilled onto activated 3 Å molecular sieves. Calcium hydride was purchased from Sigma Alrich and 3 Å molecular sieves were purchased from Fisher Scientific.

### 7.5.2 Photocatalytic formation of platinum nanoparticles on semiconductor surfaces (0.15-Pt-Bi<sub>2</sub>WO<sub>6</sub> and 0.15-Pt-BiVO<sub>4</sub>)

Chloroplatinic acid solution (10 mL, 5 mg mL<sup>-1</sup>) was made up with distilled water. Semiconductor (1.0 g), a known amount of chloroplatinic acid solution and ethanol (4 mL) were added to a Schlenk tube and made up to 20 mL with distilled water. The Schlenk tube was sealed and the solution degassed with nitrogen for 30 minutes, the solution was continually stirred to disperse the semiconductor. The mixture was then irradiated with a 30 W blue LED array at a distance of 2 cm with an irradiance of 230 mW/cm<sup>2</sup> for 15 h; after irradiation, the catalyst was removed using centrifugation at 4000 rpm for 30 min. The material was washed alternately with distilled water and ethanol and then dried overnight at 60 °C.

For 0.15-Pt-Bi<sub>2</sub>WO<sub>6</sub>, powder X-ray diffraction data of 0.15-Pt-Bi<sub>2</sub>WO<sub>6</sub> were consistent with crystalline orthorhombic Bi<sub>2</sub>WO<sub>6</sub> (JCPDS No. 39-0256). Specific area electron diffraction showed diffraction spots that correspond to the orthorhombic Bi<sub>2</sub>WO<sub>6</sub> (Miller indices (131), (200), (202) and (133)) and platinum metal (Miller indices (111), (200) and (220)).

### 7.5.3 Photocatalytic dimerization of phenylacetic acid using blue light irradiated 0.15-Pt-Bi<sub>2</sub>WO<sub>6</sub>

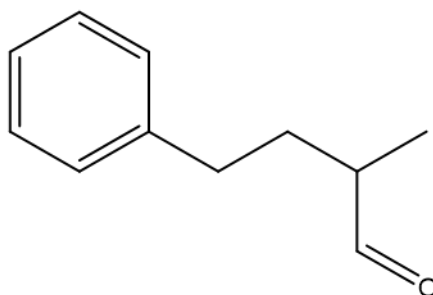
Phenylacetic acid (13.6 mg, 100  $\mu$ mol) and 0.15-Pt-Bi<sub>2</sub>WO<sub>6</sub> (108 mg, 150  $\mu$ mol) were added to a schlenk tube which was purged and backfilled with nitrogen. Dry, degassed acetonitrile (3 mL) was subsequently added. The mixture was then irradiated with a 30

W blue LED array at a distance of 2 cm with an irradiance of 230 mW/cm<sup>2</sup>. The mixture reached ca. 40 °C by the end of the reaction and after irradiation, the catalyst was removed using centrifugation at 4000 rpm for 30 min. For GC analysis, 1 mL of supernatant was taken and 1 μL injected.

#### 7.5.4 Photocatalytic Giese reaction between phenylacetic acid analogues and electron deficient alkenes initiated by blue light irradiated platinumised bismuth tungstate (0.15-Pt-Bi<sub>2</sub>WO<sub>6</sub>)

Phenylacetic acid (13.6 mg, 100 μmol) and 0.15-Pt-Bi<sub>2</sub>WO<sub>6</sub> (108 mg, 150 μmol) were added to a Schlenk tube which was purged and backfilled with nitrogen. Dry, degassed acetonitrile (3 mL) and a known amount of alkene (250 μmol) were subsequently added. The mixture was then irradiated with a 30 W blue LED array at a distance of 2 cm with an irradiance of 230 mW/cm<sup>2</sup>. The mixture reached ca. 40 °C by the end of the reaction and after irradiation, the catalyst was removed using centrifugation at 4000 rpm for 30 min. For GC analysis, 1 mL of supernatant was taken and 1 μL injected. For NMR analysis, the supernatant was reduced in volume using a rotary evaporator at 70 mbar at 20 °C, and the residue dissolved in d<sub>3</sub>-MeCN containing methanol as an internal standard. Compounds were purified by a silica column with a solvent mixture of 20% ethyl acetate in hexane.

#### 5.1



**<sup>1</sup>H NMR:** (CDCl<sub>3</sub>, 400 MHz) δ<sub>H</sub>

9.62 (1H, d, J = 1.8 Hz, CHO), 7.27 (2H, m, H<sub>ar</sub>), 7.19 (3H, m, H<sub>ar</sub>), 2.66 (2H, dt, J = 9.2 Hz, 6.9 Hz, PhCH<sub>2</sub>), 2.36 (1H, ddt, J = 7.3 Hz, 1.8 Hz, CHCHO) 2.06 (1H, ddt, J = 9.2 Hz, 6.9 Hz, CH<sub>2</sub>CH<sub>2</sub>CH), 1.66 (1H, ddt, J = 9.2 Hz, 6.9 Hz, CH<sub>2</sub>CH<sub>2</sub>CH), 1.14 (3H, d, J = 7.3 Hz, CHCH<sub>3</sub>)

**<sup>13</sup>C NMR:** (CDCl<sub>3</sub>, 100.6 MHz) δ<sub>C</sub>

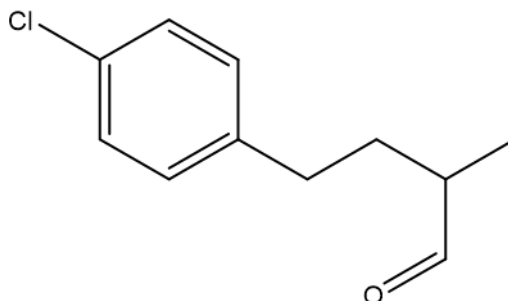
205.0, 141.3, 128.6, 128.5, 126.3, 45.7, 33.1, 32.2, 13.4

**ESI-MS:**

Calc for  $[C_{11}H_{14}O]+Na^+$  = 185.0937 Found 185.0942 (-3.7 ppm error)

**GC:**

$R_t = 4.82$  min



**$^1H$  NMR:** ( $CDCl_3$ , 400 MHz)  $\delta_H$

9.61 (1H, d,  $J = 1.8$  Hz, *CHO*), 7.23 (2H, d,  $J = 8.2$  Hz,  $H_{ar}$ ), 7.10 (2H, d,  $J = 8.2$  Hz,  $H_{ar}$ ), 2.61 (2H, ddd,  $J = 10.0, 6.9, 3.2$  Ph $CH_2$ ), 2.34 (1H, ddt,  $J = 6.9$  Hz, 1.8 Hz, *CHCHO*) 2.01 (1H, ddt,  $J = 9.2$  Hz, 6.9 Hz,  $CH_2CH_2CH$ ), 1.62 (1H, ddt,  $J = 9.2$  Hz, 6.9 Hz,  $CH_2CH_2CH$ ), 1.13 (3H, d,  $J = 7.3$  Hz,  $CHCH_3$ )

**$^{13}C$  NMR:** ( $CDCl_3$ , 100.6 MHz)  $\delta_C$

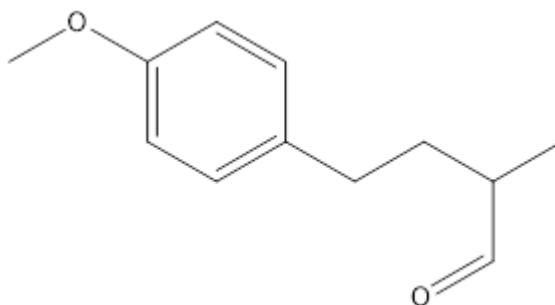
204.7, 139.9, 131.9, 129.8, 128.7, 45.6, 32.5, 32.1, 13.5

**ESI-MS:**

Calc for  $[C_{11}H_{13}ClO]+K^+$  = 235.0292 Found 235.0223 (-29.3 ppm error)

**GC:**

$R_t = 6.10$  min



**$^1H$  NMR:** ( $CDCl_3$ , 400 MHz)  $\delta_H$

9.60 (1H, d,  $J = 1.8$  Hz, *CHO*), 7.08 (2H, d,  $J = 8.7$  Hz,  $H_{ar}$ ), 6.82 (2H, d,  $J = 8.7$  Hz,  $H_{ar}$ ), 3.77 (3H, s,  $CH_3O$ ), 2.60 (2H, dt,  $J = 9.2$  Hz, 6.9 Hz, Ph $CH_2$ ), 2.35 (1H, ddt,  $J = 6.9$  Hz,

Chapter 7

1.8 Hz,  $CHCHO$ ), 2.02 (1H, ddt,  $J = 9.2$  Hz, 6.9 Hz,  $CH_2CH_2CH$ ), 1.62 (1H, ddt,  $J = 9.2$  Hz, 6.9 Hz,  $CH_2CH_2CH$ ), 1.12 (3H, d,  $J = 6.9$  Hz,  $CHCH_3$ )

$^{13}C$  NMR: ( $CDCl_3$ , 100.6 MHz)  $\delta_C$

205.1, 158.0, 133.5, 129.4, 114.0, 55.3, 45.7, 32.5, 32.2, 13.4

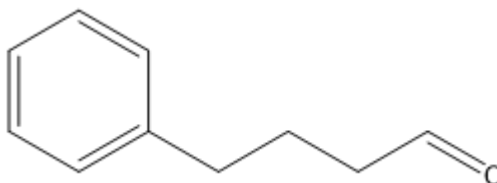
ESI-MS:

Calc for  $[C_{12}H_{16}O_2]+H^+-H_2O = 175.1117$  Found 175.1116 (-0.6 ppm error)

GC:

$R_t = 6.36$  min

5.2



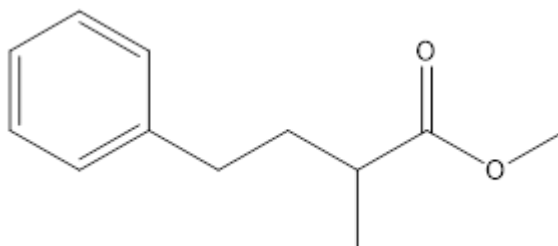
$^1H$  NMR: ( $CDCl_3$ , 400 MHz)  $\delta_H$

9.65 (1H, d,  $J = 1.8$  Hz,  $CHO$ ), 7.27 (2H, m,  $H_{ar}$ ), 7.18 (3H, m,  $H_{ar}$ ), 2.59 (2H, t,  $J = 7.3$  Hz,  $PhCH_2$ ), 2.39 (2H, t,  $J = 7.3$  Hz,  $CHCHO$ ) 1.85 (2H, quin,  $J = 7.8$  Hz,  $CH_2CH_2CH$ ),

GC:

$R_t = 4.45$  min

5.3



$^1H$  NMR: ( $CDCl_3$ , 400 MHz)  $\delta_H$

7.27 (2H, m,  $H_{ar}$ ), 7.17 (3H, m,  $H_{ar}$ ), 3.67 (3H, s,  $CH_3O$ ), 2.60 (2H, tt,  $J = 7.8$  Hz,  $CH_2Ph$ ), 2.47 (1H, dtt,  $J = 6.7$  Hz,  $CHCOO$ ), 2.00 (1H, dq,  $J = 13.3, 7.8$  Hz,  $CH_2CH_2CH$ ), 1.70 (1H, m,  $CH_2CH_2CH$ ), 1.18 (3H, d,  $J = 6.7$  Hz,  $CH_3CH$ )

$^{13}C$  NMR: ( $CDCl_3$ , 100.6 MHz)  $\delta_C$

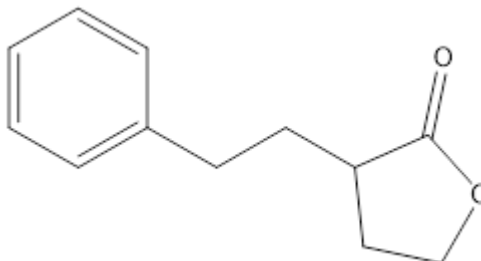
176.9, 141.7, 128.5, 128.4, 126.1, 51.7, 39.0, 35.5, 33.6, 17.3

**ESI-MS:**

Calc for  $[C_{12}H_{16}O_2]+Na^+$  = 215.1048 Found 215.1035 (-6.0 ppm error)

**GC:**

$R_t$  = 5.38 min

**5.4**

**$^1H$  NMR:** ( $CDCl_3$ , 400 MHz)  $\delta_H$

7.29 (2H, m,  $H_{ar}$ ), 7.20 (3H, m,  $H_{ar}$ ), 4.34 (1H, td,  $J$  = 8.7, 2.8 Hz,  $CH_2O$ ), 4.16 (1H, dt,  $J$  = 9.6 Hz, 6.4 Hz,  $CH_2O$ ), 2.75 (2H, m,  $PhCH_2$ ), 2.48 (1H, m), 2.37 (1H, m), 2.24 (1H, m), 1.95 (1H, m), 1.76 (1H, m)

**$^{13}C$  NMR:** ( $CDCl_3$ , 100.6 MHz)  $\delta_C$

192.2, 140.9, 128.6, 128.5, 126.3, 66.5, 38.5, 33.4, 32.1, 28.9

**ESI-MS:**

Calc for  $[C_{12}H_{14}O_2]+Na^+$  = 213.0886 Found 213.0880 (3.2 ppm error)

**GC:**

$R_t$  = 7.3 min

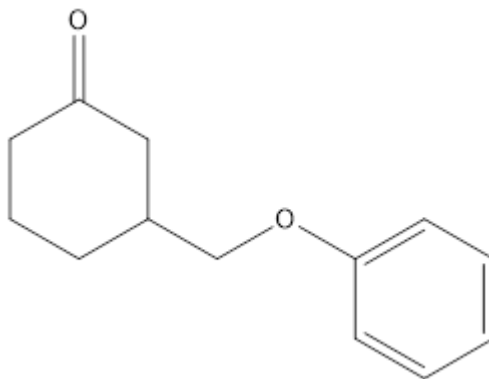
**7.5.5 Photocatalytic Giese reaction between phenoxyacetic acid and electron deficient alkenes initiated by blue light irradiated platinumised bismuth tungstate (0.15-Pt-Bi<sub>2</sub>WO<sub>6</sub>)**

Phenoxyacetic acid (15.0 mg, 100  $\mu$ mol) and 0.15-Pt-Bi<sub>2</sub>WO<sub>6</sub> (108 mg, 150  $\mu$ mol) were added to a Schlenk tube which was purged and backfilled with nitrogen. Dry, degassed acetonitrile (3 mL) and a known amount of alkene (250  $\mu$ mol) were subsequently added. The mixture was then irradiated with a 30 W blue LED array at a distance of 2 cm with an irradiance of 230 mW/cm<sup>2</sup>. The mixture reached ca. 40 °C by the end of the reaction and after irradiation, the catalyst was removed using centrifugation at 4000 rpm for 30 min. For GC analysis, 1 mL of supernatant was taken and 1  $\mu$ L injected. For NMR analysis, the supernatant was reduced in volume using a rotary evaporator at 70 mbar at

## Chapter 7

20 °C, and the residue dissolved in  $d_3$ -MeCN containing methanol as an internal standard. Compounds were purified by a silica column with a solvent mixture of 20% ethyl acetate in hexane.

### 5.5



**$^1\text{H NMR}$ :** ( $\text{CDCl}_3$ , 400 MHz)  $\delta_{\text{H}}$

7.27 (2H, m,  $\text{H}_{\text{ar}}$ ), 6.94 (1H, t,  $J = 7.3$  Hz,  $\text{H}_{\text{ar}}$ ), 6.87 (2H, d,  $J = 7.8$  Hz,  $\text{H}_{\text{ar}}$ ), 3.86 (2H, d,  $J = 5.5$  Hz,  $\text{CH}_2\text{OPh}$ ), 2.48-2.60 (1H, m), 2.37-2.46 (1H, m), 2.21-2.36 (3H, m), 2.07-2.16 (1H, m), 1.99-2.07 (1H, m), 1.66-1.79 (1H, m), 1.54-1.66 (1H, m)

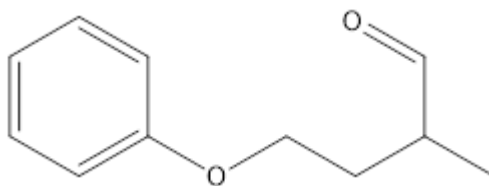
**$^{13}\text{C NMR}$ :** ( $\text{CDCl}_3$ , 100.6 MHz)  $\delta_{\text{C}}$

211.3, 158.6, 129.6, 120.7, 114.8, 71.6, 44.9, 41.3, 39.0, 28.4, 24.8

**ESI-MS:**

Calc for  $[\text{C}_{13}\text{H}_{16}\text{O}_2] + \text{Na}^+$  = 227.1043 Found 227.1034 (2.3 ppm error)

### 5.6



**$^1\text{H NMR}$ :** ( $\text{CDCl}_3$ , 400 MHz)  $\delta_{\text{H}}$

9.71 (1H, d,  $J = 1.4$  Hz,  $\text{CHO}$ ), 7.25 (2H, m,  $\text{H}_{\text{ar}}$ ), 6.93 (1H, m,  $\text{H}_{\text{ar}}$ ), 6.86 (2H, m,  $\text{H}_{\text{ar}}$ ), 4.03 (2H, m,  $\text{PhOCH}_2$ ), 2.65 (1H, ddt,  $J = 6.9$  Hz, 1.8 Hz,  $\text{CHCHO}$ ), 2.23 (1H, ddt,  $J = 6.9$  Hz, 5.5 Hz,  $\text{CH}_2\text{CH}_2\text{CH}$ ), 1.86 (1H, m,  $\text{CH}_2\text{CH}_2\text{CH}$ ), 1.17 (3H, d,  $J = 6.9$  Hz,  $\text{CHCH}_3$ )

**$^{13}\text{C NMR}$ :** ( $\text{CDCl}_3$ , 100.6 MHz)  $\delta_{\text{C}}$

204.5, 158.7, 129.6, 121.0, 114.5, 65.0, 43.6, 30.2, 13.5

**ESI-MS:**

Chapter 7

Calc for  $[\text{C}_{11}\text{H}_{13}\text{O}_2] + \text{Na}^+$  = 201.0891 Found 201.0903 (6.0 ppm error)

**GC:**

$R_t = 5.57$  min

## Abbreviations and terms

acac	acetyl acetate
ATRIR	attenuated total reflectance infrared spectroscopy
bpy	bipyridinyl
BET	Brunauer-Emmett-Teller
Bi <sub>V</sub>	bismuth defect at a vanadium site
Bi <sub>vac</sub>	bismuth vacancy defect
BiVO <sub>4</sub>	bismuth vanadate
nan-BiVO <sub>4</sub>	bismuth vanadate nanoparticles
$\theta$	Bragg diffraction angle
$\tau$	charge carrier lifetime
$\delta$	chemical shift in NMR
CoP <sub>i</sub>	cobalt phosphate
C <sub>p</sub>	concentration of product at a given time
C <sub>t</sub>	concentration of starting material at a given time
C <sub>o</sub>	concentration of starting material at the start of a reaction
CB	conduction band
k	continuous quantum wavenumber
E <sub>k</sub>	continuous quantum wavenumber energy
J	coupling constant in NMR
DCE	dichloroethane
DCM	dichloromethane
DFT	density functional theory
DMPO	dimethylpyrroline- <i>N</i> -oxide
DMSO	dimethylsulphoxide
dtbbpy	diterbutylbipyridinyl
m*	effective mass



ESI-MS	electrospray ionisation mass spectrometry
EDX	energy dispersive X-ray
$\alpha$	energy of electronic orbital on an isolated atom
EDTA	ethylenediaminetetraacetic acid
$E_f$	Fermi level
$\beta_{fw}$	full width at half maximum (term)
FWHM	full width at half maximum (abbreviation)
GC	gas chromatography
HMBC	heteronuclear multiple bond coupling experiment in NMR
$h^+$	hole
h	hour(s)
ICP-MS	inductively coupled plasma mass spectrometry
JCPDS	Joint Committee on Powder Diffraction Standards
F(R)	Kubelka-Munk function
LED	light emitting diode
MS	mass spectrometry
D	minimum crystalline particulate size
MoO <sub>x</sub>	molybdenum oxide
NP(s)	nanoparticle(s)
$\beta$	neighbouring atomic orbital interaction constant
NHE	normal hydrogen electrode
NMR	nuclear magnetic resonance spectroscopy
O <sub>int</sub>	oxygen interstitial defect
O <sub>vac</sub>	oxygen vacancy defect
% wt	percentage by weight
%C <sub><math>\tau</math></sub>	percentage contribution from charge carrier with lifetime $\tau$
u(x)	periodic wavefunction

ppy	phenylpyridinyl
0.15-Pt-Bi <sub>2</sub> WO <sub>6</sub>	platinised bismuth tungstate with 0.15% platinum by weight
V <sub>o</sub>	potential energy
PXRD	powder X-ray diffraction
TFAPNO	pyridyl trifluoroacetate ester
k <sub>D</sub>	rate of reaction using a deuterated starting material
k <sub>H</sub>	rate of reaction using a proto starting material
ħ	reduced Planck constant
R	reflectance
mol%	relative molar percentage
R <sub>t</sub>	retention time
RHE	reversible hydrogen electrode
SEM	scanning electron microscopy
r	semiconductor transition constant
k <sub>sf</sub>	shape factor
Φ <sub>B</sub>	Schottky barrier
I	signal intensity
SAED	specific area electron diffraction
TRPLS	time resolved photoluminescence spectroscopy
TiO <sub>2</sub>	titanium dioxide
Pt/TiO <sub>2</sub>	titanium dioxide with surface adsorbed platinum nanoparticles
Ag/TiO <sub>2</sub>	titanium dioxide with surface adsorbed silver nanoparticles
TEM	transmission electron microscopy
UV	ultraviolet
VB	valence band
V <sub>Bi</sub>	vanadium defect at a bismuth site
V <sub>int</sub>	vanadium interstitial defect

$V_{\text{vac}}$	vanadium vacancy defect
VOC	volatile organic compound
$\psi(x)$	wavefunction
$\chi(x)$	wavefunction for an electron on an isolated atom
$\lambda_{\text{max}}$	wavelength of maximal absorption
XAS	X-ray absorption spectroscopy
XES	X-ray emission spectroscopy
XRF	X-ray fluorescence
XPS	X-ray photoelectron spectroscopy
$k_0$	zero-order kinetic rate constant

## References

1. M. A. Lazar and W. A. Daoud, *RSC Adv.*, 2013, **3**, 4130-4140.
2. C. K. Prier, D. A. Rankic and D. W. MacMillan, *Chem. Rev.*, 2013, **113**, 5322-5363.
3. X. Lang, X. Chen and J. Zhao, *Chem. Soc. Rev.*, 2014, **43**, 473-486.
4. D. Friedmann, A. Hakki, H. Kim, W. Choi and D. Bahnemann, *Green Chem.*, 2016, **18**, 5391-5411.
5. M. H. Shaw, J. Twilton and D. W. C. MacMillan, *J. Org. Chem.*, 2016, **81**, 6898-6926.
6. G. Palmisano, V. Augugliaro, M. Pagliaro and L. Palmisano, *Chem. Commun.*, 2007, **0**, 3425-3437.
7. N. Hoffmann, *Chemosuschem.*, 2012, **5**, 352-371.
8. F. Dinçer, *Renew. Sust. Energy Rev.*, 2011, **15**, 713-720.
9. M. Šúri, T. A. Huld, E. D. Dunlop and H. A. Ossenbrink, *Sol. Energy*, 2007, **81**, 1295-1305.
10. E. V. Efremov, F. Ariese and C. Gooijer, *Anal. Chim. Acta*, 2008, **606**, 119-134.
11. F. M. Hoffmann, *Surf. Sci. Rep.*, 1983, **3**, 107-192.
12. W. E. Moerner and D. P. Fromm, *Rev. Sci. Instrum.*, 2003, **74**, 3597-3619.
13. F. de Groot, *Chem. Rev.*, 2001, **101**, 1779-1808.
14. S. Yurdakal, G. Palmisano, V. Loddo, V. Augugliaro and L. Palmisano, *J. Am. Chem. Soc.*, 2008, **130**, 1568-1569.
15. S. Higashimoto, N. Kitao, N. Yoshida, T. Sakura, M. Azuma, H. Ohue and Y. Sakata, *J. Catal.*, 2009, **266**, 279-285.
16. S. Yurdakal, G. Palmisano, V. Loddo, O. Alagoz, V. Augugliaro and L. Palmisano, *Green Chem.*, 2009, **11**, 510-516.
17. S. Higashimoto, N. Suetsugu, M. Azuma, H. Ohue and Y. Sakata, *J. Catal.*, 2010, **274**, 76-83.

18. F. Su, S. C. Mathew, G. Lipner, X. Fu, M. Antonietti, S. Blechert and X. Wang, *J. Am. Chem. Soc.*, 2010, **132**, 16299-16301.
19. X. Lang, H. Ji, C. Chen, W. Ma and J. Zhao, *Angew. Chem. Int. Ed.*, 2011, **50**, 3934-3937.
20. D. Tsukamoto, M. Ikeda, Y. Shiraiishi, T. Hara, N. Ichikuni, S. Tanaka and T. Hirai, *Chem. Eur. J.*, 2011, **17**, 9816-9824.
21. X. Lang, W. Ma, Y. Zhao, C. Chen, H. Ji and J. Zhao, *Chem. Eur. J.*, 2012, **18**, 2624-2631.
22. B. Yuan, R. Chong, B. Zhang, J. Li, Y. Liu and C. Li, *Chem. Commun.*, 2014, **50**, 15593-15596.
23. L. Zhang, D. Liu, J. Guan, X. Chen, X. Guo, F. Zhao, T. Hou and X. Mu, *Mater. Res. Bull.*, 2014, **59**, 84-92.
24. Y. Zhang and Y.-J. Xu, *RSC Adv.*, 2014, **4**, 2904-2910.
25. X. Lang, W. Hao, W. R. Leow, S. Li, J. Zhao and X. Chen, *Chem. Sci.*, 2015, **6**, 5000-5005.
26. X. Lang, W. R. Leow, J. Zhao and X. Chen, *Chem. Sci.*, 2015, **6**, 1075-1082.
27. R. Negishi, S. Naya and H. Tada, *J. Phys. Chem. C*, 2015, **119**, 11771-11776.
28. M. Qamar, R. B. Elsayed, K. R. Alhooshani, M. I. Ahmed and D. W. Bahemann, *ACS Appl. Mater. Interfaces*, 2015, **7**, 1257-1269.
29. B. Zhang, J. Li, B. Q. Zhang, R. F. Chong, R. G. Li, B. Yuan, S. M. Lu and C. Li, *J. Catal.*, 2015, **332**, 95-100.
30. D. W. Manley, R. T. McBurney, P. Miller, R. F. Howe, S. Rhydderch and J. C. Walton, *J. Am. Chem. Soc.*, 2012, **134**, 13580-13583.
31. D. W. Manley and J. C. Walton, *Org. Lett.*, 2014, **16**, 5394-5397.
32. J. W. Beatty, J. J. Douglas, K. P. Cole and C. R. J. Stephenson, *Nat. Commun.*, 2015, **6**, 1-6.
33. V. T. Bhat, P. A. Duspara, S. Seo, N. S. B. Abu Bakar and M. F. Greaney, *Chem. Commun.*, 2015, **51**, 4383-4385.
34. J. J. Devery, J. J. Douglas, J. D. Nguyen, K. P. Cole, R. A. Flowers and C. R. J. Stephenson, *Chem. Sci.*, 2015, **6**, 537-541.

35. O. O. Fadeyi, J. J. Mousseau, Y. Q. Feng, C. Allais, P. Nuhant, M. Z. Chen, B. Pierce and R. Robinson, *Org. Lett.*, 2015, **17**, 5756-5759.
36. P. Riente and M. A. Pericas, *ChemSusChem*, 2015, **8**, 1841-1844.
37. A. Millet, Q. Lefebvre and M. Rueping, *Chem. Eur. J.*, 2016, **22**, 13464-13468.
38. K. Fidaly, C. Ceballos, A. Falguieres, M. S.-I. Veitia, A. Guy and C. Ferroud, *Green Chem.*, 2012, **14**, 1293-1297.
39. J. Zhao, S. Ji, W. Wu, W. Wu, H. Guo, J. Sun, H. Sun, Y. Liu, Q. Li and L. Huang, *RSC Adv.*, 2012, **2**, 1712-1728.
40. Y. Yoshimi, *J. Photochem. Photobiol. A*, 2017, **342**, 116-130.
41. Z. C. Huang, Y. Gu, X. D. Liu, L. F. Zhang, Z. P. Cheng and X. L. Zhu, *Macromol. Rapid Commun.*, 2017, **38**, 1-8.
42. K. Ohkubo, K. Suga, K. Morikawa and S. Fukuzumi, *J. Am. Chem. Soc.*, 2003, **125**, 12850-12859.
43. J. T. Xu, S. Shanmugam, H. T. Duong and C. Boyer, *Polym. Chem.*, 2015, **6**, 5615-5624.
44. Q. Liu, Y.-N. Li, H.-H. Zhang, B. Chen, C.-H. Tung and L.-Z. Wu, *Chem. Eur. J.*, 2012, **18**, 620-627.
45. R. Zhou, H. Liu, H. Tao, X. Yu and J. Wu, *Chem. Sci.*, 2017, **8**, 4654-4659.
46. K. Mase, S. Aoi, K. Ohkubo and S. Fukuzumi, *J. Porphyr. Phthalocyanines*, 2016, **20**, 935-949.
47. H. Rao, W. Q. Yu, H. Q. Zheng, J. Bonin, Y. T. Fan and H. W. Hou, *J. Power Sources*, 2016, **324**, 253-260.
48. J. Sykora, *Coord. Chem. Rev.*, 1997, **159**, 95-108.
49. X. Long, Y. Xi, A. Q. Zhang and H. S. Yang, *Prog. Chem.*, 2005, **17**, 412-416.
50. C. Catastini, M. Sarakha, G. Mailhot and M. Bolte, *Sci. Total Environ.*, 2002, **298**, 219-228.
51. J. Bonin, M. Chaussemier, M. Robert and M. Routier, *ChemCatChem*, 2014, **6**, 3200-3207.
52. A. A. Panagiotopoulos, E. G. Fasoulakis, E. E. Vardalachaki and A. G. Coutsolelos, *J. Porphyr. Phthalocyanines*, 2016, **20**, 1200-1206.

53. A. Juris, V. Balzani, F. Barigelletti, S. Campagna, P. Belser and A. von Zelewsky, *Coord. Chem. Rev.*, 1988, **84**, 85-277.
54. C. Bock, J. Connor, A. Gutierrez, T. J. Meyer, D. Whitten, B. Sullivan and J. Nagle, *J. Am. Chem. Soc.*, 1979, **101**, 4815-4824.
55. K. King, P. Spellane and R. J. Watts, *J. Am. Chem. Soc.*, 1985, **107**, 1431-1432.
56. J. D. Slinker, A. A. Gorodetsky, M. S. Lowry, J. Wang, S. Parker, R. Rohl, S. Bernhard and G. G. Malliaras, *J. Am. Chem. Soc.*, 2004, **126**, 2763-2767.
57. G. Zhao, C. Yang, L. Guo, H. Sun, C. Chen and W. Xia, *Chem. Commun.*, 2012, **48**, 2337-2339.
58. D. A. Nicewicz and D. W. C. MacMillan, *Science*, 2008, **322**, 77-80.
59. C. Pac, Y. Miyauchi, O. Ishitani, M. Ihama, M. Yasuda and H. Sakurai, *J. Org. Chem.*, 1984, **49**, 26-34.
60. S. Fukuzumi, S. Mochizuki and T. Tanaka, *J. Phys. Chem.*, 1990, **94**, 722-726.
61. J. W. Tucker, J. D. Nguyen, J. M. Narayanam, S. W. Krabbe and C. R. Stephenson, *Chem. Commun.*, 2010, **46**, 4985-4987.
62. Y. Yasu, T. Koike and M. Akita, *Org. Lett.*, 2013, **15**, 2136-2139.
63. R. Tomita, Y. Yasu, T. Koike and M. Akita, *Angew. Chem. Int. Ed.*, 2014, **53**, 7144-7148.
64. H. Cano-Yelo and A. Deronzier, *Tetrahedron Lett.*, 1984, **25**, 5517-5520.
65. Y. Su, L. Zhang and N. Jiao, *Org. Lett.*, 2011, **13**, 2168-2171.
66. M. Rueping, S. Zhu and R. M. Koenigs, *Chem. Commun.*, 2011, **47**, 12709-12711.
67. J. Jin and D. W. C. MacMillan, *Nature*, 2015, **525**, 87-90.
68. D. Kalyani, K. B. McMurtrey, S. R. Neufeldt and M. S. Sanford, *J. Am. Chem. Soc.*, 2011, **133**, 18566-18569.
69. Z. Zuo, D. T. Ahneman, L. Chu, J. A. Terrett, A. G. Doyle and D. W. C. MacMillan, *Science*, 2014, **345**, 437-440.
70. M. Rueping, J. Zoller, D. C. Fabry, K. Poscharny, R. M. Koenigs, T. E. Weirich and J. Mayer, *Chem. Eur. J.*, 2012, **18**, 3478-3481.

71. R. K. Dhokale, H. M. Yadav, S. N. Achary and S. D. Delekar, *Appl. Surf. Sci.*, 2014, **303**, 168-174.
72. M. Baar and S. Blechert, *Chem. Eur. J.*, 2015, **21**, 526-530.
73. J. Zhao, J. Yan, H. Jia, S. Zhong, X. Zhang and L. Xu, *J. Mol. Catal. A: Chem.*, 2016, **424**, 162-170.
74. R. a. He, S. Cao, P. Zhou and J. Yu, *Chin. J. Catal.*, 2014, **35**, 989-1007.
75. M. Qamar and A. Khan, *RSC Adv.*, 2014, **4**, 9542-9550.
76. J. Schneider, M. Matsuoka, M. Takeuchi, J. Zhang, Y. Horiuchi, M. Anpo and D. W. Bahnemann, *Chem. Rev.*, 2014, **114**, 9919-9986.
77. T. Saison, N. Chemin, C. Chanéac, O. Durupthy, L. Mariey, F. Maugé, V. Brezová and J.-P. Jolivet, *J. Phys. Chem. C*, 2015, **119**, 12967-12977.
78. P. A. Cox, *The Electronic Structure and Chemistry of Solids*, Oxford University Press, Oxford, 1987.
79. C. Di Valentin and A. Selloni, *J. Phys. Chem. Lett.*, 2011, **2**, 2223-2228.
80. K. E. Kweon, G. S. Hwang, J. Kim, S. Kim and S. Kim, *Phys. Chem. Chem. Phys.*, 2015, **17**, 256-260.
81. J. Peral, X. Domenech and D. F. Ollis, *J. Chem. Technol. Biotechnol.*, 1997, **70**, 117-140.
82. U. I. Gaya and A. H. Abdullah, *J. Photochem. Photobiol. C*, 2008, **9**, 1-12.
83. M. A. Mahmood, S. Baruah, A. K. Anal and J. Dutta, *Environ. Chem. Lett.*, 2012, **10**, 145-151.
84. H. Kisch, *Angew. Chem. Int. Ed. Engl.*, 2013, **52**, 812-847.
85. Y. Park, K. J. McDonald and K. S. Choi, *Chem. Soc. Rev.*, 2013, **42**, 2321-2337.
86. J. Hong, W. Zhang, J. Ren and R. Xu, *Anal. Methods*, 2013, **5**, 1086-1097.
87. S. Dong, J. Feng, M. Fan, Y. Pi, L. Hu, X. Han, M. Liu, J. Sun and J. Sun, *RSC Adv.*, 2015, **5**, 14610-14630.
88. M. Pelaez, N. T. Nolan, S. C. Pillai, M. K. Seery, P. Falaras, A. G. Kontos, P. S. M. Dunlop, J. W. J. Hamilton, J. A. Byrne, K. O'Shea, M. H. Entezari and D. D. Dionysiou, *Appl. Catal. B-Environ.*, 2012, **125**, 331-349.
89. S. C. Yan, Z. S. Li and Z. G. Zou, *Langmuir*, 2009, **25**, 10397-10401.



90. S. Chakrabarti and B. K. Dutta, *J. Hazard. Mater.*, 2004, **112**, 269-278.
91. G. K. Zhang, Y. Y. Gao, Y. L. Zhang and Y. D. Guo, *Environ. Sci. Technol.*, 2010, **44**, 6384-6389.
92. X. Zhang, Z. H. Ai, F. L. Jia and L. Z. Zhang, *J. Phys. Chem. C*, 2008, **112**, 747-753.
93. G. C. Xi and J. H. Ye, *Chem. Commun.*, 2010, **46**, 1893-1895.
94. D. Chen and J. H. Ye, *Adv. Funct. Mater.*, 2008, **18**, 1922-1928.
95. W. Luo, L. H. Zhu, N. Wang, H. Q. Tang, M. J. Cao and Y. B. She, *Environ. Sci. Technol.*, 2010, **44**, 1786-1791.
96. M. Luo, Y. Liu, J. C. Hu, H. Liu and J. L. Li, *ACS Appl. Mater. Interfaces*, 2012, **4**, 1813-1821.
97. S. X. Ouyang, P. Li, H. Xu, H. Tong, L. Q. Liu and J. H. Ye, *ACS Appl. Mater. Interfaces*, 2014, **6**, 22726-22732.
98. H. Wang, J. Gao, T. Q. Guo, R. M. Wang, L. Guo, Y. Liu and J. H. Li, *Chem. Commun.*, 2012, **48**, 275-277.
99. M. Ge, N. Zhu, Y. P. Zhao, J. Li and L. Liu, *Ind. Eng. Chem. Res.*, 2012, **51**, 5167-5173.
100. C. Jaramillo-Paez, J. A. Navio, M. C. Hidalgo, A. Bouziani and M. El Azzouzi, *J. Photochem. Photobiol. A-Chem.*, 2017, **332**, 521-533.
101. X. Xiao, R. P. Hu, C. Liu, C. L. Xing, C. Qian, X. X. Zuo, J. M. Nan and L. S. Wang, *Appl. Catal. B-Environ.*, 2013, **140**, 433-443.
102. B. Sun, E. P. Reddy and P. G. Smirniotis, *Environ. Sci. Technol.*, 2005, **39**, 6251-6259.
103. J. K. Yang and A. P. Davis, *Environ. Sci. Technol.*, 2000, **34**, 3789-3795.
104. V. N. Salomone, J. M. Meichtry, G. Zampieri and M. I. Litter, *Chem. Eng. J.*, 2015, **261**, 27-35.
105. M. A. Ferguson and J. G. Hering, *Environ. Sci. Technol.*, 2006, **40**, 4261-4267.
106. V. W. Atul, G. S. Gaikwad, M. G. Dhonde, N. T. Khaty and S. R. Thakare, *Res. J. Chem. Environ.*, 2013, **17**, 84-94.

107. J. A. Rengifo-Herrera, J. Sanabria, F. Machuca, C. F. Dierolf, C. Pulgarin and G. Orellana, *J. Sol. Energy Eng. Trans.-ASME*, 2007, **129**, 135-140.
108. Y. Wu, G. Zhang, W. Guan and X. Zhang, *Micro Nano Lett.*, 2014, **9**, 119-122.
109. T. Yoshida, Y. Minoura, Y. Nakano, M. Yamamoto, S. Yagi, H. Yoshida and Iop, *J. Phys. Conf. Ser.*, 2016, **712**, 1-4.
110. L. Kong, Y. Dong, P. Jiang, G. Wang, H. Zhang and N. Zhao, *J. Mater. Chem. A*, 2016, **4**, 9998-10007.
111. M. Qamar, Z. H. Yamani, M. A. Gondal and K. Alhooshani, *Solid State Sci.*, 2011, **13**, 1748-1754.
112. M. Zhang, Q. Wang, C. Chen, L. Zang, W. Ma and J. Zhao, *Angew. Chem. Int. Ed.*, 2009, **48**, 6081-6084.
113. K. Inumaru, M. Murashima, T. Kasahara and S. Yamanaka, *Appl. Catal. B- Environ.*, 2004, **52**, 275-280.
114. M. A. Lazar and W. A. Daoud, *RSC Adv.*, 2012, **2**, 447-452.
115. D. Robert, A. Piscopo and J.-V. Weber, *Environ. Chem. Lett.*, 2004, **2**, 5-8.
116. Y. Ide, Y. Koike and M. Ogawa, *J. Colloid Interface Sci.*, 2011, **358**, 245-251.
117. C. P. Canlas, J. Lu, N. A. Ray, N. A. Grosso-Giordano, S. Lee, J. W. Elam, R. E. Winans, R. P. Van Duyne, P. C. Stair and J. M. Notestein, *Nat Chem*, 2012, **4**, 1030-1036.
118. O. S. Mohamed, A. E.-A. M. Gaber and A. A. Abdel-Wahab, *J. Photochem. Photobiol. A*, 2002, **148**, 205-210.
119. C. R. López, E. P. Melián, J. A. Ortega Méndez, D. E. Santiago, J. M. Doña Rodríguez and O. González Díaz, *J. Photochem. Photobiol. A*, 2015, **312**, 45-54.
120. C.-J. Li, G.-R. Xu, B. Zhang and J. R. Gong, *Appl. Catal. B-Environ.*, 2012, **115**, 201-208.
121. A. R. Fujishima, T. N.; Tryk, D. A., *J. Photochem. Photobiol. C*, 2000, **1**, 1-21.
122. W. Kim, T. Tachikawa, G.-h. Moon, T. Majima and W. Choi, *Angew. Chem. Int. Ed.*, 2014, **53**, 14036-14041.
123. O. A. Ibhaddon and P. Fitzpatrick, *Catalysts*, 2013, **3**, 189-218.

124. D. A. Armstrong, R. E. Huie, S. Lyman, W. H. Koppenol, G. Merényi, P. Neta, D. M. Stanbury, S. Steenken and P. Wardman, *Pure Appl. Chem.*, 2013, **87**, 1139-1150.
125. K. Imamura, K. Hashimoto and H. Kominami, *Chem. Commun.*, 2012, **48**, 4356-4358.
126. H. Wang, J. Yan, W. Chang and Z. Zhang, *Catal. Commun.*, 2009, **10**, 989-994.
127. H. Tada, T. Ishida, A. Takao, S. Ito, S. Mukhopadhyay, T. Akita, K. Tanaka and H. Kobayashi, *ChemPhysChem*, 2005, **6**, 1537-1543.
128. P. Ciambelli, D. Sannino, V. Palma and V. Vaiano, *Catal. Today*, 2005, **99**, 143-149.
129. Y. Luo and D. F. Ollis, *J. Catal.*, 1996, **163**, 1-11.
130. F. Parrino, A. Ramakrishnan and H. Kisch, *Angew. Chem. Int. Ed.*, 2008, **47**, 7107-7109.
131. L. Bai, F. Li, Y. Wang, H. Li, X. Jiang and L. Sun, *Chem. Commun.*, 2016, **52**, 9711-9714.
132. W.-K. Jo and T. S. Natarajan, *J. Colloid Interface Sci.*, 2016, **482**, 58-72.
133. O. Tomita, T. Otsubo, M. Higashi, B. Ohtani and R. Abe, *ACS Catal.*, 2016, **6**, 1134-1144.
134. X. Xiao, R. Hu, C. Liu, C. Xing, C. Qian, X. Zuo, J. Nan and L. Wang, *Appl. Catal., B*, 2013, **140-141**, 433-443.
135. T. Gao, Z. Chen, Y. X. Zhu, F. Niu, Q. L. Huang, L. S. Qin, X. G. Sun and Y. X. Huang, *Mater. Res. Bull.*, 2014, **59**, 6-12.
136. J. Liu, H. Wang, S. Wang and H. Yan, *Mater. Sci. Eng., B*, 2003, **104**, 36-39.
137. W. T. Sun, M. Z. Xie, L. Q. Jing, Y. B. Luan and H. G. Fu, *J. Solid State Chem.*, 2011, **184**, 3050-3054.
138. L. Zhang, W. Wang, Z. Chen, L. Zhou, H. Xu and W. Zhu, *J. Mater. Chem.*, 2007, **17**, 2526-2532.
139. B. Zhang, J. Li, B. Zhang, R. Chong, R. Li, B. Yuan, S.-M. Lu and C. Li, *J. Catal.*, 2015, **332**, 95-100.

140. R. Abe, H. Takami, N. Murakami and B. Ohtani, *J. Am. Chem. Soc.*, 2008, **130**, 7780-7781.
141. S. Sakthivel, B. Neppolian, M. V. Shankar, B. Arabindoo, M. Palanichamy and V. Murugesan, *Sol. Energy Mater. Sol. Cells*, 2003, **77**, 65-82.
142. A. McLaren, T. Valdes-Solis, G. Q. Li and S. C. Tsang, *J. Am. Chem. Soc.*, 2009, **131**, 12540-12541.
143. Y. S. Hu, A. Kleiman-Shwarscstein, A. J. Forman, D. Hazen, J. N. Park and E. W. McFarland, *Chem. Mater.*, 2008, **20**, 3803-3805.
144. S. Y. Zeng, K. B. Tang, T. W. Li, Z. H. Liang, D. Wang, Y. K. Wang, Y. X. Qi and W. W. Zhou, *J. Phys. Chem. C*, 2008, **112**, 4836-4843.
145. Y. Q. Wang, Z. J. Zhang, Y. Zhu, Z. C. Li, R. Vajtai, L. J. Ci and P. M. Ajayan, *ACS Nano*, 2008, **2**, 1492-1496.
146. H. L. Fei, H. J. Zhou, J. G. Wang, P. C. Sun, D. T. Ding and T. H. Chen, *Solid State Sci.*, 2008, **10**, 1276-1284.
147. M. Fujihira, Y. Satoh and T. Osa, *Nature*, 1981, **293**, 206-208.
148. L. Cermenati, A. Albin, L. Cermenati, C. Richter and A. Albin, *Chem. Commun.*, 1998, **7**, 805-806.
149. T. Ohno, *J. Catal.*, 2001, **204**, 163-168.
150. T. Ohno, T. Tsubota, K. Kakiuchi, S. Miyayama and K. Sayama, *J. Mol. Catal. A: Chem.*, 2006, **245**, 47-54.
151. A. Hakki, R. Dillert and D. Bahnemann, *Catal. Today*, 2009, **144**, 154-159.
152. M. I. Qadir, J. D. Scholten and J. Dupont, *J. Mol. Catal. A: Chem.*, 2014, **383-384**, 225-230.
153. Y. L. Liu, M. F. Zhang, C. H. Tung and Y. F. Wang, *ACS Catal.*, 2016, **6**, 8389-8394.
154. P. L. Liao, M. C. Toroker and E. A. Carter, *Nano Lett.*, 2011, **11**, 1775-1781.
155. T. P. Ruoko, K. Kaunisto, M. Bartsch, J. Pohjola, A. Hiltunen, M. Niederberger, N. V. Tkachenko and H. Lemmetyinen, *J. Phys. Chem. Lett.*, 2015, **6**, 2859-2864.
156. K. A. Newton and F. E. Osterloh, *Top. Catal.*, 2016, **59**, 750-756.

157. M. P. Dare-Edwards, J. B. Goodenough, A. Hamnett and P. R. Trellick, *J. Chem. Soc.*, 1983, **79**, 2027-2041.
158. R. K. Quinn, R. D. Nasby and R. J. Baughman, *Mater. Res. Bull.*, 1976, **11**, 1011-1017.
159. K. Itoh and J. O. M. Bockris, *J. Appl. Phys.*, 1984, **56**, 874-876.
160. Z. Zhao, Z. Li and Z. Zou, *PCCP*, 2011, **13**, 4746-4753.
161. K. E. Kweon and G. S. Hwang, *Phys. Rev. B*, 2012, **86**, 1-8.
162. J. K. Cooper, S. Gul, F. M. Toma, L. Chen, P.-A. Glans, J. Guo, J. W. Ager, J. Yano and I. D. Sharp, *Chem. Mater.*, 2014, **26**, 5365-5373.
163. H. A. Ahsaine, A. El Jaouhari, A. Slassi, M. Ezahri, A. Benlhachemi, B. Bakiz, F. Guinneton and J. R. Gavarri, *RSC Adv.*, 2016, **6**, 101105-101114.
164. S. G. Kumar and K. S. R. K. Rao, *Appl. Surf. Sci.*, 2015, **355**, 939-958.
165. H. Fu, L. Zhang, W. Yao and Y. Zhu, *Appl. Catal. B-Environ.*, 2006, **66**, 100-110.
166. S. Sun and W. Wang, *RSC Adv.*, 2014, **4**, 47136-47152.
167. M. Mączka, L. Macalik, K. Hermanowicz, L. Kępiński and P. Tomaszewski, *J. Raman. Spectrosc.*, 2010, **41**, 1059-1066.
168. M. Oshikiri and M. Boero, *J. Phys. Chem. B*, 2006, **110**, 9188-9194.
169. A. J. E. Rettie, H. C. Lee, L. G. Marshall, J.-F. Lin, C. Capan, J. Lindemuth, J. S. McCloy, J. Zhou, A. J. Bard and C. B. Mullins, *J. Am. Chem. Soc.*, 2013, **135**, 11389-11396.
170. Z. H. Zhu, P. Sarker, C. Q. Zhao, L. T. Zhou, R. L. Grimm, M. N. Huda and P. M. Rao, *ACS Appl. Mater. Interfaces*, 2017, **9**, 1459-1470.
171. R. Hailili, G. H. Dong, Y. C. Ma, S. Jin, C. Y. Wang and T. Xu, *Ind. Eng. Chem. Res.*, 2017, **56**, 2908-2916.
172. A. V. Egorysheva, O. M. Gajtko, P. O. Rudnev, O. G. Ellert and V. K. Ivanov, *Eur. J. Inorg. Chem.*, 2016, DOI: 10.1002/ejic.201501159, 2193-2199.
173. C. Liu, X. B. Li, J. Z. Su and L. J. Guo, *Int. J. Hydrogen Energy*, 2016, **41**, 12842-12851.
174. H. Golmojdeh and M. A. Zanjanchi, *Cryst. Res. Technol.*, 2012, **47**, 1014-1025.

175. Y. Zhang, N. Zhang, Z.-R. Tang and Y.-J. Xu, *Chem. Sci.*, 2013, **4**, 1820-1824.
176. J. L. Ortiz-Quiñonez, D. Díaz, I. Zumeta-Dubé, H. Arriola-Santamaría, I. Betancourt, P. Santiago-Jacinto and N. Nava-Etzana, *Inorg. Chem.*, 2013, **52**, 10306-10317.
177. M. Sakar, S. Balakumar, P. Saravanan and S. N. Jaisankar, *Mater. Res. Bull.*, 2013, **48**, 2878-2885.
178. T. Soltani and M. H. Entezari, *J. Mol. Catal. A: Chem.*, 2013, **377**, 197-203.
179. T. Soltani and M. H. Entezari, *Chem. Eng. J.*, 2014, **251**, 207-216.
180. C. Y. Song, J. B. Xu, A. Yimamu and L. Wang, *Integr. Ferroelectr.*, 2014, **153**, 33-41.
181. Q. Y. Zeng, J. Bai, J. H. Li, L. G. Xia, K. Huang, X. J. Li and B. X. Zhou, *J. Mater. Chem. A*, 2015, **3**, 4345-4353.
182. J. W. Jang, C. Du, Y. F. Ye, Y. J. Lin, X. H. Yao, J. Thorne, E. Liu, G. McMahan, J. F. Zhu, A. Javey, J. H. Guo and D. W. Wang, *Nat. Commun.*, 2015, **6**, 5.
183. S. Zhang, C. Zhang, Y. Man and Y. Zhu, *J. Solid State Chem.*, 2006, **179**, 62-69.
184. I. Tamiolakis, I. N. Lykakis and G. S. Armatas, *Catal. Today*, 2015, **250**, 180-186.
185. X. Zhou, F. Li, X. N. Li, H. Li, Y. Wang and L. C. Sun, *Dalton Trans.*, 2015, **44**, 475-479.
186. X. C. Song, Y. F. Zheng, R. Ma, Y. Y. Zhang and H. Y. Yin, *J. Hazard. Mater.*, 2011, **192**, 186-191.
187. C. Zhang and Y. Zhu, *Chem. Mater.*, 2005, **17**, 3537-3545.
188. X. Zhang, Z. Ai, F. Jia, L. Zhang, X. Fan and Z. Zou, *Mater. Chem. Phys.*, 2007, **103**, 162-167.
189. V. D. Nithya, R. Kalai Selvan, D. Kalpana, L. Vasylechko and C. Sanjeeviraja, *Electrochim. Acta*, 2013, **109**, 720-731.
190. S. Basu and D. Chakravorty, *J. Non-Cryst. Solids*, 2006, **352**, 380-385.
191. A. Jitianu, M. Crisan, A. Meghea, I. Rau and M. Zaharescu, *J. Mater. Chem.*, 2002, **12**, 1401-1407.

192. K. Brezesinski, R. Ostermann, P. Hartmann, J. Perlich and T. Brezesinski, *Chem. Mater.*, 2010, **22**, 3079-3085.
193. M. Schlesinger, M. Weber, S. Schulze, M. Hietschold and M. Mehring, *Chemistryopen*, 2013, **2**, 146-155.
194. S. Tamilvanan, G. Gurumoorthy, S. Thirumaran and S. Ciattini, *Polyhedron*, 2017, **123**, 111-121.
195. T. Hashimoto, H. Ohta, H. Nasu and A. Ishihara, *Int. J. Hydrogen Energy*, 2016, **41**, 7388-7392.
196. Y. Yan, Z. Zhou, Y. Cheng, L. Qiu, C. Gao and J. Zhou, *J. Alloys Compd.*, 2014, **605**, 102-108.
197. H. Jiang, H. Dai, X. Meng, K. Ji, L. Zhang and J. Deng, *Appl. Catal., B*, 2011, **105**, 326-334.
198. U. M. García Pérez, S. Sepúlveda-Guzmán, A. Martínez-de la Cruz and U. Ortiz Méndez, *J. Mol. Catal. A: Chem.*, 2011, **335**, 169-175.
199. Y. Liang, T. Tsubota, L. P. A. Mooij and R. van de Krol, *J. Phys. Chem. C*, 2011, **115**, 17594-17598.
200. T. W. Kim and K. S. Choi, *Science*, 2014, **343**, 990-994.
201. R. Mitchell, R. Brydson and R. E. Douthwaite, *Nanoscale*, 2014, **6**, 4043-4046.
202. Y. X. Liu, H. X. Dai, J. G. Deng, L. Zhang and C. T. Au, *Nanoscale*, 2012, **4**, 2317-2325.
203. P. Kohls, D. Jadhav, G. Pandey and O. Reiser, *Org. Lett.*, 2012, **14**, 672-675.
204. J. Lalevee, F. Dumur, C. R. Mayer, D. Gigmes, G. Nasr, M. A. Tehfe, S. Telitel, F. Morlet-Savary, B. Graff and J. P. Fouassier, *Macromolecules*, 2012, **45**, 4134-4141.
205. W. Luo, L. Zhu, N. Wang, H. Tang, M. Cao and Y. She, *Environ. Sci. Technol.*, 2010, **44**, 1786-1791.
206. J. An, L. Zhu, Y. Zhang and H. Tang, *J. Environ. Sci.*, 2013, **25**, 1213-1225.
207. J. An, L. Zhu, N. Wang, Z. Song, Z. Yang, D. Du and H. Tang, *Chem. Eng. J.*, 2013, **219**, 225-237.
208. K. H. Reddy, S. Martha and K. M. Parida, *RSC Adv.*, 2012, **2**, 9423-9436.

209. Y. Peng, M. Yan, Q.-G. Chen, C.-M. Fan, H.-Y. Zhou and A.-W. Xu, *J. Mater. Chem. A*, 2014, **2**, 8517-8524.
210. J. Wang and F. E. Osterloh, *J. Mater. Chem. A*, 2014, **2**, 9405-9411.
211. A. J. Motheo, G. Tremiliosi-Filho, E. R. Gonzalez, K. B. Kokoh, J.-M. Léger and C. Lamy, *J. Appl. Electrochem.*, 2006, **36**, 1035-1041.
212. P. Ju, P. Wang, B. Li, H. Fan, S. Ai, D. Zhang and Y. Wang, *Chem. Eng. J.*, 2014, **236**, 430-437.
213. Y. Tian, B. Chang, Z. Yang, B. Zhou, F. Xi and X. Dong, *RSC Adv.*, 2014, **4**, 4187-4193.
214. Q. Yuan, L. Chen, M. Xiong, J. He, S.-L. Luo, C.-T. Au and S.-F. Yin, *Chem. Eng. J.*, 2014, **255**, 394-402.
215. X. N. Liu, Q. F. Lu and J. H. Liu, *J. Alloys Compd.*, 2016, **662**, 598-606.
216. Z. F. Zhu, Y. Yan and J. Q. Li, *J. Mater. Sci.*, 2016, **51**, 2112-2120.
217. G. Lu, F. Wang and X. J. Zou, *J. Alloys Compd.*, 2017, **697**, 417-426.
218. M. Zalfani, Z.-Y. Hu, W.-B. Yu, M. Mahdouani, R. Bourguiga, M. Wu, Y. Li, G. Van Tendeloo, Y. Djaoued and B.-L. Su, *Appl. Catal. B-Environ.*, 2017, **205**, 121-132.
219. J. A. Seabold, K. Zhu and N. R. Neale, *PCCP*, 2014, **16**, 1121-1131.
220. L. Shan, H. Liu and G. Wang, *J. Nanopart. Res.*, 2015, **17**, 181.
221. A. Yengantiwar, S. Palanivel, P. S. Archana, Y. X. Ma, S. L. Pan and A. Gupta, *J. Phys. Chem. C*, 2017, **121**, 5914-5924.
222. S. Shen, S. A. Lindley, X. Chen and J. Z. Zhang, *Energy Environ. Sci.*, 2016, **9**, 2744-2775.
223. J. Li, M. Zhang, X. Li, Q. Y. Li and J. J. Yang, *Appl. Catal. B-Environ.*, 2017, **212**, 106-114.
224. X. Zhou, F. Li, X. Li, H. Li, Y. Wang and L. Sun, *Dalton Trans.*, 2015, **44**, 475-479.
225. R. A. Sheldon, I. W. C. E. Arends and A. Dijksman, *Catal. Today*, 2000, **57**, 157-166.



226. A. Di Sotto, F. Maffei, P. Hrelia, S. Di Giacomo, E. Pagano, F. Borrelli and G. Mazzanti, *Regul. Toxicol. Pharm.*, 2014, **68**, 16-22.
227. F. Hessler, R. Betik, A. Kadlcikova, R. Belle and M. Kotora, *Eur. J. Org. Chem.*, 2014, **2014**, 7245-7252.
228. C. A. Hobbs, S. V. Taylor, C. Beevers, M. Lloyd, R. Bowen, L. Lillford, R. Maronpot and S. Hayashi, *Food Chem. Toxicol.*, 2016, **97**, 232-242.
229. S. L. Zhang and Z. Q. Deng, *Org. Biomol. Chem.*, 2016, **14**, 7282-7294.
230. C. Cidarar, M. Hoffmann, J. Oelmann, B. Wolfram and M. Broring, *Eur. J. Org. Chem.*, 2017, DOI: 10.1002/ejoc.201601243, 77-86.
231. R. Ratcliffe and R. Rodehorst, *J. Org. Chem.*, 1970, **35**, 4000-4002.
232. A. Shaabani and D. G. Lee, *Tetrahedron Lett.*, 2001, **42**, 5833-5836.
233. K. Asadolah, M. M. Heravi, R. Hekmatshoar and S. Majedi, *Molecules*, 2007, **12**, 958-964.
234. M. Y. Zheng, Y. S. Wei, G. Fan and Y. Huang, *Asian J. Chem.*, 2012, **24**, 161-164.
235. S. Aït-Mohand, F. Hénin and J. Muzart, *Tetrahedron Lett.*, 1995, **36**, 2473-2476.
236. I. E. Markó, P. R. Giles, M. Tsukazaki, I. Chellé-Regnaut, C. J. Urch and S. M. Brown, *J. Am. Chem. Soc.*, 1997, **119**, 12661-12662.
237. W. Feng, G. Wu, L. Li and N. Guan, *Green Chem.*, 2011, **13**, 3265-3272.
238. J. C. Colmenares, W. Ouyang, M. Ojeda, E. Kuna, O. Chernyayeva, D. Lisovytskiy, S. De, R. Luque and A. M. Balu, *Appl. Catal., B*, 2016, **183**, 107-112.
239. J. Yang, X. Shen, Y. Li, L. Bian, J. Dai and D. Yuan, *ChemCatChem*, 2016, **8**, 1399-1409.
240. Y. H. Xiang, P. Ju, Y. Wang, Y. Sun, D. Zhang and J. Q. Yu, *Chem. Eng. J.*, 2016, **288**, 264-275.
241. S. Selvarajan, A. Suganthi, M. Rajarajan and K. Arunprasath, *Powder Technol.*, 2017, **307**, 203-212.
242. X. Qin, L. Q. Jing, G. H. Tian, Y. C. Qu and Y. J. Feng, *J. Hazard. Mater.*, 2009, **172**, 1168-1174.

243. J. G. Yu, H. G. Yu, B. Cheng, M. H. Zhou and X. J. Zhao, *J. Mol. Catal. A-Chem.*, 2006, **253**, 112-118.
244. M. Gong, D.-Y. Wang, C.-C. Chen, B.-J. Hwang and H. Dai, *Nano Research*, 2016, **9**, 28-46.
245. Y. Kwon, S. C. S. Lai, P. Rodriguez and M. T. M. Koper, *J. Am. Chem. Soc.*, 2011, **133**, 6914-6917.
246. K. D. Dobson and A. J. McQuillan, *Spectrochim. Acta, Part A*, 2000, **56**, 557-565.
247. T. Nakayama, T. Matsushima and H. Murata, *Thin Solid Films*, 2009, **518**, 739-742.
248. R. Vianello and Z. B. Maksic, *J. Phys. Org. Chem.*, 2005, **18**, 699-705.
249. L. P. Hammett, *J. Am. Chem. Soc.*, 1937, **59**, 96-103.
250. L. Qiu, D. D. Pang, C. L. Zhang, J. J. Meng, R. S. Zhu and F. Ouyang, *Appl. Surf. Sci.*, 2015, **357**, 189-196.
251. T. Y. Lei, Q. C. Li, S. F. Chen, Z. Y. Liu and Q. Y. Liu, *Chem. Eng. J.*, 2016, **296**, 1-10.
252. Y. Yan, Y. H. Dai, H. He, Y. B. Yu and Y. H. Yang, *Appl. Catal., B*, 2016, **196**, 108-116.
253. M. F. Yu, X. D. Li, Y. Ren, T. Chen, S. Y. Lu and J. H. Yan, *Environ. Prog. Sustain. Energy*, 2016, **35**, 1265-1273.
254. L. Zhu, Z. P. Zhong, H. Yang and C. H. Wang, *Water Air Soil Pollut.*, 2016, **227**, 12.
255. M. J. Hazlett, M. Moses-Debusk, J. E. Parks, L. F. Allard and W. S. Epling, *Appl. Catal., B*, 2017, **202**, 404-417.
256. M. Monai, T. Montini, M. Melchionna, T. Duchon, P. Kus, C. Chen, N. Tsud, L. Nasi, K. C. Prince, K. Veltruska, V. Matolin, M. M. Khader, R. J. Gorte and P. Fornasiero, *Appl. Catal., B*, 2017, **202**, 72-83.
257. F. Westheimer, *Chem. Rev.*, 1961, **61**, 265-273.
258. X. B. Pang, C. C. Chen, H. W. Ji, Y. K. Che, W. H. Ma and J. C. Zhao, *Molecules*, 2014, **19**, 16291-16311.

259. X. Lang, W. Ma, C. Chen, H. Ji and J. Zhao, *Acc. Chem. Res.*, 2013, **47**, 355-363.
260. S. D. Abraham, S. T. David, R. B. Bennie, C. Joel and D. S. Kumar, *J. Mol. Struct.*, 2016, **1113**, 174-181.
261. H. L. Tan, X. Wen, R. Amal and Y. H. Ng, *J. Phys. Chem. Lett.*, 2016, **7**, 1400-1405.
262. M. Zalfani, M. Mahdouani, R. Bourguiga and B. L. Su, *Superlattices Microstruct.*, 2015, **83**, 730-744.
263. C. Karunakaran and S. Kalaivani, *Mater. Sci. Semicond. Process.*, 2014, **27**, 352-361.
264. W. Liu, Y. Yu, L. Cao, G. Su, X. Liu, L. Zhang and Y. Wang, *J. Hazard. Mater.*, 2010, **181**, 1102-1108.
265. C. Franco and J. Olmsted, *Talanta*, 1990, **37**, 905-909.
266. B. Xie, H. Zhang, P. Cai, R. Qiu and Y. Xiong, *Chemosphere*, 2006, **63**, 956-963.
267. D. K. Zhong, S. Choi and D. R. Gamelin, *J. Am. Chem. Soc.*, 2011, **133**, 18370-18377.
268. J. Ravensbergen, F. F. Abdi, J. H. van Santen, R. N. Frese, B. Dam, R. van de Krol and J. T. M. Kennis, *J. Phys. Chem. C*, 2014, **118**, 27793-27800.
269. W.-J. Yin, S.-H. Wei, M. M. Al-Jassim, J. Turner and Y. Yan, *Phys. Rev. B*, 2011, **83**, 155102.
270. I. S. Woodward, W. C. E. Schofield, V. Roucoules, T. J. Bradley and J. P. S. Badyal, *Plasma Chem. Plasma Process.*, 2006, **26**, 507-516.
271. H. Murase and T. Fujibayashi, *Prog. Org. Coat.*, 1997, **31**, 97-104.
272. Y. Zhang, C. Rocco, F. Karasu, L. G. J. van der Ven, R. van Benthem, X. Allonas, C. Croutxe-Barghorn, A. C. C. Esteves and G. de With, *Polymer*, 2015, **69**, 384-393.
273. M. Hird, *Chem. Soc. Rev.*, 2007, **36**, 2070-2095.
274. R. Berger, G. Resnati, P. Metrangolo, E. Weber and J. Hulliger, *Chem. Soc. Rev.*, 2011, **40**, 3496-3508.

275. H. J. Bohm, D. Banner, S. Bendels, M. Kansy, B. Kuhn, K. Muller, U. Obst-Sander and M. Stahl, *Chembiochem*, 2004, **5**, 637-643.
276. B. K. Park, N. R. Kitteringham and P. M. O'Neill, *Annu. Rev. Pharmacool. Toxicol.*, 2001, **41**, 443-470.
277. P. Zhou, J. W. Zou, F. F. Tian and Z. C. Shang, *J. Chem Inf. Model.*, 2009, **49**, 2344-2355.
278. E. P. Gillis, K. J. Eastman, M. D. Hill, D. J. Donnelly and N. A. Meanwell, *J. Med. Chem.*, 2015, **58**, 8315-8359.
279. P. P. Tang, T. Furuya and T. Ritter, *J. Am. Chem. Soc.*, 2010, **132**, 12150-12154.
280. D. A. Nagib and D. W. C. MacMillan, *Nature*, 2011, **480**, 224-228.
281. E. Lee, A. S. Kamlet, D. C. Powers, C. N. Neumann, G. B. Boursalian, T. Furuya, D. C. Choi, J. M. Hooker and T. Ritter, *Science*, 2011, **334**, 639-642.
282. A. Studer, *Angew. Chem.-Int. Ed.*, 2012, **51**, 8950-8958.
283. Y. Yasu, T. Koike and M. Akita, *Angew. Chem.*, 2012, **124**, 9705-9709.
284. W. An, N. Ha, H. M. Lee, Y. R. Malpani, D.-H. Lee, Y.-S. Jung and S. B. Han, *Adv. Synth. Catal.*, 2015, **357**, 3949-3960.
285. D.-F. Luo, J. Xu, Y. Fu and Q.-X. Guo, *Tetrahedron Lett.*, 2012, **53**, 2769-2772.
286. X. Wang, L. Truesdale and J.-Q. Yu, *J. Am. Chem. Soc.*, 2010, **132**, 3648-3649.
287. M. Miura, C.-G. Feng, S. Ma and J.-Q. Yu, *Org. Lett.*, 2013, **15**, 5258-5261.
288. S. Mizuta, S. Verhoog, K. M. Engle, T. Khotavivattana, M. O'Duill, K. Wheelhouse, G. Rassias, M. Médebielle and V. Gouverneur, *J. Am. Chem. Soc.*, 2013, **135**, 2505-2508.
289. C. Zhang, *Org. Biomol. Chem.*, 2014, **12**, 6580-6589.
290. P. Novák, A. Lishchynskiy and V. V. Grushin, *J. Am. Chem. Soc.*, 2012, **134**, 16167-16170.
291. B. Yang, X.-H. Xu and F.-L. Qing, *Org. Lett.*, 2015, **17**, 1906-1909.
292. Z. Ding, G. Q. Lu and P. F. Greenfield, *J. Phys. Chem. B*, 2000, **104**, 4815-4820.
293. A. Zanardi, M. A. Novikov, E. Martin, J. Benet-Buchholz and V. V. Grushin, *J. Am. Chem. Soc.*, 2011, **133**, 20901-20913.

294. A. Sato, J. Han, T. Ono, A. Wzorek, J. L. Acena and V. A. Soloshonok, *Chem. Commun.*, 2015, **51**, 5967-5970.
295. B. Wang, D.-C. Xiong and X.-S. Ye, *Org. Lett.*, 2015, **17**, 5698-5701.
296. B. Luo, Q. Cui, H. Luo, Y. Hu, P. Huang and S. Wen, *Adv. Synth. Catal.*, 2016, **358**, 2733-2738.
297. C. Li, K. Suzuki, K. Yamaguchi and N. Mizuno, *New J. Chem.*, 2017, **41**, 1417-1420.
298. J.-Y. Yang, X.-H. Xu and F.-L. Qing, *J. Fluorine Chem.*, 2016, **186**, 45-51.
299. B. Raimier, P. G. Jones and T. Lindel, *J. Fluorine Chem.*, 2014, **166**, 8-14.
300. P. J. Kerr, S. M. Pyke and A. D. Ward, *Aust. J. Chem.*, 2008, **61**, 350-358.
301. W. J. Peláez, M. A. Burgos Paci and G. A. Argüello, *Tetrahedron Lett.*, 2009, **50**, 1934-1938.
302. P. H. Tran, H. T. Nguyen, P. E. Hansen and T. N. Le, *ChemistrySelect*, 2017, **2**, 571-575.
303. B. Nammalwar and R. A. Bunce, *Tetrahedron Lett.*, 2013, **54**, 4330-4332.
304. N. Iranpoor, N. Maleki, S. Razi and A. Safavi, *Talanta*, 1992, **39**, 281-284.
305. S. Matsugo and K. Kanamori, *Coord. Chem. Rev.*, 2011, **255**, 2388-2397.
306. G. J. Reiss, W. Frank and J. Schneider, *Main Group Met. Chem.*, 1995, **18**, 287-294.
307. H. Yu, R. Liu, X. Wang, P. Wang and J. Yu, *Appl. Catal. B-Environ.*, 2012, **111-112**, 326-333.
308. G. Zhang, G. Li and X. Wang, *ChemCatChem*, 2015, **7**, 2864-2870.
309. Y. Xu, J. Song, F. Chen, X. Wang, H. Yu and J. Yu, *RSC Adv.*, 2016, **6**, 65902-65910.
310. Q. Zhai, S. Xie, W. Fan, Q. Zhang, Y. Wang, W. Deng and Y. Wang, *Angew. Chem. Int. Ed.*, 2013, **52**, 5776-5779.
311. C. D. McTiernan, S. P. Pitre, H. Ismaili and J. C. Scaiano, *Adv. Synth. Catal.*, 2014, **356**, 2819-2824.
312. Y. Shiraishi, H. Sakamoto, K. Fujiwara, S. Ichikawa and T. Hirai, *ACS Catal.*, 2014, **4**, 2418-2425.

313. K. Maeda, *J. Photochem. Photobiol. C*, 2011, **12**, 237-268.
314. D. Wang, R. Li, J. Zhu, J. Shi, J. Han, X. Zong and C. Li, *J. Phys. Chem. C*, 2012, **116**, 5082-5089.
315. T. H. Jeon, W. Choi and H. Park, *PCCP*, 2011, **13**, 21392-21401.
316. T. W. Kim and K.-S. Choi, *Science*, 2014, **343**, 990-994.
317. Y. Shiraishi, D. Tsukamoto, Y. Sugano, A. Shiro, S. Ichikawa, S. Tanaka and T. Hirai, *ACS Catal.*, 2012, **2**, 1984-1992.
318. H. Yoshida, Y. Fujimura, H. Yuzawa, J. Kumagai and T. Yoshida, *Chem. Commun.*, 2013, **49**, 3793-3795.
319. A. Tyagi, T. Matsumoto, T. Kato and H. Yoshida, *Catal. Sci. Technol.*, 2016, **6**, 4577-4583.
320. A. K. Vijh and B. E. Conway, *Chem. Rev.*, 1967, **67**, 623-664.
321. A. Mills, *J. Chem. Soc., Chem. Commun.*, 1982, **6**, 367-368.
322. A. C. Hillier, G. A. Grasa, M. S. Viciu, H. M. Lee, C. L. Yang and S. P. Nolan, *J. Organomet. Chem.*, 2002, **653**, 69-82.
323. Y. J. Deng, L. Z. Gong, A. Q. Mi, H. Liu and Y. Z. Jiang, *Synthesis*, 2003, 337-339.
324. N. Miyaura and A. Suzuki, *Chem. Rev.*, 1995, **95**, 2457-2483.
325. I. P. Beletskaya and A. V. Cheprakov, *Chem. Rev.*, 2000, **100**, 3009-3066.
326. C. D. McTiernan, X. Leblanc and J. C. Scaiano, *ACS Catal.*, 2017, **7**, 2171-2175.
327. Z. Wang, L. Zhu, F. Yin, Z. Su, Z. Li and C. Li, *J. Am. Chem. Soc.*, 2012, **134**, 4258-4263.
328. D. H. Barton, D. Crich and W. B. Motherwell, *J. Chem. Soc., Chem. Commun.*, 1983, **17**, 939-941.
329. T. Koike and M. Akita, *Synlett*, 2013, **24**, 2492-2505.
330. B. Giese, J. A. González-Gómez and T. Witzel, *Angew. Chem. Int. Ed.*, 1984, **23**, 69-70.
331. I. Ryu, S. Uehara, H. Hirao and T. Fukuyama, *Org. Lett.*, 2008, **10**, 1005-1008.
332. A. Millet, Q. Lefebvre and M. Rueping, *Chem. Eur. J.*, 2016, **22**, 13464-13468.

333. M. Sadhukhan, M. K. Kundu, T. Bhowmik and S. Barman, *Int. J. Hydrogen Energy*, 2017, **42**, 9371-9383.
334. K. Jukk, N. Kongi, P. Rauwel, L. Matisen and K. Tammeveski, *Electrocatalysis*, 2016, **7**, 428-440.
335. R. Khanam, D. Taparia, B. Mondal and D. Mohanta, *Appl. Phys. A Mater. Sci. Proc.*, 2016, **122**, 7.
336. V. Vaiano, G. Iervolino, D. Sannino, J. J. Murcia, M. C. Hidalgo, P. Ciambelli and J. A. Navio, *Appl. Catal. B-Environ.*, 2016, **188**, 134-146.
337. M. R. Gholipour, F. Béland and T.-O. Do, *ACS Sustain. Chem. Eng.*, 2017, **5**, 213-220.
338. T. Morimoto, M. Nagao and F. Tokuda, *J. Phys. Chem.*, 1969, **73**, 243-248.
339. D. J. Vyas, E. Larionov, C. Besnard, L. Guénée and C. Mazet, *J. Am. Chem. Soc.*, 2013, **135**, 6177-6183.
340. N. Humbert, D. J. Vyas, C. Besnard and C. Mazet, *Chem. Commun.*, 2014, **50**, 10592-10595.
341. J. D. Bacha and J. K. Kochi, *J. Org. Chem.*, 1968, **33**, 83-93.
342. K. B. Wiberg, *J. Org. Chem.*, 2002, **67**, 4787-4794.
343. M. Rueda-Becerril, C. Chatalova Sazepin, J. C. T. Leung, T. Okbinoglu, P. Kennepohl, J.-F. Paquin and G. M. Sammis, *J. Am. Chem. Soc.*, 2012, **134**, 4026-4029.
344. C. U. Grünanger and B. Breit, *Angew. Chem. Int. Ed.*, 2008, **47**, 7346-7349.
345. J. Hioe and H. Zipse, *Org. Biomol. Chem.*, 2010, **8**, 3609-3617.